THE UNIVERSITY
of EDINBURGH

Auto-Extinction *of* Engineered Timber

Alastair Ian Bartlett

Doctor *of* Philosophy

The University *of* Edinburgh

2018

Auto-Extinction *of* **Engineered Timber**

Alastair Ian Bartlett

The thesis has been supervised by

Dr Rory Hadden

and

Prof. Luke Bisby

The examining committee consisted of

Prof. José Torero

and

Dr Angus Law

Table of Contents

List of Figures

List of Tables

Declaration

This thesis and the work described herein have been undertaken solely by Alastair Bartlett at the University of Edinburgh unless otherwise stated. This work has not been submitted for any other degree or professional qualification.

The experimental work described in Chapter 4 and used in Chapter 5 as part of the "Compartment fires in support of tall timber construction" project was undertaken by Alastair Bartlett, Felix Wiesner, Juan Hidalgo, Simón Santamaria, and Rory Hadden, with assistance from Mark Fenton, Nikolai Gerasimov, and Timothy Putzien, and technical support from the BRE burn hall staff. All analysis presented herein was undertaken by Alastair Bartlett.

The intermediate-scale experimental work described in Chapter 6 was undertaken by Alastair Bartlett, Chris Bateman, and Lukas Rutkauskas. All analysis presented herein was undertaken by Alastair Bartlett.

Alastair Bartlett
2018

Abstract

Engineered timber products are becoming increasingly popular in the construction industry due to their attractive aesthetic and sustainability credentials. Cross-laminated timber (CLT) is one such engineered timber product, formed of multiple layers of timber planks glued together with adjacent layers perpendicular to each other. Unlike traditional building materials such as steel and concrete, the timber structural elements can ignite and burn when exposed to fire, and thus this risk must be explicitly addressed during design. Current design guidance focusses on the structural response of engineered timber, with the flammability risk typically addressed by encapsulation of any structural timber elements with the intention of preventing their involvement in a fire. Exposed structural timber elements may act as an additional fuel load, and this risk must be adequately quantified to satisfy the intent of the building regulations in that the structure does not continue burning. This can be achieved through timber's natural capacity to auto-extinguish when the external heat source is removed or sufficiently reduced.

To address these issues, a fundamental understanding of auto-extinction and the conditions necessary to achieve it in real fire scenarios is needed. Bench-scale flammability studies were undertaken in the Fire Propagation Apparatus to explore the conditions under which auto-extinction will occur. Critical conditions were determined experimentally as a mass loss rate of 3.48 ± 0.31 g/m^{2}s, or an incident heat flux of ~30 kW/m^2. Mass loss rate was identified as the better criterion, as critical heat flux was shown by comparison with literature data to be heavily dependent on apparatus.

Subsequently, full-scale compartment fire experiments with exposed timber surfaces were performed to determine if auto-extinction could be achieved in real fire scenarios. It was demonstrated that auto-extinction could be achieved in a compartment fire scenario, but only if significant delamination of the engineered timber product could be prevented. A full-scale compartment fire experiment with an exposed back wall and

ceiling achieved auto-extinction after around 21 minutes, at which point no significant delamination of the first lamella had been observed. Experiments with an exposed back and side wall, and experiments with an exposed back wall, side wall, and ceiling underwent sustained burning due to repeated delamination, and an increased quantity of exposed timber respectively.

Firepoint theory was used to predict the mass loss rate as a function of external heat flux and heat losses, and was successfully applied to the bench-scale experiments. This approach was then extended to the full-scale compartment fire experiment which achieved auto-extinction. A simplified approach based on experimentally obtained internal temperature fields was able to predict auto-extinction if delamination had not occurred – predicting an extinction time of 20-21 minutes. This demonstrates that the critical mass loss rate of 3.48 ± 0.31 g/m^{2}s determined from bench-scale experiments was valid for application to full-scale compartment fire experiments.

This was further explored through a series of reduced-scale compartment fire experiments, demonstrating that auto-extinction can only reliably be achieved if burnout of the compartment fuel load is achieved before significant delamination of the outer lamella takes place. The quantification of the auto-extinction phenomena and their applicability to full-scale compartment fires explored herein thus allows greater understanding of the effects of exposed timber surfaces on compartment fire dynamics.

Lay Summary

This thesis presents a methodology to quantify the fire risk associated with exposed timber structural walls and floors within modern building design. Cross-laminated timber (CLT) is one such engineered timber product, formed of multiple layers of timber planks glued together, such that each layer is glued at 90° to the adjacent layers. This enables the use of timber as structural wall or floor slabs within a building. Increasingly, architects wish to expose some of this timber, with implications for fire safety, and therefore the fire risk associated with this must be understood. If left exposed, then in the event of a fire, these timber walls and floors will ignite and burn, contributing additional energy to the fire. In order for the exposed timber to sustain burning, there must be a source of heat – in a building fire, this will come from the burning of the room contents. After the building contents have been burnt, this heat source will no longer be available, and the main source of energy will come from the burning of the timber itself. This heat source will be lower than the heat supplied in the initial stages of the fire, when both the exposed timber and the room contents are burning. As these exposed timber surfaces continue to burn, they will build up a layer of char, which serves to reduce the burning rate of the timber. If the exchange of heat between timber surfaces becomes sufficiently low, the timber will stop burning, and the fire will go out.

Small-scale experimentation is undertaken to measure and describe the thermal conditions required for sustained burning of engineered timber products and the conditions under which sustained burning is not supported.

A series of full-scale room fire experiments with exposed timber walls and ceilings were performed to determine the conditions under which sustained burning of the compartment walls and ceiling would occur in a typical sized room, and whether this could be prevented in realistic conditions. It was demonstrated that whilst this could be achieved under specific compartment geometries, conditions under which sustained burning would occur were also identified.

To further explore this, a series of reduced-scale experiments were undertaken, demonstrating the relationship between fuel load and the potential for sustained burning.

An approach to link the bench scale phenomena to large scale fires was developed. A simplified method based on experimental measurements could predict if sustained burning would occur, provided glue-line failure had not occurred and uncertainties in the experimental measurements could be reduced sufficiently. This knowledge provides insight into the effects of exposed timber surfaces on the fire behaviour.

Acknowledgements

First of all, I would like to thank my supervisors, Dr Rory Hadden and Prof. Luke Bisby for their support and input throughout the PhD.

I gratefully acknowledge the support from Arup and the EPSRC in facilitating this research. Thanks to my various industrial supervisors Angus Law, Neal Butterworth, and Susan Deeny for their support throughout, and many fruitful discussions along the way. Thanks are also due to Arup for generous financial support, without which the large-scale experiments would not have been possible.

Significant thanks are due to Michal Krajčovič for all his help and assistance in the laboratory.

Thanks to Felix, Juan, Simón, and Rory for being part of "team timber" down at BRE, for keeping me (relatively) sane for the long time spent down in Watford, and for the many fruitful discussions since.

Thanks to all at BRE, in particular Tom Lennon and Harry Granados for their assistance with the large-scale compartment fire experiments.

KLH are thanked for their generous material support in supplying all the timber needed for the full- and intermediate-scale compartment fire experiments.

Thanks to Chris and Lukas for their help in the intermediate-scale compartment experiments, for ensuring the experiments were completed and for making the lab a fun place to be!

Finally, thanks to all those in John Muir and the Fire Group for making my PhD such an enjoyable experience, both in fruitful discussions about research, and for the many enjoyable barbeques and paellas.

Related Publications

The following journal and conference papers have been published over the course of this thesis. Where these are based on part or whole of a chapter of this thesis, this is indicated.

Journal Papers

Structural Response of Fire-Exposed Cross-Laminated Timber Beams under Sustained Loads, Lineham S., Thomson D., Bartlett A., Bisby, L., and Hadden, R. 2016. *Fire Safety Journal (85) pp. 23-34,* https://doi.org/10.1016/j.firesaf.2016.08.002

Effects of Exposed Cross Laminated Timber on Compartment Fire Dynamics, Hadden R., Bartlett A., Hidalgo J., Santamaria S., Wiesner F., Bisby, L., Deeny, S., and Lane, B. 2017. *Fire Safety Journal (91) pp. 480-489,* https://doi.org/10.1016/j.firesaf.2017.03.074

Auto-Extinction of Engineered Timber: Application to Compartment Fires with Exposed Timber Surfaces, Bartlett A., Hadden, R., Hidalgo J., Santamaria S., Wiesner F., Bisby L., Deeny, S., and Lane B. 2017. *Fire Safety Journal (91) pp. 407-413,* https://doi.org/10.1016/j.firesaf.2017.03.050 - this is based on part of Chapter 5.

Conference Papers

Removing the Fire Barrier to Tall Timber Construction, Bartlett A., Gajewski K., Lineham S., Thomson D., Hadden R., Bisby L., and Butterworth N. 2015. *Infrastructure and Environment Scotland 3rd Postgraduate Conference,* 9 December, Edinburgh, UK.

Sectional Analysis of Cross-Laminated Timber Beams as a Design for Fire Methodology, Bartlett A., Hadden R., Bisby L., and Lane B. 2016. *Structures in Fire, 9th International Conference,* 8-10 June, Princeton, USA.

Auto-Extinction of Engineered Timber: The Application of Firepoint Theory, Bartlett A., Hadden R., Bisby L., and Lane B. 2016. *Interflam, 14th International Symposium,* 4-6 July, Nr Windsor, UK – this is based on Chapter 3.

Auto -Extinction of Engineered Timber as a Design Methodology, Bartlett A., Hadden R., Bisby L., and Lane B. 2016. *World Conference on Timber Engineering,* 22-25 August, Vienna, Austria – this is based on Chapter 3.

Needs for Total Fire Engineering of Mass Timber Buildings, Bartlett A., Wiesner F., Hadden R., Bisby L., Lane B., Lawrence A., Palma P., and Frangi A. 2016. *World Conference on Timber Engineering,* 22-25 August, Vienna, Austria.

Uncertainty Quantification Applied to a Fire-Exposed Glued-Laminated Timber Beam, Bartlett A., Lange D., Anderson J., and Hadden R. 2016. *14th International Probabilistic Workshop,* 5-7 December, Ghent, Belgium.

Nomenclature

Lower-case Latin symbols

a	Absorptivity (-)
c	Distance from corner to differential strip (m)
d	Sample thickness (m, mm)
d_0	Zero-strength layer (mm)
f	Strength (MPa, kN)
f_v	Soot volume fraction (-)
g	Gravitational acceleration (m/s^2)
h	Heat transfer coefficient (W/m^{2}K)
h	Relative humidity (%)
k	Fire plume coefficient (m$^{1/2}$/s, m/kW$^{1/5}$s, m$^{4/3}$/kW$^{1/3}$s)
k	Thermal conductivity (W/mK)
k_0	Zero-strength layer coefficient (-)
m	Mass (kg)
$\dot{m}$	Mass loss rate (g/s, kg/s)
$\dot{m}''$	Mass loss rate per unit area (kg/m^{2}s)
$\dot{m}'''$	Mass loss rate per unit volume (kg/m^{3}s)
n	Number of elements (-)
n	Number of sticks per layer (-)
p	Combination factor (-)
$\dot{q}''$	Heat flux per unit area (kW/m^2)
r	Radius (m)
s	Separation (m, cm)
t	Time (s, min, h)
t^*	Parametric equivalent time (h)
t	Thickness (mm)
u	Gas velocity (m/s)
v	Flame spread rate (m/s)

w	Moisture content (%)
w	Width (mm, cm, m)
x	Depth below char line (mm)
x	Distance (mm)
x_c	Char depth (mm)
y	Wood crib spacing factor (-)
y	Distance (mm)
z	Height above fire source (m)

Upper-case Latin symbols

A	Area (cm^2, m^2)
A	View factor parameter
B	Spalding's B-number
B	Stress-type factor (-)
B	View factor parameter
C	Smoke absorption coefficient ($K^{-1}m^{-1}$)
C	TSC Calibration factor
C	View factor parameter
C_f	Friction coefficient (-)
C_p	Specific heat capacity (kJ/kgK)
D	View factor parameter (-)
E	Heat release per mass of oxygen consumed (kJ.g)
E	View factor parameter (-)
F	View factor (-)
Fo	Fourier number (-)
G	Geometric parameter (-)
H	Height (cm, m)
J	View factor parameter (-)
K	Duct coefficient (-)
L	Length (mm, cm, m)

L	Latent Heat (kJ/kg)
M	Molecular mass (g/mol)
N	Number of layers (-)
$\overline{Nu_L}$	Nusselt number (-)
O	Opening factor ($m^{1/2}$)
P	Perimeter (m)
P	Pressure (kPa)
Pr	Prandtl number (-)
Q_l	Heat losses (MJ/kg)
$\dot{Q}$	Heat release rate (kW)
R	Gas constant (Nm/Kmol)
Ra_L	Rayleigh number (-)
Re_L	Reynolds number (-)
S	Extinction parameter (kW/m^2)
T	Temperature (°C, K)
V	Volume (m^3)
$\dot{V}$	Volumetric flow (m^3/s)
W	View factor parameter (-)
X	Mole fraction (-)
X	View factor parameter (-)
Y	Mass fraction (-)

Lower-case Greek symbols

α	Absorptivity (-)
α	Angle (-)
α	Volumetric expansion factor (-)
α	Thermal diffusivity (m^2/s)
β	Charring rate (mm/min)
β	Inverse film temperature (K^{-1})
γ	Transient compensation factor (-)

ε	Emissivity (-)
η	Distance (mm)
θ	Normalised temperature (-)
ι	Wood crib growth rate (g/s^2)
κ	Absorption coefficient (m^{-1})
λ	Wavelength (μm)
μ	Average devolatilisation rate (s^{-1})
ν	Kinematic viscosity (m^2/s)
ξ	Distance (mm)
ρ	Density (kg/m^3)
ρ_w	Dry density (kg/m^3)
σ	Stefan-Boltzmann constant (W/m^{2}K^4)
υ	Oxygen-fuel stoichiometric ratio (-)
ϕ	Heat of combustion fraction (-)
ϕ	Oxygen depletion factor (-)
χ	Fraction of heat radiated to environment (-)
ω	Molar mass of gaseous oxygen (g/mol)

Upper-case Greek symbols

Γ	Parametric time factor function (-)
Δx	Element thickness (m)
ΔH_c	Heat of combustion (MJ/kg)

Subscripts

a	Applied
abs	Absolute
abs	Absorbed
air	Air
atm	Atmosphere
c	Char
c	Characteristic

c	Convective
cond	Conductive
cr	Critical
d	Design
d	Duct
disc	TSC disc
e	External
eff	Effective
ent	Entrained
et	Exhaust
ex	Extinction
f	Failure
f	Flame
fi	Fire
fo	Flashover
g	Gas
i	Element i
i	Species i
ig	Ignition
in	Incident
int	Internal
j	Element j
k	Characteristic
l	Losses
max	Maximum
n	Net
n	Nominal
ox	Oxygen
p	Pyrolysis
r	Radiant
r	Residual

s	Surface
t	Time
t	Total
v	Vaporisation
v	Ventilation
vv	Vertical ventilation
w	Compartment walls
w	Wood
x	Distance
CO	Carbon Monoxide
CO_2	Carbon Dioxide
H_2O	Water vapour
L	Average over length L
T	Total
0	Initial
∞	Ambient

Abbreviations

ASTM	American Society for Testing and Materials
CLT	Cross-Laminated Timber
DSC	Differential Scanning Calorimetry
FPA	Fire Propagation Apparatus
HD	High Definition
HRR	Heat Release Rate
H-TRIS	Heat Transfer Rate Inducing System
IR	Infrared
OSB	Oriented Strand Board
PU	Polyurethane
TGA	Thermogravimetric Analysis
TSC	Thin Skin Calorimeter

Chapter 1 Introduction

1.1 Background

From as early as the 11th century, timber construction has been recognised as a fire risk due to its combustible nature and superseded by non-combustible stone structures [1, 2]. Over the following centuries, catastrophic city-wide fires across the globe have prompted legislation to limit construction using combustible building materials such as timber. As such, large, complex buildings constructed in the last century have been built primarily of steel, masonry, or concrete, and research into compartment fire dynamics has been developed based on the assumption of non-combustible compartment linings.

Over recent years, sustainability has become a more significant consideration in the built environment. As such, there has been a push to use more sustainable construction materials, to reduce the embedded energy (carbon) and reduce the energy consumption. Because of this, a timber renaissance has emerged, aided by the development of novel engineered timber products such as glued-laminated timber and cross-laminated timber (CLT). This changes the approaches needed in fire safety engineering, because timber used as the structure may ignite and contribute to the fire load, changing the fire dynamics and potentially invalidating current design assumptions based on traditional compartment fire research.

1.1.1 Cross-Laminated Timber (CLT)

Cross-laminated timber is engineered from multiple timber panels, which allows the impact of imperfections such as voids and knots to be reduced compared to solid timber [3]. This results in reduced uncertainty in its bulk mechanical properties. Adjacent layers (lamellae) are glued together with their grain directions perpendicular to each other, as shown in Figure 1.1, thus providing significant structural capacity in both directions. As CLT is manufactured from multiple small pieces of timber, it can be produced to any desired size, limited only by the capabilities of the production plant and transport considerations. Primarily used as structural wall and floor slabs, CLT

offers bending strengths competitive with concrete. This creates the opportunity for multi-story, architecturally unique buildings composed predominantly of exposed structural timber. As a result, this product is becoming increasingly popular with architects, many of whom desire to expose some of the structural timber elements for aesthetic reasons. Polyurethane adhesives are typically used to bind the lamellae together, and therefore the thermal and mechanical behaviour of this adhesive, and not just that of the timber, will affect the overall structural performance. Individual planks are typically joined together using finger joints to maximise the bond area between planks, as illustrated in Figure 1.1.

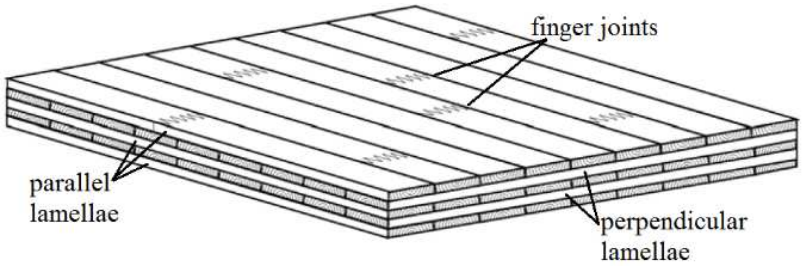

Figure 1.1: Illustration of cross-laminated timber showing alternating grain directions and finger joints (from [4])

1.1.2 Current Design Guidance

Due to the precedence of steel and concrete construction for multi-story buildings during the last century, available fire design guidance for mass timber lags behind the current architectural vision, placing potentially arbitrary restrictions on application of CLT. Building codes in many countries prohibit the use of "combustible materials" in buildings above a certain height, or insist that they are completely encapsulated with plasterboard to prevent their involvement in a potential fire scenario [5].

Eurocode 5 [6] represents the state-of-the-art of current design guidance, and focuses on predicting the rate of char formation and resulting loss of load-bearing capacity when subjected to a standard temperature-time curve such as ISO-834 [7]. In this respect, the current design guidance is similar to that for steel or concrete, and no explicit consideration is made for the combustible nature of timber.

Such standard fire-resistance tests are intended to provide comparative ratings between different materials, but do not provide any understanding of a material's behaviour in a real fire (indeed, the suitability of using a standard furnace to test a combustible material requires further consideration). It is necessary when using a combustible structural material to explicitly consider its flammability. Current design approaches based on fire resistance periods implicitly assume an inert structure – i.e. the fire will burn out after all the contents of the compartment have been consumed. When timber makes up a significant portion of the compartment linings, this assumption may not be valid – the timber has the potential to continue burning after burnout of the compartment contents [8]. This issue requires explicit consideration to enable the safe use of exposed structural timber within a compartment.

1.2 Aims

The aims of this research are to make an explicit consideration of the effects of exposed structural timber within a compartment, to identify and quantify the resulting fire risks, and to make recommendations for the safe use of exposed structural timber in design. To achieve these aims, the following objectives are pursued:

- Review the state-of-the-art of the fire behaviour of timber, engineered timber products, and their potential contribution to a compartment fire scenario;
- Quantify the conditions under which structural timber will undergo sustained burning;
- Produce a methodology to predict if sustained burning of structural timber will occur;
- Validate the conditions for sustained burning and predictive methodology for use in full-scale compartment fires;
- Identify any additional complexities present in full-scale compartment fires, and amend the methodology accordingly.

1.3 Summary of Chapters

This thesis contains seven chapters; a brief summary of the succeeding six chapters is given below.

1.3.1 Chapter 2 Literature Review

An extensive review of the fire behaviour of timber and engineered timber products is undertaken, exploring the pyrolysis, ignition, combustion, and extinction of timber products. A review of recent compartment fire tests and experiments with exposed and/or encapsulated CLT surfaces is then undertaken. The key findings show that the fire behaviour of compartments with combustible linings is poorly understood.

1.3.2 Chapter 3 Bench-scale Determination of Auto-Extinction Parameters

Experimental work using the Fire Propagation Apparatus is presented in this chapter. The critical conditions for sustained flaming are presented in terms of a critical heat flux, and a critical mass loss rate. The dependence of the critical mass loss rate on heat flux, preheating, oxygen concentration, and airflow is explored. A methodology based on firepoint theory is presented to enable prediction of auto-extinction based on the external heat flux and the heat losses.

1.3.3 Chapter 4 Full-Scale Compartment Fire Experiments with Exposed Timber Surfaces

This chapter presents the experimental work undertaken for the “Compartment fires in support of tall timber construction” project with assistance from Felix Wiesner, Juan Hidalgo, Simon Santamaria, and Rory Hadden, with assistance from Mark Fenton, Nikolai Gerasimov, and Timothy Putzien, and technical support from the BRE burn hall staff. The setup and instrumentation of the experiments is described in detail, an experimental narrative provided for each of the five experiments, and relevant data presented. The effects of delamination and encapsulation failure are discussed.

1.3.4 Chapter 5 Application of Firepoint Theory to Full-Scale Compartment Fire Experiments

This chapter presents two energy balances performed on the experiments described in the previous chapter. It uses the data presented in Chapter 4 and the methodology presented in Chapter 3 to predict the conditions for sustained burning in full-scale compartment fire experiments. The complexities arising from delamination and encapsulation failure are addressed, and a proposed methodology presented. The limitations of the two energy balance methods are discussed, and key sources of uncertainty identified.

1.3.5 Chapter 6 Intermediate-Scale Compartment Fire Experiments with Exposed Timber Surfaces

This chapter presents the final experimental series, exploring additional variables identified by the analyses in Chapter 5. The experimental work undertaken in this chapter was performed by Alastair Bartlett, Chris Bateman, and Lukas Rutkauskas. Intermediate-scale compartment fire experiments are presented, and the effects of fuel load and lamella thickness are explored. It was shown that delamination could be prevented (and thus auto-extinction achieved) if the fuel load burned out before thermal penetration of the outermost lamella.

1.3.6 Chapter 7 Conclusions

The main conclusions from the thesis are presented, and recommendations for further work and refinement of the proposed methodology are made.

Chapter 2 Literature Review

2.1 Wood as a Material

Wood is a naturally occurring material, which consists of three main polymers – cellulose, hemicellulose, and lignin [9-16]. The ratios of each polymer will vary between species [9-15], but are typically around 40 to 50% cellulose, 21 to 35% hemicellulose, and 22 to 32% lignin [9-12, 14, 16]. Each of these polymers have different contributions to mechanical properties and pyrolysis. Elementally, wood is approximately 50% carbon, 6% hydrogen, and 44% oxygen by mass [14, 16]. Cellulose is the main contributor to the wood's tensile strength [9, 17]. Hemicelluloses link the cellulose and lignin, affecting the wood's mechanical behaviour and its stability [9], providing wood with its compressive strength [17]. Lignin serves to bind cells together [9, 10, 14], giving wood its rigidity and compressive and shear strength [9].

2.2 Behaviour at Elevated Temperatures

Having considered the chemical makeup of wood, its behaviour upon exposure to heating can now be discussed.

2.2.1 Pyrolysis

Pyrolysis is the fundamental process through which a material will decompose into smaller molecules upon exposure to heat. This process effects changes in material properties, as well as ignition, burning, and extinction behaviour, and thus understanding and quantifying its effects is of fundamental importance in predicting a material's response to fire.

In order to burn, polymers must first break down into smaller molecules that can then vaporise. To create a self-sustaining reaction, these combustible gases must feedback sufficient heat to continue the production of volatiles [15]. Upon heating, the constituent polymers present in timber will begin to degrade, producing inert and combustible gases (the nature and composition of which will be dependent on char

yield [11]), liquid tars, a solid carbonaceous char (which is typically around 20% the density of virgin wood [18]) and an inorganic ash. This can occur before dehydration is completed if the heating rate is fast enough, but will be faster after the sample has dried [19]. These pyrolysis products can then undergo further pyrolysis themselves [9]. This process is particularly complex due to charring and inherent material variability [9], and the chemical processes occurring are numerous and interdependent [20]. Whilst pyrolysis is commonly modelled by an Arrhenius function, secondary reactions must also be considered to provide an accurate representation of the processes [16]. It is necessary to distinguish at this point the differences between pyrolysis and combustion. Pyrolysis simply refers to the thermal decomposition of a substance, is by definition endothermic, and can occur without an oxidant. Combustion, on the other hand, is a rapid, exothermic reaction with oxygen, and is discussed in Section 2.2.3. Thermal decomposition can proceed by oxidative processes or just by heat, with many polymers' decomposition processes being accelerated by oxidants [15].

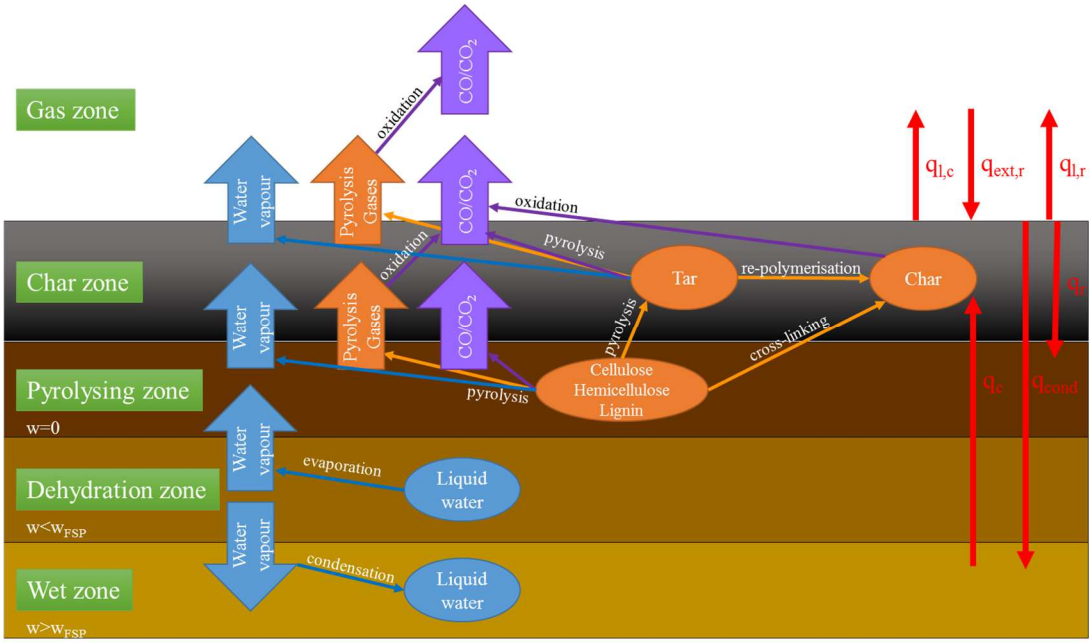

Figure 2.1: Chemical and physical processes within a burning timber sample.

The pyrolysis behaviour can be limited by either the chemical reactions (kinetic regime) or heat transfer phenomena (heat transfer regime), during which the heating rate of wood is much slower than the chemical reactions. This is the regime that is typically critical for structural problems, and creates large temperature gradients, thus pyrolysis occurs over a relatively narrow zone [21]. Wood typically undergoes four main stages of pyrolysis [22] due to its relatively low thermal conductivity and density and relatively high specific heat:

2.2.1.1 Temperatures below 200°C

Prior to the onset of pyrolysis, free water will begin to evaporate once temperatures within a timber member exceed 100°C, at which point the rate of temperature increase will slow down [23], typically until reaching 115°C [24], due to the energy being used for evaporation rather than heating. Once the fibre saturation point has been reached (the point at which all free moisture has been evaporated, typically around 30% moisture content [14]), moisture will start to be evaporated from the cell walls [10]. This will generate an internal pressure build-up [10], which at high temperatures can be up to 50% higher than that at ambient conditions [25]. This will cause some water vapour to permeate deeper into the sample [9, 19, 25-27], where it will then re-condense [28] increasing the moisture content there [9, 26, 27]. This then creates three zones – a dry zone at the front of the sample (in which pyrolysis occurs); a dehydrating zone behind this; and a wet zone behind this [27], illustrated in Figure 2.1.

Most [19] of the water vapour, however, will leave from the surface [9, 19, 25, 26]. As wood dries, it will begin to shrink – upon reaching 12% moisture content, it will typically have shrunk by 5% tangentially and 3% radially [14], and less than this longitudinally [9] – and grow in strength [9, 29]. Wood may start to shrink at temperatures as low as 70°C [30]. At low heat fluxes, dehydration and pyrolysis will take place independently; at higher heat fluxes, they will occur simultaneously [18, 31]. Where they occur simultaneously, moisture slows the temperature rise [31], and cools the pyrolysis zone through convective mass flow of water vapour [31]. Bound water is typically freed later, at temperatures around 240°C [30].

Mass loss due to pyrolysis occurs slowly at these temperatures [18, 22, 23]. Pyrolyzate consists mostly of non-combustible volatiles [9, 18, 32, 33] such as carbon dioxide, formic acids, and acetic acids [22]. At these temperatures, hemicellulose is the most reactive polymer, followed by lignin [10]. Thus, prolonged heating at low temperatures can convert hemicellulose (and lignin) into a carbonaceous char [32] at temperatures as low as 95°C [22] or 120°C [11], leaving cellulose largely unreacted [10]. Cellulosic materials have no fluid state, but can soften before breaking down into vapours [15]. In so doing, they may undergo a glass transition, altering their structure and becoming softer and more rubbery [15]. For lignin, this occurs at temperatures around 55°C to 170°C [30, 34-37], consequently permanent reductions in strength have been observed to occur at temperatures as low as 65°C [32]. At around 150°C, darkening of the wood can be seen [24]. Lautenberger et al. [10] found reactions to be endothermic in these temperature ranges, whereas Browne [22] found that exothermic oxidation reactions occur and may lead to self-heating and self-ignition given the right boundary conditions. Friquin [18] found that below 500°C, hemicellulose and lignin pyrolyse exothermically, whereas cellulose pyrolyses endothermically, with the opposite being the case above 500°C. It should be noted that by definition, pyrolysis is entirely endothermic, thus a reaction being characterised as exothermic implies that it is additional, secondary reactions that are causing the overall reaction to be classified as exothermic.

Overall at these temperatures, there is strong agreement between authors that dehydration will occur, followed by slow pyrolysis, producing non-combustible gases. This may be visible through some darkening of the timber. Shrinkage will occur due to dehydration, although there are limited data relating to how much it will shrink, and at which temperature(s) it will start.

2.2.1.2 Temperatures around 200°C to 300°C

Pyrolysis reactions at these temperatures remain slow [9, 18, 22, 38]. Carbon monoxide and glyoxal may also now be found in the pyrolyzate [22], which is still mainly non-combustible [9, 18, 22]; Shen et al. [33] found it to be primarily carbon dioxide and water vapour. The nature of the volatiles is dictated by the chemical and

physical properties of the original polymer and the decomposition products – they must be small enough to be volatile at the decomposition temperature, otherwise they will remain in the liquid phase until further decomposition [15]. Visible discolouration will begin [26] (or become more intense [24]), with prolonged exposure to these temperatures causing the wood to slowly become charred [20, 22] – uncharred wood remains at moderate temperatures even in long fires due to the protection of the char layer [15, 26, 39]; by 6 mm below the charline, the temperature is reduced to around 180°C [32]; with a total thickness of approximately 35 mm below the char layer being heated in standard furnace tests [18, 26, 40]. The resulting temperature profile below the char line can be expressed as an exponential or power term for thick wood in standard furance tests [32], or alternatively as a quadratic function [26]. Once formed, char is much more resistant to pyrolysis than the virgin wood [41]. Dehydration reactions around 200°C are large contributors to pyrolysis of hemicellulose and lignin, and result in high char yields [32]. Wood typically starts to discolour and char around 200°C to 250°C [11], with the main pyrolysis reactions starting to occur from 225°C to 275°C [9] as detailed below.

2.2.1.2.1 Hemicellulose

Hemicellulose is the most reactive wood component [42], and typically decomposes first; temperatures are quoted by various authors as 120°C to 180°C [30], 200°C to 260°C [11, 15, 22], 220°C to 315°C [13, 43], or 200C to 300°C [32]; initially increasing with external heat flux, before becoming largely independent of heat flux above 40 kW/m^2 [31]. Pyrolysis temperature is dependent on the temperature development within a fire, and may also depend on species, density, or moisture content [18]. The typical activation energy of hemicellulose is 100 kJ/mol [44], and it has a heat of combustion around 17.3 MJ/kg [10] to 18.6 MJ/kg [32]. Yang et al. [43] heated 10 mg samples of powdered cellulose, hemicellulose, and lignin to 900°C at a rate of 10°C/min in nitrogen – thus ensuring only pyrolysis took place, and not oxidation. The mass loss rates are summarised in Figure 2.4. They found hemicellulose's maximum mass loss rate to occur around 268°C. On completion of the test, approximately 20% of the original mass remained. Hemicellulose decomposition

was found to be exothermic until around 500°C. Guo et al. [13] found xylan pyrolysis in nitrogen heating at 20°C/min from 30°C to 800°C to yield 14.1% gas, 54.3% tar, 11.5% water, and 20.1% char. They also found its peak mass loss rate to occur at around 260°C. Hemicellulose produces more gases than cellulose [22], (namely water vapour, carbon dioxide, carbon monoxide, ethylene, benzene, formic and acetic acids, methanol, 2-methylfuran, and 2-furaldehyde [13]) and more tar than lignin [18], as well as being the main source of acetic acid [22].

2.2.1.2.2 Cellulose

Cellulose is typically the next to decompose, with temperatures quoted as 240°C to 350°C [11, 22], 250°C to 350°C [15], 315°C to 400°C [43], 280°C to 400°C [30] or 300°C to 350°C [32], with typical activation energies of 126 kJ/mol [42] to 236 kJ/mol [44] (which have been found by Milosavljevic et al. [45] to undergo an apparent shift in global decomposition kinetics at around 323°C to a lower activation energy process), and a heat of combustion of 17.3 MJ/kg [10] to 18.6 MJ/kg [32]. Cellulose pyrolysis is very sensitive to catalysis [42]. Yang et al. [43] found cellulose's peak mass loss rate to occur around 355°C, at which point it showed a large endothermic peak before returning to exothermic decomposition. On completion of the test, 6.5% of the original mass remained. Cellulose produces water vapour before any other significant changes, such as the breaking of C-O bonds resulting in the breaking of the polymer chains [22] (see Figure 2.2). Char yield thus depends on the temperature at which conversion takes place, and on the heating rate [11]. There are two main methods by which cellulose can decompose: the first is when a link in the carbon ring breaks, cross-linking to produce char alongside carbon monoxide, carbon dioxide, and H_2O [11, 15, 46], shown in Figure 2.2; and the second is chain scission [15] which is when a link in the polymer chain is broken, and levoglucosan molecules (a tar which will break down further into combustible gases [15, 41, 46, 47], or alternatively repolymerise to form char [32, 41, 47]; since the hydrocarbon yield does not increase as rapidly as tar production falls, this suggests some tars do repolymerise to char, possibly forming water vapour in the process [41]) can break away [11], as shown in Figure 2.3, typically at temperatures around 250°C to 300°C [15]. Low heating rates

tend to favour the char formation [11, 31, 46, 48] alongside largely non-combustible vapours, releasing energy [22]. High heating rates favour the production of levoglucosan [48], yielding flammable vapours and little or no char [31, 32], consuming energy [22]. Cellulose produces proportionally more tar than either lignin [18] or hemicellulose [22]. Below 310°C, a larger number of cellulose bonds are broken in air than in nitrogen, leading to faster pyrolysis [18] but perhaps lower char yield. If material is left as char, less is given off as flammable gases, and at very high rates of heating, no char is formed [15].

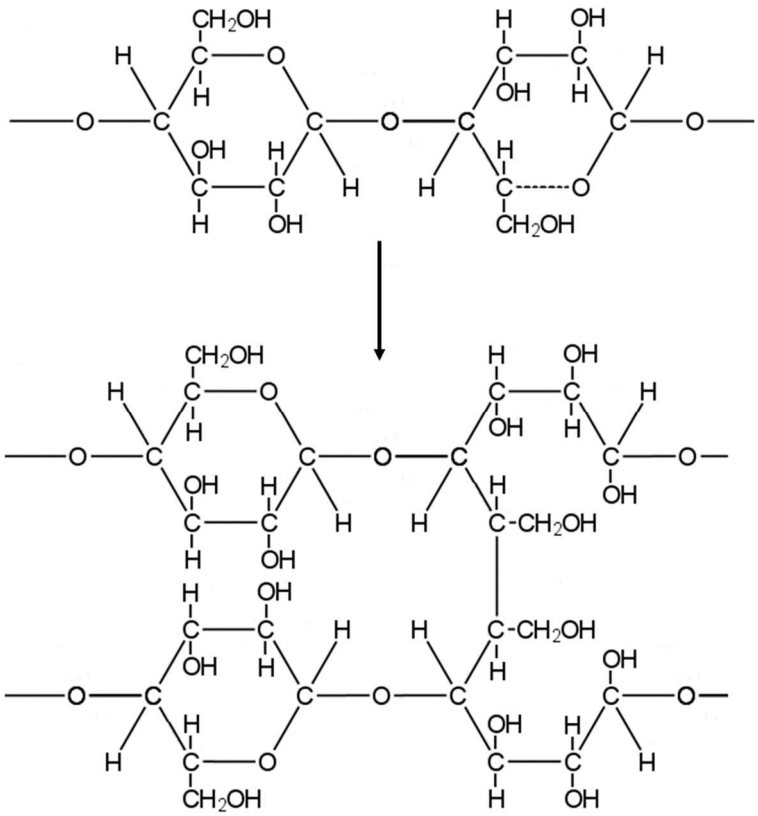

Figure 2.2: Cross-linking of cellulose chains forming char.

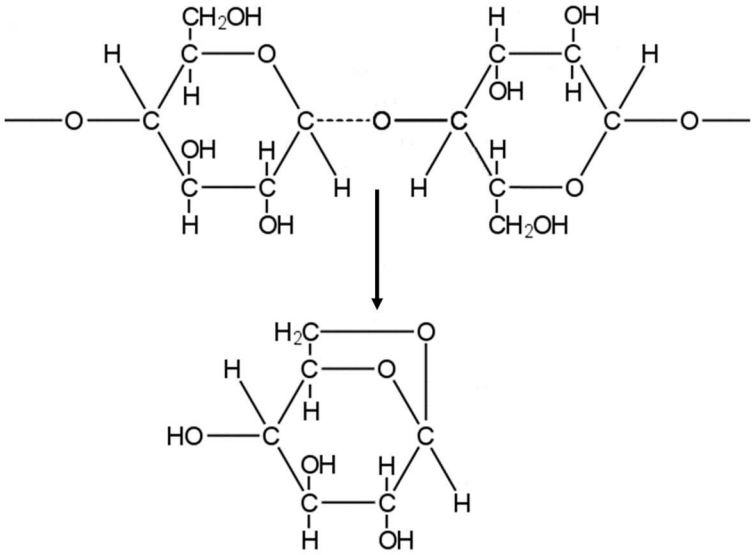

Figure 2.3: Breakdown of cellulose chain to form a levoglucosan molecule.

The presence of organic impurities also affects the production of levoglucosan [48]. There are several other paths through which cellulose can decompose, detailed in [46]. These pathways are suspected to depend on heating process, oxygen content/permeation, and the presence of impurities [47]. Thermogravimetric analyses (TGA) typically use very slow heating rates and very small sample sizes, offering little chance for interaction between the pyrolysis gases and the char. Thus extrapolation from TGA-size samples to thick timber slabs should be done with caution.

2.2.1.2.3 Lignin

Lignin is the least reactive wood component [18, 42], and thus usually the last to break down, with decomposition temperatures quoted as 110°C to 400°C [30], 280°C to 500°C [11, 15, 22] or 225°C to 450°C [32], with typical activation energies of 38 kJ/mol [42] to 46 kJ/mol [44], and a heat of combustion of 23.2 MJ/kg [32] to 26.7 MJ/kg [10]. Schaffer [30] found lignin to begin melting around 160°C, followed by re-hardening from 160°C to 210°C, with only 10% of its weight loss having occurred by 280°C. Yang et al. [43] found lignin to slowly decompose over the range 20°C to 900°C, with no peaks in mass loss rate, with exothermic reactions up until 500°C. This was attributed to the complex, multi-branched structure of lignin, with

many different chemical bonds whose activities cover a wide range. On completion of the test, 45.7% of the original mass remained. Lignin produces aromatic products on pyrolysis [22], and yields more char than cellulose [11, 18, 22] – upon heating to 400°C to 450°C, approximately half of lignin remains as char [11], contributing significantly to the char yield [15]. Since softwoods have higher lignin contents than hardwoods, they consequently give higher char yields [11].

2.2.1.2.4 Impurities

As well as the three polymers, wood also contains inorganic impurities, which upon complete decomposition, will remain as an inorganic ash [15]. These impurities have typical heats of combustion of 32 MJ/kg to 37 MJ/kg [32], giving wood an overall heat of combustion of 15 MJ/kg [49] to 20 MJ/kg [32], differing by species due to different contributions from each organic component. The effective heat of gasification of wood is around 5 to 12 MJ/kg [50].

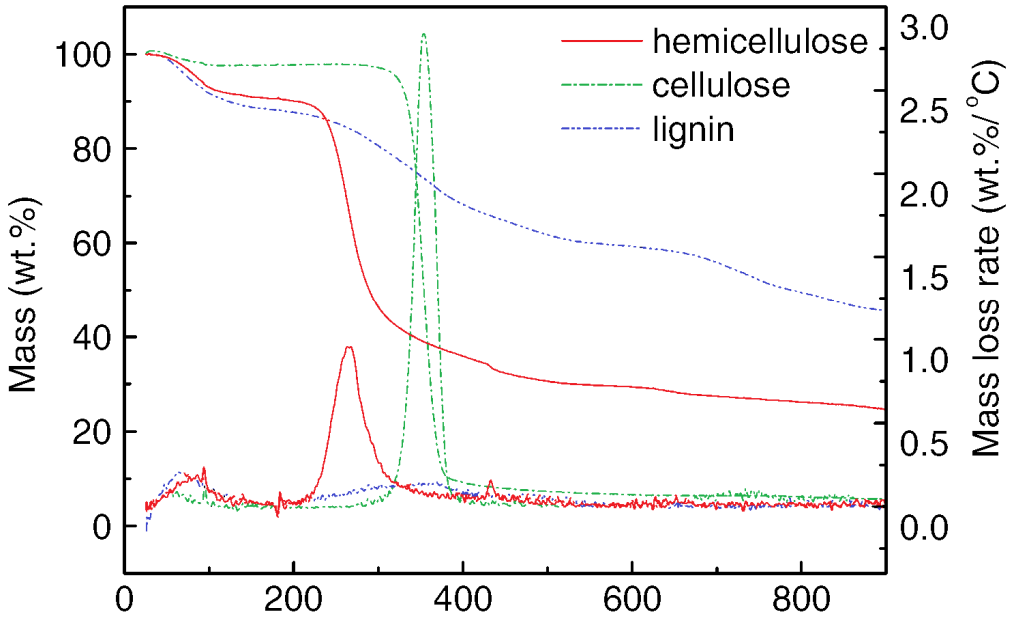

Figure 2.4: Mass loss rates of cellulose, hemicellulose, and lignin on pyrolysis in nitrogen (from [43]).

Whilst there is significant agreement between authors on the order in which these constituent polymers react, their chemical processes, and their char yields, there is

wide scatter in the literature regarding decomposition temperatures, activation energies, and heats of combustion. These differences may be partially attributed to differences in species, heating rate, and testing methods.

2.2.1.3 Temperatures around 300°C to 500°C

At these temperatures, pyrolysis rates increase rapidly [9, 22, 32, 33, 38] and prompt additional exothermic reactions [22], causing the temperatures to increase rapidly unless evolved heat can be dissipated [22]. The pyrolyzate now contains flammable gases [23, 33] such as methane, formaldehyde, methanol, and hydrogen in addition to earlier gases [20, 22], and as such, flaming ignition will usually have occurred by the time the surface reaches these temperatures. These gases also carry drops of highly flammable tars appearing as smoke [22, 41]; it is these temperatures that favour the production of levoglucosan [48]. Whilst some of these molecules will be light enough to vaporise immediately, some will remain in the liquid or solid phase for a time, where they may decompose further [15].

The structure of the wood starts to break down rapidly [11, 18, 23], due to the aliphatic chains in lignin starting to break down around 300°C, followed by the C-C bonds breaking around 370°C to 400°C, [32] leaving a residual char [9, 18, 22], which is less easily volatilised than the virgin wood [15, 47]. The physical characteristics of the char, most importantly density, continuity, coherence, adherence, oxidation resistance, thermal insulation, and permeability, will affect the continued thermal decomposition of the virgin material [15]. Thermal conductivity is roughly proportional to density during char formation – once a porous char has formed, radiative transfer though the pores dominates [47]. Cracks will then form in the char perpendicular to the grain, resulting in very different heat transfer mechanisms to that of virgin wood [18, 26, 42], which can compromise one-dimensional assumptions commonly made in analyses [51]. These cracks allow the ready escape of volatiles towards the surface [11, 26, 42], however pressure differences will drive some pyrolyzate towards the centre [42]. The surface of the char layer will be at a temperature similar to that of the gas phase [26]. Once the char layer has formed, there is a subsequent gradual decline in mass flux [19,

38], following a $t^{-1/2}$ relationship [11]. A thicker char layer grants tar a longer residence time [47], thus allowing more cracking or polymerisation. Charring has been found to be highly exothermic, whereas production of volatiles is endothermic [43]. Additionally, char has a greater emissivity and absorptivity than that of wood (around 0.95 compared to 0.7) [47], increasing re-emitted energy from the surface, which lowers the surface temperature, whilst simultaneously increasing absorbed radiant flux, which raises the in-depth temperature. Once a char layer has formed, volatiles from the virgin material must pass through the char layer, the heat from which may prompt secondary reactions [15]. A char created under oxygen-deficient conditions may create a char that is more reactive than a char created under oxidative conditions [10]. The char yield from cellulose is heavily dependent on organic impurities, with pure α-cellulose yielding only 5% char upon prolonged heating at 300°C, but viscose rayon giving up to 40% [11].

These main pyrolysis products then pyrolyse further, and interact with each other before escaping, with the char potentially acting as a catalyst [16, 22]. Secondary decomposition of tars is strongly exothermic [22], and can produce water vapour as one of the products [46-48]. At 400°C, levoglucosan can decompose in the vapour phase to carbon monoxide and carbon dioxide [48]. Cellulose- and lignin- derived vapours tend to induce levoglucosan decomposition, whereas xylan-derived vapours tend to inhibit it [48]. Whilst levoglucosan (and isomers thereof) comprise a large proportion of the tar fraction, the chemical composition of the tars has been found to be very diverse, also containing large amounts of acetic acid [41].

Carbonisation is considered complete at 400°C to 600°C, at which point the crystalline structure of graphite is developed [22]; above 450°C, volatile production stops [32]. Above 400°C, significant cracks start to develop in the char, the spacing of which is typically inversely proportional to surface temperature [52]. There is a visible difference between hardwoods and softwoods in this area – hardwoods typically produce flat scales with shallow cracks, whereas softwoods produce curved scales [52].

Overall in this temperature range, there is strong agreement that temperatures around 300°C represent the onset of rapid pyrolysis and char formation. The formation of cracks in the char is of particular significance in that the physical structure of the timber changes, altering the heat transfer mechanisms and allowing volatiles to escape from deeper within the timber.

2.2.1.4 Temperatures above 500°C

If the surface temperature is able to rise further before completion of carbonisation, further secondary reactions will take place [22].

Hosoya et al. [53] carried out tests on Japanese cedar wood flour, cellulose powder and xylan from beech, and glucomannan and lignin from Japanese cedar in a pyrex glass tube in nitrogen at a constant temperature of 800°C for 30 s. Of the two hemicelluloses tested, xylan yielded 20% char, 54% tar, and 14% gases, and glucomannan yielded 30% char, 41% tar, and 13% gases. Cellulose yielded 10% char, 72% tar, and 13% gases. This differs from that found by Browne [22], but this may be due to different temperatures and durations, which have previously been stated to affect pyrolysis rates- particularly in that slower pyrolysis yields more char and much less tar [22]. The lignin yielded 41% char, 38% tar, and 12% gases, and wood 38% char, 42% tar, and 11% gases. The pyrolysis of wood was substantially different from the sum of its components – most notably in the char, with wood giving 38%, yet the weighted sum of its components just 23%. This is expected to be partially due to the presence of inorganic substances such as potassium salts, which are known to suppress the formation of levoglucosan, however this cannot account for the full difference, suggesting that complex interactions between pyrolysis products from the various components affect the overall reaction.

2.2.2 Ignition

Once pyrolysis is underway, in the presence of oxygen, the products of pyrolysis may then undergo a rapid, exothermic reaction with oxygen, combustion. This is discussed extensively in Section 2.2.3.1, but before this, the process of the onset of combustion, ignition, is worthy of its own discussion. Ignition can lead to either smouldering or

flaming combustion (both of which are discussed further in Section 2.2.3), however flaming ignition will be discussed herein unless explicitly mentioned otherwise. Furthermore, ignition can either be piloted, in which a spark or flame energises the gaseous species, aiding ignition, or unpiloted, in which the volatiles must achieve the necessary energy for ignition through heating alone.

Criteria for ignition are typically defined by either the "critical heat flux", the lowest heat flux for which ignition will occur, or "critical surface temperature", the lowest *surface* temperature for which ignition will occur. Values for these criteria from various authors are presented in Table 2.1. It can be seen that there is reasonable agreement, and that critical heat fluxes for piloted and unpiloted ignition are around 10 to 13 kW/m^2 and 25 to 33 kW/m^2 respectively, with the results of Hottel [54], Simms [55], and Simms and Law [56] appearing to be outliers. There is much more scatter in the results for critical surface temperature, but in each case, ignition occurs at temperatures well below those experienced in fires; wood-based panel products have similarly been found to ignite at temperatures well below those experienced in fires [57]. Critical surface temperature for ignition is also heavily dependent on the external heat flux [58].

In reality, these factors will vary significantly with test setup [11, 32, 58-62], sample orientation [11, 59], ambient temperature [51], and heat transfer mode [11, 32, 51, 62, 63]; auto-ignition temperature can vary by more than 150°C for the same material depending on external factors, but introduction of a pilot can reduce the effects of environmental variables [51]. In addition, density, moisture content, thickness, arrangement of wood pieces, and time are all important for the amount of heat necessary for ignition [64], with wood pieces above 10 mm thick not being easily ignitable [65]. Spontaneous ignition can be aided by exothermic char oxidation, which causes an increase in surface temperature, which can then raise the gas temperature to that required for ignition [47]. Sustained smouldering ignition has been found to occur around heat fluxes of 5 to 10 kW/m^2 [41, 66] typically at surface temperatures around 200°C [32].

Rather than it being the incident heat flux or surface temperature which effects ignition, in reality it is the *gas phase* temperature [11, 32, 47]; for ignition to occur, a flammable mixture must exist somewhere in the gas phase, which must then be elevated to a temperature at which a combustion reaction can occur [32, 51, 67]. This can be split into two segments – the pyrolysis time (the time needed to produce a flammable mixture), and the induction time (the time needed for the temperature to reach one at which ignition can occur) [51]. Typically the pyrolysis time dominates [51]. Prior to ignition, the gradually increasing surface temperature may be subject to a number of temperature "spikes" corresponding to flashes before sustained ignition is achieved [68]. Drysdale [11] suggests that to generate the sufficient conditions for ignition, a critical *mass flow rate* of volatiles from the surface must be achieved, given by Equation (2.1):

$$(\phi \Delta H_c - L_v)\dot{m}''_{cr} + \dot{q}''_e - \dot{q}''_l > 0 \qquad (2.1)$$

where ϕ is the fraction of the heat of combustion of the vapour transferred back to the surface, typically around 0.3, ΔH_c is the heat of combustion, L_v is the heat of gasification, $\dot{m}''_{cr}$ is the critical mass flow rate of volatiles, $\dot{q}''_e$ is the external heat flux, and $\dot{q}''_l$ is the heat losses.

Table 2.1: Critical heat fluxes and surface temperatures for piloted and unpiloted ignition of wood

Author(s)	Critical heat flux [kW/m^2]		Critical surface temperature [°C]	
	Piloted	Unpiloted	Piloted	Unpiloted
Angell et al. [63]	-	-	204	-
Ashton [65]	12	33	-	-
Atreya et al. [69]	-	-	382-405 (mahogany) 372-395 (red oak)	-
Bixel and Moore [70] (cited by [20]	-	-	-	203-257 (sawdust, long exposure)
Brown [71, 72] (cited by [20])	-	-	-	192-220 (long exposure)
Browne [22]	12.6	25.1	-	-
Drysdale [11]	12	28	350	600
Fangrat et al. [73]	10.1-12.1 (plywood)	-	296-330 (plywood)	-
Fons [74]	-	-	343	-
Graf [75]	-	-	236-321	-
Hill and Comey [76]	-	-	218-330	-
Hottel [54]	28 (vertical)	63-79 (vertical)	-	-
Lawson and Simms [77]	14.6 (western red cedar) 14.6 (American whitewood) 15.1 (freijo) 12.6 (African mahogany) 15.1 (oak) 15.1 (iroko)	26.8 (western red cedar) 25.5 (American whitewood) 26.4 (freijo) 23.8 (African mahogany) 27.6 (oak)	-	-
Moghtaderi et al. [58]	10.3 (Pacific maple) 13.2 (radiata pine) 14.0 (sugar pine)	-	298-400	-
Simms [78]	-	25.1	-	-
Simms [55]	-	42-50	-	-
Simms and Hird [79]	14.7	25.1	-	-

continued...

Author(s)	Critical heat flux [kW/m^2]		Critical surface temperature [°C]	
	Piloted	Unpiloted		Piloted
Simms and Law [56]	15	-	-	-
Smith and King [80]	-	-	408	488
Spearpoint and Quintiere [81]	-	-	200-400	-
Tran and White [82]	10 (basswood) 10.5 (red oak) 10.7 (southern pine) 12.4 (redwood)	-	-	-
White and Dietenberger [32]	10-13	25	300-400	270-470 (convective) 600 (radiative)
Yang et al. [19]	-	-	190-310	-

Formulae for time to ignition exist to attempt to simplify the gas phase problem, which is complex to predict and model [83], and will vary according to the parameters discussed above, particularly at lower heat fluxes [59]. Different relationships exist for thermally thin solids (Equation (2.2)) and thermally thick solids (Equation (2.3)):

$$t_{ig} = \rho C_p t \frac{T_{s,ig} - T_\infty}{\dot{q}_n''} \tag{2.2}$$

$$t_{ig} = \frac{\pi}{4} k\rho C_p \left(\frac{T_{s,ig} - T_\infty}{\dot{q}_n''}\right)^2 \tag{2.3}$$

where $T_{s,ig}$ is the surface temperature at ignition, T_∞ is the ambient temperature, $\dot{q}_n''$ is the net heat flux to the surface, and t is the sample thickness. From these formulae, the minimum heat flux for ignition can thus be calculated by extrapolating for $t_{ig} \to \infty$ [83]. Whilst lower heat fluxes will yield longer ignition times (e.g. White and Dietenberger [32] found times to ignition at 55 kW/m^2 of 3 s and 930 s at 18 kW/m^2), the internal temperatures at the point of ignition will be higher [19].

Moisture delays ignition, and increases the minimum intensity required for ignition [31]; for wood it has been found that $t_{ig} \propto (1 + 4w)^2$ where w is the moisture content [83]. Dry wood will thus ignite in about half the time of wood with 12% moisture content.

Simms [78] explored the effect of sample absorptivity at the surface by testing the ignition properties of oak and mahogany both at their natural colours, and coated with carbon black. He found that the minimum critical heat fluxes to ignite oak and mahogany respectively were around 35 to 45% and 10 to 30% lower when coated with carbon black. This difference is time-variant, as samples will naturally blacken and char with increased heat exposure.

Several differences are noted between piloted and unpiloted (or auto-) ignition. Drysdale [11] notes that auto-ignition occurs at a lower temperature with convective heating than with radiative heating, whereas piloted ignition occurs at a lower temperature with radiative heating than with convective heating. He further notes that auto-ignition occurs more readily on horizontal surfaces than on vertical surfaces, as vertical surfaces are exposed to more effective convective cooling than horizontal ones and volatiles will be more diluted. Whilst this may be the case for test setups, the complex fire dynamics of a compartment may mean that the trend is somewhat different in reality. If there is no pilot flame, ignition may not occur until pyrolysis below the char layer slows sufficiently to allow the char to come into contact with the air [22]. Charcoal has the lowest spontaneous ignition temperature of all the combustion products, reported as low as 150 to 250°C [22].

The nature of the pilot source will also affect the ignition criteria, both its power and location, with power having the greatest influence [84]. Ignition with an impinging flame can occur at much lower heat fluxes than regular piloted ignition (4 kW/m^2 compared with 12 kW/m^2 for pinewood) [11]. The size and properties of the impinging flame govern; as size of the flame increases, the dominant mode of heat transfer will move from convection to radiation [11], and the flame will provide an additional heat flux, which is very difficult to quantify. This has serious implications for scaling from

tests with sparks as ignition sources to walls with burning furniture adjacent acting as the ignition source. Drysdale [11] found that for vertical wood samples with a pilot flame, piloted ignition temperature was around 320°C to 325°C, increasing as the flame moves away from the surface, with the time to ignition also increasing. Piloted ignition will only occur when the pilot is within the visible stream of volatiles [55]. Simms [55] and Simms and Hird [79] found this distance to be around 20 mm for samples with a surface area of 50 x 50 mm, with ignition times increasing as distance between the sample and the pilot flame increases. Simms [55] distinguishes two types of piloted ignition: regular piloted ignition, in which the flame is not in contact with the surface; and surface ignition, in which the flame spreads over the igniting surface. Ignition occurs much earlier and at lower heat fluxes for surface radiation than for piloted ignition [55], as would be the case during flame spread across a surface.

Koohyar et al. [85, 86] tested oven-dried oak, fir, redwood, mahogany, and pine samples exposed to radiation from a flame, as this is the most prominent ignition source in a building fire. Samples were placed in a flame cabinet, and were subjected to flames from both one side and two sides, with "guide panels" on the other sides of the flames to provide stability. Two screens and a honeycomb section are placed underneath the apparatus to smooth the airflow and allow increased flame stability. Liquid fuel is fed in at a constant rate to control the flames. Heat flux is controlled by moving the flames closer to or further away from the sample, to a maximum of around 35 kW/m^2. An additional, premixed propane-oxygen flame can be introduced on each side of the sample to study piloted radiation. Mass loss was recorded throughout. Sample size or mass were not specified. They then produced a model to correlate the results, using the differential heat transfer Equation (2.4):

$$\frac{\partial \Delta T}{\partial t} = \alpha \frac{\partial^2 \Delta T}{\partial x^2} \tag{2.4}$$

When the appropriate boundary conditions are applied, such that heat transfer at the front surface is only due to the incident irradiation, and that heat transfer at the rear (or centre for two-sided heating) is negligible, Equation (2.5) is obtained:

$$\frac{\Delta T_s k}{\dot{q}'' L} = Fo + \frac{1}{3} - \frac{2}{\pi^2}\sum_{n=1}^{\infty}\frac{1}{n^2}\left[e^{-n^2\pi^2 Fo}\right] \tag{2.5}$$

where L is the thickness of the sample and Fo is the Fourier number. They then considered the heat losses at the surface to come up with the following relationship in Equation (2.6):

$$-k\frac{\partial T}{\partial x} = p\dot{q}'' \tag{2.6}$$

where p is a combination factor, found empirically to be 0.4 for oak and 0.23 for other species. Applying these led to a strong fit to the model, as shown in Figure 2.5.

Due to the insulating qualities of char, if ignition has not occurred by the time a char layer has formed then the presence of char will require a higher surface temperature to provide the necessary heat flux to the virgin wood [11]. The char can reach very high temperatures, resulting in vigorous oxidation (smouldering combustion), which can serve to catalyse gas-phase ignition [51].

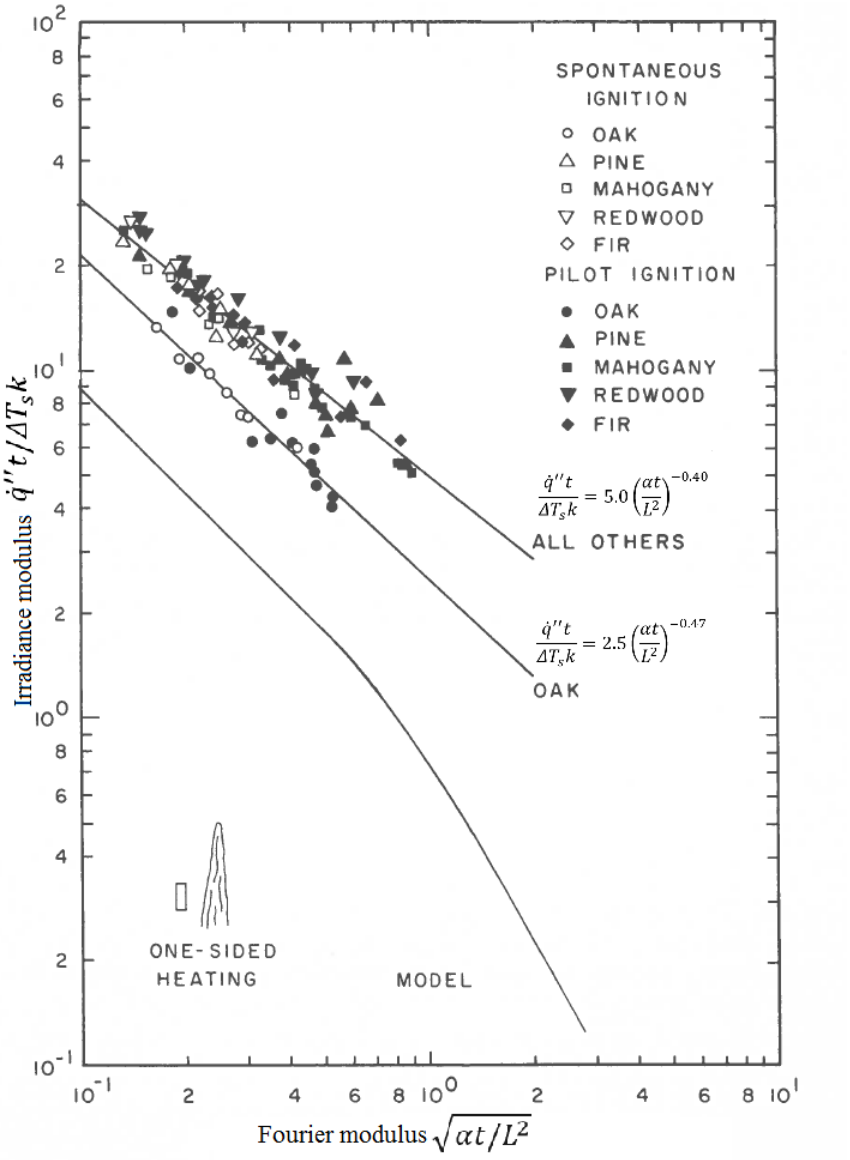

Figure 2.5: Experimental and theoretical ignition data for one-sided heating from Koohyar et al.'s tests [85].

Ashton [65] states that there is no danger of ignition below 100°C, however Lautenberger et al. [10] have suggested that wood can be ignited by long term (on the order of months or years) exposure to temperatures of 75°C to 200°C. This is lower than the ignition temperatures presented in Table 2.1, but high enough to cause thermal decomposition over long periods. For ignition to occur in such a way, exothermic reactions occurring inside the member must produce more heat than is lost to the environment.

Lautenberger et al. [10] placed 200 mm Douglas fir cubes in an oven at 200°C, one of which had the end grain sealed to prevent longitudinal oxygen diffusion. This cube underwent thermal runaway after 9 days – the unsealed cube after 1 day. They then placed 100 mm x 100 mm samples of Douglas fir, poplar, cedar, mahogany, birch, red oak, maple, OSB, and particleboard of thicknesses varying from 10 mm to 30 mm in an oven at 0.1 atm pressure (equivalent to 2% oxygen concentration) and 200°C for seven weeks. The softwoods showed the lowest mass loss rates, which was attributed to them having the lowest proportions of hemicellulose.

Matson et al. [20] reviewed existing data on the auto-ignition of wood at prolonged exposure to moderate temperatures. One set of tests exposed wood to a steam pipe at temperatures of 138°C to 163°C for 67 days, and 6 mm of the sample was charred, with a further 16 mm showing visible discolouration, however no ignition was observed. Unpiloted samples of sawdust 13 mm deep ignited at temperatures around 203°C to 257°C upon prolonged exposure, with charcoal igniting at lower temperatures of 159°C (moist) and 216°C (dry). It should be noted that upon prolonged exposure the moisture content should have no effect upon ignition due to the moisture being driven off well before ignition, and thus the two samples should have behaved similarly. This highlights the lack of repeatability in these results. Their review concluded that although there is some disagreement on the matter, prolonged or repeated exposures of wood to temperatures above 100°C to 120°C should be avoided due to the possibility of char formation at this temperature, which they found to have a lower ignition temperature, and thus prolonged or repeated exposures to these temperatures could result in ignition. Repeated exposures with variable moisture contents were found to be particularly problematic due to these conditions allowing greater oxygen adsorption by the char layer.

McAllister et al. [60, 61] note that whilst ignition theories based on temperature or heat flux are only applicable in the conditions in which they were measured, a critical mass flux as suggested by Drysdale [11] (Equation (2.1)) can be applied across various apparatus and length scales. If a fuel and air mixture exists within flammability limits, a premixed flame will form in the presence of a pilot source. For this to self-sustain,

generation of pyrolysis gases must be sufficient that the heat losses from the flame are not enough to extinguish it. Temperature and the rate of heat release from the flame increase with the fuel to air ratio, thus there is a critical mass flux required to initiate and sustain flaming. This has been found to increase with heat flux, possibly due to a steeper temperature gradient, with only a small surface region at a sufficient temperature to pyrolyse.

2.2.3 Burning Behaviour

After the ignition of these pyrolysis gases, the pyrolysis products will undergo combustion, a process involving the mixing of pyrolysis gases with ambient air. The heat generated thereby can then further drive the pyrolysis processes discussed in Section 2.2.1 [87]. Oxidation in the gas phase of volatiles produced by thermal degradation produces flaming combustion, and solid-phase char oxidation produces smouldering combustion [18]. The available heat of wood is about 15-20 MJ/kg [9, 88], about half to two-thirds of which is released through flaming, the rest through smouldering [22, 23, 81]. These two modes are discussed in turn.

2.2.3.1 Flaming Combustion

Exothermic conditions are reached sooner when in contact with air – typically around 192°C to 260°C [22]. The mass loss rates of radiata pine in air and nitrogen are shown in Figure 2.6. Cellulose is the main contributor to flaming combustion [89], as it has been demonstrated (Section 2.2.1.2.2) to produce more volatiles than char.

At first the pyrolysis gases are too rich in carbon dioxide to sustain flaming, but upon secondary pyrolysis become more flammable [22]. After ignition, the majority of the available oxygen will be consumed by the flame, thus post-ignition thermal decomposition will occur in a largely vitiated environment [15]. During stable flaming, volatiles produced by the decomposing wood are transported just outside the solid material into the reaction zone [9], with flaming combustion occurring entirely in the gas phase [22], thus rate of combustion is mainly determined by rate of pyrolysis [9].

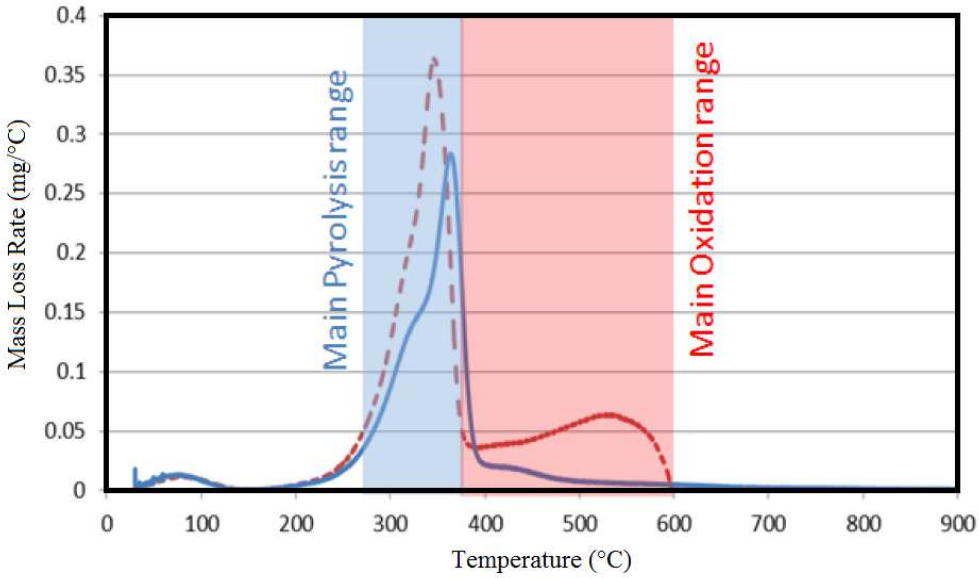

Figure 2.6: Pyrolysis and combustion temperature ranges of radiata pine in air (dashed line) and nitrogen (solid line) (from [9]).

The flow of these volatiles is defined by the flames and the environment geometry, and produce complex flow patterns which can only be established by detailed measurements or modelling; these patterns will differ somewhat from the more simplistic scenarios in standard test methods [51]. The fire size influences the mass flux from fuels due to heat feedback from gas-phase combustion [90]. Since char has a much lower thermal conductivity than wood, it delays the onset of pyrolysis of the virgin wood [22]. Thus, flaming is often strong at first, before weakening until the deeper wood portions can be pyrolysed [22, 25, 32, 81]. The flame provides an additional heat flux to that provided by the external source [91]. The heat from the flame, however, is not enough to provide sustained burning on its own [91]. The heat flux from the flame is intimately coupled to the burning rate which can be considered constant after the initial strong flaming [81]. Just after ignition, the net heat flux can be given by Equation (2.7) from [81].

$$\dot{q}''_{\mathrm{n}} = \dot{q}''_{\mathrm{e}} + \dot{q}''_{\mathrm{f}} - \sigma(T_s^4 - T_\infty^4) \tag{2.7}$$

where $\dot{q}''_{\mathrm{f}}$ is the heat flux from the flames, and σ is the Stefan-Boltzmann constant. This equation is significantly simplified, as it does not consider heat losses by

conduction through the solid, heat losses by convection, or cross-radiation between burning surfaces, all of which must be considered in a real fire. A more complete equation would be as Equation (2.8):

$$\dot{q}''_{\mathrm{n}} = \dot{q}''_{\mathrm{e}} + \dot{q}''_{\mathrm{f}} - \sigma(T_s^4 - T_\infty^4) - h_c(T_s - T_\infty) - k\frac{\partial T}{\partial x} \tag{2.8}$$

where h_c is the convective heat transfer coefficient.

2.2.3.1.1 Flame Extinction

The concept of flaming extinction is an important consideration when using engineered timber products within a compartment. Since any exposed timber will add to the fuel load and burn as described above, it is vital to understand the conditions in which it will continue to burn, and the conditions in which it will extinguish.

Piloted ignition and flame extinction at a sample surface have the same critical conditions – assuming chemical composition of volatiles is the same at both conditions [11, 92]. Both can be related to fire point conditions [9]. A flame will extinguish if its heat losses exceed its heat release [93]. For this to occur, the mass flux of flammable gases must drop below a critical value [11]. Extinction is possible above the critical mass flux, but such samples are then susceptible to re-ignition [11]. Extinction is governed by the oxidation kinetics, and is difficult to accurately predict [93].

One critical extinction parameter is the Damköhler number [93] – the ratio of heat loss time to reaction time, which can be found from Equation (2.9):

$$Da = \frac{\dot{m}'''\Delta H_c}{kTu_\infty^2/\alpha^2} \tag{2.9}$$

where $\dot{m}'''$ is the mass loss rate per unit volume, u_∞ is the ambient gas velocity, and α is the thermal diffusivity. When applying this equation to timber, it is important to note that the thermal conductivity and diffusivity are temperature-dependent. Quintiere and Rangwala [93] present Equation (2.10) for determining the critical mass

flux for extinction, based on Tewarson and Pion's [94] work on PMMA. This expression highlights a clear dependence on oxygen concentration, external heat flux, and heat losses.

$$\dot{m}''_{cr,ex} = \frac{1}{L_v}\left[\frac{h_c}{C_p}\left[\frac{Y_{ox,\infty}\Delta H_c}{\upsilon} - C_p\left(T_p - T_\infty\right)\right] + \dot{q}''_{e,r} - \sigma\left(T_p^4 - T_\infty^4\right)\right] \quad (2.10)$$

The mass loss rate per unit area can be expressed in terms of the imposed heat flux by Equation (2.11):

$$\dot{m}'' = \frac{\dot{q}''_e + \dot{q}''_f - \dot{q}''_l}{L_v} \quad (2.11)$$

where L_v is the heat of gasification (typically 1820 kJ/kg for wood [94]), equal to $\Delta H_v + C_p(T_p - T_\infty)$, where ΔH_v is the heat of vaporisation. Since gasification will occur for the virgin wood rather than the char, it is the net heat flux at the char:timber interface that is of interest. At this point, the timber has already been raised to the pyrolysis temperature, thus $L_v = \Delta H_v$.

Bamford et al. [24, 95] noted that for 230 mm x 230 mm wood panels of varying thicknesses from 9.5 mm to 50.8 mm heated by flames on two sides, after a given period of time, flaming will be self-sustaining upon removal of external heat sources. Panels heated only on one side, however, will not achieve self-sustained flaming if over 3 mm thick. The time to reach sustained flaming was proportional to the square of sample thickness, with thicker samples taking longer. They found that the centreline temperature at the time of self-sustained heating was always around 200°C. They relate the conditions necessary for self-sustained flaming to the rate of volatile production, finding that a rate of 2.5 g/m^{2}s was required for self-sustained burning.

Subsequently experiments on 50 mm thick oak and Columbian pine samples at heat fluxes ranging from 18 to 54 kW/m^2 were undertaken. Samples subject to heat fluxes at or below 30 kW/m^2 extinguished after around 2 to 7 minutes, reaching char depths

of around 4 to 8 mm. The samples subjected to 50 kW/m^2 however, continued burning until the majority of the sample had charred.

Further tests [24] explored the combustion behaviour of two vertical wood panels set parallel and opposite each other. The thickness of the samples was found to have no effect. Square panels of length 229 mm and rectangular panels 914 mm x 381 mm were tested. The smaller panels were found to cease undergoing sustained flaming for separations above 51 mm, and for the larger panels, around 127 mm. Given the separation, radiation will be the dominant mode of heat transfer. The view factors between the two panels can be calculated by Equation (2.12) [96, 97]:

$$F_{ij} = \frac{2}{\pi XY}\left\{\ln\left[\frac{(1+X^2)(1+Y^2)}{1+X^2+Y^2}\right]^{\frac{1}{2}} + X\sqrt{1+Y^2}\tan^{-1}\frac{X}{\sqrt{1+Y^2}} + Y\sqrt{1+X^2}\tan^{-1}\frac{Y}{\sqrt{1+X^2}} - X\tan^{-1}X - Y\tan^{-1}Y\right\} \quad (2.12)$$

where $X = \frac{L}{s}$ and $Y = \frac{w}{s}$, where L and w are the length and width respectively, and s is the separation. This yields view factors of 0.66 and 0.65 respectively. Assuming a similar flame temperature, this view factor corresponds to a critical radiant heat flux for sustained flaming. The effect of airflow was also explored; as expected, a greater airflow resulted in longer times to ignition due to initial cooling, but once ignited resulted in more complete combustion due to improved mixing conditions. For this reason, when these tests were repeated on horizontal panels, the burning was much less vigorous.

Hottel [54] tested 25 mm x 152 mm x 305 mm spruce samples, conditioned at approximately 32% relative humidity, in a vertical configuration under radiant heating. He found that an incident heat flux of 31.5 kW/m^2 was required to sustain a flame for over ten minutes (the heat flux was reduced to this value after ignition). Further experiments in which the irradiation was ceased after ignition found that samples

ignited at lower heat fluxes tended to take longer to extinguish, which was attributed to a greater heating time and thus shallower thermal gradient, as char will form more slowly allowing more conduction further into the sample, thus reducing the conductive heat losses later in the experiment. He also found critical heat fluxes for ignition of around 28 kW/m^2 (piloted) and 71 kW/m^2 (unpiloted), which are significantly higher than those from other authors, suggesting that the apparatus and/or test method used had a significant effect on the sample behaviour.

Inghelbrecht [9] tested 100 mm x 100 mm CLT radiata pine (ρ = 635 kg/m^3) samples 72 mm thick and hoop pine (ρ = 540 kg/m^3) samples 96 mm thick, Gympie messmate (an Australian hardwood) glulam samples (ρ = 823 kg/m^3) 60 mm thick, and solid hoop pine (ρ = 560 kg/m^3) samples 70 mm thick in the vertical orientation in a cone calorimeter under imposed heat fluxes of 25, 40, 60, and 80 kW/m^2 perpendicular to the grain for exposure times of 10, 20, 30, and 60 minutes. Temperature was recorded using K-type thermocouples at depths of 5 mm, 15 mm, 25 mm, 35 mm, and 45 mm from the heated surface; additionally mass loss was recorded throughout the experiments. For the experiments at 25 kW/m^2, delamination occurred followed by flaming ignition. Upon removal of the external heat flux, the 80 kW/m^2 samples (10 minutes exposure) extinguished after 2.5 minutes. The 25 kW/m^2 samples (60 minutes exposure) had delayed auto-extinction due to the delaminated first layer leaning against the rest of the sample serving as additional fuel. A decrease in mass flux will result in flameout. The critical mass flux can be approximated by Equation (2.13):

$$\dot{m}''_{cr,ex} = \frac{h_c}{C_p}\ln(1+B) \tag{2.13}$$

which typically gives a critical mass flux of 4 to 5 g/m^{2}s, where B is Spalding's B-number, which is the ratio of the heat produced per molecule burning to the heat required to vaporise an additional molecule. Thus if $B > 1$, burning will be sustained, but if $B < 1$, burning will cease.

Emberley et al. [98] undertook similar experiments in a mass loss calorimeter with 120 mm x 120 mm CLT manufactured from hoop pine (ρ = 540 kg/m^3), radiata pine (ρ = 635 kg/m^3), or European spruce (ρ = 425 kg/m^3); and 100 mm x 100 mm solid timber, either hoop pine (ρ = 560 kg/m^3) or gympie messmate (ρ = 823 kg/m^3). Samples were tested to incident heat fluxes from 6 to 100 kg/m^3, and instrumented with K-type thermocouples, with mass loss rate and temperature measured simultaneously in all experiments, potentially leading to interference in the mass loss data from the thermocouples. A critical mass loss rate for extinction of approximately 4 g/m^{2}s for all species was identified.

Rangwala [99] notes that the B-number is not constant, but varies with time and space. This can be defined by Equation (2.14) for adiabatic flames, and Equation (2.15) incorporating surface losses.

$$B_A = \frac{\left(\Delta H_C Y_{ox,\infty}\right) - C_{P,\infty}(T_p - T_\infty)}{\Delta H_v} \tag{2.14}$$

$$B_T = \frac{(1-\chi)\left(\Delta H_C Y_{ox,\infty}\right) - C_{P,\infty}(T_p - T_\infty)}{L_v + Q_l} \tag{2.15}$$

where χ is the fraction of heat radiated by flame to the environment rather than the fuel, L_v is the heat of gasification, and Q_l is the heat losses, calculated from Equation (2.16):

$$Q_l = \frac{\dot{q}''_{s,cond} + \dot{q}''_{s,r} - \dot{q}''_{f,r}}{\dot{m}''} \tag{2.16}$$

where $\dot{q}''_{s,cond}$ is the conductive heat flux into the sample, and $\dot{q}''_{s,r}$ and $\dot{q}''_{f,r}$ are the radiative losses from the surface and gains from the flame respectively. Charring also causes a reduction in the B-number, but this is much more difficult to accurately quantify.

2.2.3.2 Smouldering Combustion

After a fire, the heat contained within a timber element, under the right conditions, may lead to continued sustained smouldering. The processes and effects of this are reviewed below.

The presence of oxygen both accelerates the initial char formation [47], and causes the char itself to undergo smouldering combustion upon exposure to air, although not usually at the same time as significant gas-phase combustion [15] (due to flaming combustion consuming the available oxygen). Smouldering is a form of combustion which is flameless, and typically slower and at a lower temperature than flaming combustion [67]. From temperatures around 200 to 300°C, when flaming combustion is only possible with piloted ignition [9], oxygen can exothermically react with the exposed char layer [32]; this can be catalysed by alkali metal impurities [67]. Lignin is the main contributor to smouldering combustion of wood [89], as it typically has the highest char yield (see Section 2.2.1.2.3). This solid phase char oxidation is the main heat source in smouldering processes [67], and can lead to self-sustained smouldering combustion [9, 15, 67], which can provide a pathway to flaming combustion [67], and may lead to sustained charring after removal of the external heat flux under appropriate conditions [9]. However, due to wood's low permeability and high density, smouldering has been found to only continue if exposed to an external heat flux of around 10 kW/m^2 [9]. The char cannot oxidise whilst the flow of pyrolysis gases prevent oxygen from reaching the surface [18, 22, 26, 100]. As a result, the char layer will continue to increase in thickness [22]. At temperatures above 450-500°C, production of volatiles is complete; char can then smoulder, causing further mass loss [9, 15, 18, 32, 90, 100], producing carbon dioxide, carbon monoxide, and water vapour, as well as other pyrolysis products [9]. At high temperatures (above 500°C), the char may visibly glow whilst undergoing oxidation [22]. The exothermic char oxidation process adds to the external heat flux, accelerating pyrolysis [11, 41] and increasing the surface temperature (and thus internal temperatures) [47], thus smouldering helps sustain flaming and may result in prolonged fire duration [23].

Upon cooling, the temperature within the wood may rise above the gas temperature, due to the increase of char combustion after gas-phase combustion has ceased [100].

Friquin [18] has demonstrated that low heat fluxes allow for greater char oxidation, as volatile flow is low and oxygen is able to reach and react with the surface char. Thermogravimetric analyses at 5°C/min found char to oxidise at 400 to 500°C, but at temperatures exceeding 650°C at 40 kW/m^2 [41]. The yield of carbon monoxide and carbon dioxide increases dramatically in oxygen, due to the increased heat release rate leading to faster pyrolysis and thus increased char oxidation [9, 41, 47]. The yield of toxic species is also typically larger than that of flaming combustion [67].

Propagation of smoulder is heavily dependent on the rate of oxygen flow to the reaction zone [67]. One-dimensional smoulder is an idealised scenario often approximated in real fires. This is characterised relative to the direction of the oxygen flow – either forward or reverse propagation. Reverse propagation is when the oxygen travels from the surface through the unburned fuel towards the reaction front. The time for the smoulder front to propagate through a fuel layer is proportional to its thickness squared. Oxygen surrounds the fuel particles as they are heated by the smoulder front. This can trigger the exothermic thermal degradation in the presence of oxygen for cellulosic materials. The heat produced can be sufficient to allow the smoulder to propagate without any char oxidation. Smoulder velocity is always of the order of 10^{-4} m/s (6 mm/min). Forward propagation is where the oxygen diffuses in the same direction as the smoulder front. This smoulder mode will self-extinguish if the heat generated through oxidation of char is insufficient to drive the pyrolysis reactions in the reaction zone. Forward smoulder is approximately ten times slower than reverse smoulder – i.e. in the order of 0.6 mm/min. In reality, smouldering is usually two- or three-dimensional due to factors such as ignition source, orientation, and buoyant flow.

Crielaard [66] tested twelve 100 mm x 100 mm x 50 mm thick softwood CLT samples under a cone calorimeter at 75 kW/m^2. Temperature was recorded by K-type thermocouples at various depths throughout the samples. When the samples had achieved a char depth of 20 mm, the sample was moved under a second cone

calorimeter, at a heat flux of 0 to 10 kW/m^2, to determine the critical heat flux for smouldering extinction. This was found to be around 5 to 6 kW/m^2. The final two experiments had an additional airflow of 0.5 m/s and 1.0 m/s over the sample respectively. Whilst the 0.5 m/s airflow led to quicker extinction than with no airflow, the 1.0 m/s led to sustained burning at 6 kW/m^2. Thus the natural convective airflow within a compartment may have a significant effect on smouldering extinction.

2.2.4 Properties Influencing the Burning of Wood

The above phenomena are all heavily influenced by material properties and the testing conditions. To enable the fire safe use of timber, it is necessary to obtain an understanding of the relative effects of various material, system, and fire properties on the burning behaviour. A summary of available works investigating these effects is given below, with "charring rate" used as a proxy for pyrolysis rate.

2.2.4.1 Material Properties

Charring rate is demonstrated to be strongly dependent on density [11, 18, 23, 26, 28, 32, 42, 65, 82, 87, 89, 101-113], with various charring models [87, 89, 104] being strongly dependent on density. Overall, it can be concluded that samples with higher density will char more slowly due to there being a greater mass of material to pyrolyse; thus more energy is required to drive this endothermic process. This only has a significant effect over wide density ranges, and thus is unlikely to be the governing factor in design, where typical softwoods used in construction are unlikely to vary in density by much more than around 200 kg/m^3 – over this range, a 14% difference in charring rate is observed from the available literature.

Similarly, the presence of moisture is widely acknowledged as retarding pyrolysis [17, 18, 24-26, 31-33, 52, 58, 87, 89, 101, 104, 106, 108, 112, 114] due to the additional energy required to evaporate the water, and thus less energy is available for pyrolysis. Expressions from [115] give typical equilibrium moisture contents from around 18 to 19% in winter and 13 to 15% in summer in the UK. Over these ranges (13-19%), an 18% difference in charring rate is observed from the available literature.

Another significant factor affecting pyrolysis rate is the species of the wood [18, 23, 28, 31, 32, 65, 82, 87, 89, 101-104, 106, 108, 111, 116, 117]. Whilst the species will affect other factors such as density, moisture content, and permeability, there will also be additional factors specific to a species, such as chemical composition [18, 32, 82, 87, 101, 106] (primarily lignin content [18, 82, 87]) and anatomy [18, 89] which influence the rate of pyrolysis. These differences in chemical composition and anatomy will give different yields and rates of formation of char and pyrolysis gases.

Permeability is also known to affect charring rate [18, 32, 39, 82, 87, 89, 101, 102, 106]. This is largely due to grain direction, as permeability along the grain is around four orders of magnitude higher than that across the grain [14, 18, 106]. Increased permeability allows an increased flow of oxygen, thus releasing more energy in the char, so increasing the rate of pyrolysis. Insufficient data are available to systematically quantify the relationship.

2.2.4.2 System Properties

As with any material, the pyrolysis rate of wood is affected by its orientation [59, 65, 87, 109, 110], due to its effects on fire dynamics and airflow. In vertical orientations, buoyancy will drive convection upwards parallel to the sample, resulting in very different conditions to horizontally orientated samples [91]. Charring rates are thus expected to be greater for vertically orientated samples due to increased radiation from the flame. There is poor agreement from authors as to the effect orientation has however, and thus no firm conclusions on the effects of sample orientation can be drawn.

As well as the orientation of the sample, the size will also affect the pyrolysis behaviour [18, 76, 90]. Increase in scale usually means lower heat losses per unit volume of material, thus making samples easier to ignite [67]. There is generally good agreement that pyrolysis rate increases with sample size, although relatively few authors have investigated this effect. Hadden et al. [118] found that the relative effects of sample size (for polyurethane foams) decrease asymptotically with increasing

sample size; thus this is unlikely to be an issue with application to buildings, where the size is an order of magnitude greater.

The grain direction is also recognised as having an effect on pyrolysis behaviour [11, 16, 18, 101, 106, 113], largely due to the large increase (around 10000 times) in permeability parallel to the grain [18, 106], due to the alignment of tracheids. As a result of this, small changes in grain angle can result in large changes in moisture and oxygen movement, thus affecting the charring rate [106]. Additionally, thermal conductivity is greater parallel to the grain than perpendicular to it [18]. As such, it is expected that charring rate will be greater parallel to the grain than perpendicular. However, no significant difference was observed from the available literature. It is also noteworthy that in design, timber elements will not have faces with parallel grains exposed, and thus only charring perpendicular to grain will occur in practice.

The application of gypsum board (or similar) is a well-known method of increasing the time which a timber member can withstand heating under a given scenario [6, 28, 119-124]. Gypsum can fail in a fire through dehydration and cracking, then falling off and exposing the underlying timber (or next layer of gypsum).

Similarly, the presence of a char layer also acts as protection for the underlying virgin wood [11, 18, 26, 28, 39, 58, 89, 90, 103, 104, 106, 107, 111, 117, 120, 121, 124-126]. As a result, the pyrolysis rate in a fire-exposed timber member is initially high whilst no protective layer exists, before decreasing to a lower quasi-constant value once a char layer has formed [11, 18, 19, 25, 26, 38, 45, 47, 58, 81, 87, 90, 104, 110, 121, 127]. It is also commonly acknowledged that when a layer falls off – either gypsum board or a lamella of an engineered timber product – the pyrolysis rate subsequently increases due to the absence of a protective char layer [57, 119, 120, 128]. The thickness of the lamellae is thus important to the fire behaviour – if the lamellae are sufficiently thick, then CLT will behave like solid timber [121]. Whilst the effects of delamination are understood, its causes are still largely unpredictable. In particular, the failure modes and conditions of different adhesives are not well understood.

2.2.4.3 Thermal Exposure

The heating scenario (conventionally this is defined as either a temperature-time curve or an incident heat flux) is known to have a significant effect on the pyrolysis rate [9, 17, 25, 31-33, 42, 47, 52, 76, 82, 91, 100, 103, 104, 107, 110, 113, 116, 117, 125, 129-131]. There is good agreement between authors that charring rate increases with increasing heat flux, due to higher heat fluxes providing more energy to initiate pyrolysis reactions. Heat fluxes up to 270 kW/m^2 [132] have been noted in compartment fires, compared to much lower heat fluxes of (e.g.) 30 kW/m^2 from openings [133] – over this range charring rate varies by around 800%.

The oxygen concentration in the environment surrounding the exposed timber also influences its pyrolysis and combustion behaviour – a lower oxygen concentration will result in lower char oxidation rates, thus there will be more char to reduce the heat transfer into the underlying timber. This has been found to result in a decreased charring rate with decreasing oxygen concentration [25, 47, 52, 106, 114], with the exception of Butler [91], who found that tests in nitrogen and air showed little difference in charring rate, however this is likely due to the high heat fluxes explored, at which pyrolysis will dominate over other reactions. Reduced oxygen concentrations in fully developed fires will result in an approximately 50% reduction in charring rate.

2.2.4.4 Summary

Whilst numerous parameters have been shown to have an effect on charring rate, it can be seen that the effect of incident heat flux is by far the most dominant, an order of magnitude higher than the other parameters over ranges to be expected in design. Therefore, it is vital that this be properly understood to allow safe, robust design. Thus it is also crucial to have a proper understanding of the fire exposures experienced in timber compartments.

2.3 Fire Dynamics

As with any fire in a building, the interaction between the fire and the compartment linings is important. This becomes more complex for flammable linings such as timber,

as any exposed walls, ceilings and floors are susceptible to pyrolysis producing additional fuel, which will contribute to the compartment fuel load. This will produce additional heat, causing a complex coupling between the burning of the fuel and the burning of the compartment.

2.3.1 The Compartment Fire

Whilst an infinite number of gas temperature-time curves are possible for any specific compartment [134] in design the fire is typically implicitly defined by a single (standard) temperature-time curve [7, 135] assumed uniform throughout the compartment, e.g. ISO 834 [7]. In reality, gas temperature depends on material properties, room dimensions, wall construction, exposed materials, arrangement and surface area of combustible products, air movement, and ambient temperature [134]. Additionally, real fires are not infinitely increasing in severity, but can be characterised by growth (pre-flashover), fully developed (post-flashover), and decay phases [136], with fires typically (but not always) fuel-controlled in the growth phase, and ventilation-controlled in the fully developed phase [128]. In a compartment fire, the energy balance can be written as in Equation (2.17) [137]:

$$\frac{dQ_{CV}}{dt} = \dot{Q}_{in} - \dot{Q}_{out} + \dot{Q}_f - \dot{Q}_l \tag{2.17}$$

where $Q_{CV}, \dot{Q}_{in}, \dot{Q}_{out}, \dot{Q}_f,$ and $\dot{Q}_l$ are the energy in any defined control volume, the energy in and out of the control volume, the heat release rate from the compartment fire, and the heat losses to the boundaries. It has been established that $\dot{Q}_{in} \ll \dot{Q}_{out}$ and that due to typical characteristic heating times for (inert) walls, that $\frac{1}{\dot{Q}_f}\frac{d\dot{Q}_{CV}}{dt} \approx 0$ [137], as the heat produced by the fire will be much greater than the change in energy caused by the temperature rise within the compartment. Equation (2.17) can thus be re-written as Equation (2.18):

$$1 = \frac{\dot{Q}_{out}}{\dot{Q}_f} + \frac{\dot{Q}_l}{\dot{Q}_f} \tag{2.18}$$

2.3.1.1 Pre-Flashover Compartment Fires

Compartment fires typically start with a single ignition source, igniting an item of furniture (in real buildings) or a wood crib (in fire tests) which will then start to burn, growing in size and eventually spreading to other nearby items. Pre-flashover fires are typically important for life safety, in terms of providing the necessary egress times, but unimportant for structural fire safety [26].

2.3.1.2 Flashover

Under the right conditions, a fire may grow large enough for flashover to occur. Several criteria exist for determining if and when flashover will occur. There are several criteria commonly cited for determining whether flashover has happened or will occur these are: temperature exceeds 600°C [11]; when the incident heat flux to the fuel load exceeds 20 kW/m^2 (typically on the floor) Waterman [138], or when the burning rate exceeds 40 g/s. Hägglund [139] relates the flashover criterion to air inflow, suggesting that flashover will occur if airflow numerically exceeds $0.5A_v\sqrt{h_v}$, where A_v is the area of the ventilation openings, and h_v is the height of the ventilation openings. Babrauskas [140] relates the heat release rate for flashover to the ventilation area, giving a heat release rate for flashover in kW of $750A_v\sqrt{h_v}$. Thomas [141] also considers the total linings, stating that heat release rate (in kW) must exceed $7.8A_T + 378A_v\sqrt{h_v}$ for flashover to occur, where A_T is the internal area of walls and floors, excluding openings. McCaffrey et al. [142] add in a further factor, based on data from over 100 fires, stating that the heat release rate must exceed $610\sqrt{h_k A_T A_v\sqrt{h_v}}$, where the effective heat transfer coefficient, $h_k = \sum_i \frac{A_i}{A_T}\sqrt{\frac{k\rho C_{p_i}}{t_c}}$ where i represents different surfaces, and t_c is the fire's "characteristic time" – for a steady-state fire, defined here as the time taken to reach the peak room temperature. It should be noted that all these expressions are derived for and from compartment fires with non-flammable surfaces, and as such, the presence of exposed, structural timber elements will not be explicitly accounted for in any of them.

In order to illustrate the differences between these correlations, an arbitrary compartment with internal dimensions 3 m x 3 m x 3 m was modelled by four of the above expressions (Hägglund's [139] expression expresses the flashover criterion in terms of airflow, and thus cannot be directly compared to the others). A single opening of height 1.8 m was chosen, with width varying from 0.5 m to 1.8 m. The surfaces were chosen to be entirely exposed timber, and thus for the expression of McCaffrey et al. a thermal inertia of 2.5×10^5 W^2s/m^4K^2 [11] was assumed. The chosen fuel load was wood cribs with a heat of combustion of 15 kJ/g [11], and based on [142], the characteristic time was taken as 600 s. The heat release rates required for flashover are shown in Figure 2.7. It is evident from this figure that there is considerable scatter between authors, rising with the width of the opening. This highlights the level of complexity in predicting compartment fire behaviour, even without the added complexity of exposed, structural timber elements contributing to the fire dynamics. It can also be seen that (with the exception of Waterman's criterion [138], which is constant), that the necessary heat release rate for flashover increases with an increased opening width (and thus area).

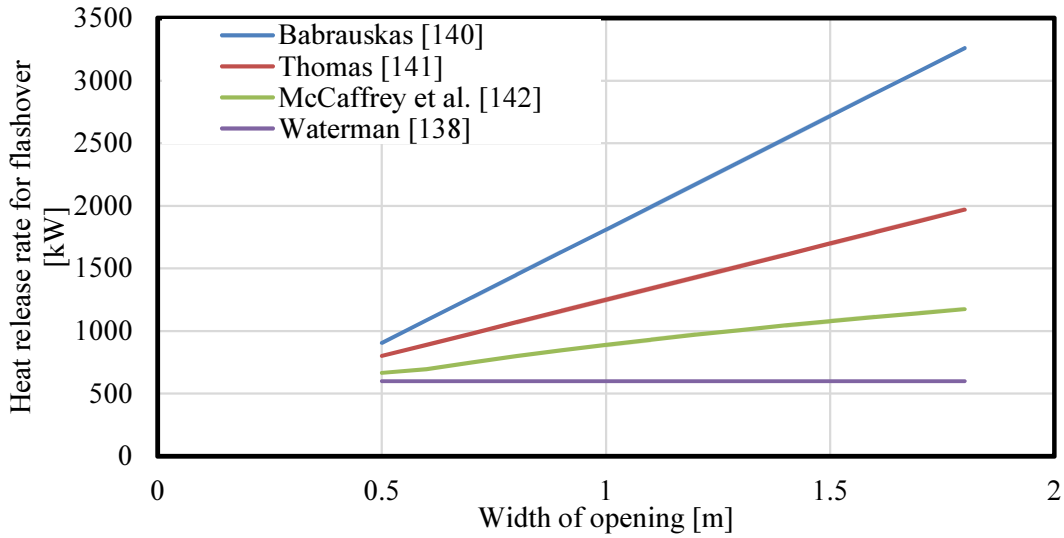

Figure 2.7: Heat release rates for flashover by various researchers varying with opening width.

2.3.1.3 Post-Flashover Compartment Fires

After flashover, all combustible surfaces within the compartment are burning, and the fire dynamics have been traditionally thought to follow one of two modes or "regimes" of burning, initially set out by Thomas et al. [143]. Two parameters are typically used to define the post-flashover compartment fire: the ventilation factor, $A_v\sqrt{h_v}$, and the opening factor, defined by Thomas et al. [143] as:

$$O = A_t/A_v\sqrt{h_v} \tag{2.19}$$

where A_t is the total area of the walls and ceiling excluding the opening. An opening factor of less than 8-10 $m^{-1/2}$ is typically assumed to correspond to a *fuel-controlled* fire, termed *Regime II,* and values above this are typically assumed to correspond to a *ventilation-controlled fire*, termed *Regime I.*

Burning rate has typically been assumed to be independent of the type of fuel, with the burning rate given by Equation (2.20):

$$\dot{m}_b'' = \kappa A_v\sqrt{h_v} \tag{2.20}$$

where for wood cribs, $\kappa = 0.09 \pm 0.01\ kg/m^{5/2}s$. Thomas et al. [143] suggest that as the ventilation factor increases, this relationship ceases to hold due to burning becoming less dependent on the opening factor. For lower opening factors, the inflow will reach a limit where there are velocity changes but no pressure changes, like a buoyant plume. These lower opening factors lead to whereas higher opening factors lead to Thomas and Heselden [144] show experimentally that κ is not constant, but increases with opening factor and appears to asymptote on the order of $0.2\ kg/m^{5/2}s$, albeit at opening factors far higher than conventionally used in experiments (tending towards 100 $m^{-1/2}$ – this is equivalent to a single opening ~0.7 m x 0.7 m in a 3 m x 3 m x 3 m compartment). This suggests significant external flaming. The relationship was also obtained for compartments with low thermal capacity boundaries, resulting in a quasi-constant heat loss coefficient, resulting in peak temperatures being reached

early in the fire. The correlation is also then unique to compartments with the same geometry and boundaries.

Many researchers have explored the fire dynamics of post-flashover compartment fires; it is not the purpose of the current paper to review all these in detail, but to summarise the key aspects in relation to compartment fires with exposed timber surfaces.

Various formulae exist to attempt to define the boundary between *Regime I* and *Regime II* burning. Two are set out by Drysdale [11] in Equations (2.21) and (2.22):

$$R_b = \frac{\rho_g \sqrt{g} A_v \sqrt{h_v}}{A_f} \tag{2.21}$$

where ρ_g is the density of the hot gases, A_f is the surface area of the fuel, and R_b is a parameter defining the burning regime. If $R_b < 0.235$, this indicates a *Regime I* post-flashover fire; if $R_b > 0.29$, this indicates a *Regime II* post-flashover fire. However, since this equation is intended for application to wood crib fires, it may not be suitable for fires from exposed timber surfaces.

$$\dot{m}_b > \kappa A_v \sqrt{h_v} \tag{2.22}$$

Equation (2.22) relates the burning rate to the stoichiometric burning rate – if the condition in Equation (2.22) holds true, the fire is a *Regime I* fire, otherwise the fire is a *Regime II* fire. This expression, however, relies on the assumptions of infinitely fast mixing and reaction between pyrolyzate and oxygen, which are both invalid in real fires. This is evident as external flaming can be observed when the compartment gases are still fuel-lean.

Thomas and Heselden [144] also present plots of average compartment temperature as a function of opening factor for different compartment aspect ratios and wood crib arrangements, with one example shown in Figure 2.8. The peak of the curve is taken

as the boundary between R*egime I* and *Regime II* burning. They observed that compartment aspect ratio did not affect the temperature significantly (for the small compartments tested), but different wood crib size and spacings had a significant effect; changing the fuel configuration entirely away from wood cribs to solid timber surfaces will likely have an even larger effect. Thus the specific data in Figure 2.8 should not be applied to a compartment with any fuel load other than 20 mm x 20 mm wood cribs spaced 20 mm apart.

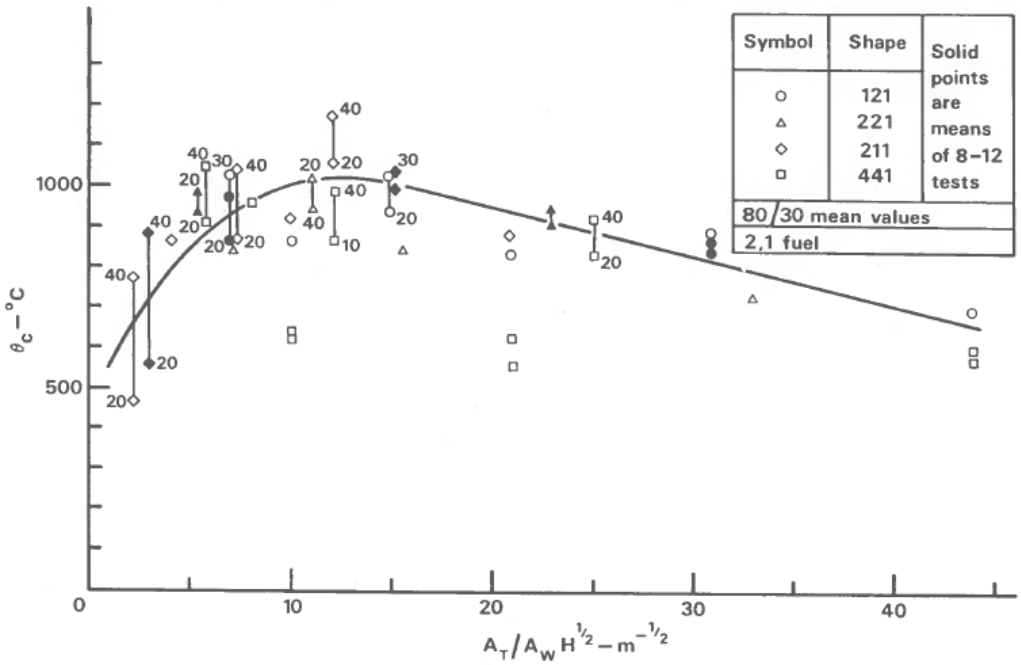

Figure 2.8: Average compartment temperatures for crib factors as a function of opening factor [144].

Thomas and Heselden [144] state that A_T is "the effective internal surface area over which heat is lost" (implicitly through conduction). As such, for a traditional compartment with a fuel load on the floor, A_T is simply calculated as the area of the walls and ceiling minus the opening area. However, when exposed timber surfaces ignite, heat will no longer be lost through these surfaces, and thus reformulation of the opening factor may be required. As the initial fuel load burns out, the floor will eventually be considered as part of A_T again, changing the opening factor (and fire

dynamics) once more. In order to accurately describe the fire dynamics in such a case, a full compartment energy balance will be necessary.

2.3.2 Heat Transfer Within a Compartment

To determine the structure's response to the fire, a heat transfer analysis can be carried out. The fire growth will be dependent on both the combustion process and the building properties [137]; especially for a combustible building material such as timber. The external heat flux onto a compartment boundary during a fire can be defined by Equation (2.23) [9]:

$$\dot{q}_e'' = \dot{q}_{r,f}'' + \dot{q}_{r,g}'' + \dot{q}_{r,w}'' + \dot{q}_c'' \tag{2.23}$$

where $\dot{q}_{r,f}''$ is the radiant heat flux from the compartment fire, $\dot{q}_{r,g}''$ is the radiant heat flux from the hot smoke gases, $\dot{q}_{r,w}''$ is the radiant heat flux from the compartment walls, and $\dot{q}_c''$ is the convective heat transfer between structural elements and hot gases. Radiative flux will begin to dominate over convective flux with increasing fire size [145]. When this is combined with the heat losses, estimates can be made for ignition times and pyrolysis rates of exposed timber members.

2.3.2.1.1 Radiant Heat Exchange

The radiant heat fluxes between surfaces can be calculated by Equation (2.24):

$$\dot{q}_{r,w}'' = F_{ij}\varepsilon\sigma(T_i^4 - T_j^4) \tag{2.24}$$

where F_{ij} is the view factor between objects i and j, for which many geometrical relationships exist, ε is the emissivity of the surface, and σ is the Stefan-Boltzmann constant, 5.670 x 10^{-8} W/m^{2}k^4. This needs to be solved for the net radiation exchange between multiple surfaces, in addition to the incident radiant heat from the fire. To calculate the radiant heat from the hot smoke, Equation (2.25) can be used:

$$\dot{q}_{r,g}'' = \varepsilon_g\sigma T_g^4 \tag{2.25}$$

where the smoke emissivity can be calculated by Equation (2.26) [9]:

$$\varepsilon_g = 1 - e^{-\kappa t} \tag{2.26}$$

where t is the thickness of the smoke layer, and the absorption coefficient, κ, can be found from Equation (2.27) [9]:

$$\kappa = C f_v T_g \tag{2.27}$$

where f_v is the soot volume fraction, and C a constant. Fully developed fires have typical absorption coefficients of 1 m^{-1} [9]. During the fully developed phase of the fire, this radiant flux will dominate, as due to smoke's high absorptivity, radiant inputs from the fire or compartment walls are often absorbed by the smoke in fully developed compartment fires, whereas in the decay phase, net radiation between compartment walls will dominate [9]. This is based on the assumption of inert walls, therefore the implications for exposed timber surfaces may be significantly different due to changed re-radiation conditions.

Also important to consider is the emission spectrum of an emitted flame, and how closely this resembles the emission in experimental apparatus [146]. Flames from burning wood typically emit radiation around 1 to 6 μm in wavelength, mostly emitted from carbon dioxide and water vapour, with some additional radiation from soot particles, the relative contribution of which has been found to increase with flame thickness [146]. Comparing this with typical lab apparatus, the infrared lamps of the Fire Propagation Apparatus (FPA) have their spectral energy emission peaks at 1.15 microns [147], whereas propane-fired radiant panels typically have spectral energy emission peaks above 2 microns [148]. However, it has been found for timber char that:

$$a = 0.78 + \frac{0.18}{\sqrt{\bar{\lambda}}} \tag{2.28}$$

where a is the absorptivity and λ is the radiation wavelength in microns [149]. Thus for wood flames, a = 0.85 to 0.96, for the FPA, a = 0.95, and for propane-fired radiant panels, a = 0.91. Consideration should also be given to the absorptivity of timber surfaces before a char layer has formed, and the effects this could have on interpretation of test results.

2.3.2.1.2 Convective Heat Exchange

The convective heat flux from a hot gas layer to a wall can be calculated by Equation (2.29); similar correlations exist for ceilings and floors.

$$\dot{q}_c'' = h_c(T_g - T_w) \tag{2.29}$$

where the average convective heat transfer coefficient, h_c, is calculated by Equation (2.30):

$$h_c = \frac{\overline{Nu_L} k_g}{L} \tag{2.30}$$

where k_g is the thermal conductivity of air, which is a function of temperature [150], L is the characteristic length scale of the problem and the Nusselt number, $\overline{Nu_L}$, is found from Equation (2.31) [150] for turbulent flow over a vertical plate under free convection:

$$\overline{Nu_L} = \left(0.825 + \frac{0.387 Ra_L^{\frac{1}{6}}}{\left[1 + \left(\frac{0.492}{Pr}\right)^{\frac{9}{16}}\right]^{\frac{4}{9}}} \right)^2 \tag{2.31}$$

where the Rayleigh, Prandtl, and Grashof numbers are calculated by Equations (2.32)-(2.35) [150]:

$$Ra_L = Gr_L Pr \tag{2.32}$$

$$Pr = \frac{\nu}{\alpha} \tag{2.33}$$

$$Gr_L = \frac{g\beta(T_g - T_w)L^3}{\nu^2} \tag{2.34}$$

$$\beta = \frac{2}{T_w + T_g} \tag{2.35}$$

where ν is the kinematic viscosity, α is the thermal diffusivity, and g is the gravitational constant. As smoke is mostly made up of air, the properties in Figure 2.9 can be applied to smoke also.

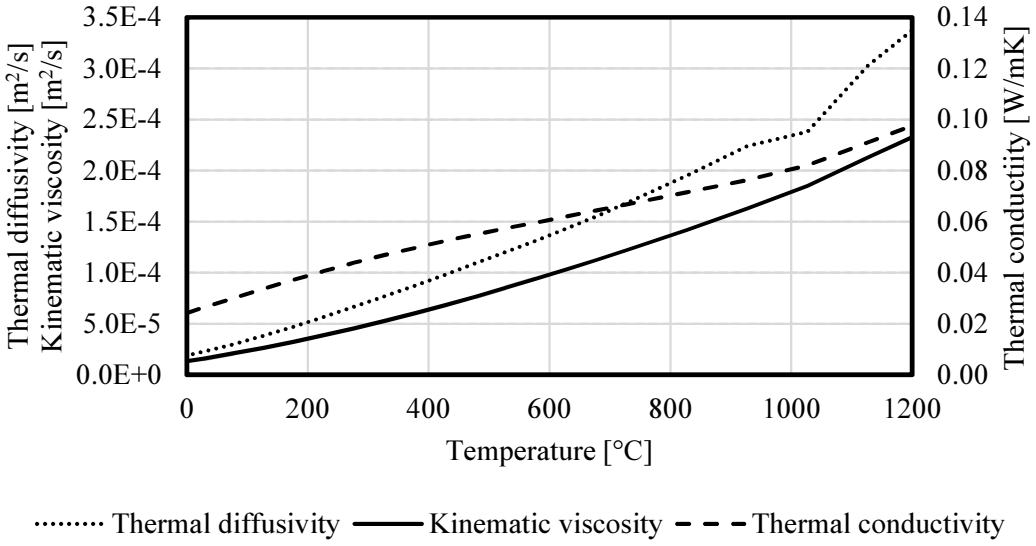

Figure 2.9: Temperature-dependent thermal properties of air at 1 atmosphere (from [150])

This yields convective heat transfer coefficients in the order of 4 to 6 W/m^{2}K. Alternatively, if the flow is turbulent, the Nusselt number is instead found by Equation (2.36) [150] for turbulent flow over a flat plate:

$$\overline{Nu_L} = \left(0.037 Re_L^{\frac{4}{5}} - 871\right) Pr^{\frac{1}{3}} \tag{2.36}$$

where the Reynolds number is given in Equation (2.37):

$$Re_L = \frac{uL}{\nu} \tag{2.37}$$

where u is the gas velocity. The interactions between flames and walls is not well characterised, so calculating this velocity remains a significant challenge. Experimentally, in compartment fires h_c is commonly cited to be between 10 and 40 W/m^{2}K [9], with an average value of 25 W/m^{2}K cited by Eurocode 1 [151].

As with the expressions for flashover criteria, these correlations do not explicitly consider the effects of exposed, combustible timber surfaces, but do allow initial estimates of heat transfer within the compartment.

2.3.3 Timber Compartment Fire Tests

A number of tests have been carried out on heavy timber compartments, which allow some insight into the interdependence of the fuel burning and the burning of the timber linings.

Figure 2.10: External flaming from modular timber hotel with flammable internal linings (from [152]).

Frangi and Fontana [152] undertook full scale tests on modular timber hotels. One series of three tests investigated the response times and efficiency of detection and sprinkler systems, and the other series of three tests investigated the structural response. The modules were 6.6 m long, 3.1m wide, and 2.8 m high. The short wall had a 1.5 m x 1.7 m window, corresponding to an opening factor of 21.7 $m^{-1/2}$, as calculated by Equation (2.19).

Four different modules were used: H1 and H2 had combustible oriented strand board (OSB) linings, and G1 and G2 were lined by non-combustible gypsum plasterboard. H1, H2, and G1 had timber board flooring, and G2 had a floor formed from hollow core concrete elements. All floors were covered in linoleum. For the detection and sprinkler tests, all modules were fitted with an automatic detection system with four different sensors and two sprinkler positions, one on the ceiling, one on a wall. Activation temperatures were 68°C; the sprinklers activated around 3.5 minutes into the tests with combustible linings, which was around a minute later than for tests without combustible linings. The fire load in each module was a 1.6 m x 2 m mattress,

and 11 wooden pallets. Total fire load density for rooms with non-combustible linings was 363 to 366 MJ/m^2, and for rooms with combustible walls and ceilings, 855 MJ/m^2 (due to combustible walls and ceilings). For the loaded tests, two modules were used, one on top of the other, with the windows open in the lower floor, and closed in the upper floor for each of the three tests. The lower modules used for the three tests were G1, H1, and G2, and the upper modules were all H2. Temperature was recorded at over 100 points throughout the tests using K-type thermocouples. Mass loss of the entire construction, and oxygen, carbon dioxide, and carbon monoxide concentrations were also recorded at an unspecified location. Flashover occurred earliest in the H1 module with combustible linings, at around 4.5 minutes, compared with 6 and 7 minutes for the modules with non-combustible linings. External flaming was much more severe (~3 m compared to ~1 m) in the combustible-lined test, shown in Figure 2.10, with the first pane of the upper window failing after 6 minutes, and the second pane at around 7.5 minutes, compared to around 14 and 40 to 42 minutes for the other tests for the first and second panes respectively. Due to lack of oxygen at the rear of the rooms, temperatures were lower at these points, and excess pyrolysis gases were burned outside the room. No significant differences were found between compartment temperatures with combustible and non-combustible linings; average temperatures were around 600 to 800°C in the first 20 minutes of the tests, before rising to around 1000°C for the remainder. These tests show that (as would be expected) the presence of combustible surfaces reduces the time to flashover, and as a result of increased fuel load, increases the severity of external flaming.

Hakkarainen [128] carried out 3 tests on heavy laminated timber structures – one using unprotected timber and the other using 1 and 2 layers of gypsum protection. The room measured 4.5 m x 3.5 m x 2.5 m with a 2.3 m x 1.2 m window, equivalent to an opening factor of 17.5 m$^{-1/2}$, again suggesting a *Regime I* fire. A fire load of wooden cribs equivalent to 720 MJ/m^2 was used, approximately double that of Frangi and Fontana's [152]. In addition to measuring gas-phase temperatures throughout the compartment, and solid-phase temperatures between and behind the gypsum boards using K-type thermocouples, incident heat flux on the façade 2.2 m above the window was measured. In the unprotected test, the compartment temperature averaged 700°C –

about 300°C to 500°C lower than that predicted by a parametric fire curve, as per Equations (2.38) to (2.40) [151]:

$$T_g = 20 + 1325(1 - 0.324e^{-0.2t^*} - 0.204e^{-1.7t^*} - 0.472e^{-19t^*}) \quad (2.38)$$

$$t^* = t\Gamma \quad (2.39)$$

$$\Gamma = \frac{\left(\frac{A_v\sqrt{h_v}/A_T}{\sqrt{k\rho C_p}}\right)^2}{\left(\frac{0.04}{1160}\right)^2} \quad (2.40)$$

Due to insufficient oxygen for complete combustion, after flashover, excess unburnt gases flowed out the compartment, where they burned due to the availability of oxygen, as found by Frangi and Fontana [152]. Approximately 50% of burning took place outside the compartment for exposed timber surfaces, compared to 15% for protected timber surfaces. Temperature increased towards the end of the test, as more oxygen was available due to a decreased rate of pyrolysis gas formation and consumption inside the compartment. Initially protected tests resulted in higher gas temperatures, contrary to the results of Frangi and Fontana [152]. Incident heat fluxes on the external façade peaked at around 140 kW/m^2 in the test with two layers of plasterboard, around 20 minutes post-flashover, although were typically significantly lower (~40-100 kW/m^2) than this for most of the duration of each test. The other two tests showed a gradually increasing heat flux until the fire was manually extinguished.

Frangi et al. [153] performed a full-scale fire test on a 3 storey CLT building, with a 7 m x 7 m floor area, and height of 10 m. External walls were 85 mm thick, and an inner wall dividing the building in two was also 85 mm. Walls had various claddings: 27 mm mineral wool and 12 mm standard gypsum board on all walls, and an additional 12 mm fire-rated gypsum board on three of the four walls. The floors were formed of 142 mm thick CLT, with 60 mm sand, a polyethylene sheet, a 50 mm concrete topping, and 20 mm wood flooring on top. The ceilings were protected with 27 mm mineral

wool and 12 mm fire-rated gypsum board. The fire room was on the first floor, and had dimensions 3.34 m x 3.34 m x 2.95 m. It had two 1m x 1m windows, and a 0.9 m x 2.1m door. The door remained closed, and windows were opened to 25% of their area, sliding horizontally, corresponding to an opening factor of 100.1$m^{-1/2}$, significantly larger than in [128, 152] The fire load was two polyurethane mattresses and four wooden cribs. The fire load was estimated as 790 MJ/m^2 (assuming 50% of the floor was involved, and that the gypsum prevented the involvement of the CLT wall panels), similar to [128]. Windows started breaking after 20 and 30 minutes, and were completely broken by 36 minutes into the test, with external flaming as shown in Figure 2.11. This increased the opening factor to 24.3 $m^{-1/2}$, more similar to previous tests [128, 152].

Figure 2.11: External flaming from encapsulated CLT compartment (from [153]).

Flashover occurred around 40 minutes into the test, significantly later than the unprotected, better ventilated tests in [128, 152]. The door failed after 53 minutes, enabling smoke flow into adjoining rooms, and increasing the opening factor to 10.3 $m^{-0.5}$, potentially changing its regime of burning. After 55 minutes the fire was reported to start decaying at an unspecified rate, and was manually extinguished after 60

minutes. Windows in the room above remained intact, and thus upwards fire spread to the adjoining room did not occur. Gypsum board was assumed to fail at 600°C, after which the CLT surface temperature rose rapidly to almost 800°C. Visual observations confirmed that gypsum fell off in the last ten minutes of the test. Similarly, gypsum on the ceiling failed after 40 minutes, leading to similar temperatures. Charring depth after the test on the wall was measured as varying between 5 to 10 mm. As the CLT panels were completely encapsulated, the knowledge of the behaviour of timber compartment fires that can be obtained from this test is severely limited, however the importance of maintaining effective encapsulation can be seen.

Li et al. [154], McGregor et al. [155], and Li et al. [156] present a series of eleven tests in a 4.5 m x 3.5 m x 2.5 m CLT room with an opening factor of 17.7 $m^{-1/2}$, very similar to [128]. Conflicting numbering systems are used throughout, and so the system in Table 2.2, based on Li et al. [154] will be referred to herein.

Table 2.2: Test matrix for compartment fire tests in [154-156].

Test number	Interior linings	Number in [155]	Number in [156]
1	Fully unprotected CLT	3	
2	Fully protected CLT	1	
3	Fully unprotected CLT	5	3
3a*	Fully unprotected CLT	2	1
4	Fully protected CLT	4	2
5	Back and side wall exposed CLT		
6	Two side walls exposed		
7	One side wall exposed		
8	Fully protected LTF† with 2 layer PB		8
9	Fully protected LTF† with 1 layer PB		9
10	Fully protected LSF‡ with 1 layer PB		10

* not included in [154], † Light Timber Frame,‡ Light Steel Frame

The floors were built up of 15.9 mm Type X gypsum, then 12.7 mm cement board, then 19 mm hardwood tongue and groove maple flooring. Tests 1-2 used propane as a

fuel load; the others used furniture comprising a double bed, two bedside tables, and two chests of drawers, giving fuel loads of 541±13 MJ/m^2 (including the maple floor). The tests were started by igniting the pillow with a propane burner. The tests in CLT compartments recorded temperature using K-type thermocouples in the form of 4 thermocouple trees, each with 6 thermocouples every 0.4 m from the floor. A plate thermometer was also used 1.5 m above the floor. 8 groups of six thermocouples were embedded in the structure (6 in the wall, 2 in the ceiling), one between the gypsum layers, one at the gypsum/CLT interface, and the other 4 at 6, 12, 18, and 24 mm into the CLT. Heat release rate (HRR) was calculated by oxygen consumption – this included burning outside the room. After flaming combustion in test 2, smouldering continued for about 40 minutes, in which time some localized delamination occurred. In test 1, the CLT panels became involved during the growth phase of the fire as the HRR exceeded 1 MW – resulting in a much increased growth rate. The ceiling panels ignited first, and within 20 s all exposed CLT panels ignited leading to flashover. The HRR of the CLT settled at around 5 MW, with no delamination occurring. In test 3, the CLT panels became involved as the HRR reached 0.4 MW. The total HRR settled around 6 MW after 45 minutes; delamination occurred around 40 minutes. Burning continued, and after about an hour, the joints between the CLT panels started to open up and the test was manually extinguished. Involvement of CLT panels did not have a noticeable effect on the temperature inside the room, as observed by [152], however with only 24 thermocouples, such effects may have occurred without being noticed. Timber panels becoming involved in the fire increased the fire growth rates, leading to reduced time to flashover and tenability times; and increased generation of volatiles and smoke. Of the two fully unprotected CLT tests, both had a typical CLT contribution of around 5 MW. Delamination was seen to momentarily increase the HRR, due to burning of the newly exposed timber, before declining again once a fresh char layer had accumulated.

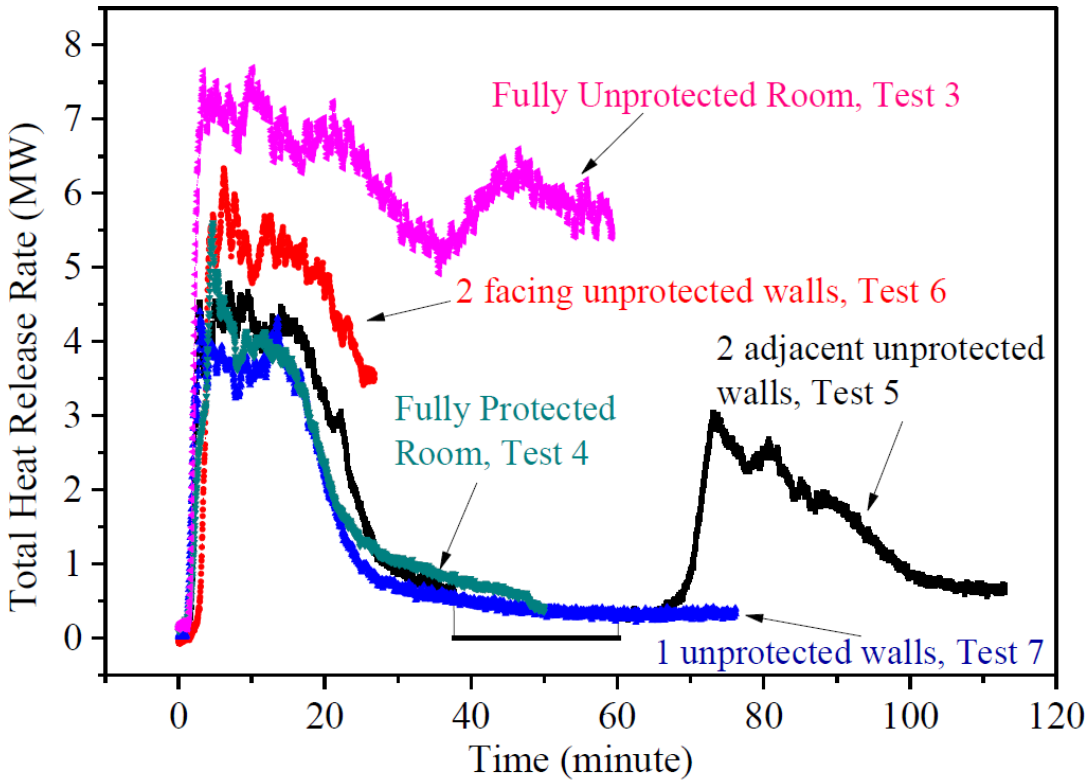

Figure 2.12: Heat release rates from protected and unprotected CLT compartment fires (from [154]).

Tests 1, 2, 3a, and 4 started to decay around 20 to 25 minutes into the test. The enhanced burning of test 3 was attributed to the burning of the CLT panels (in other tests, the wall drywall fell off around 53 minutes into the test. This time is not noted for test 3). Flashover occurred around 5.3 to 8.6 minutes into the tests. They calculated that in test 3, of the 7.1 MW average HRR, 4.5 MW was outside the room, compared to 0.8 MW of 4.0 MW for tests 2 and 3a. This was calculated by Equation (2.41):

$$\dot{Q}_{int} = \dot{m}_{ent} Y_{ox} H_{c,ox} \tag{2.41}$$

where $\dot{m}_{ent}$ is the mass of the air entrained, Y_{ox} is the oxygen concentration, and $H_{c,ox}$ is the heat of combustion of fuel per unit mass of oxygen consumed. The external heat release rate was then calculated by taking this away from the total HRR. Tests 5-7, which had a combination of exposed and protected CLT surfaces, are shown in Figure 2.12. Tests 5 and 6 both experienced a secondary flashover after the onset of delamination, whereas test 7 achieved auto-extinction – i.e. the heat transfer into the

exposed timber surfaces reduced such that the rate of volatile production dropped below the critical mass loss rate for sustained flaming (see Equation (2.11)). Again, the importance of maintaining effective encapsulation was observed. Delamination was also identified as having the potential to significantly affect the fire dynamics, through exposing fresh timber and thus increasing the burning rate, potentially leading to a secondary flashover. It was also demonstrated that for a compartment with only one exposed surface, auto-extinction is possible.

Hox and Baker [157] present a full-scale fire test of a structure built from CLT elements. The compartment was 5.75 m x 2.3 m x 2.73 m high, with an opening of dimensions 0.9 x 2 m. One corner of the room was subdivided as a bathroom, giving an opening factor of 21.7 $m^{-1/2}$, as in [152]. The long wall opposite the bathroom, and the ceiling were unprotected. A fuel load of 660 MJ/m^2 was applied using wooden pallets, a mattress, some wooden furniture, and a small amount of heptane. 9 K-type thermocouples were inserted in the timber walls. Flashover occurred after 250 s, and after 345 s, the window opposite the door broke, decreasing the opening factor to 10.7 $m^{-1/2}$, now on what is assumed to be the boundary between traditional *Regime I* and *Regime II* fires. After 70 minutes, part of the exposed CLT wall near the window was completely burned through, with large parts of this wall burning through by 85 minutes. The test was terminated at 96 minutes when the ceiling collapsed.

Crielaard et al. [158] present a series of small scale experiments on CLT compartments with varying numbers of exposed timber surfaces, to study the auto-extinction behaviour of CLT once the contents of a fire compartment have burned out. 100 mm thick CLT with 5 uniform lamellae was used, with either 1, 2, or 3 surfaces exposed. Internal dimensions were 0.5 m x 0.5 m x 0.5 m, with a 0.18 m x 0.5 m opening, giving an opening factor of 18.2 $m^{-1/2}$. A constant heat release rate of 41 kW was applied by propane burners within the compartment. Temperature was measured in the timber using K-type thermocouples inserted at depths of 20, 30, 40, 50, and 60 mm. It was shown that delamination of CLT lamellae during the cooling phase of a compartment fire can sustain flaming combustion, or lead to a transition from smouldering back to flaming combustion (i.e. secondary flashover), however, given the right conditions,

the CLT was unable to sustain flaming without an external heat source, and eventually extinguished. Experiments with one exposed CLT surface extinguished, as did two experiments with two exposed surfaces. One experiment with two exposed surfaces extinguished before delamination triggered a re-ignition of the exposed surfaces. The test with three exposed surfaces did not extinguish or tend towards extinction. He goes on to show that delamination of exposed CLT linings can be prevented in some cases by an increased thickness of the top lamella, such that the charring front does not reach the adhesive line.

Using fundamental material properties from small-scale tests as reviewed in Section 2.2 combined with the energy balance presented herein can allow the response of a timber element to a given fire scenario to be calculated. The key findings from the compartment fire tests reviewed herein are summarised in Table 2.3.

From the available tests, it can be confirmed that encapsulation with gypsum board can delay or prevent involvement of timber elements in the fire, and that auto-extinction can be achieved in certain scenarios. However, if architects' wishes to express more of the timber within the structure are to be realised, further research is necessary looking into the changes in fire dynamics and auto-extinction behaviour when multiple exposed timber surfaces are present.

Table 2.3: Summary of timber compartment fire tests.

Work	Fuel load	Opening factor	Key findings
Frangi and Fontana [152]	Furniture, 363-366 MJ/m^2	21.7 m$^{-1/2}$	Timber surfaces reduce time to flashover and increase severity of external flaming.
Hakkarainen [128]	Wood cribs, 720 MJ/m^2	17.5 m$^{-1/2}$	Fully exposed timber surfaces will lead to sustained flaming.
Frangi et al. [153]	Furniture and wood cribs, 790 MJ/m^2	100 m$^{-1/2}$	Maintaining integrity of the encapsulation is important to prevent involvement of protected timber surfaces in the fire. A single layer of gypsum on top of mineral wool lasted 40-50 minutes in these experiments.
Li et al. [154-156]	Furniture, 541±13 MJ/m^2	17.7 m$^{-1/2}$	Delamination can lead to re-ignition of exposed surfaces. Burnout can be achieved if only one surface is exposed.
Hox and Baker [157]	Furniture and heptane, 660 MJ/m^2	21.7 m$^{-1/2}$	-
Crielaard et al. [158]	Propane burners, 41 kW	18.2 m$^{-1/2}$	Burnout can be achieved in only one surface is exposed. Burnout can be achieved if two surfaces are exposed, if delamination is prevented. Three exposed timber surfaces will lead to sustained flaming.

2.4 Conclusions

This chapter has presented a review of the pyrolysis, ignition, and combustion processes associated with timber products, and reviewed the factors that influence these processes. The burning of timber depends on material, system, and fire properties. Heating scenario and encapsulation and/or delamination have been demonstrated to be the most critical factors influencing the pyrolysis and subsequent combustion of timber.

The majority of works undertaken exploring the effects of various parameters on pyrolysis rates have been carried out in isolation, resulting in testing and reporting that provide inconsistent results, and many unnecessarily repeated results. As such, some factors, such as density and moisture content for instance, have a large data pool, whilst other factors, such as sample orientation and grain direction, have limited data. To provide a data pool useful for application to tall timber construction, it is recommended that future work explores the likely variability in design, and build on the data presented herein to fill some of the knowledge gaps identified. Key data, such as the parameters listed in Section 2.2.4 should be noted for all subsequent experiments to allow meaningful comparisons and separation of variables.

A number of compartment fire experiments with exposed timber surfaces have found that exposed timber increases the heat release rate of the fire, and can result in sustained burning of the exposed timber surfaces after burnout of the compartment fuel load. There is currently limited understanding of the phenomena leading to sustained burning or extinction. This thesis will explore topics to link the fundamental timber flammability to the compartment fire dynamics with a view to exploring the conditions under which auto-extinction can occur, and how this can be used in modern building design.

Chapter 3 Bench-Scale Testing of Auto-Extinction Parameters

3.1 Introduction and Background

A review of the literature on the fire behaviour of engineered timber products, and subsequent application to compartment fires has identified that under certain conditions, exposed timber surfaces within a compartment may stop burning (i.e. auto-extinguish) when they cease receiving an external heat flux from the compartment fuel load. Quantification of these parameters was identified as a key knowledge gap, which is explored experimentally in this chapter. Firepoint theory has previously been used to explore ignition and extinction conditions of a solid fuel in relation to the mass flow of volatiles released [88]. This can be adapted to predict auto-extinction of a charring polymer by capturing the necessary heat transfer phenomena. A summary of the relevant theory is given below.

When heated, charring solids pyrolyse producing flammable and inert gases (pyrolyzate), tars, and a rigid, carbonaceous char layer [22]. Flaming ignition of the volatiles is possible only if a mixture of gases and air exists within the flammability limits and at the right temperature, in the presence of a competent ignition source. The composition of the gas products is not well known so theoretical prediction of this is not possible. Smouldering ignition of the char layer is also possible, but does not usually occur simultaneously with significant flaming combustion [22, 26]. As a result, under flaming conditions, the char layer will continue to increase in thickness [22], reducing the rate of heat transfer to the virgin material and resulting in a subsequent gradual decline in pyrolysis rate and hence mass flux of pyrolyzate [19, 38]. This results in a reduced heat release rate, and thus a lower heat flux from the flame. Therefore, an external heat flux is necessary to sustain pyrolysis above the critical value required for combustion.

When charring polymers as building materials make up a substantial portion of the fuel load in a compartment, they may continue flaming after the compartment contents burn out due to re-radiation between compartment linings. Therefore determining the

extinction criteria will allow the continued burning behaviour of such polymers to be predicted with the potential for use in design. Principally this will determine whether the re-radiation between surfaces is sufficient to sustain flaming, or whether auto-extinction occur. For any material, flaming extinction and piloted ignition have the same critical conditions [11, 92], with both being dependent on fire point conditions [9]; Torero [159] relates this to a critical Damkohler number. In other words, a flame will extinguish if the production of flammable vapours drops below a critical value, $\dot{m}''_{cr,}$ due to the mixture of air and fuel (pyrolyzate) adjacent to the solid surface dropping below the lower flammability limit. It should be noted that for a charring solid however, the material at extinction will be different to the original material at ignition due to the presence of a char layer. Thus the heat transfer through the material and consequently the critical conditions for sustained flaming will differ. The critical pyrolysis rate per unit area can be expressed in terms of the net heat flux by Equation (3.1) [94]:

$$\dot{m}''_{cr} = \frac{\dot{q}''_n}{L_v} \tag{3.1}$$

where $\dot{m}''_{cr}$ is the mass loss rate per unit area, $\dot{q}''_n$ is the net heat flux, and L_v is the heat of vaporisation of the solid fuel (equal to the heat of pyrolysis plus the heat needed to raise the fuel from ambient to pyrolysis temperature). Since vaporisation will occur for the virgin polymer rather than the char, it is the net heat flux at the charline that is of interest – a detailed understanding of heat transfer and surface losses is necessary to estimate this value. This has been developed in the context of firepoint theory.

3.2 Firepoint Theory

Rasbash et al. [88] present a method for quantifying the ignition and extinction conditions of a solid fuel in relation to the mass flow of volatiles released. This was accomplished by conducting a series of experiments using the "firepoint apparatus" – a radiant panel heating a sample from above – to determine the effects of incident heat flux, air flow and oxygen concentration on the critical mass flux required for sustained flaming of PMMA. Close to the critical heat flux for piloted ignition (12 kW/m^2 to

19 kW/m^2), the critical mass flux was found to increase with heat flux, from about 3.8 g/m^{2}s to 5.2 g/m^{2}s; thereafter it became independent of external heat flux. This initial variation was attributed to flame behaviour varying with heat flux, hypothesised to be caused by changes in the composition of volatiles affecting the heat of combustion. The effects of airflow were also explored; an initial drop from around 5.3 g/m^{2}s to 3.2 g/m^{2}s was observed over the range of 0 to 0.6 g/s of airflow, before rising again to around 5.0 g/m^{2}s at 1.2 g/s airflow; this was attributed to changes in convective heat transfer. Reducing the oxygen concentration below 21% (vol.) resulted in a sharp increase in critical mass flux from around 3.3 g/m^{2}s to 10.4 g/m^{2}s at 19% O_2; this was attributed to lower oxygen concentrations yielding lower flame temperatures which are more easily quenched.

Rasbash et al. [88] concluded that that firepoint theory may be used to determine if a sample will continue burning in the absence of a supporting heat flux through Equation (3.2):

$$S = \left(\phi \Delta H_{c,n} - L_v\right)\dot{m}'' + \dot{q}_e'' - \dot{q}_l'' \tag{3.2}$$

where ϕ is the critical ratio of convective heat transfer to the heat of combustion of the volatiles, $\Delta H_{c,n}$ is the net heat of combustion of the solid, L_v is the heat of vaporisation, and $\dot{q}_e''$ and $\dot{q}_l''$ are the external heat flux and heat losses respectively. S represents the "excess" net heat flux above that required to sustain flaming; if $S>0$, the flame will be sustained, but if $S<0$, extinction will occur. Equation (3.2) is an expansion of Equation (3.1), with the net heat flux expanded into different components. Using Equation (3.2), Equation (3.1) can be expanded:

$$\dot{m}_{cr}'' = \frac{\dot{q}_e'' + \dot{q}_f'' - \dot{q}_l''}{L_v} \tag{2.11}$$

where $\dot{q}_f''$ is the heat flux from the flames to the sample surface, here assumed to be equal to $\phi \Delta H_{c,n} \dot{m}_{cr}''$.

Tewarson and Pion [94] experimentally determined values for the heat of vaporisation, for various solids using differential scanning calorimetry (DSC). For timber, they found a heat of vaporisation of 1.82 kJ/g. The heat of vaporisation includes the heat required to raise the solid to its pyrolysis temperature and the heat of pyrolysis. Assuming a pyrolysis temperature of 300°C [32, 38] (noting that some pyrolysis will occur below this temperature, however the mass loss will be low and can be neglected [160]), the heat of pyrolysis can be calculated from Equation (3.3) [94]:

$$L_p = L_v - \int_{T_\infty}^{T_p} C_p dT \tag{3.3}$$

where C_p is the specific heat capacity of the timber (using temperature dependent values from e.g. Eurocode 5 [6], which are consistent with literature values [128]), and T_∞ and T_p are the ambient and pyrolysis temperatures respectively. This gives a heat of pyrolysis of 1.1 kJ/g. Since the virgin timber at the charline will already be heated to 300°C, it is this value, rather than the heat of vaporisation that should be used in Equations (3.2) and (2.13).

3.3 Experimental Investigations

To determine critical values for flaming extinction of timber, an experimental setup with well-controlled boundary conditions was desired. From Equation (2.11), the energy balance is the controlling factor for extinction; the external or applied heat flux is the only variable which can be directly manipulated. As such, this was selected as the variable of interest. Two series of experiments were undertaken: 1) experiments run at a constant incident heat flux, enabling auto-extinction or sustained flaming due to the increase in the char layer thickness, thus keeping $\dot{q}_e''$ constant and allowing $\dot{q}_l''$ to increase as a function of time; and 2) two-phase experiments in which the sample was exposed to a "high" heat flux for a prescribed time before reducing the heat flux to a "low" value. This is analogous to the transition in heating from a fully developed compartment fire to heating from another burning CLT surface. To achieve this, an apparatus allowing control of heat flux with a quick thermal response time was required, and thus the FM Global Fire Propagation Apparatus (FPA) was selected.

3.3.1 The Fire Propagation Apparatus (FPA)

The FPA comprises four tungsten filament lamps which give uniform irradiation over the surface of a sample [147]. It is noteworthy that the FPA has its spectral energy emission peaks at 0.89 and 1.15 microns, [147] whereas flames from bio-based materials can have emission peaks as high as 4.5 microns [161]. The quartz around the heating elements in the FPA absorb any emissions above c.2 microns [147].

It has been found for timber char that the absorptivity, α varies as:

$$\alpha = 0.78 + \frac{0.18}{\sqrt{\lambda}} \tag{3.4}$$

where λ is the radiation wavelength in microns [149]. Thus for the FPA, α = 0.95 to 0.97, whereas for luminous flames α = 0.87. Whilst the absorption spectrum of timber will be different to that of char, the surface will have charred by the time extinction occurs, and thus it is the absorptivity of char that is of interest for the present study. In addition, no in-depth absorption of radiation is considered.

The FPA allows control of the combustion environment by altering the oxygen concentration and flow rate entering the combustion chamber. This is used to explore extinction parameters in a vitiated environment.

3.3.2 Experimental Material

Spruce/pine CLT samples (density measured as 447 kg/m^3 ± 20 kg/m^3, thermal conductivity is taken as 18 W/mK from Inghelbrecht [9], and specific heat capacity can be taken from literature [128]) of total thickness 100 mm comprising 3 lamellae of uniform thickness bonded with a melamine formaldehyde adhesive were cut to nominal sizes of 85 mm x 85 mm x 100 mm. Samples were then wrapped in aluminium foil on all but the exposed sides to limit escape of pyrolysis gases along the grain, and wrapped in two layers of ceramic paper bound by steel wire to limit heating and heat losses through the sides in order to approximate one-dimensional heat transfer. Before commencing testing, samples were placed in a conditioned room at 20°C and 50%

relative humidity. After two weeks of conditioning, and after six weeks, moisture contents were taken of two and four offcuts respectively of nominal dimensions 40 mm x 100 mm x 100 mm using ASTM D 4442 [162]. This yielded moisture contents in the range of 10.5 to 11.0%, with a difference of less than 0.1% between those taken after two weeks and those after 6 weeks.

3.3.3 Experimental Matrix

The experiments undertaken at ambient oxygen concentration are listed in Table 3.1 and Table 3.2. Ignition experiments consisted of a single, constant heat flux imposed on the sample, which was ignited by a non-luminous, premixed ethylene-air flame. Once ignition was observed, the pilot flame was extinguished and the sample left to attain auto-extinction before the lamps were turned off and the sample removed. The exceptions to this were the first four experiments (IM-15-1, IM-15-2, IM-14-1, and IM-14-2) in which a luminous pilot flame was used. Additionally, in the first two experiments (IM-15-1 and IM-15-2), the sample was not left to attain auto-extinction.

Table 3.1: Bench-scale ignition experiments at ambient oxygen concentration.

Incident heat flux [kW/m^2]	Measurement [Mass loss/Temperature]	Number of experiments	Time to ignition [s]
14	M	4	3347±1391*
15	M	2	2978±217
16	M	2	2193±248
20	M	3	764±47*
25	M	2	270±33
27	M	2	244±4
30	M	4	121±20
31	M	4	88±19
32	M	3	86±3
35	M	4	51±16
15	T	2	2587±18
16	T	2	1288±78
25	T	4	172±92
30	T	2	153±7
31	T	2	153±2

*one sample did not ignite

Extinction experiments were run at a constant heat flux of 40 kW/m^2 for 30 minutes (unless stated otherwise) before decreasing to the "low heat flux" detailed in Table 3.2.

Table 3.2: Bench-scale extinction experiments at ambient oxygen concentration.

Low heat flux [kW/m^2]	Measurement [Mass loss/Temperature]	Number of experiments	Time to ignition [s]
15	M	4*	78±42
20	M	2	98±8
22	M	2	102±17
25	M	2	106±4
27	M	2	108±6
31	M	4	54±23

*2 experiments were only kept at 40kW/m^2 for 10 minutes

Throughout the experiments oxygen, carbon monoxide, and carbon dioxide concentrations were recorded, as well as either mass loss or temperature. Temperature was recorded using K-type thermocouples, inserted into pre-drilled holes at the back face as shown in Figure 3.1. This data could then be used to calculate heat release rate, temperature profiles, mass loss rate, and charring rate. Before each experiment, initial mass was recorded with and without the sample holder, and initial dimensions measured by digital callipers, with width and breadth averaged over the front, midpoint, and back of the top surface, and thickness averaged over the midpoint over each of the four sides. These measurements were repeated after each experiment, and additional measurements taken at the midpoint of each side to determine visual char depth.

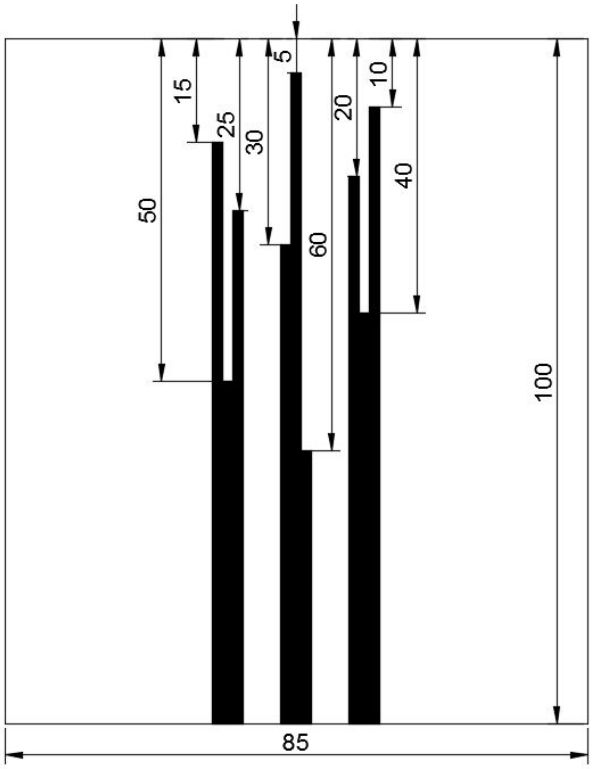

Figure 3.1: Thermocouple arrangement from bench-scale experiments. All dimensions in mm.

Photographs were taken of each face of each sample before and after testing to allow visual comparisons. Additionally, videos were taken of each experiment to allow visual analyses of the ignition and extinction phenomena. From these videos, time to ignition, and where appropriate, time to extinction were recorded. Prior to each experiment the heat flux was measured and allowed to stabilise.

3.3.3.1 Reduced oxygen experiments

Further to the experiments detailed in Table 3.1 and Table 3.2, experiments were undertaken at reduced oxygen concentrations to determine the effect of this on auto-extinction parameters. These are listed in Table 3.3 and Table 3.4.

Table 3.3: Bench-scale ignition experiments at reduced oxygen concentration.

Incident heat flux [kW/m^2]	Oxygen concentration [%]	Measurement [Mass loss/Temperature]	Number of experiments	Time to ignition [s]
15	17.2	M	2	3048±840
20	17.2	M	4	581±152
25	17.2	M	4	205±34
30	17.2	M	4	144±57
15	17.2	T	4	2357±1253
25	17.2	T	2	236±36
30	17.2	T	4	123±37
15	18.7	M	3	1614±1040
20	18.7	M	2	449±119
25	18.7	M	3	156±71
30	18.7	M	3	81±35
15	18.7	T	2	2249±87
30	18.7	T	3	123±27

Table 3.4: Bench-scale extinction experiments at reduced oxygen concentration.

Low heat flux [kW/m^2]	Oxygen concentration [%]	Measurement [Mass loss/Temperature]	Number of experiments	Time to ignition [s]
15	17.2	M	2	60±9
30	17.2	M	2	65±2
15	18.7	M	2	37±11
30	18.7	M	2	47±3
15	18.7	T	2	54±2
30	18.7	T	2	53±13

These experiments were undertaken by creating an airflow past the sample to create nominal oxygen concentrations of 18% and 16%. This was achieved by mixing 86 lpm air with 14 lpm nitrogen and 76 lpm air with 24 lpm nitrogen respectively, giving a total airflow of 100 lpm, or 2.04 g/s. It should be noted that the airflow enters the chamber from below the sample and flows up around the sample, thus velocity over the sample will not be the same as that entering the chamber. To ensure that differences in mass loss rates were not just due to the presence of an airflow, additional reference experiments, listed in Table 3.5, were undertaken with 100 lpm of air.

Table 3.5: Bench-scale ignition experiments at ambient oxygen concentration with airflow.

Incident heat flux [kW/m^2]	Measurement [Mass loss/Temperature]	Number of experiments	Time to ignition [s]
15	M	2	2051±272
20	M	2	499±113
25	M	3	171±95
30	M	3	106±17

3.3.3.1.1 Determination of Oxygen Concentration

To determine the actual oxygen concentration achieved in the reduced oxygen concentration experiments, a sample was placed in the FPA as described above, and the airflow set up as in the experiments. A portable oxygen analyser was then used to measure the oxygen concentration immediately above the sample for each different oxygen concentration. For the nominal 18% oxygen experiments, oxygen concentration was found to be 18.7%, and for the 16% nominal oxygen experiments, it was 17.2%. It is hypothesised that these are higher than the target due to the absence of a quartz tube resulting in mixing with the surrounding ambient air.

3.3.4 Results

3.3.4.1 Ignition

The critical heat flux for piloted ignition was determined by recording the time to ignition for each experiment. The surface temperature at ignition can then be calculated from Equation (3.5):

$$T_{s,ig} = T_\infty + \frac{a\dot{q}_e''}{h_T}\left[1 - e^{\frac{t_{ig}}{t_c}}\operatorname{erfc}\left(\left(\frac{t_{ig}}{t_c}\right)^{\frac{1}{2}}\right)\right] \tag{3.5}$$

which gives a first order Taylor series expansion as in Equation (3.6):

$$\frac{1}{\sqrt{t_{ig}}} = \frac{2}{\sqrt{\pi}}\frac{a}{\sqrt{k\rho C_p}}\frac{\dot{q}_e''}{T_{s,ig} - T_\infty} \text{ for } t_{ig} \ll t_c \tag{3.6a}$$

$$\frac{1}{\sqrt{t_{ig}}} = \frac{\sqrt{\pi} h_T}{\sqrt{k\rho C_p}} \left[1 - \frac{h_T \left(T_{s,ig} - T_\infty \right)}{a \dot{q}_e''} \right] \text{ for } t_{ig} \gg t_c \tag{3.6b}$$

where h_T is a total heat transfer coefficient, equal to the sum of h_c and h_r as defined in Equation (3.7), and t_c is a characteristic heating time, given by Equation (3.8).

$$h_r \left(T_i - T_j \right) = \varepsilon \sigma (T_i^4 - T_j^4) \tag{3.7}$$

$$t_c = \frac{k\rho C_p}{h_T^2} \tag{3.8}$$

Thus in order to determine the critical heat flux for ignition, $1/\sqrt{t_{ig}}$ must be plotted against $1/\dot{q}_e''$ for $t_{ig} > t_c$. For low heat fluxes, Equation (3.6b) can be used, and when a linear fit is applied, the intercept will be equal to $\sqrt{\pi} h_T / \sqrt{k\rho C_p}$, from which t_c can be easily determined. This can then verify that the correct regime is being used to determine critical heat flux for ignition, which can be found from the y-intercept in either case. This leaves three unknowns in Equation (3.6b): the total heat transfer coefficient, h_T; the surface temperature at ignition, $T_{s,ig}$; and the thermal inertia, $k\rho C_p$. Various methods exist for estimating the heat transfer coefficient; this can be done by calculating the Nusselt number for a horizontal plate [150] as shown in Equation (3.9):

$$h_c = 0.54 \sqrt[4]{\frac{g(T_s - T_\infty)}{L T_s \nu \alpha}} k \tag{3.9}$$

where L is the surface length, T_s is the surface temperature, ν is the kinematic viscosity of air, and α is the thermal diffusivity of air. Mowrer [163] notes that in small-scale experiments, the convective heat transfer coefficient reaches a constant value relatively quickly, whilst the radiative heat transfer coefficient increases rapidly as a function of surface temperature. Thus the convective heat transfer coefficient can be assumed to be independent of temperature for the times of interest. This gives a total heat transfer coefficient of 34 W/m^{2}K at the ignition period, resulting in a characteristic

time of 225 s and a surface temperature at ignition of 415°C. Experiments which ignited within 225 s can thus be analysed using Equation (3.6a), whereas experiments which ignited after 225 s can be analysed using Equation (3.6b). The correlation for the "slow" ignition times ($t_{ig} > t_c$) shows less scatter than the correlation for "fast" ignition times, as shown in Figure 3.2(a), and the intercept of this line of best fit with the x-axis (i.e. when time to ignition is infinite) gives a critical heat flux for ignition in this setup of 13.4 kW/m^2. Equation (3.6a) cannot be applied in this way, as this equation forces the line through the origin. Plotting the times to ignition against the external heat flux shows a clear asymptote between 13 kW/m^2 and 14 kW/m^2, as shown in Figure 3.2(b), consistent with Equation (3.6b) and literature data.

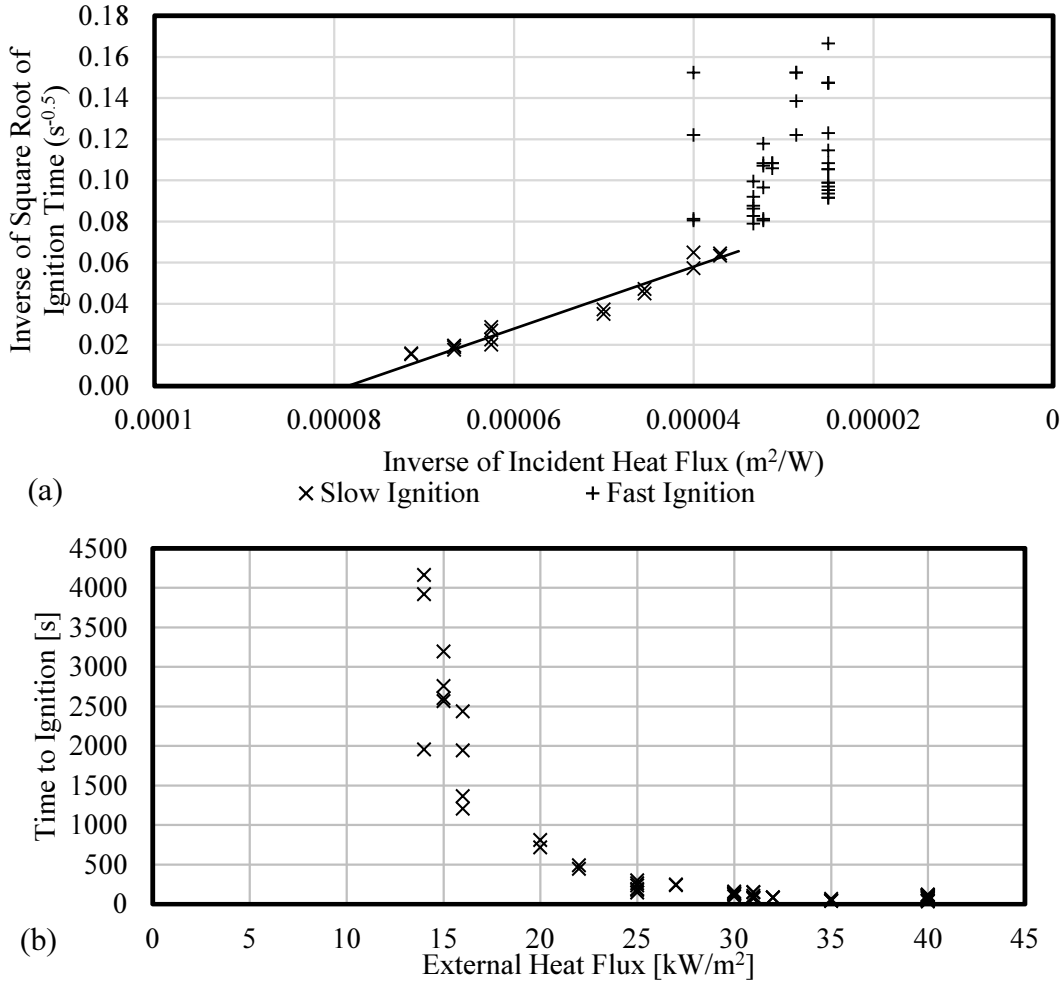

Figure 3.2: (a) Critical heat flux for ignition plot for experiments at ambient oxygen concentration for "fast" ignition ($t_{ig}<t_c$) and "slow" ignition ($t_{ig}>t_c$); (b) critical heat flux for ignition plotted against external heat flux for experiments at ambient oxygen concentration.

3.3.4.2 Extinction

Having established ignition criteria for CLT samples in the FPA, the extinction criteria can then be explored. As discussed previously, it is hypothesised that the char layer will result in different critical values for extinction than for ignition.

Experiments at or below 30-31 kW/m^2 were found to eventually undergo flaming extinction, whereas experiments at or above this value were found to undergo sustained flaming for an hour, at which point the experiment was terminated, showing no signs of tending towards extinction. Typical mass loss data are shown in Figure 3.3 for samples in which auto extinction, did or did not occur. In all cases the initial part of the mass loss rate (MLR) is dominated by a peak which subsequently decreases as the char layer builds up, reducing heat transfer into the virgin timber. The mass loss curves followed two primary shapes as shown in Figure 3.3: 1) the mass loss decreased from a peak value for a time, before reaching a quasi-constant, "steady state" value (as illustrated by the upper curve in Figure 3.3); 2) the mass loss decreased from a peak value, and continued to decrease until reaching a critical value whereupon the flame quenched (as illustrated by the lower curve in Figure 3.3). These two modes are representative of sustained flaming and auto-extinction respectively. In each case, the mass loss rate initially decreases due to the build-up of a char layer, acting as effective thermal insulation (increasing the radiative heat losses) and reducing heat transfer into the virgin timber, and thus reducing the mass loss rate. In mode 1, it appears that after a time, the incident heat flux (from the external source and the surface flames) is sufficient to allow oxidation of the surface char at approximately the same rate as the char formation, resulting in a steady-state char thickness thus allowing continued heat penetration into the sample resulting in continued pyrolysis and thus sustained flaming at a quasi-steady rate. Conversely, in mode 2, it appears that the rate of char consumption is less than the rate of char generation, resulting in a continually increasing char thickness which consequently continually reduces the heat transfer into the virgin timber until it drops below the critical mass flux. This was observed visually in that flaming was initially intense, before becoming less severe, as shown in Figure

3.4, as an increased char layer built up, insulating the remaining virgin timber and reducing the pyrolysis rate.

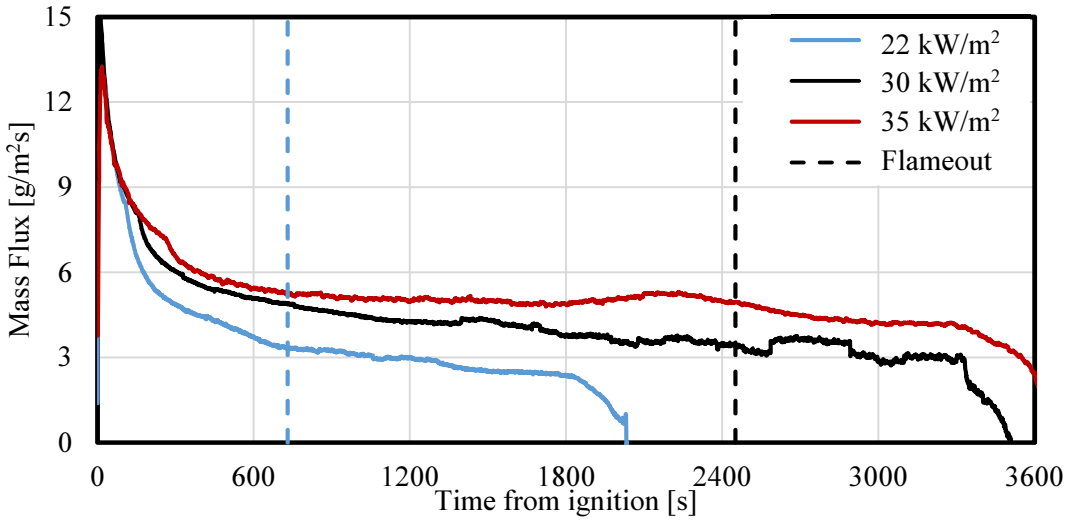

Figure 3.3: Mass loss rate as a function of time for samples at 22kW/m², 30kW/m², and 35kW/m², with flameout highlighted by vertical lines.

Figure 3.4: Initial (left) and residual (right) flaming during experiment IM-14-1.

The critical mass flux for extinction under these conditions was found to be 3.48 g/m²s ± 0.31 g/m²s; this resulted in flaming extinction and was found to be independent of the external heat flux.

3.3.4.3 Two-phase experiments

In a real compartment fire, the heat flux to an exposed timber surface will not be constant, and thus it was desired to conduct further experiments exploring the effect

of varying heat flux on the critical conditions for extinction. A two-phase heat flux was selected to represent a scenario in which the heat flux to an exposed timber surface reduces.

The two-phase experiments had an initial heating phase of a constant 40 kW/m^2 incident heat flux for 30 minutes, before dropping to a constant heat flux of between 15 kW/m^2 and 31 kW/m^2. Most samples extinguished within two minutes after the drop in heat flux, with the notable exception being the samples for which the heat flux dropped to 31 kW/m^2; two of which failed to extinguish and one of which only extinguished after an additional 37.5 minutes. This compares with approximately 17 minutes to extinguishing when exposed to a constant heat flux of 31 kW/m^2. This again suggests a critical heat flux for extinction of around 30-31 kW/m^2 in this setup, and further suggests that the value being independent of the pre-heating conditions (i.e. that the surface heat losses dominate). The mass loss rate at extinction was not affected.

The mass flow of oxygen can be calculated from the ideal gas law:

$$\dot{m}_{ox} = \frac{P\dot{V}Y_{ox}M_{ox}}{RT} \tag{3.10}$$

where P is the pressure (assumed ambient), $\dot{V}$ is the volumetric flow rate (100 lpm), Y_{ox} is the volumetric oxygen fraction, M_{ox} is the molecular mass of oxygen, R is the gas constant, and T is the flow temperature (assumed ambient). This gives values of 0.46 g/s, 0.41 g/s, and 0.38 g/s for 21%, 18.7%, and 17.2% oxygen respectively.

The critical mass loss rate was found to increase to 3.79 g/m^{2}s ± 0.23 g/m^{2}s at 18.7% oxygen, and to 4.05 g/m^{2}s ± 0.51 g/m^{2}s at 17.2% oxygen. Increasing the airflow did not appear to have any effects on extinction criteria, as shown in Figure 3.5. It is evident that mass loss rate at extinction is independent of heat flux, as reported for PMMA samples tested by Rasbash et al. [88]. In this regard, the principles of firepoint theory may be used to predict auto-extinction in terms of a critical mass loss rate.

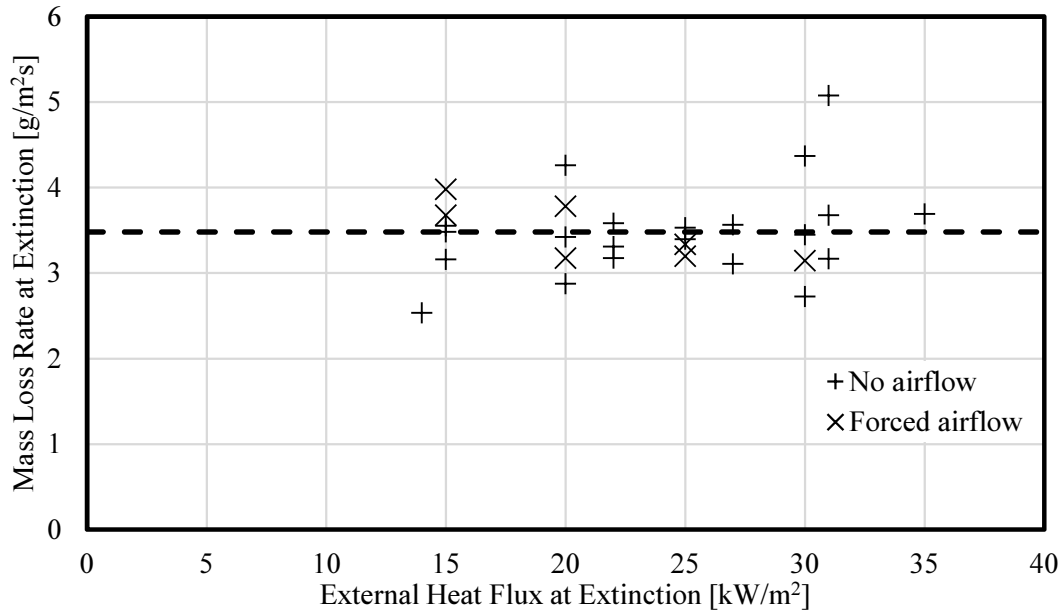

Figure 3.5: Mass loss rate at extinction for experiments at ambient oxygen concentration.

Final char depths and thicknesses were measured with digital callipers, and are shown for the experiments at 30 kW/m^2 along with experiment duration, ignition, and extinction times in Figure 3.6. Section loss was determined by subtracting the average final thickness (as determined by measuring the thickness at multiple points) from the average initial thickness.

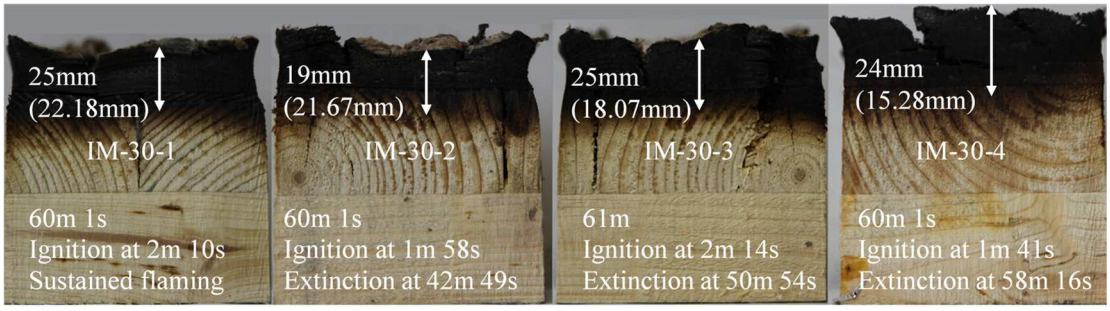

Figure 3.6: Measured char depths with section loss shown in brackets for 30kW/m^2 ignition experiments.

3.3.4.4 Temperature Data

A typical temperature evolution is presented in Figure 3.7, with the times of ignition and extinction highlighted. Plateaus are evident at 100°C due to the evaporation of moisture. Sharp rises in temperature are evident after ignition, continuing after extinction due to continued propagation of the thermal wave through the sample.

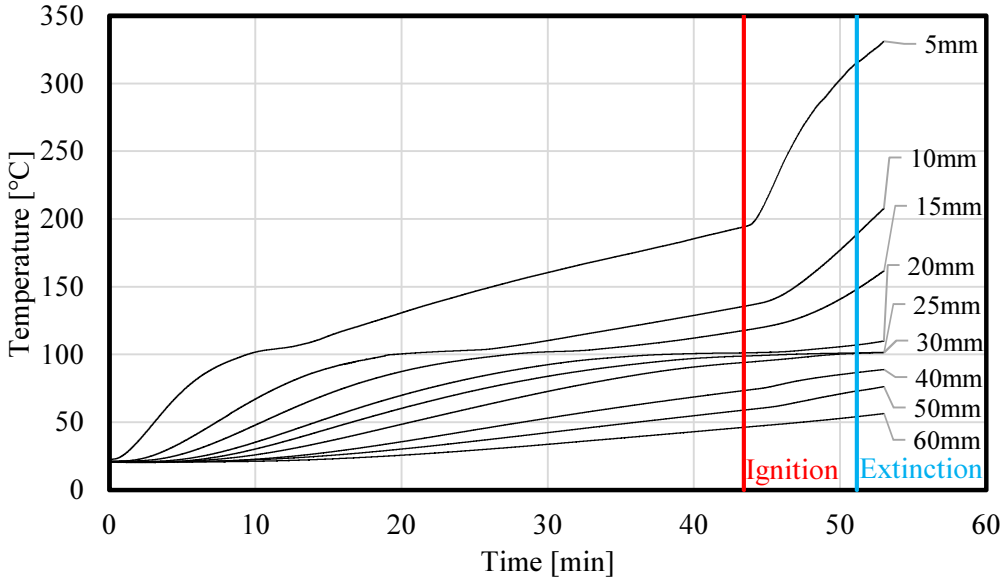

Figure 3.7: Temperature evolution for experiment IT-15-1 at various depths below the heated surface, highlighting ignition and extinction times.

The temperature profiles for a range of heat fluxes as noted in Table 3.1 are shown in Figure 3.8, with ignition and extinction highlighted. Plateaus at 100°C are again evident, particularly at higher heat fluxes due to increased thermal penetration, with steep thermal gradients forming by the time of extinction. It can also be seen that higher temperatures are observed with increasing heat fluxes, however shorter ignition times result in shallower thermal gradients and less heated timber at the point of ignition.

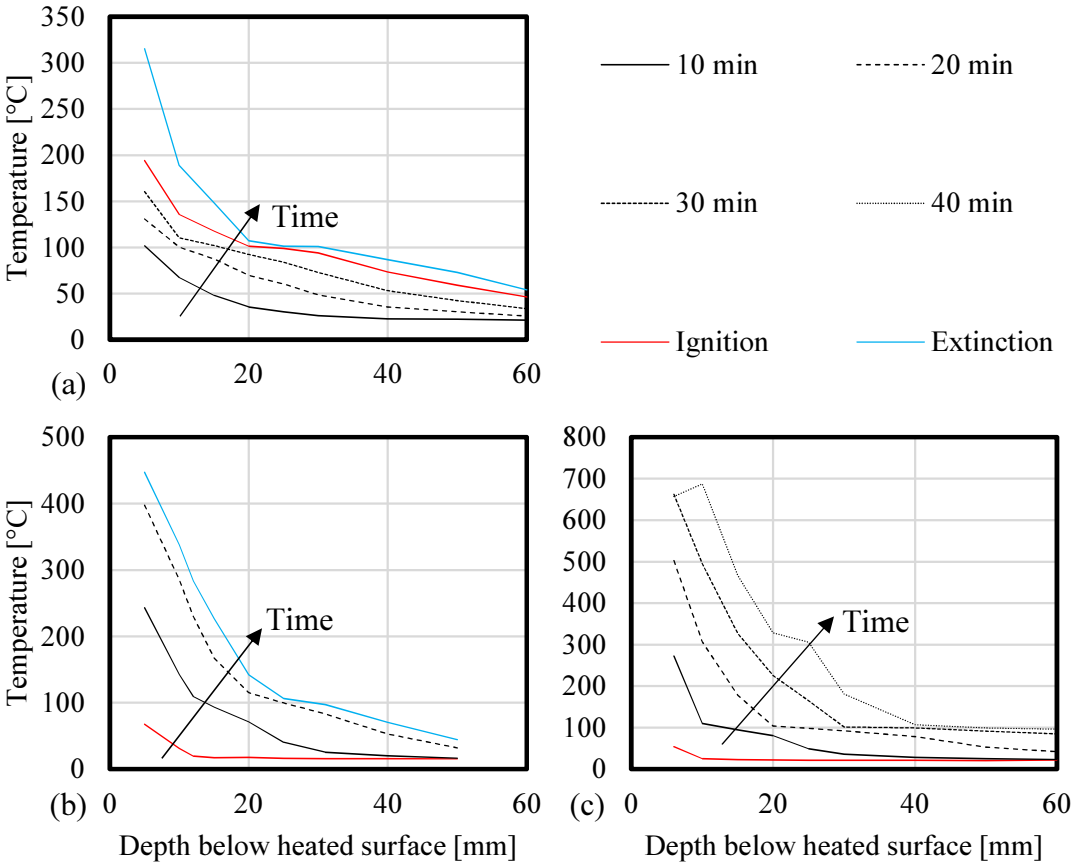

Figure 3.8: In-depth temperature profiles for FPA experiments at (a) 15 kW/m², (b) 25 kW/m², (c) 31 kW/m².

3.4 Application of Firepoint Theory

As previously discussed, Equation (2.11) can be used to predict if auto-extinction will occur. In this section an assessment is made of each of the three parameters to predict if auto-extinction occurs for a given scenario.

3.4.1 External Heat Flux

The first parameter in Equation (2.11) is the external heat flux, necessary to enable burning of a thermally thick wood sample [11]. This serves as the control variable in the experimental investigations herein. In the case of these experiments, this heat flux is the incident heat flux from the lamps, which is a known value.

The incident heat flux was calibrated before each experiment using a Schmidt-Boelter heat flux gauge. The certificate of calibration gives an error of 3%, which is accounted for in the analysis.

3.4.2 Heat Flux from Flames

The second parameter is the heat flux from the flames, which can be estimated using Equation (3.11) (from Rasbash et al. [88]):

$$\dot{q}_f'' = \phi \Delta H_{c,n} \dot{m}'' \tag{3.11}$$

where $\Delta H_{c,n}$ can be taken as 17.5 MJ/kg ± 2.5 MJ/kg [11, 32]. ϕ is the proportion of energy from the flames transferred back to the surface and can be estimated through Equation (3.12) [88]:

$$\dot{m}_{cr}'' = \frac{h_c}{C_{p,air}} \ln\left(1 + \frac{Y_{ox}}{r\phi}\right) \tag{3.12}$$

where $C_{p,air}$ is the specific heat capacity of air, taken as 1.01 kJ/kgK [150], Y_{ox} is the mass concentration of oxygen in air (0.23 at ambient oxygen concentration), r is the stoichiometric ratio of oxygen to fuel (taken as 3.43 [88]) and h_c is the convective heat transfer coefficient, calculated by evaluating the Nusselt number over a horizontal plate using Equation (3.9) [150]. The resulting convective heat transfer coefficient varies with surface temperature up to around 380°C, at which point it achieves a constant value of around 9.1 W/m^{2}K, thus $h_c/C_{p,air}$ = 9.0 g/m^{2}s. Rasbash et al. [88] assume $h_c/C_{p,air}$ = 10 g/m^{2}s for turbulent natural convection, similar to the value calculated herein. Substituting in the experimentally obtained values into Equation 7, gives ϕ = 0.14 ± 0.02, and $\dot{Q}_f''$ = 8.7 kW/m^2 ± 3.4 kW/m^2 for an ambient oxygen concentration, reducing to 7.4 kW/m^2 ± 2.3 kWm^2 and 6.5 kW/m^2 ± 3.4 kW/m^2 for 18% and 16% oxygen concentrations respectively.

3.4.3 Heat Losses

The total heat losses from an FPA sample are due to: radiative and convective losses to the surroundings, conductive losses into the sample, and the heat absorbed by the char layer. To calculate these parameters, an estimate of surface temperature is required. Since surface temperature cannot be directly measured., the errors present in calculation of the heat losses will be significant. Therefore, to enable an appreciation of the potential ranges, total heat losses are calculated as a function of surface temperature.

3.4.3.1 Radiative Heat Losses

Radiative heat losses can be calculated from surface temperatures using Equation (3.13):

$$\dot{q}''_{l,r} = F_{s,atm}\varepsilon\sigma(T_s^4 - T_\infty^4) \tag{3.13}$$

where $F_{s,atm}$ is the view factor from the sample to the surroundings. This can be calculated from Equation (3.14) [164]:

$$F_{s,atm} = \frac{1}{A_1}\sum_{i=1}^{2}\sum_{j=1}^{2}\sum_{k=1}^{2}\left[(-1)^{i+j+k}G\left(x_i, y_j, \eta_k\right)\right] \tag{3.14}$$

where

$$G = -\frac{(\eta - y)\sin^2\alpha}{2\pi}\int_{\xi_1}^{\xi_2}\left(\frac{(x - \xi\cos\alpha)\cos\alpha - \xi\sin^2\alpha}{\sqrt{(x^2 - 2x\xi\cos\alpha + \xi^2)}\sin^2\alpha}\tan^{-1}\left[\frac{\eta - y}{\sqrt{(x^2 - 2x\xi\cos\alpha + \xi^2)}}\right]\right.$$
$$+\frac{\cos\alpha}{(\eta - y)\sin^2\alpha}\left\{\sqrt{[\xi^2\sin^2\alpha + (\eta - y)^2]}\tan^{-1}\frac{x - \xi\cos\alpha}{\sqrt{[\xi^2\sin^2\alpha + (\eta - y)^2]}}\right.$$
$$\left.\left.-\xi\sin\alpha\tan^{-1}\left(\frac{x - \xi\cos\alpha}{\sin\alpha}\right)\right\} + \frac{\xi}{2(\eta - y)}\ln\left[\frac{x^2 - 2x\xi\cos\alpha + \xi^2 + (\eta - y)^2}{x^2 - 2x\xi\cos\alpha + \xi^2}\right]\right)d\xi$$

The dimensions are shown in Figure 3.9, and ε is the surface emissivity, and σ the Stefan-Boltzmann constant. Applying Equation (3.14) to Figure 3.9 gives the view factor from the sample to one lamp. As there are four lamps, and it is the view factor from the sample to ambient that is of interest, this answer needs to be multiplied by four and subtracted from one, yielding approximately 0.87.

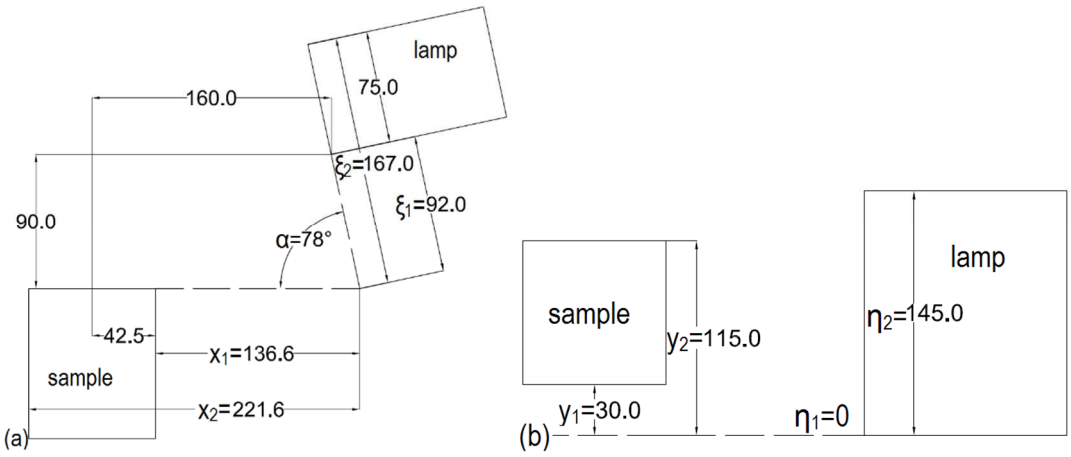

Figure 3.9: FPA lamp and sample dimensions in (a) elevation and (b) plan.

3.4.3.2 Convective Heat Losses

Convective heat losses can be calculated simply from Equation (3.15):

$$\dot{q}''_{l,c} = h_c(T_s - T_\infty) \tag{3.15}$$

where h_c is as calculated by Equation (3.9).

3.4.3.3 Conductive Heat Losses

Conductive heat losses can be calculated from Equation (3.16) [9]:

$$\dot{q}''_{l,cond} = -k_w \left.\frac{\partial \mathrm{T}}{\partial \mathrm{x}}\right|_{\mathrm{x}=\mathrm{x_c}} \tag{3.16}$$

where k_w is the thermal conductivity of the wood at the char line, taken as 0.18 W/mK [9].

3.4.3.4 Heat absorbed by char

Finally, the heat absorbed by the char layer can be estimated from Equation (3.17):

$$\dot{q}''_{abs,c} = \int_0^{x_c} \frac{C_p(T)m}{At} dT \tag{3.17}$$

If char thickness is assumed constant over the time of interest, then this can be simplified to Equation (3.18):

$$\dot{q}''_{abs,c} = \beta \int_{T_c}^{T_s} \rho(T)C_p(T)dT \tag{3.18}$$

where β is the experimentally-determined charring rate.

3.4.4 Comparison with Experimental Data

From Equations (3.13)-(3.18), the heat losses can be calculated as a function of surface temperature. Radiative losses can be easily calculated for a given surface temperature, however, the other components require further calculation. The convective heat transfer coefficient, h_c, is temperature-dependent, and the kinematic viscosity of air, and thermal diffusivity of air also vary with temperature. These data are available in [150], and thus the convective losses can be solved as a function of temperature with high confidence. Conductive losses require a knowledge of the temperature gradient behind the char layer at extinction. From experimental data, this is typically around 28 K/mm, and this value gives a conductive heat loss of 5.0 kW/m^2 – this value is not explicitly dependent on surface temperature. Heat absorbed by the char layer was calculated from Equation 15 using thermal properties from [6] and a char rate from experimental data of approximately 0.55 mm/min. This gave a maximum value of approximately 1 kW/m^2, and changing the char rate was not found to significantly affect this value (a 100% change in charring rate resulted in a 0.8% change in total heat losses), especially when compared to the other heat loss components. The results of this analysis are shown in Figure 3.10. It can be seen that radiative heat losses dominate, varying significantly with increases in surface temperature. Convective heat

losses vary only slightly with surface temperature, from 2.44 kW/m^2 at 300°C to 7.86 kW/m^2 at 800°C. Furthermore, above ~380°C, the variation in the convective heat transfer coefficient decreases significantly, and therefore a constant value suitable for use in simplified analyses. It is evident from Figure 3.10 that radiative heat losses dominate for temperatures above 400°C. Therefore, without accurate surface temperature measurements, the error in the heat loss term of Equation (3.2) will be significant.

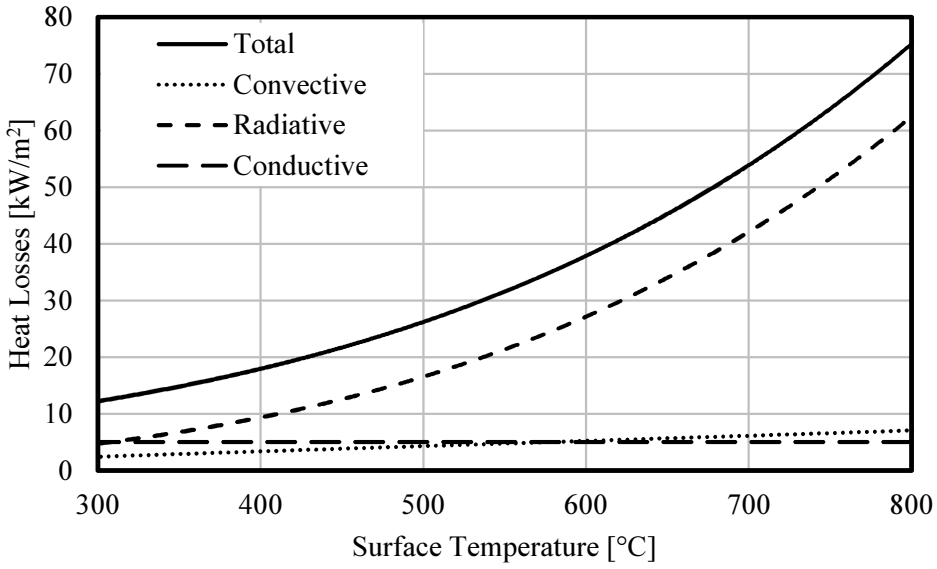

Figure 3.10: Heat losses as a function of surface temperature for FPA experiments.

Having quantified the external heat flux, heat feedback from the flames, heat losses and their associated errors, firepoint theory can now be applied to the experimental data. As a result of the large uncertainties associated with surface temperature, solving Equation (2.13) based on assumed surface temperatures would not be meaningful – the errors in the theoretical mass loss rate will be large even for relatively small errors in estimations of surface temperature. Rather, Equation (2.13) has been solved to determine the heat losses, from which surface temperatures are estimated through Figure 3.10. These can then be compared to experimentally obtained temperature data to compare experimental and theoretical mass loss rates, and thus determine the suitability of firepoint theory for predicting extinction. Equation (2.13) is rearranged

to give Equation (3.19); the external heat flux is multiplied by the absorptivity to give the absorbed heat flux:

$$\dot{q}_l'' = \alpha\dot{q}_e'' + \dot{q}_f'' - L_p\dot{m}_{cr}'' \tag{3.19}$$

Heat losses as predicted by firepoint theory can thus be calculated based on the previous analysis, using the experimentally obtained values for $\dot{m}_{cr}''$. These can then be compared to experimentally obtained surface temperatures, through extrapolation of the in-depth temperature data. For each experiment with thermocouples which achieved extinction, the surface temperature was estimated through linear extrapolation from the two thermocouples nearest the heat-exposed surface. Errors were calculated based on temperature and position error – the error in temperature measurement for a K-type thermocouple is the greater of 2.2°C or 0.75%. The error in position of each thermocouple was assumed to be 1mm, however since it was considered unlikely that the "worst-case" scenario of both thermocouples being out by 1mm in opposite direction, a value of 0.5 mm was applied.

It was appropriate to correct for surface regression in cases where experiments were terminated immediately after flameout had occurred. This was not applied in cases where significant surface regression could have occurred after flameout. Thickness of each sample was measured using digital callipers before and after each experiment. The section loss was significant (3-8 mm) for some samples, especially those exposed to higher heat fluxes/longer durations. Applying the above analysis yields Figure 3.11 for ambient oxygen concentration. With the exception of the sample tested at 16 kW/m^2, all samples fit comfortably within the error bounds, suggesting that with adequate surface temperature measurements, firepoint theory can be used to predict auto-extinction of a charring polymer. The sample at 16 kW/m^2 extinguished very soon after ignition, at which point there was only a minimal char layer formed. As such, the thermal wave had not penetrated as deep into the sample as in the other cases, resulting in a shallower temperature gradient and a lower predicted surface temperature.

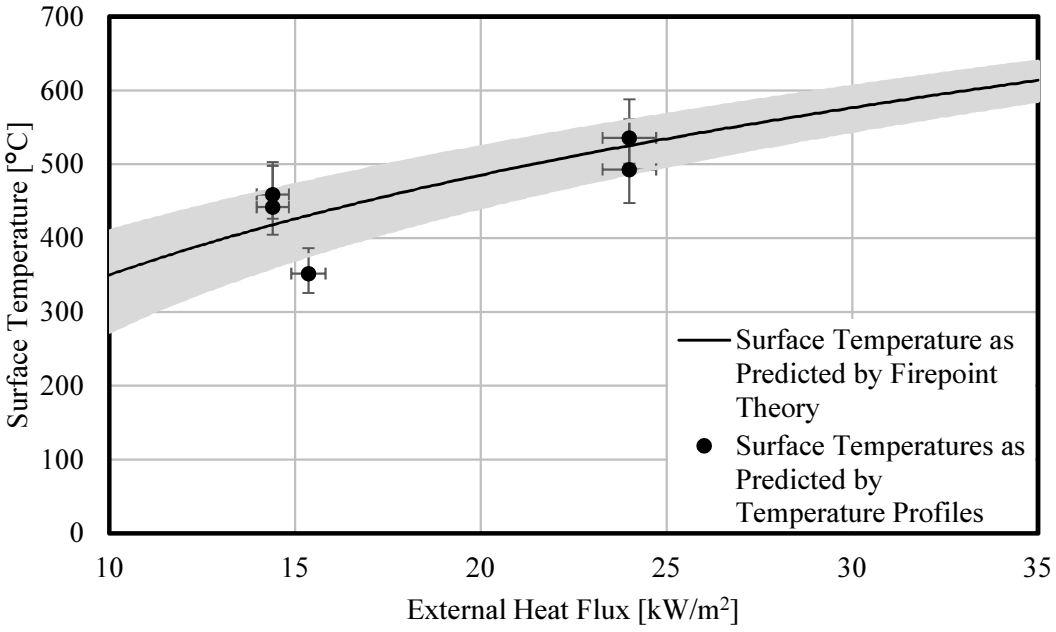

Figure 3.11: Comparison between experimental and theoretical surface temperatures for samples tested at ambient oxygen concentration.

3.5 Application Beyond Bench-Scale

In order to apply the above analysis to different situations, care must be taken to calculate each of the different components. It is clear that each of the three main components (external heat flux, heat transferred from flames, and heat losses) may vary widely from one scenario to another. For example, similar experiments undertaken by Emberley et al. [165] in the cone calorimeter (vertical orientation) found critical mass loss rates of 3.65 ± 0.2 g/m^{2}s (Radiata Pine) and 3.93 ± 0.4 g/m^{2}s (European Spruce) – very similar to the value presented herein. However, the critical heat fluxes for extinction were identified as 44.6 ± 0.9 kW/m^2 and 43.6 ± 4.7 kW/m^2 respectively – around 50% larger than those identified in the FPA. These differences are attributed to differences in apparatus and orientation, resulting in differences in the formulation and quantification of the energy balance, however there is insufficient quantification to identify the exact causes of the differences. As such, applying the critical heat flux obtained herein to a compartment fire scenario is not appropriate. In-depth heat transfer analyses as conducted herein are necessary to model and predict auto-extinction on such a scale.

3.6 Conclusions and Further Work

From the data presented in this chapter, it can be reasonably hypothesised that if the heat flux to an exposed spruce/pine timber element within a fire compartment is such that the mass loss rate will be less than 3.5 g/m^{2}s at ambient oxygen concentrations, then auto-extinction will occur. This can be expressed through the logic diagram in Figure 3.12, which will be expanded in later chapters once more data are available.

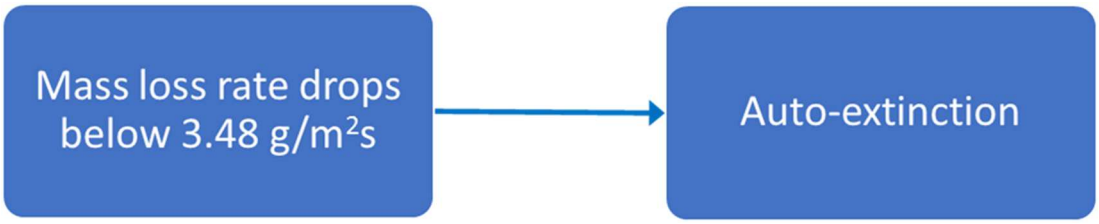

Figure 3.12: Logic diagram showing conditions for auto-extinction.

The critical mass loss rate was found to increase linearly with decreasing oxygen concentration up to 4.1 g/m^{2}s at 17.2% oxygen, consistent with the findings of Rasbash et al. [88]. Airflow was found to have no clear effect on critical mass loss rate or critical heat flux for extinction over the range studied.

Whilst different heat fluxes change the energy balance, it is clear that the heat losses dominate; an increase in heat flux results in an increase in the char surface temperature, which as evident from Figure 3.10. This results in a significant increase in heat losses, accompanied by a comparatively smaller increase in net heat flux into the timber. Thus it is the characteristics of the char that is critical in increasing the heat losses and thus determining whether auto-extinction will occur.

Firepoint theory has been successful in predicting critical mass loss rate at extinction within reasonable error bounds largely in relation to surface temperature. Since the method is sensitive to surface temperature, accurate predictions of surface temperature are vital if the method is to be used in a predictive (or design) capacity.

Chapter 4 Full-Scale Compartment Fire Experiments with Exposed Timber Surfaces

4.1 Introduction and Background

Extinction parameters have been obtained through bench-scale testing, where the heat source is well defined. However, extending this to determine the extinction behaviour in a compartment fire with real materials remains challenging due to the additional complexities introduced. There are complexities associated with the material response: delamination and encapsulation failure. Delamination is a phenomenon in which failure at the glue-line results in the front lamella, or part thereof, detaching from the underlying timber and exposing it directly to the fire. Encapsulation failure is a failure of the plasterboard system, resulting in the underlying timber being directly exposed to the fire. Other complexities are associated with the fire dynamics: the heat source is less well defined, and convective flows inside a compartment are not well known. It was thus desirable to explore the application of fire point theory to full-scale compartment fires with exposed timber surfaces. Five full-scale compartment fire experiments were undertaken as part of the "Compartment fires in support of tall timber construction" project, the key aims of which are to understand the changes in fire dynamics caused by exposed timber linings and to understand auto-extinction on the large scale. This chapter will describe the experimental setup and instrumentation, and present the key data obtained.

4.2 Experimental Programme

A total of five experiments were carried out with three different configurations of exposed timber. 100 mm thick CLT panels with five uniform lamellae of 20 mm thickness were used for all surfaces. Wall panels were of dimensions 2.75 m x 2.85 m, and ceiling panels 2.95 m x 2.95 m. This resulted in approximately cubic compartments with an internal side length on the order of 2.75 m. Cubic compartments were selected to make the re-radiation between all surfaces equal, and thus simplify comparisons between configurations. A door-shaped opening of dimensions 0.8 m

wide x 2.0 m high was cut in the centre of one of the panels. This was selected to give an opening factor large enough to ensure ventilation-controlled burning. The wall panels were joined overlapping as shown in Figure 4.1.

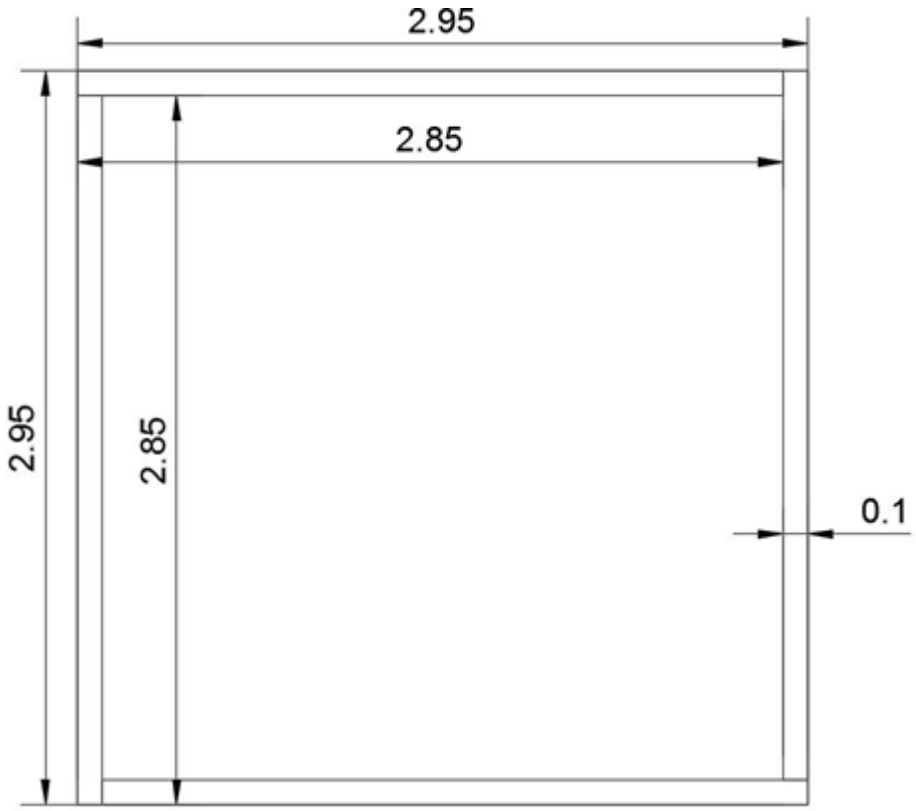

Figure 4.1: Section view of compartment. All dimensions in m.

The three configurations are detailed in Table 4.1. The configurations are denoted α, β, and γ (and are defined as such throughout the thesis) to avoid confusion with Latin symbols used for exposed surfaces and thermocouple identifiers.

Table 4.1: Experimental configurations for full-scale compartment fire experiments.

Configuration	α	β	γ
Exposed surfaces	Back wall and right wall	Back wall and ceiling	Back wall, ceiling, and right wall
Number of experiments	2	2	1

These configurations allowed an exploration of the effects of different numbers of exposed timber surfaces of approximately equal area (2 or 3) as well as exploring the

effects of changing the relative positions of the exposed timber (wall or ceiling). In each experiment, the unexposed surfaces were also constructed with identical CLT panels, and encapsulated with an insulation system comprising one layer of 12.5 mm type F rated gypsum plasterboard (from this point forward, all references to "plasterboard" refer to 12.5 mm type F rated gypsum plasterboard unless otherwise stated), one layer of 25 mm mineral wool, and then two further layers of plasterboard on the exposed face, illustrated in Figure 4.2. The exception to this was experiment α-1, in which only two layers of plasterboard were used. The inside of the door frame was protected with two layers of plasterboard, as was the outside timber face above and beside the door opening.

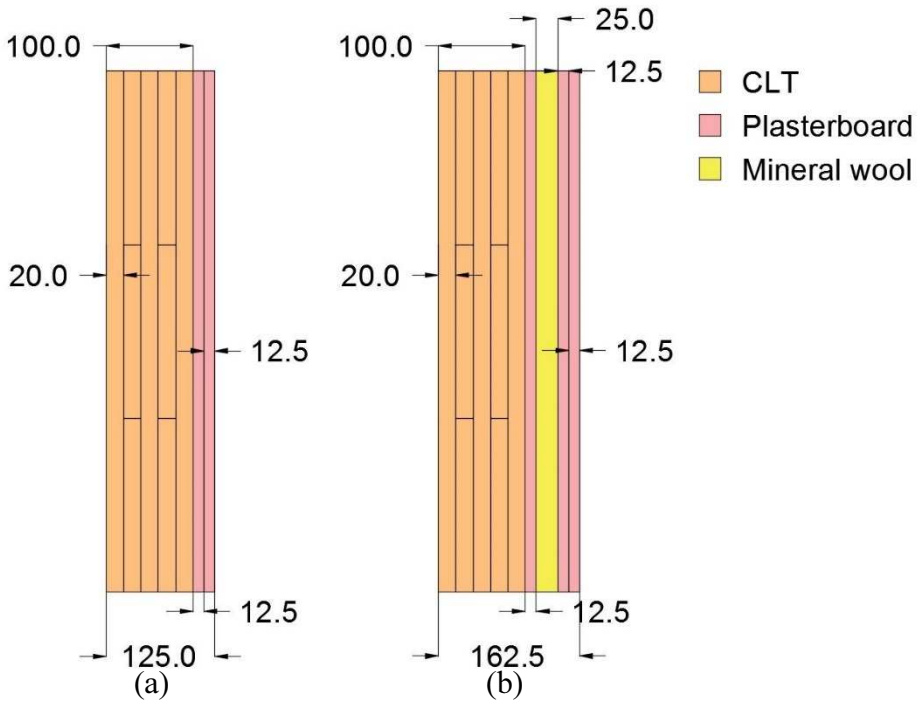

Figure 4.2: Encapsulation cross-section for (a) experiment α-1; (b) all other experiments. All dimensions in mm.

The compartments were built in the burn hall at BRE Global (Watford), directly onto the concrete floor. A false floor system was constructed within the compartment to accommodate four load cells. The load cells were of total height 100 mm, and a false floor was placed on top of each load cell, allowing them to operate independently. The false floor comprised of one layer of 9 mm MDF, 2 layers of plasterboard, and then

one or two layers of 25 mm mineral wool (one layer in experiments α-1 and γ-1, two layers in all the others), as shown in Figure 4.3. This reduced the opening height to approximately 1.79-1.82 m. Full dimensions for each experiment are given in Table 4.2. Opening width in each case was 0.75 m.

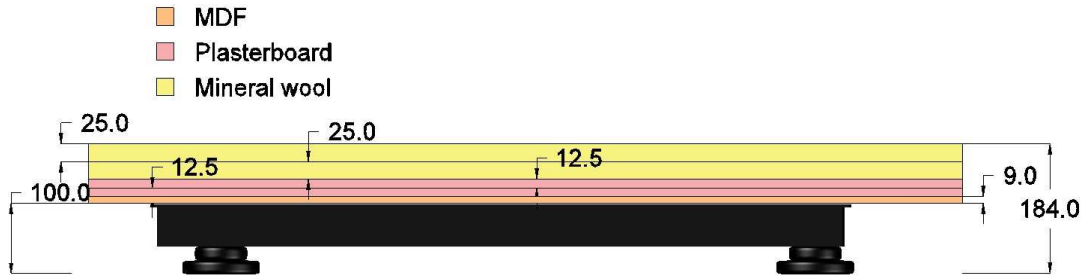

Figure 4.3: False floor build up. All dimensions in mm.

Table 4.2: Internal and opening dimensions of compartments.

Experiment	α-1	α-2	β-1	β-2	γ-1
Width [m]	2.73	2.69	2.63	2.63	2.69
Depth [m]	2.73	2.69	2.69	2.69	2.69
Height [m]	2.77	2.70	2.77	2.77	2.79
Opening height [m]	1.82	1.79	1.79	1.79	1.82
Opening area [m^2]	1.36	1.34	1.34	1.34	1.36
Opening factor [$m^{-1/2}$]	20.4	20.1	20.2	20.2	20.2

4.2.1 Fuel Load

In order to ignite the exposed timber surfaces, an initial compartment fuel load was required. Previous compartment fire experiments and tests have used three main types of fuel load – 1) propane burners [166], 2) wood cribs [166], 3) furniture [154]. The third option was not considered due to its lack of repeatability and reproducibility. The main advantage of propane burners over wood cribs is that it allows the burning rate of the compartment fuel load to be precisely controlled, and flashover can be ensured. However, propane burners do not allow any exploration of the interaction of the exposed timber and the compartment fuel load, which was of interest for the project. For this reason, wood cribs were selected as the fuel load.

4.2.1.1 Wood crib calculations

A number of theoretical predictions were used to determine flashover requirements based on the compartment geometry and the burning dynamics of the wood cribs. The compartment dimensions in Table 4.2 gave an inverse opening factor of 0.050 $m^{0.5}$. Using Thomas' flashover criterion [141] in Equation (4.1):

$$\dot{Q}_{fo} = 7.8A_T + 378A_v\sqrt{h_v} \tag{4.1}$$

where A_T is the total surface area, and A_v and h_v are the ventilation area and height respectively, gives a value of 940 kW ± 14 kW.

Assumptions must then be made about the wood cribs to calculate their growth rate and burning rate. A typical density of 450 kg/m^3 was assumed, and a calorific value of 17.5 MJ/kg, as an average of [32, 49]. The burning dynamics of the crib then depends on the stick dimensions, spacing, and overall crib size. For simplicity, one single large crib was assumed for the calculations, although four separate cribs were used in the experiments. First, the burning rate of the crib will be calculated to determine if flashover is achieved. This is calculated based on [167], which gives the steady state burning rate as in Equation (4.2):

$$\dot{m}_{ss} = \frac{0.0017\sqrt{A_s A_{vv} H}}{(A_s A_{vv})^{0.52}} \tag{4.2}$$

where A_s and A_{vv} are the total exposed surface area of the crib and the area of the vertical ventilation openings in the crib respectively, in cm^2, H is the total height of the crib in cm, and A_{vv} can be calculated by Equation (4.3):

$$A_{vv} = n^2 s^2 \tag{4.3}$$

where n is the number of sticks per layer (two or more sticks placed end to end are counted as one stick for this purpose), and s is the spacing between sticks in cm. A_s is

more complicated to calculate due to the overlapping of sticks, but can be calculated through Equation (4.4):

$$A_s = 2N\mathrm{n}w(L + w) + nLw + 2n^2ws(N - 1) \tag{4.4}$$

where N is the total number of layers, w is the width of each stick in cm, and L is the total crib length in cm. $\dot{m}$ can then be calculated based on the crib dimensions. From the burning rate, the heat release rate can be calculated using the heat of combustion.

The growth rate, and thus time to flashover is then calculated from [168], who found that a linear growth model gave the best correlation to experimental results. The growth parameter is calculated through Equation (4.5):

$$\iota = \dot{m}_{ss}(0.0158y - 0.0039) \tag{4.5}$$

where y is found from Equation (4.6):

$$y = \frac{(n - 1)s}{L} \tag{4.6}$$

Time to flashover can thus be estimated by Equation (4.7):

$$t_{fo} = \frac{\dot{Q}_{fo}}{\iota \Delta H_c} \tag{4.7}$$

The final design of the wood crib was based on the following three criteria:

- Flashover must occur,
- Exposed timber surfaces must ignite, and
- Time from flashover to crib burnout should be “short”.

A short crib burning duration was desired in order to allow exploration of the impact of the exposed timber surfaces on the compartment fire dynamics. Using wood cribs covering 4 m^2, 5 layers of 2.5 cm square sticks with a 7.5 cm separation gives a burning

rate from Equation (4.2) of 82 g/s, equivalent to a heat release rate of 1435 kW, which is greater than that required for flashover, thus the first criterion is satisfied. Time to flashover calculated by Equation (4.7) is less than one minute. Although this is unrealistically quick, it gives a high level of confidence that flashover will occur quickly and after determining the mass of wood remaining after this time, the remaining burning time (assuming a constant burning rate of 82 g/s to burnout) is around 17 minutes, satisfying the third criterion. Therefore, four wood cribs of area 1 m^2, stick size 2.5 cm, stick spacing 7.5 cm, and five layers were used in the experiments.

4.2.2 Instrumentation

In each experiment, the following data were collected:

- gas and solid-phase temperature data using K-type thermocouples;
- flow velocity in and out of the opening using bi-directional McCaffrey probes;
- surface temperature data using thin skin calorimeters (TSCs);
- crib mass loss data using load cells;
- exhaust gas concentrations using gas analysers;
- and visual data using HD video cameras.

Each of these are now discussed in turn.

4.2.2.1 Gas phase temperature measurements

Inconel sheathed type-K thermocouples were assembled into “trees” of twelve thermocouples at 20 cm spacing. This allowed measurements of the gas phase temperatures as a function of height, allowing data such as the depth of the hot upper layer to be determined. Five to ten trees per experiment were used, in the layout shown in Figure 4.4. One tree was placed in the centre, and others arranged in a 2 m x 2 m grid system around it, labelled using a co-ordinate system. After experiment α-1, trees T12, T23, T32, and T21 were not used. An additional tree was used in experiments α-1, β-1, and γ-1 at position TXX to measure gas phase temperatures immediately in front of the exposed back wall. Positioning the trees in this manner allowed the

variation in gas temperatures across the compartment to be obtained, and any potential correlation with location of exposed surfaces explored. The lowest thermocouple was positioned 40 cm above the concrete floor (and thus approximately 20 cm above the false floor) with the uppermost thermocouple 240 cm above this. Each thermocouple was identified by its tree position and height – e.g. T12.80 is the thermocouple in tree T12 positioned 80 cm from the ground.

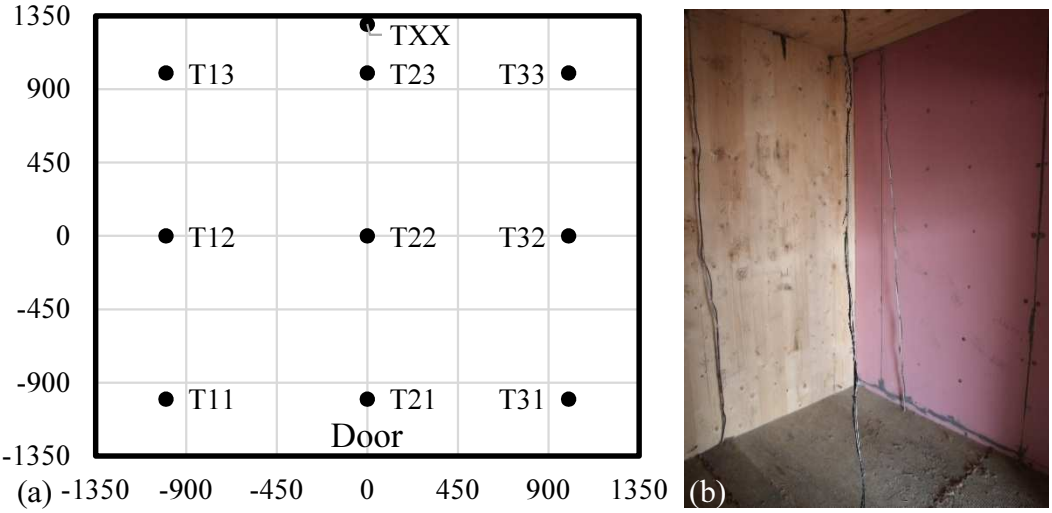

Figure 4.4: (a) thermocouple tree positions for full-scale compartment fire experiments, distances from centre shown in mm; (b) thermocouple trees T22, TXX, and T33 in experiment β-1.

Each thermocouple had its tip bent at 90° approximately 15 mm from the end. The trees were supported by binding the thermocouples together and to a 2 mm diameter steel wire using metal ties. The steel wires had a loop created at each end – the top loop was hung on a second 2 mm steel wire running just below the ceiling, and the lower loop was attached to a hook drilled into the floor. The trees were tensioned to minimise the lateral movement during the experiments. In the first experiment, α-1, these wires failed during the fire, and the thermocouple trees collapsed, resulting in some being damaged. From the initial data gathered, it was seen that five trees (T13, T33, T22, T11, and T31) were sufficient to capture the spatial variation in temperature, and thus trees T12, T23, T32, and T21 were not replaced for future experiments. For the remaining experiments, the 2 mm diameter steel wire was replaced with 4 mm diameter wire, which held the thermocouple trees in place for the duration of the

experiments. An additional thermocouple tree, TDD, was placed in the opening, and is discussed in section 4.2.2.4.

4.2.2.2 Solid-phase temperature measurements

In addition to the gas-phase thermocouples, thermocouples were inserted into the CLT panels to measure the in-depth temperature profiles. Two thermocouple densities were used – a "high" density, with thermocouples at 5 mm, 10 mm, 15 mm, 20 mm, 25 mm, 30 mm, 35 mm, 40 mm, 50 mm, 60 mm, and 80 mm from the fire-exposed surface, and "low" density, with thermocouples at 10 mm, 20 mm, 40 mm, 60 mm, and 80 mm from the fire-exposed surface. The layout of these is shown in Figure 4.5. These thermocouples were identified by a letter denoting the exposed surface, the co-ordinate of the thermocouple "bundle" (left to right, bottom to top) and then the distance from the exposed surface - e.g. B23.15 is the thermocouple in the back wall, 2nd column from the left, 3rd row from the bottom, and 15 mm from the exposed surface.

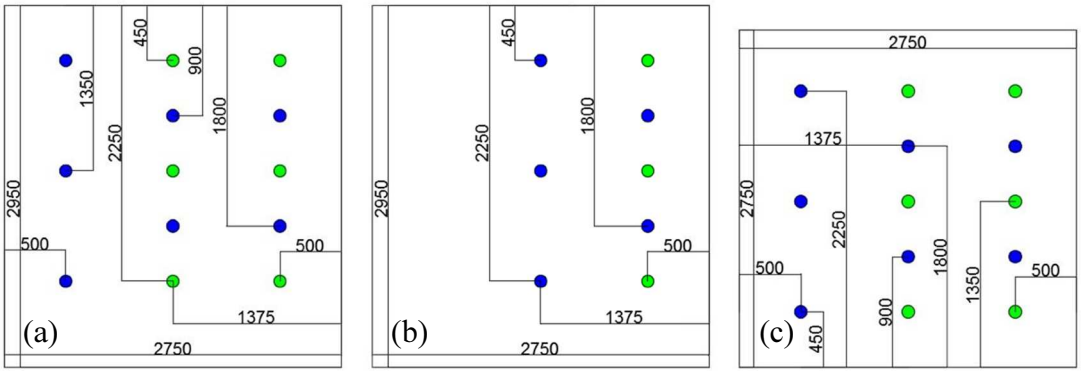

Figure 4.5: Through-thickness thermocouple layouts for (a) exposed back wall, (b) exposed side wall, and (c) exposed ceiling. Blue circles correspond to "low" thermocouple density, green circles correspond to "high" thermocouple density. All dimensions in mm from timber-timber interfaces (encapsulation not considered).

The distances in Figure 4.5 refer to the position of the central thermocouple of each bundle – the additional thermocouples were placed around the centre thermocouple as shown in Figure 4.6.

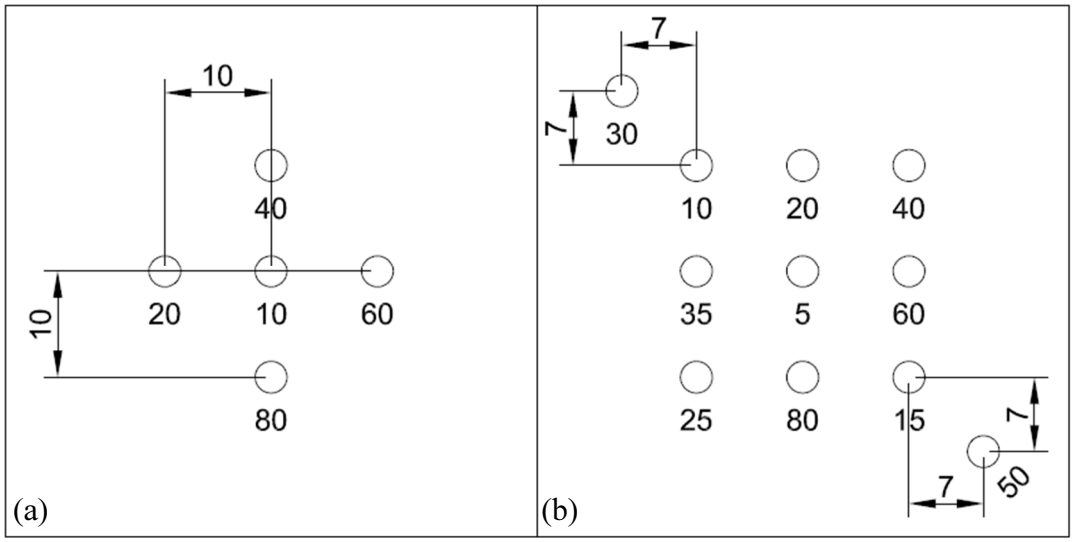

Figure 4.6: Detailed thermocouple positioning for (a) low density thermocouple bundles and (b) high density thermocouple bundles. All dimensions in mm. Numbers adjacent to thermocouples indicate distance from exposed surface.

All thermocouples were inserted into pre-drilled holes from the back of the timber. K-type thermocouples of 1.5 mm diameter were used. Holes were drilled using a 2 mm diameter drill bit to enable ease of installation, apart from the final 8 mm, which was drilled using a 1.5 mm drill bit to ensure good contact with the solid. A pillar drill stand was used to ensure accuracy in depth achieved and drilling angle. Thermocouples were marked with the target depth before insertion, and any deviation from the target depth was recorded to an accuracy of ± 1 mm.

Additionally, thermocouples were placed in the encapsulated right-side wall in experiment β-1, in order to measure the thermal penetration through the encapsulation and into the protected timber. A total of 27 thermocouples were placed in the encapsulated right wall, at positions S15 (high density), S21 (low density), and S33 (high density). Thermocouples were placed in-depth in the encapsulated left side wall in experiments α-2, β-2, and γ-1. The same co-ordinate system was used as in Figure 4.5, with the letter "U" used to denote unexposed surface. Fifteen thermocouples were inserted at positions U11, U13, U22, U31, and U33 at 5 mm, 10 mm, and 15 mm from the CLT-plasterboard interface. In experiment α-2, five additional thermocouples were

inserted into the protected ceiling, at positions C21.5, C21.25, C23.25, C23.30, and C25.5.

4.2.2.3 Thin skin calorimeters

Internal and external thin skin calorimeters, as described by Hidalgo et al. [169] were used to obtain estimates of incident radiant heat flux. External TSCs were embedded in squares of vermiculite board 100 mm x 100 mm square and 25 mm thick. Internal TSCs were embedded directly onto the timber surface, at the same positions as the thermocouple bundles shown in Figure 4.5. All TSCs were coated with an aqueous based colloidal graphite dispersion, and then oven-dried at 80°C to give the TSCs a similar emissivity to that of charred timber [170].

External TSCs were used in all experiments. Number and positioning of external TSCs varied from one experiment to another. In experiment α-1, two external TSCs were used – one at 2.5 m from the opening, and the other at 3 m, both at heights of approximately 1.8 m. In experiment β-1, only one external TSC at 2.5 m from the opening and a height of 1.8 m was used. In the remaining experiments, two TSC "towers" were prepared, each with four TSCs at heights of 0.6 m, 1.1 m, 1.6 m, and 2.1 m. These were positioned 2 m and 4 m from the opening, as shown in Figure 4.7. These were staggered horizontally to avoid the front TSC tower blocking radiation to the rear tower.

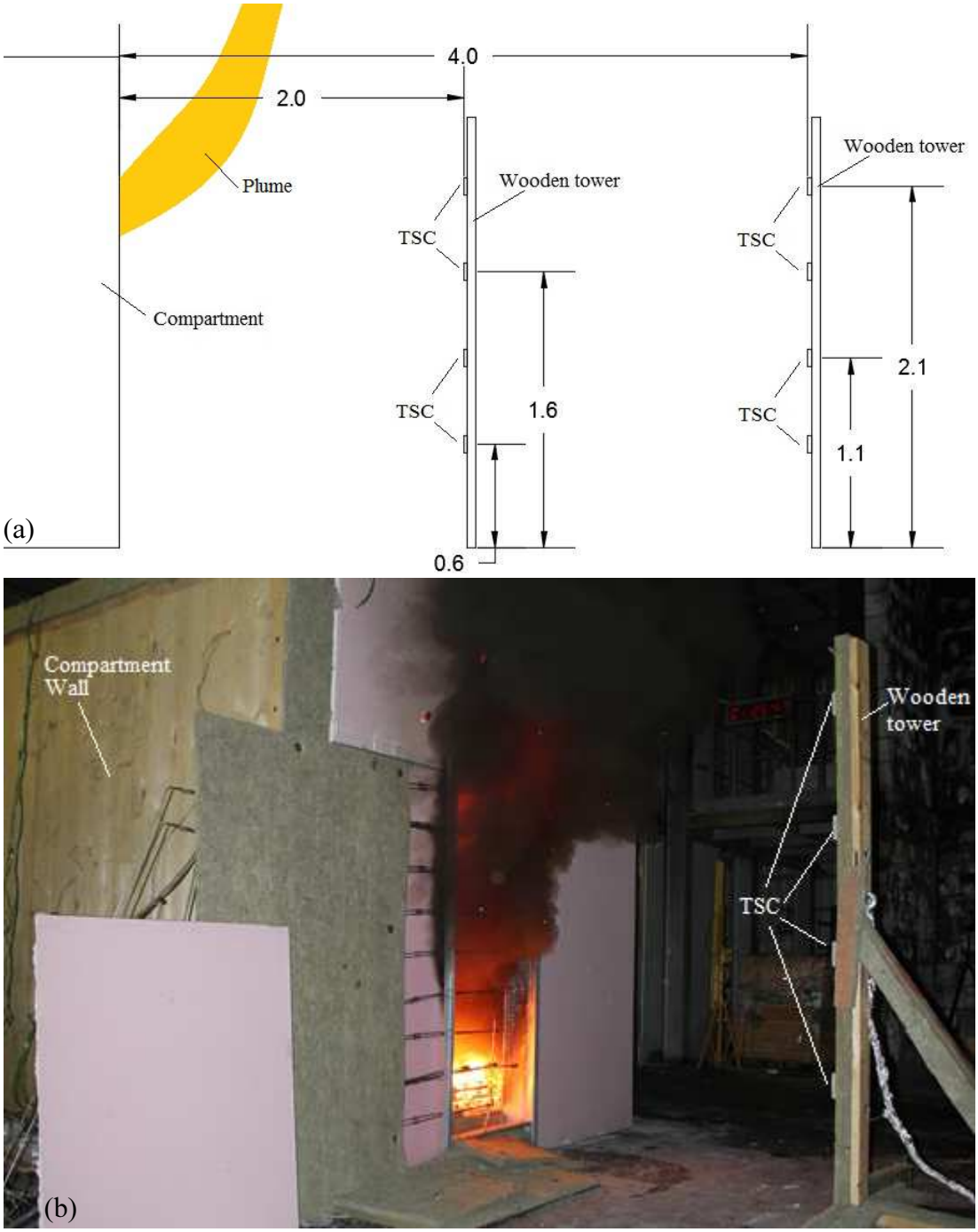

Figure 4.7: (a) external TSC "towers" used in experiments α-2, β-2, and γ-1 (all dimensions in m); (b) photograph of external TSC tower in experiment α-2.

Internal and external TSCs were calibrated after the experiments were completed, according to the procedure used by Hidalgo et al. [169]. One TSC was prepared as per the external TSCs, embedded into a 100 mm x 100 mm square of vermiculite, and five

TSCs were prepared in the centre of 400 mm x 300 mm x 100 mm thick 5-lamella CLT panels. Two TSCs were used for the timber calibrations to account for possible variability, and to allow the impact of different heating and cooling rates to be determined. All TSCs were calibrated using H-TRIS [171] to enable a time-varying heat flux to be imposed. Combining the relevant equations from [169], the calibration factor for a given TSC can be calculated from Equation (4.8):

$$C = \frac{\alpha_{disc}\dot{q}''_{in} - [\gamma \frac{m_{disc}}{A_{s,disc}} C_{p,disc} \frac{dT_{disc}}{dt} + \varepsilon_{disc}\sigma T_{disc}^4 - h_c(T_g - T_{disc})}{\alpha_{disc}\dot{q}''_{in}} \quad (4.8)$$

where α_{disc} is the absorptivity of the disc, $\dot{q}_{in}$ is the known incident heat flux from H-TRIS, γ is a transient compensation factor, taken as 0.8 [169], m_{disc} and $A_{s,disc}$ are the mass and surface area of the disc respectively, and h_c is determined by considering an empirical correlation of the Nusselt number over a vertical hot plate in laminar flow [169]. $C_{p,disc}$ is calculated through Equation (4.9) [169], where T is the disc temperature in Celsius.

$$C_{p,disc} = 450 + 0.28T - 2.91 \cdot 10^{-4}T^2 + 1.34 \cdot 10^{-7}T^3 \quad (4.9)$$

The heat flux can then be calculated from the experimental TSC temperatures and this C-factor through Equation (4.10):

$$\dot{q}''_{in} = \frac{1}{\alpha_{disc}(1-C)}\left[\gamma \frac{m_{disc}}{A_{s,disc}} C_{p,disc} \frac{dT_{disc}}{dt} + \varepsilon_{disc}\sigma T_{disc}^4 + h_c\left(T_g - T_{disc}\right)\right] \quad (4.10)$$

Timber TSC calibrations were of a short duration (45 min) to avoid significant regression of the timber surface, which could result in separation of the disc from the timber surface, thus potentially invalidating the data. Therefore, experimental heat flux data are only valid if significant char oxidation had not occurred. This is discussed further in Section 4.4.3. Two calibrations were carried out for the timber TSCs – one stepping down from 40 kW/m^2 to 10 kW/m^2 in 10 kW/m^2 intervals over a period of 45 min, and one stepping up in the same way. (Data were only used up to 30 kW/m^2

in this calibration, as significant surface regression was evident during the 40 kW/m^2 stage.) From these calibrations, the calibration factor was found to be $C = -2.04 \cdot 10^{-3}T + 1.50$, with T in Celsius, with good agreement between calibrations (± 3%).

4.2.2.4 Gas flow measurements

Thirteen bi-directional McCaffrey pressure probes [142] were placed in a frame in the doorway, in nine rows spaced at 20 cm intervals from 20 cm to 180 cm in height. A further thermocouple tree was also placed in the doorway at heights corresponding to each row of pressure probes. Each row had one pressure probe in the centre of the opening; rows 2 and 8 (at heights of 40 cm and 160 cm respectively) had two additional pressure probes 20 cm to the left and right of the central probe to capture any horizontal variations in flow. This is illustrated in Figure 4.8. The pressure probes were connected to transducers using plastic tubing, which produced a voltage which can be translated to a differential pressure using a known calibration factor. Six Omega PX278-0.1D5V transducers were used, and seven Gems 5266 transducers.

Pressure probes were calibrated in a wind tunnel, during which the probes were subjected to a known velocity, and the voltage produced from each velocity recorded, thus allowing a calibration factor to be obtained. This was determined to be 2.49 Pa/V for the Omega transducers, and 10 Pa/V for the Gems transducers.

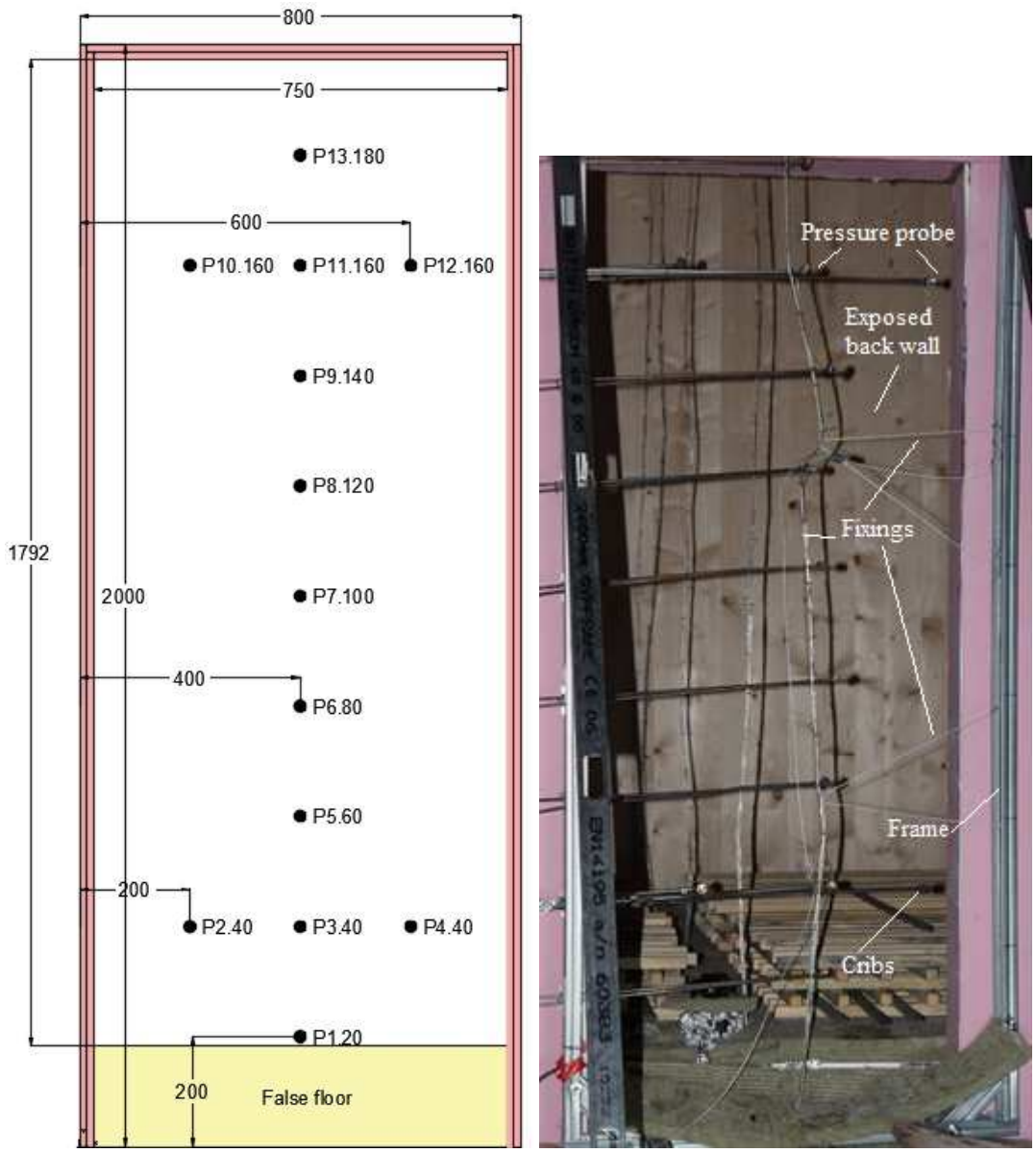

Figure 4.8: Schematic and photograph of pressure probes within compartment opening for experiment α-1.

4.2.2.5 Crib mass measurements

Four load cells manufactured by *Levantina de Pesaje* (Spain) were placed under the false floor system to record the mass loss from each wood crib independently. Each load cell measured 1 m x 1 m in plan, and had a maximum capacity of 300 kg with an accuracy of ± 20 g, according to class C5 of OIML R 60: Metrological Regulation for

Load Cells [172]. This allowed the burning rate and heat release rate from the wood cribs to be calculated.

4.2.2.6 Combustion gas composition

The entire compartment was built underneath the BRE 15 MW calorimeter which measured the oxygen, carbon dioxide, and carbon monoxide concentrations throughout each experiment, enabling the total heat release rate to be calculated through oxygen consumption calorimetry.

One or two additional gas analysers were used in each experiment with sampling points in the door frame alongside pressure probes P9.140 and/or P8.120, to measure the oxygen concentration in the exhaust gas. This allowed internal heat release rate to be estimated as described in Section 4.4.2.4.

4.2.2.7 Infrared imaging

An infrared (IR) camera was used in experiments α-1, α-2, and β-2. In experiment α-1, this was placed looking at the back corner of the compartment from the outside, to investigate thermal penetration to the rear face. In experiments α-2 and β-2, the IR camera was placed in front of the compartment looking at the external plume.

4.2.2.8 Visual observations

In each experiment, visual data was also recorded through three HD video cameras. One camera was positioned looking through the opening, one from the side to capture the external plume, and one from above capturing the whole compartment. These data were used to verify recorded times to flashover, delamination, and the onset of extinction. All video cameras were started simultaneously before each experiment to allow accurate cross-referencing of the visual data obtained.

4.2.2.9 Summary

A summary of the instrumentation for each experiment is given in Table 4.3.

Table 4.3: Instrumentation used in full-scale compartment fire experiments.

Experiment	α-1	α-2	β-1	β-2	γ-1
In-depth thermocouples	159	179	229	217	275
Gas-phase thermocouples	129	69	81	69	81
Total thermocouples	288	248	310	286	356
Surface TSCs	21	21	26	26	34
External TSCs	2	8	1	8	8
Pressure probes	13	13	13	13	13
Video cameras	3	3	3	3	3
Network cameras	3	1	0	1	3
Infrared camera	1	1	0	1	0

4.2.3 Ignition Protocol

Each of the compartments was constructed and encapsulated by external contractors. Timber panels were connected as shown in Figure 4.1 using 8 mm diameter, 240 mm long wood screws at 200 mm spacing. Each layer of encapsulation was screwed onto the walls separately, using 40 mm diameter washers to hold the mineral wool and the outer layer of plasterboard in place. After the compartments were built, the thermocouple trees and false floor system were installed as described in Section 4.2.2.5. The cribs were then built, having been stored in a conditioned room to allow moisture content to stabilise at a nominal 12%. Cribs were ignited by placing six fibre strips soaked in white spirit in one of the spaces in the bottom level, and igniting these. During the experiments, time to flashover was recorded, and any observations in terms of delamination, trends towards extinction, and secondary flashovers were recorded. Experiments were terminated when auto-extinction had occurred, or it became clear that sustained burning was not going to result in auto-extinction.

4.3 Experimental Narrative

A description of each experiment is given below, with times to flashover, failure mode, and other key observations noted.

4.3.1 Summary

Key events are summarised in Table 4.4. Crib burnout times showed good repeatability for the same configuration, with configuration β burning out 2.2 minutes faster than configuration α, and configuration γ burning out 4.9 minutes faster than configuration α. Likewise, reduction in burning rate occurred at similar times (around 15) minutes for most experiments (α-1, β-1, and β-2), suggesting good repeatability, particularly for configuration β. However, only experiment β-1 resulted in auto-extinction, which occurred 22 minutes after ignition. Flashover was also consistent between experiments (within ± 40 s with the exception of experiment β-1), where the ignition procedure did not result in uniform ignition of the cribs.

Table 4.4: Timing of key events in full-scale compartment fire experiments.

Event	Approximate time after ignition [min]				
	α-1	α-2	β-1	β-2	γ-1
Flashover	4.6	5.1	8.6	4.2	5.4
Burnout of wood cribs	17.7	17.2	15.6	14.9	12.6
Reduction in burning rate	15	32	16	12, 27, 50	n/a
Increase in burning rate	32	45	n/a	20, 43	n/a
Severe plasterboard fall-off	44 (27.8 kg)	n/a	n/a	n/a	n/a
Auto-extinction	n/a	n/a	22	n/a	n/a
Manual suppression	61	60	98	62	78

In summary, each of the five experiments resulted in three distinct outcomes – auto-extinction, decay, and sustained flaming; as summarised below.

4.3.1.1 Outcome 1: Auto-extinction

Experiment β-1 resulted in auto-extinction approximately 6 minutes after the fuel load burned out. This can be largely attributed to a lack of significant delamination (below 15% of total exposed area) and a sufficiently low proportion of exposed timber.

4.3.1.2 Outcome 2a: Decay leading to secondary flashover

Experiment β-2 initially followed the same trend as experiment β-1, with a rapid reduction in burning rate, until extensive delamination on all surfaces resulted in sufficient fresh timber becoming exposed to provide a secondary flashover.

4.3.1.3 Outcome 2b: Decay leading to sustained flaming

Experiment α-2 exhibited similar behaviour to experiment β-2, however the decay rate occurred over a much longer period. Delamination occurred in multiple small stages, rather than a few large events, resulting in moderate areas of fresh timber constantly being exposed and sustaining the burning. In this case, a secondary flashover was not observed, instead high burning rates (>3MW) were observed throughout the majority of the fire. Experiment α-1 exhibited similar behaviour in the early stages of the experiment until encapsulation failure occurred.

4.3.1.4 Outcome 3: Sustained flaming

Experiment γ-1 (and α-1 after encapsulation failure) had a greater proportion of exposed timber, resulting in a higher radiative feedback to the exposed surfaces. No significant decay was observed in this experiment, and burning continued at near-peak rate for the entire fire duration.

4.3.2 Experiment α-1

Plasterboard fall-off times were confirmed by visual observations and video recordings, with masses obtained from load cells. A total plasterboard mass of 99.1 kg fell off during this experiment, starting around 22 minutes after ignition. The peak plasterboard fall-off time at 44 minutes after ignition (27.8 kg) coincided with the visual observations of a rapid increase in burning rate, which was due to freshly exposed timber igniting and contributing to the fuel load. This encapsulation failure led to the development of the novel encapsulation system shown in Figure 4.2 being used for subsequent experiments. The continued burning in this experiment after encapsulation failure can be attributed to the proportion of CLT exposed (100%) –

resulting in a much higher re-radiation heat flux into the exposed surfaces. Key events are shown in Figure 4.9.

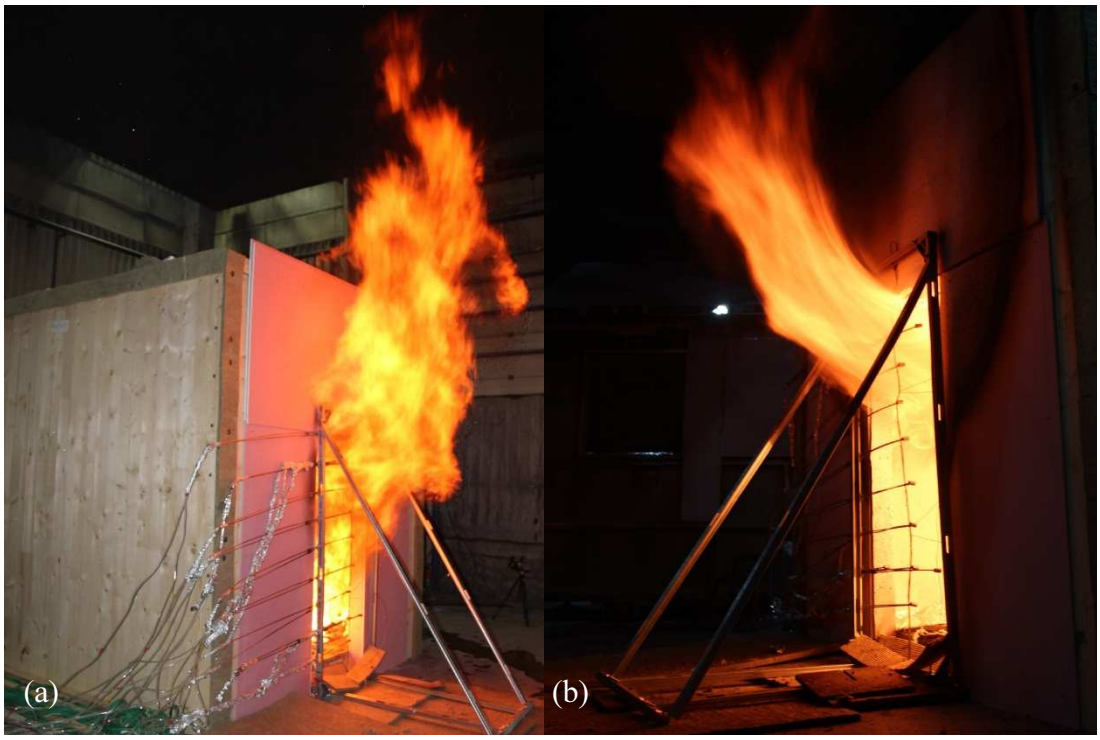

Figure 4.9: Experiment α-1 (a) 5 minutes after ignition showing peak external flaming, (b) 25 minutes after ignition showing reduced external flaming.

4.3.3 Experiment α-2

Experiment α-2 was a repeat of experiment α-1, but using the novel encapsulation system developed for this experimental programme. Similar to experiment α-1, a total mass of 105.9 kg of plasterboard fall-off was recorded by the load cells, again corresponding to complete fall-off of the outer two layers of plasterboard. Due to the enhanced encapsulation system however, the mineral wool and additional layer of plasterboard stayed in place, preventing the underlying timber from igniting and contributing to the fire. Thermocouple readings in the exposed surface confirmed that at 5 mm from the timber surface, the temperature did not exceed 70°C. The sustained flaming in this experiment therefore cannot be attributed to encapsulation failure. Localised delamination was observed throughout the experiment, with small pieces of

char detaching from the CLT panel and exposing the fresh underlying timber. This is hypothesised to be responsible for the sustained flaming observed. Overall, the observed behaviour in experiments α-1 and α-2 can be seen to quite similar, suggesting good repeatability. Key events are shown in Figure 4.10.

Figure 4.10: Experiment α-2 (a) 5 minutes after ignition, showing flaming on back wall prior to flashover, (b) 9 minutes after ignition, showing peak external flaming, (c) 30 minutes after ignition, showing reduced external flaming and flaming on side wall, (d) 56 minutes after ignition, showing return to peak external flaming.

4.3.4 Experiment β-1

Figure 4.11: Experiment β-1 (a) 9 minutes after ignition, showing peak burning, (b) 21 minutes after ignition, showing cessation of external flaming and tendency towards auto-extinction, (c) 31 minutes after ignition showing localized delamination resulting in localized surface flaming.

After burnout of the wood crib, the burning started to rapidly decrease, with a cessation of external flaming at around 20 minutes after ignition, shown in Figure 4.11(b). As the external flaming decreased, flaming was visible on the back wall, which also gradually reduced until around 21-22 minutes after ignition, at which point auto-extinction had been achieved. After this, some localised delamination occurred leading to small regions of flaming on the back wall, shown in Figure 4.11(c), but this did not result in re-ignition, and the local flames also auto-extinguished after around 15-20 minutes. No fall-off of plasterboard was observed during this experiment. Delamination was measured after the experiment, and was limited to <20% of the exposed wall and <10% of the ceiling.

4.3.5 Experiment β-2

Unlike experiment β-1, experiment β-2 displayed a cyclical increase and decrease of burning rate. Burning rate reached minima before secondary and tertiary flashovers, at which point the external plume had decreased to less than 10% of the opening height, and flaming was visible across the exposed back wall, suggesting the fire behaviour was tending towards fuel-controlled burning. One of the data loggers stopped recording after approximately 30 minutes, limiting the temperature data collected. 7.8 kg of plasterboard fall-off was recorded over the duration of this experiment. This did not correspond to a significant portion of the encapsulation. The continued burning of this experiment can be attributed to large-scale delamination which did not occur in experiment β-1.

Key events are shown in Figure 4.12.

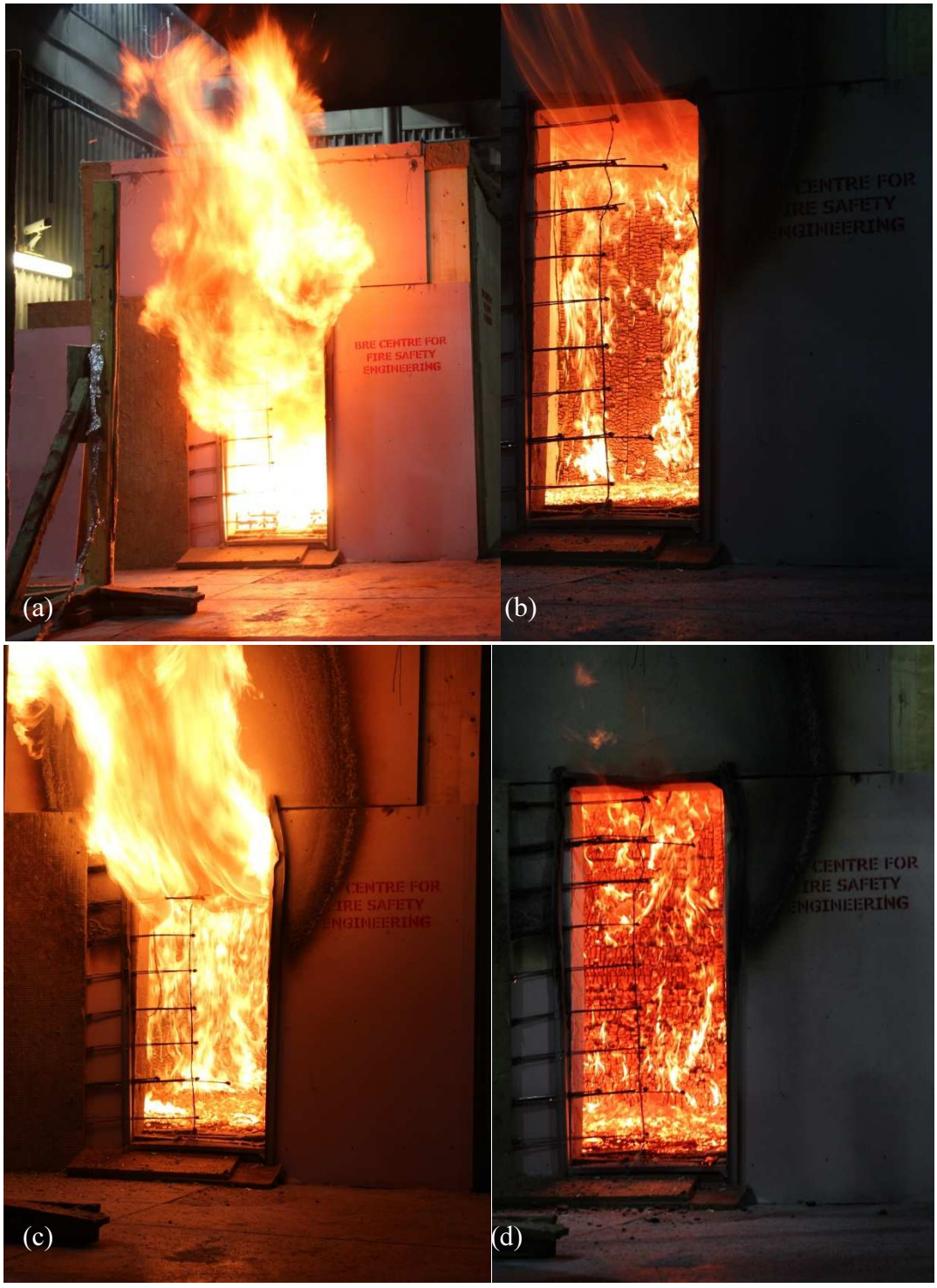

Figure 4.12: Experiment β-2 (a) 6 minutes after ignition, showing peak burning, (b) 18 minutes after ignition, showing reduction in external flaming and flaming on back wall, (c) 24 minutes after ignition, showing peak external flaming after secondary flashover, (d) 40 minutes after ignition, showing the reduction in external flaming during the second decay phase and flaming on back wall.

4.3.6 Experiment γ-1

Experiment γ-1 was manually extinguished as no evidence of decay was seen. Failure of the load cells means that no quantification of the mass of plasterboard which fell off was possible. The continued burning in this experiment can be attributed to the proportion of CLT exposed resulting in a much higher re-radiation heat flux into the exposed surfaces, as with experiment α-1. Key events are shown in Figure 4.13.

Figure 4.13: Experiment γ-1 (a) 6 minutes after ignition, showing peak burning, (b) 35 minutes after ignition, showing quasi-steady burning.

4.4 Results and Discussion

4.4.1 Time to flashover

In Section 4.3, the time to flashover for each experiment is estimated from visual observations. In each case, a distinct, transition to a Regime I post-flashover fire was clearly observed, and thus a flashover time for each experiment can be stated with confidence. To allow a more robust comparison however, this can be compared to the time taken for all upper-layer gas-phase thermocouples to reach 600°C, a common definition for flashover [11]. This comparison is shown for each experiment in Figure

4.14, from which it is clear that there is strong agreement (average ± 6%) between the two methods, and thus the visual observations are valid for comparisons.

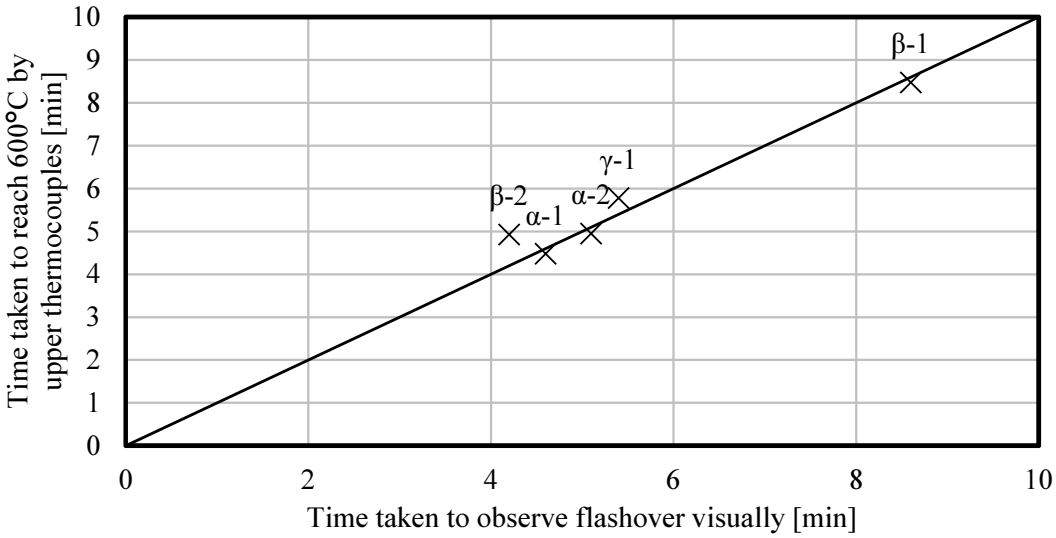

Figure 4.14: Time to flashover for each full-scale compartment fire experiment calculated from visual observations and the "600°C criteria".

4.4.2 Heat release rate calculations

Heat release rate for each experiment can be calculated in three different ways:

1) *Total* heat release rate can be calculated using oxygen consumption calorimetry.
2) The heat release rate of the *wood cribs* can be calculated based on mass loss data.
3) The *internal* heat release rate can be calculated from the flow rates, temperatures, and oxygen concentrations in the opening.

Performing each of these calculations allows the total heat release rate to be calculated and divided in two different ways – crib and CLT heat release rate, and internal and external heat release rate.

4.4.2.1 Total heat release rate

The total heat release rate can be calculated from Equation (4.11) [173]:

$$\dot{Q} = \left[E\phi - (E_{CO} - E)\frac{1-\phi}{2}\frac{X_{CO,et}}{X_{ox,et}}\right]\frac{\dot{m}_e}{1+\phi(\alpha-1)}\frac{M_{ox}}{M_{air}}\left(1 - X_{H_2O,air}\right)X_{ox,air} \quad (4.11)$$

where E is the heat release per mass of oxygen consumed, taken as 13.1 kJ/g, ϕ is the oxygen depletion factor, given in Equation (4.12) [173], E_{CO} is the heat release per mass unit of oxygen consumed for combustion of CO to CO_2, taken as 17.6 kJ/g, X is the mole fraction of various gases in the air or exhaust, α is the volumetric expansion factor, taken as 1.105, M_{ox} is the molecular mass of oxygen, 28 g/mol, and M_{air} is the molecular mass of air, 29 g/mol.

$$\phi = \frac{X_{ox,air}\left(1 - X_{CO_2,et} - X_{CO,et}\right) - X_{O_2,et}\left(1 - X_{CO_2,et}\right)}{\left(1 - X_{O_2,et} - X_{CO_2,et} - X_{CO,et}\right)X_{ox,air}} \quad (4.12)$$

This gives the heat release rates shown in Figure 4.15, shown from flashover to allow comparisons between post-flashover burning for different experiments.

The trends observed in the visual analyses match those in Figure 4.15. It can be seen that the first 7-8 minutes post-flashover are very similar for each experiment, with the exception of experiment α-2, which has a slightly lower peak HRR. The decay phases of experiments β-1 and β-2 are very similar, again suggesting good repeatability, but the deviation from approximately 15 minutes post-flashover suggests a high dependency on delamination – leading to either auto-extinction in the absence of large-scale delamination, or secondary (or later tertiary) flashover in the case of significant delamination. The auto-extinction behaviour of experiment β-1 is clear in the HRR profile. The HRRs of experiments α-1 and α-2 are very similar until approximately 30 minutes post-flashover – at which point α-1 has a higher HRR due to encapsulation failure.

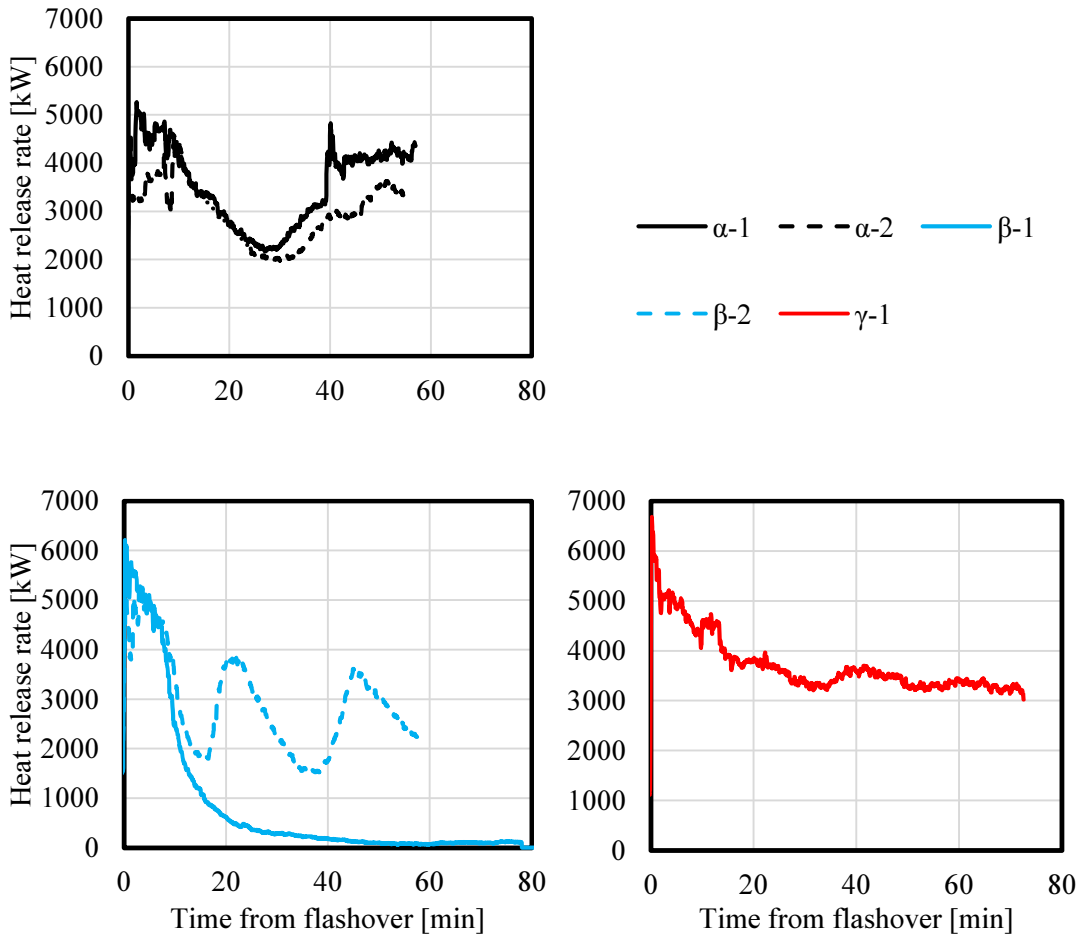

Figure 4.15: Total heat release rate of each full-scale compartment fire experiment.

4.4.2.2 Crib heat release rate

The crib heat release rate can be estimated from the mass loss data using Equation (4.13):

$$\dot{Q}_{crib} = \Delta H_c \dot{m} \tag{4.13}$$

This gives the crib heat release rates shown in Figure 4.16. A heat of combustion of 17.5 kJ/g is assumed.

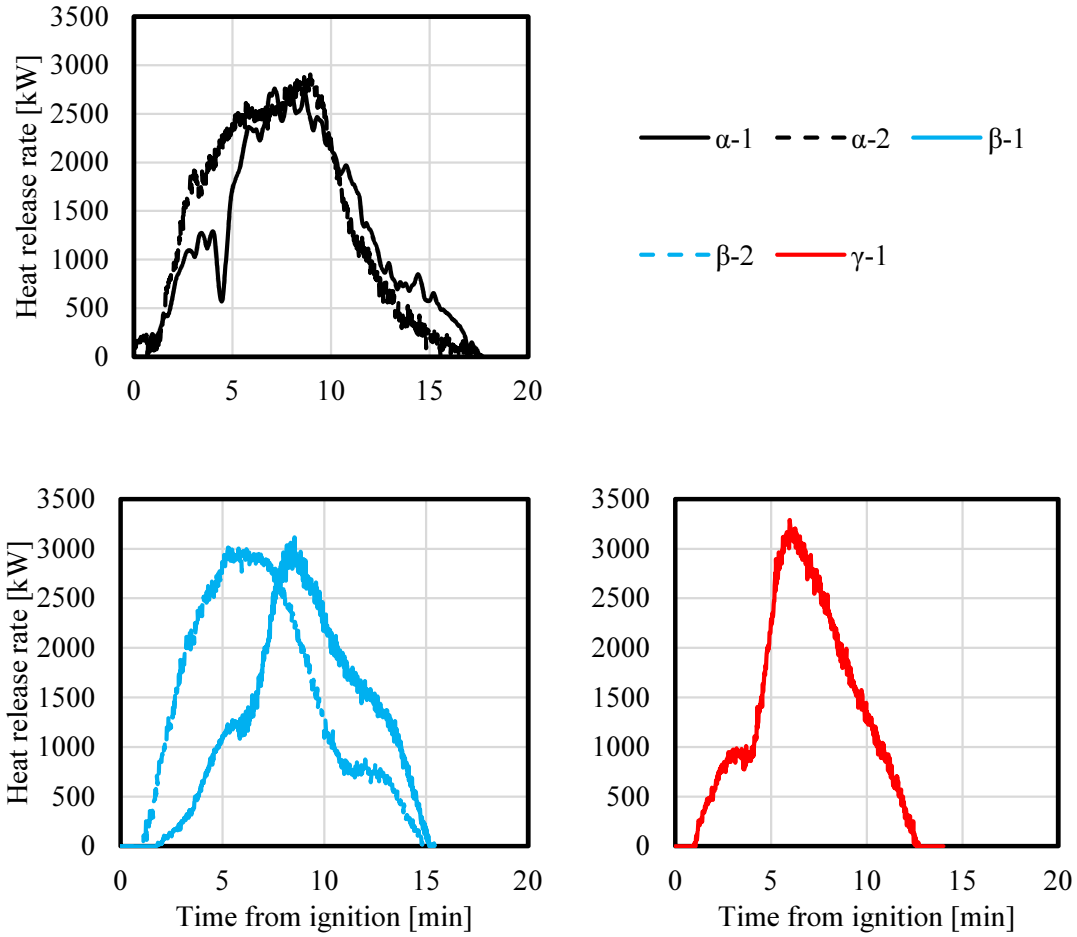

Figure 4.16: Crib heat release rate of each full-scale compartment fire experiment.

4.4.2.3 CLT heat release rate

The heat release rate from the CLT can be calculated simply by Equation (4.14):

$$\dot{Q}_{CLT} = \dot{Q} - \dot{Q}_{crib} \tag{4.14}$$

The CLT heat release rate is shown for each experiment in Figure 4.17. After burn out of the cribs this equal to the total heat release rate.

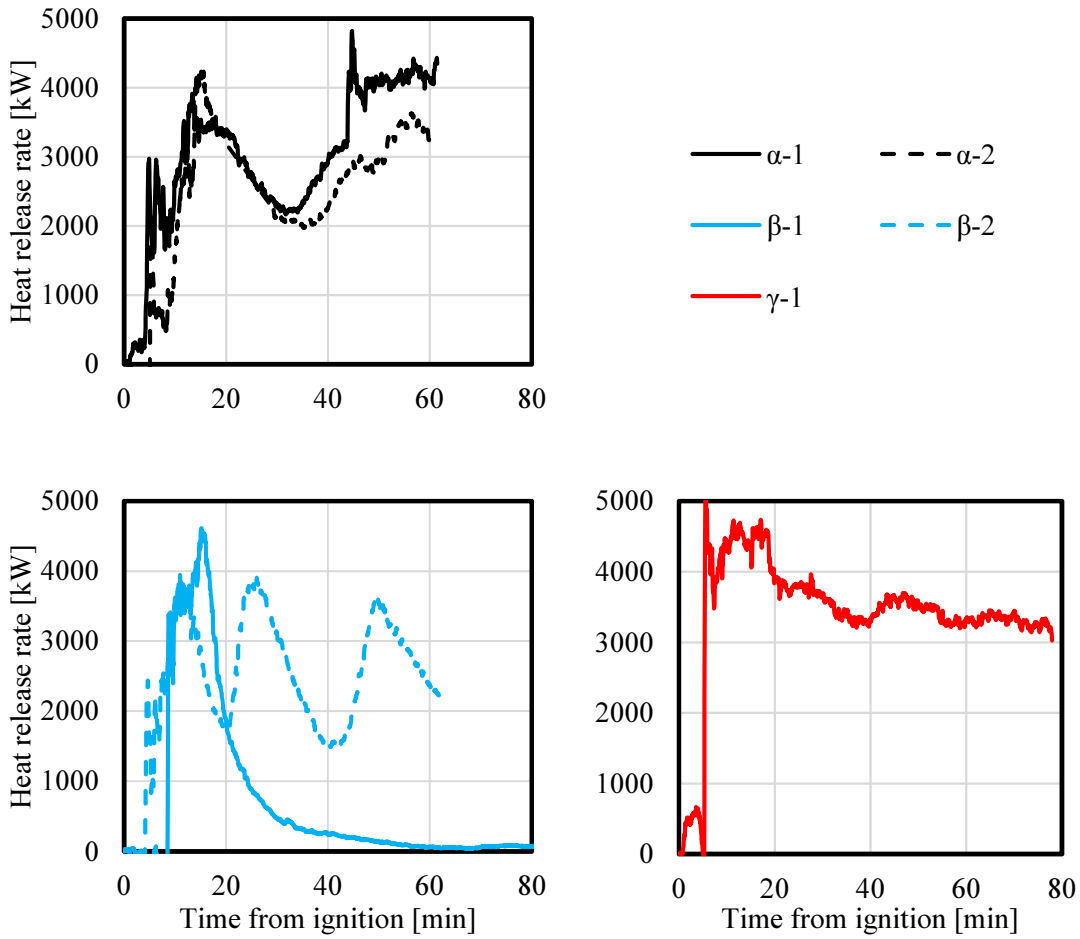

Figure 4.17: CLT heat release rate of each full-scale compartment fire experiment.

4.4.2.4 Internal heat release rate

The portion of the HRR released inside the compartment can be calculated from the data collected in the opening. The differential pressure was obtained from each probe, from which velocity and thus mass flow rate can be calculated. The data show a clear distinction between inflow (positive pressure) in the lower c.60 cm, and outflow (negative pressure) in the upper c.120 cm. The temperature from each thermocouple can be used to determine the temperature of gases flowing out of the compartment – when the gases are flowing in, these are assumed to be at ambient temperature.

From these pressures and temperatures, the velocity can be calculated by Equation (4.15):

$$v = \gamma \sqrt{\frac{2\Delta PT}{353}} \tag{4.15}$$

where ΔP is the differential pressure, T is the temperature, and γ is the probe constant, 0.94. This gives the velocity profile in Figure 4.18 for experiment γ-1. Similar data was observed for configurations α and β.

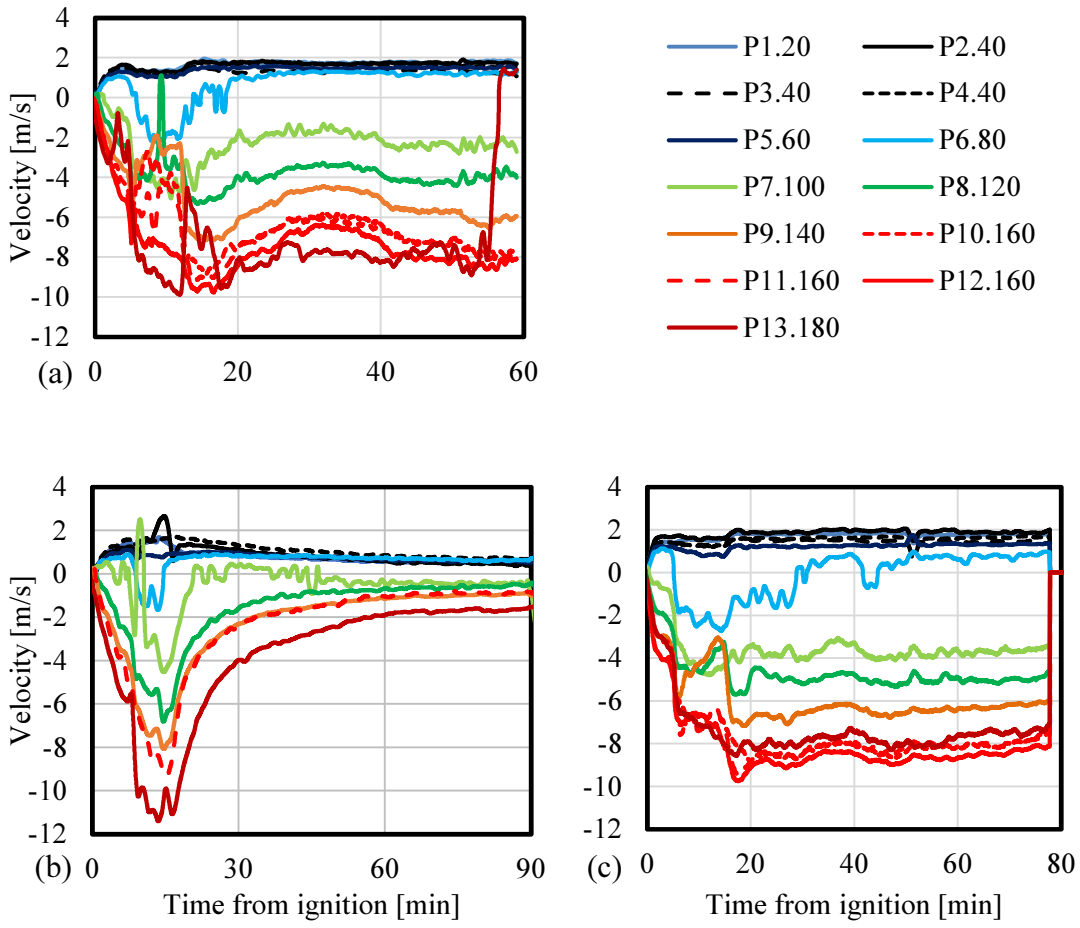

Figure 4.18: Velocity profile in the openings of experiments (a) α-2, (b) β-1, and (c) γ-1.

Subsequently, the height of the neutral plane can be determined as the position where velocity is equal to zero. This is shown in Figure 4.19. Again it is clear that experiments α-2 and γ-1 show similar behaviour, with the neutral plane stabilising around 0.7 m, whereas experiment β-1 has a slightly higher neutral plane (~0.8 m) after extinction.

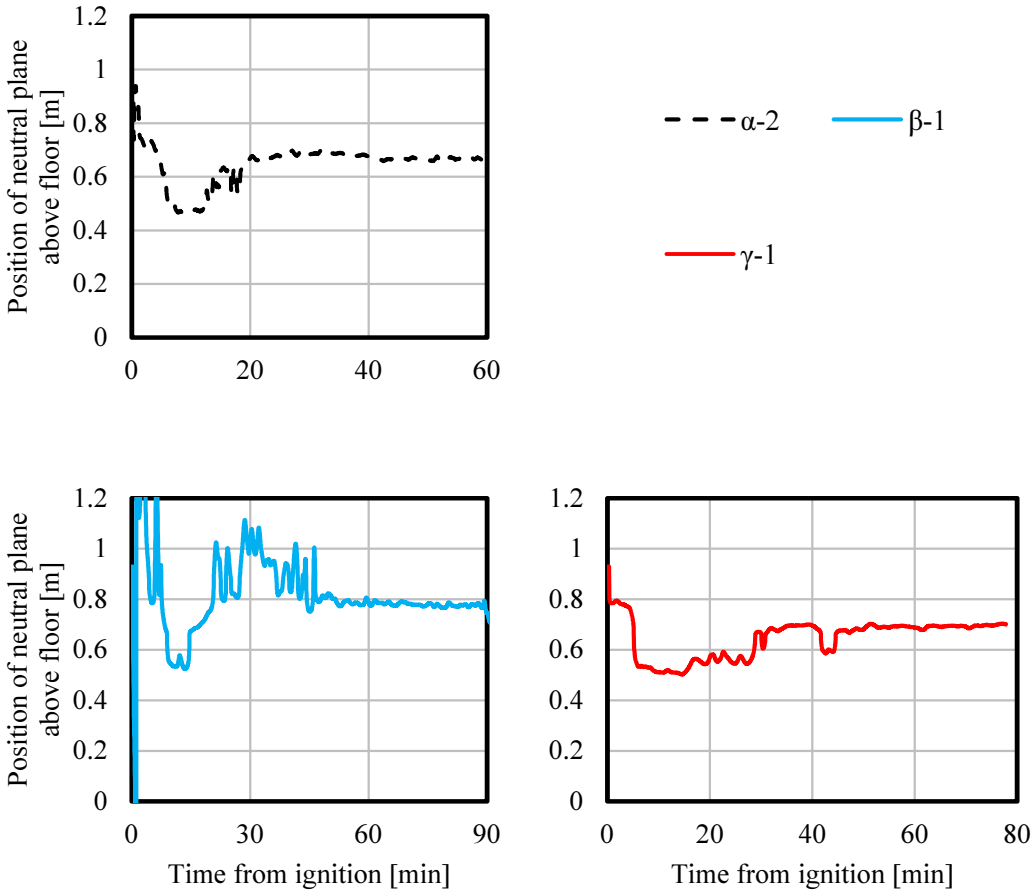

Figure 4.19: Height of neutral plane above base of opening for experiments α-2, β-1, and γ-1.

The mass flow rate in to the compartment can be calculated from the velocities through Equation (4.16):

$$\dot{m}_{in} = \sum_i \frac{353 C_D v_i A_i}{T_i} \; for \; \Delta P_i > 0 \tag{4.16}$$

where A_i is the are covered by each pressure probe, and C_d is the flow coefficient, taken as 0.68 [174]. This gives the mass flow rates in Figure 4.20. The mass flow rates are similar (between 0.6 and 0.8 kg/s) for all experiments which did not achieve auto-extinction. Experiment β-1 shows a gradual decrease, as is expected from a decay phase. Theoretical correlations from Karlsson and Quintiere [175] predicted the mass flow rate to within ~10% of the experimental values.

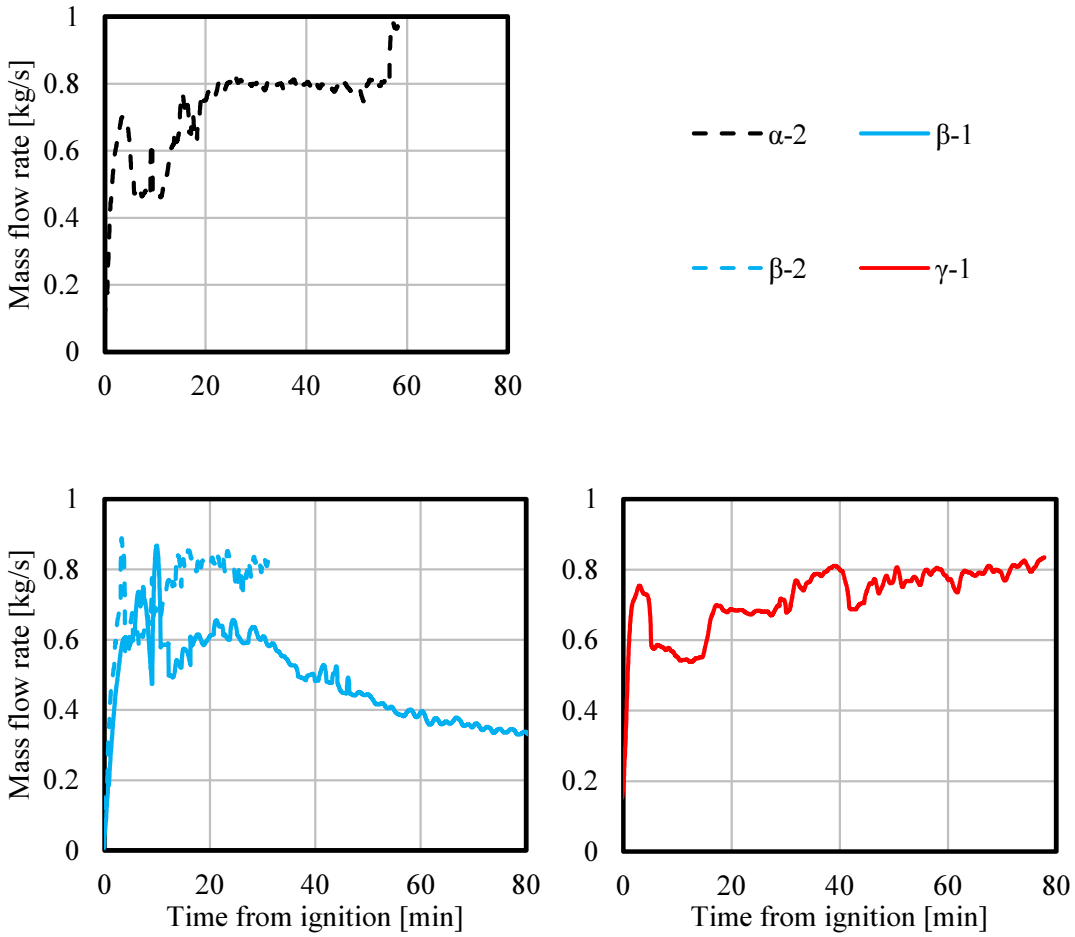

Figure 4.20: Mass flow rate into compartment for each full-scale compartment fire experiment.

The oxygen concentration was measured using the portable analysers described in Section 4.2.2.4. The plastic tubing in experiment α-1 melted shortly after flashover, resulting in faulty readings for the duration of the fire. However, for the experiments with similar behaviour visually (α-2 and γ-1), the oxygen concentration was zero for the entire post-flashover fire, and thus a value of zero was used to calculate the internal heat release rate in experiment α-1.

The internal heat release rate can then be calculated from Equation (4.17) [173]:

$$\dot{Q} = E\frac{\phi}{1+\phi(\alpha-1)}\dot{m}_{in}\frac{M_{ox}}{M_a}\left(1-X_{H_2O,air}\right)X_{ox,air} \tag{4.17}$$

where ϕ is calculated from Equation (4.18):

$$\phi = \frac{X_{ox,air} - X_{ox,et}}{(1 - X_{ox,et})X_{ox,air}} \tag{4.18}$$

This gives the internal heat release rates as shown in Figure 4.21. Experiment β-2 only has data up until 32 minutes due to the broken data logger.

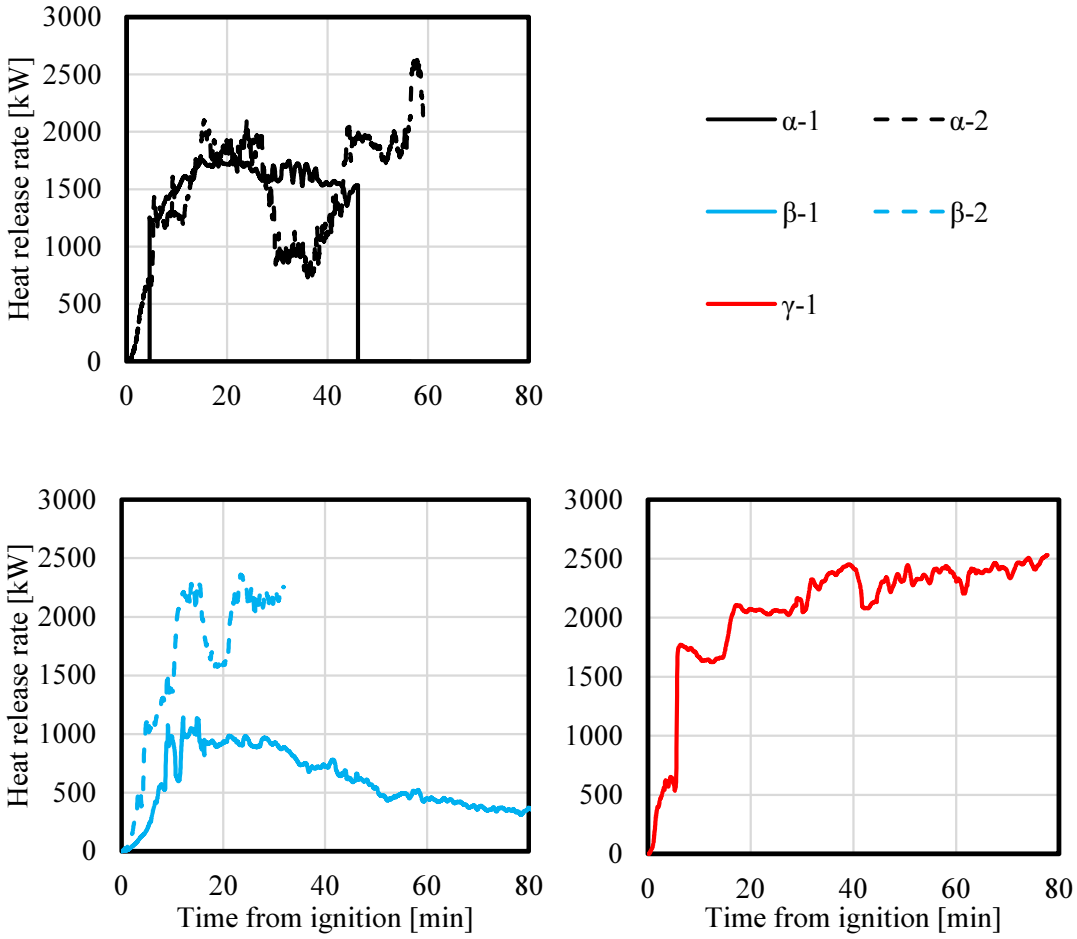

Figure 4.21: Internal heat release rate of each full-scale compartment fire experiment.

4.4.2.5 External heat release rate

The external HRR, i.e. the energy released in the external plume can thus be found by subtraction, and is shown in Figure 4.22.

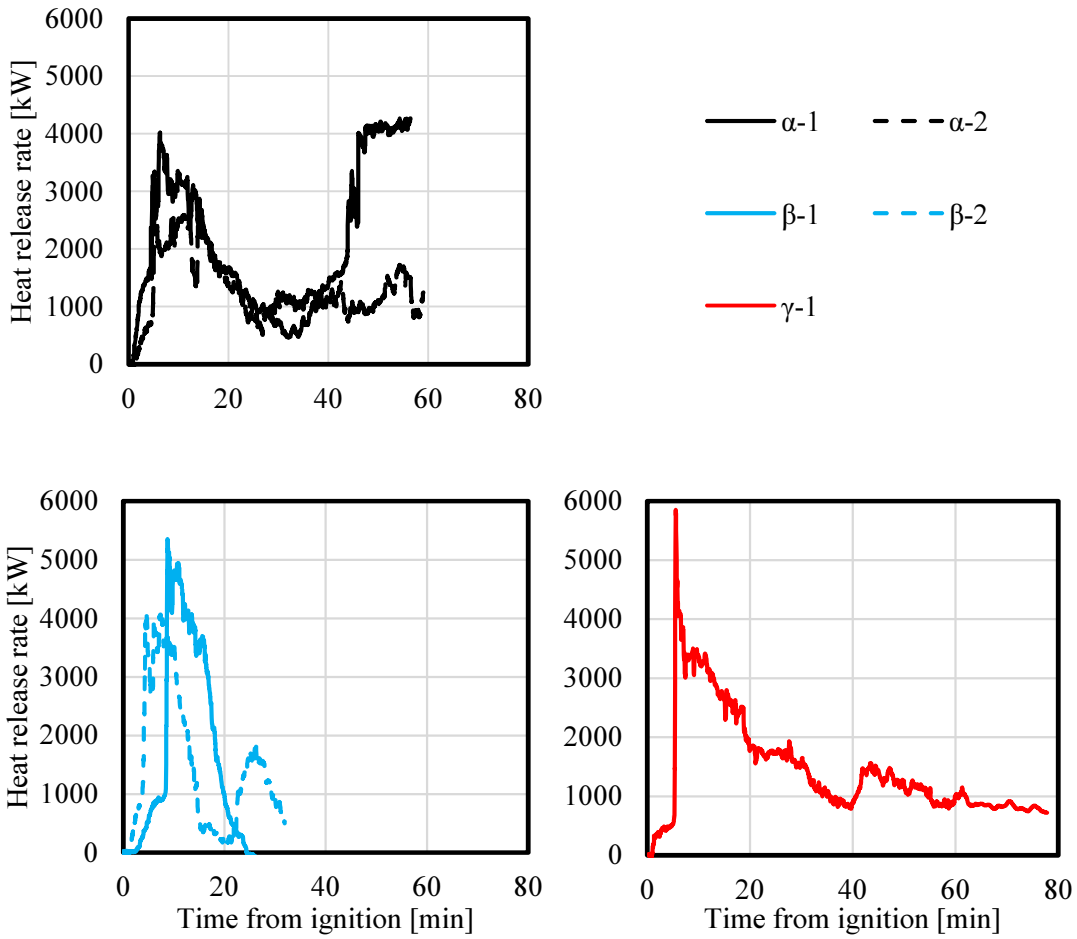

Figure 4.22: External heat release rate of each full-scale compartment fire experiment.

4.4.3 Heat flux to exposed timber surfaces

The heat flux to the exposed timber surfaces can be estimated using the TSCs described in Section 4.2.2.3. This is the data that is of most interest for auto-extinction analyses, and is presented below for each experiment. Due to the regression of the timber surface caused by char oxidation, after a time the readings from the TSCs will no longer be reliable. This is not likely to be so in the cases of interest, as heating durations were short, and peak burning occurred in a vitiated environment. The majority of char oxidation can therefore be hypothesised to have taken place after extinction (manual or auto). The heat fluxes for each experiment averaged over the back wall are shown in Figure 4.23. Experiment α-1 is excluded due to unreliable data collection.

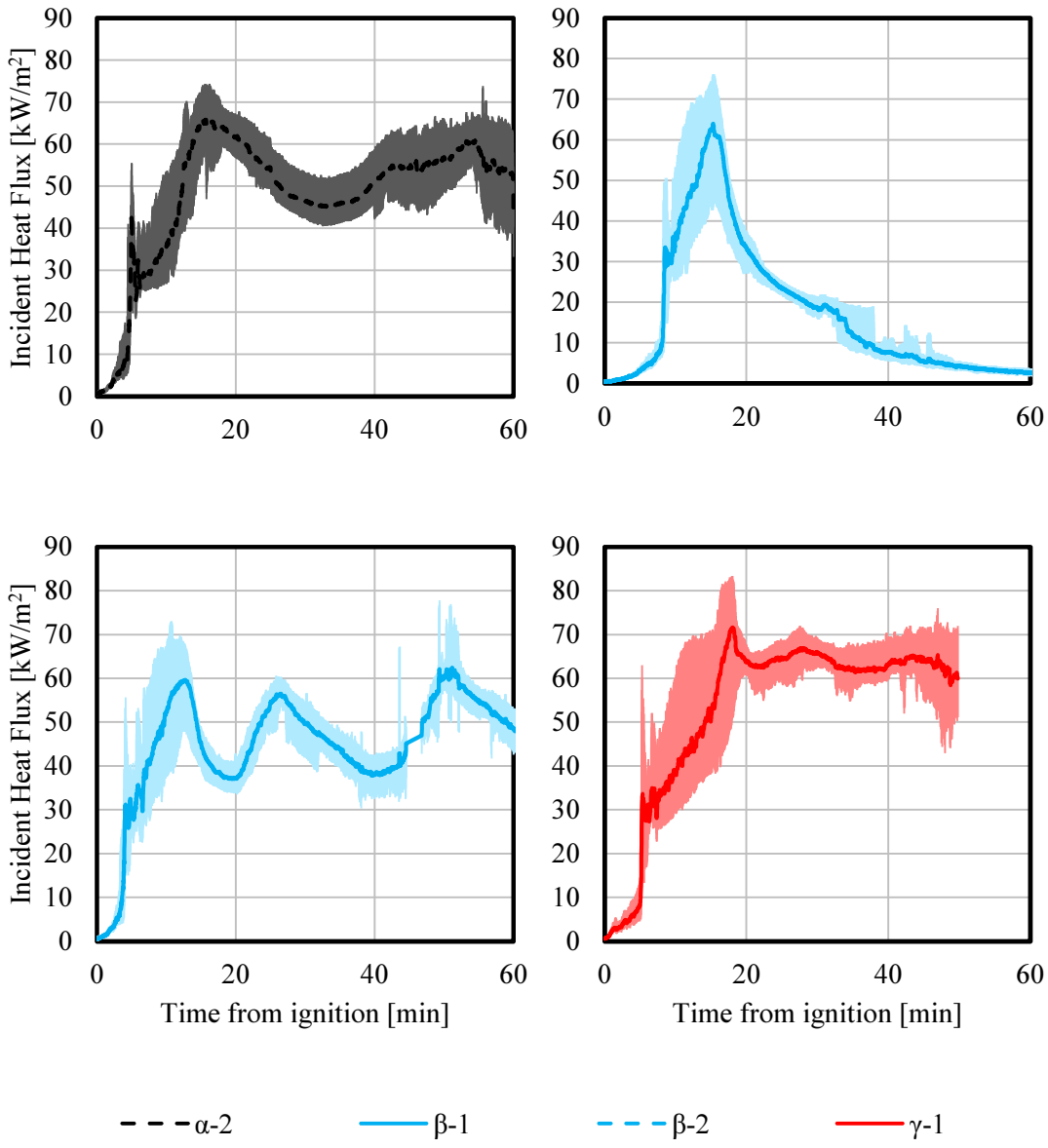

Figure 4.23: Average heat flux over exposed back walls of full-scale compartment fire experiments with maxima and minima shown.

The heat fluxes appear to follow approximately the same trend as the heat release rate. As expected, the heat flux in experiment β-1 reduces gradually, tending towards zero, and experiment β-2 fluctuates with the delamination cycles. The heat flux in experiment γ-1 is higher than in the other experiments as a result of more exposed surfaces. Whilst differences in convective flows and view factors will result in different heat losses and thus a different next heat flux than that in the FPA, it is clear

that the external heat flux experienced in experiment γ-1 is approximately double the critical heat flux for extinction of 31 kW/m^2 observed in Chapter 3.

4.4.4 Gas phase temperatures

The gas phase temperature data are useful as a further indicator of the trends observed in terms of growth and decay. These are shown averaged over the whole compartment, in Figure 4.24(a). It should be noted that these data are not corrected for radiation. From these data, the depth of the "hot layer" can be calculated. This was arbitrarily defined as the 700°C isotherm. Similar trends can be observed for 600°C and 800°C. These are averaged for each experiment, and shown in Figure 4.24(b)-(d), with the exception of experiment α-1, in which the thermocouple trees collapsed during the experiment and no meaningful data could be obtained. It can be seen that the depth of the hot layer takes up the entire compartment post-flashover (-2300 mm corresponds to the bottom-most thermocouple; below this no further data can be obtained), with some notable rises when the HRR and gas phase temperatures decrease slightly.

The same trends can be observed at each of the different positions, and are comparable to the trends observed in the HRR data. Other than hotter temperatures towards the ceiling as to be expected, the main observation of interest is the lower temperatures in the front corner, distant from exposed timber, compared to the rear corner immediately adjacent to the exposed timber. This is particularly evident in experiment γ-1, where there is the most exposed timber and temperatures are highest. The erraticism in the α-1 data is due to the collapse of the thermocouple trees – after this event all TCs were lying on the floor and do not provide meaningful data.

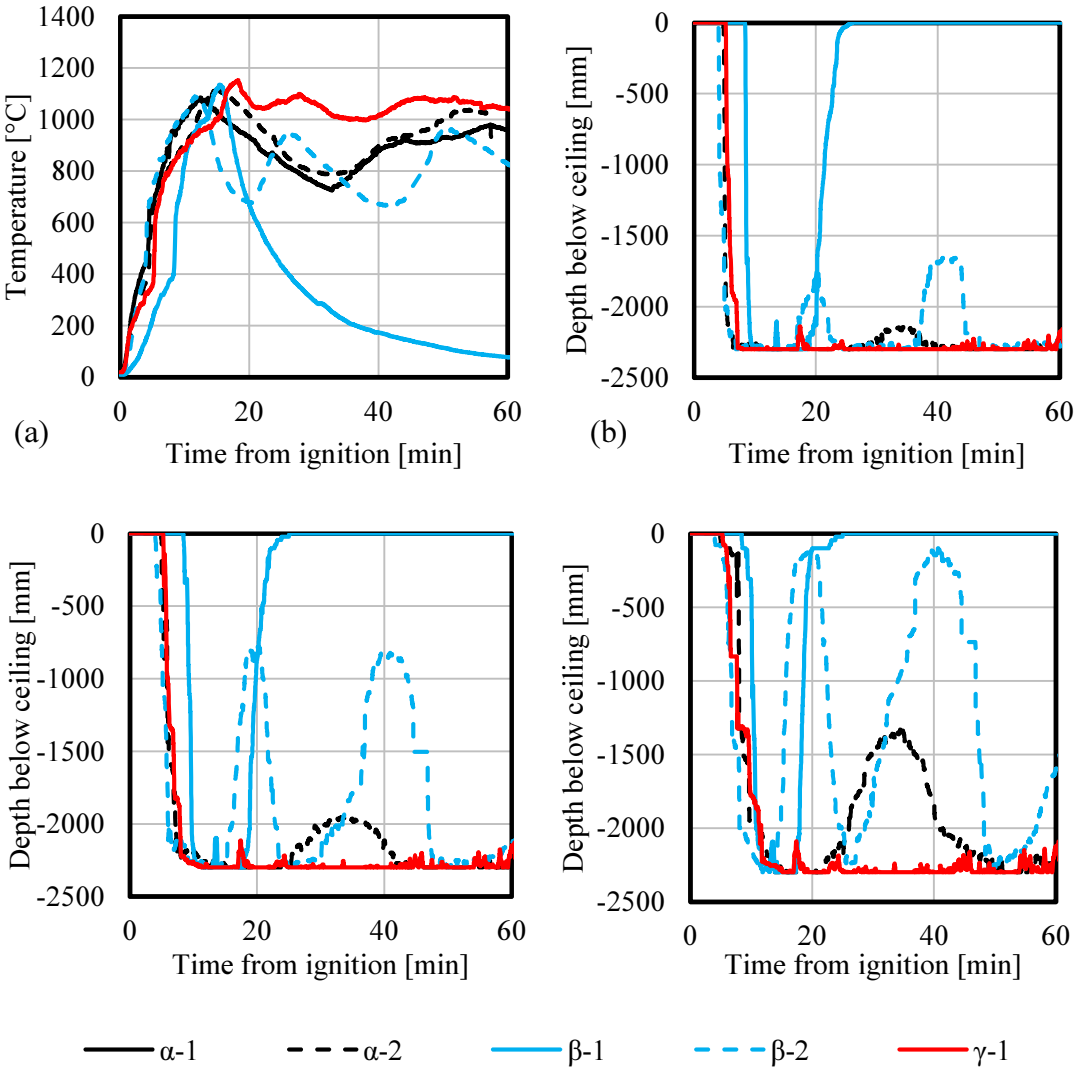

Figure 4.24: (a) Gas phase temperatures averaged over the whole compartment, (b) average height of 600°C isotherm below ceiling, (c) average height of 700°C isotherm below ceiling, and (d) average height of 800°C isotherm below ceiling.

4.4.5 Solid phase temperatures

The large quantity of solid phase temperature data is compared by looking at the thermal penetration, defined here as the position of the 300°C isotherm, at the centre of each exposed surface. This is shown in Figure 4.25. After 60 minutes, the 300°C isotherm (i.e. the char front) had penetrated approximately 50 mm in each case. This was independent of the fire dynamics where auto-extinction did not occur. As such, the continued propagation of this isotherm has significant implications for structural design.

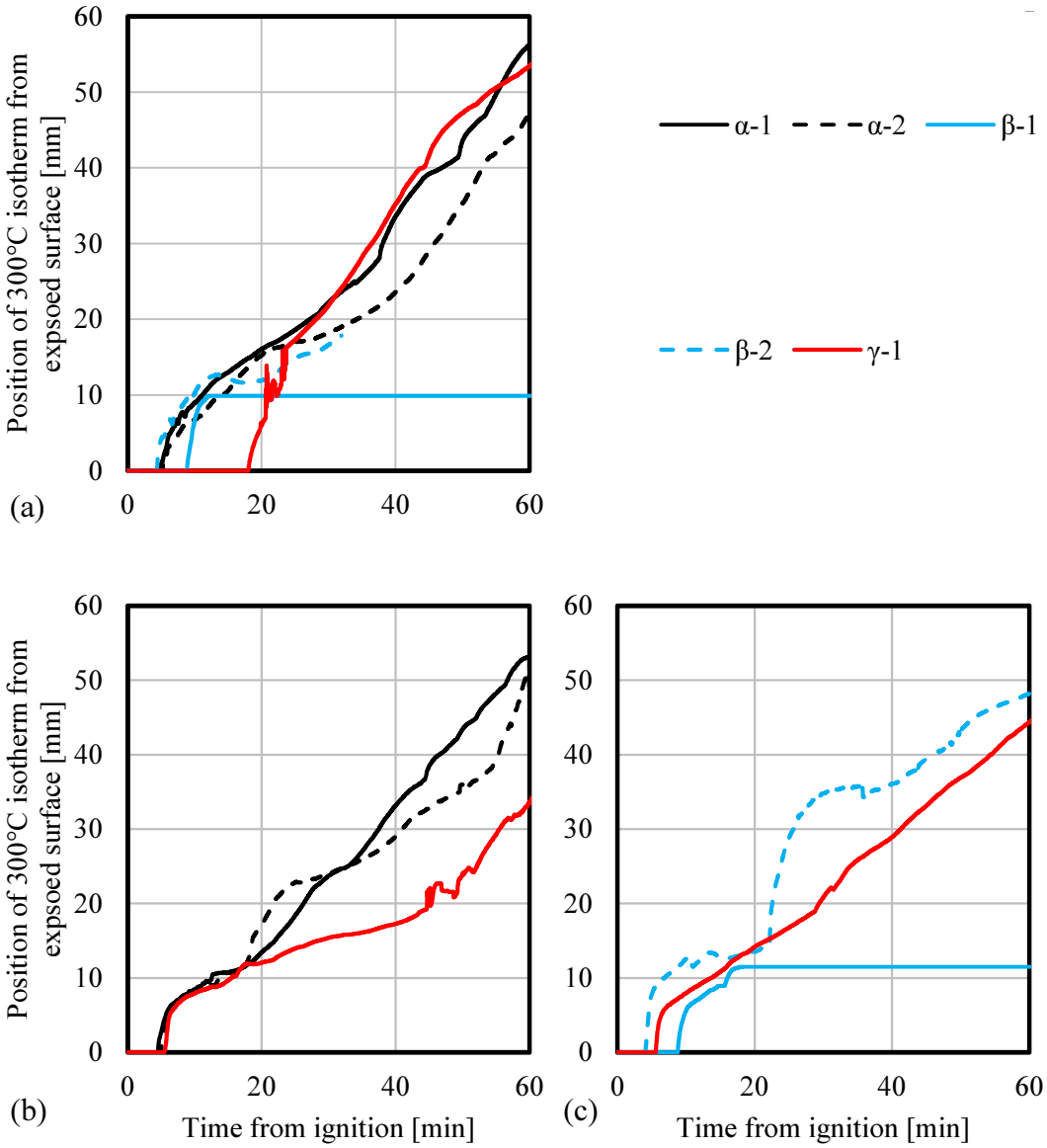

Figure 4.25: Thermal penetration (defined by 300°C isotherm) for (a) centres of back walls; (b) centres of side walls; (c) centres of ceilings.

4.5 Summary and initial conclusions

The purpose of this chapter has been to present an overview the full-scale experiments conducted and present some of the data collected; no quantitative conclusions can be drawn regarding the issues affecting auto-extinction. However, some initial conclusions based on qualitative data can be drawn.

1) Despite good repeatability between experiments of the same configuration, the uncertainties surrounding delamination mean that two drastically different outcomes have been observed from the same set of initial conditions in configuration β. Understanding the cause of these differences is of significant interest in moving towards a predictive model of auto-extinction for use in design.

2) A clear distinction can be seen between the fire dynamics of α- and β-configurations. Both β experiments tended towards extinction, whereas both α experiments decayed at approximately half the rate (~80 kW/min compared to ~160 kW/min) before reaching a quasi-steady burning rate. This is again hypothesised to be due to the "mode" of delamination, but this is again an area of further interest in terms of predicting auto-extinction.

It was clear that experiment γ-1 did not tend towards extinction, and there was indeed no significant decay in the HRR after the drop from the initial peak. This suggests that there is a critical area/number of surfaces of exposed timber with which auto-extinction can be achieved, which lies between 33% and 50% of the total internal surface area (in a cubic compartment).

Chapter 5 Application of Firepoint Theory to Full-Scale Compartment Fire Experiments

5.1 Introduction

Five full-scale compartment fire experiments were undertaken to explore the phenomena controlling auto-extinction at full scale. These experiments are discussed in detail in Chapter 4. One experiment, β-1, achieved auto-extinction, and the temperature data and heat flux measurements is used to develop an energy balance to quantify the auto-extinction phenomena based on the parameters obtained in Chapter 3. Whilst the approach is the same as for the bench-scale experiments described in Chapter 3, the approaches to quantifying the various parameters will differ. This captures the additional complexities brought about by length scale, orientation, and the fire environment.

5.2 Energy balance at char-timber interface

Due to the complexities and uncertainties in undertaking a full, global energy balance, firepoint theory can first be applied directly at the char-timber interface using the experimental results to determine if the relationship holds in full-scale applications where there are additional complexities. For direct application of Equation (3.2), the material properties L_v, ΔH_c, and ϕ must be determined, and the heat flux components calculated. The incident heat flux ($\dot{q}_e''$) can be approximated from the temperature data at the timber surface, and heat losses ($\dot{q}_l''$) estimated by summation of the radiative losses, convective losses, and the conductive losses into the sample. For an initial analysis with fewer assumptions however, Equation (3.2) can be generalised into Equation (5.1) to provide a more fundamental solution to the firepoint equation. This eliminates the need to estimate convective heat transfer, and removes the uncertainties associated with the heat flux data from the TSCs.

$$S = \dot{q}_f'' + \dot{q}_e'' - \dot{q}_l'' - L_p \dot{m}_{cr}'' \tag{5.1}$$

Combining all the heat flux terms to give a net heat flux ($\dot{q}_n''$), and setting *S* to zero to represent extinction gives Equation (5.2):

$$\dot{q}_n'' = L_p \dot{m}_{cr} \tag{5.2}$$

The net heat flux at the char line (the area of interest, as is this is the boundary of the reaction zone) can be solved by a simple energy balance, such that the net heat flux will be equal to the energy conducted through the char layer less the energy losses through conduction into the timber (neglecting radiation and convection from the char-timber interface). These heat fluxes can be obtained at a given timestep using a discretised version of Fourier's Law, assuming linear temperature gradients, along with the solid-phase temperature data, yielding Equation (5.3) (assuming a char formation temperature of 300°C):

$$\dot{m}'' = \frac{1}{L_p}\left(k_c \frac{T_c - 300}{\Delta x_c} - k_w \frac{300 - T_w}{\Delta x_w}\right) \tag{5.3}$$

where *k* is the thermal conductivity, *T* the temperature, and *x* the position, with subscripts c and w referring to the char and wood respectively. This equation was applied to each set of temperature measurement positions in the exposed wall and the exposed ceiling of experiment β-1. A char conductivity of 0.25 W/mK was assumed, and a timber conductivity of 0.18 W/mK [9]. A heat of pyrolysis of 1.1 kJ/g was assumed, as in Section 3.2. The char depth was found through cubic interpolation of the temperature profile [160]. The thermal gradients in the char and timber were calculated based on temperature data within the timber - T_c is the temperature recorded by the thermocouple in the char layer closest to the char line, and Δx_c is the distance from this thermocouple to the char line; similarly, T_w is the temperature recorded by the thermocouple in the timber closest to the char line, and Δx_w is the distance from this thermocouple to the char line. Temperature profiles with error bars in thermocouple position are shown in Figure 5.1.

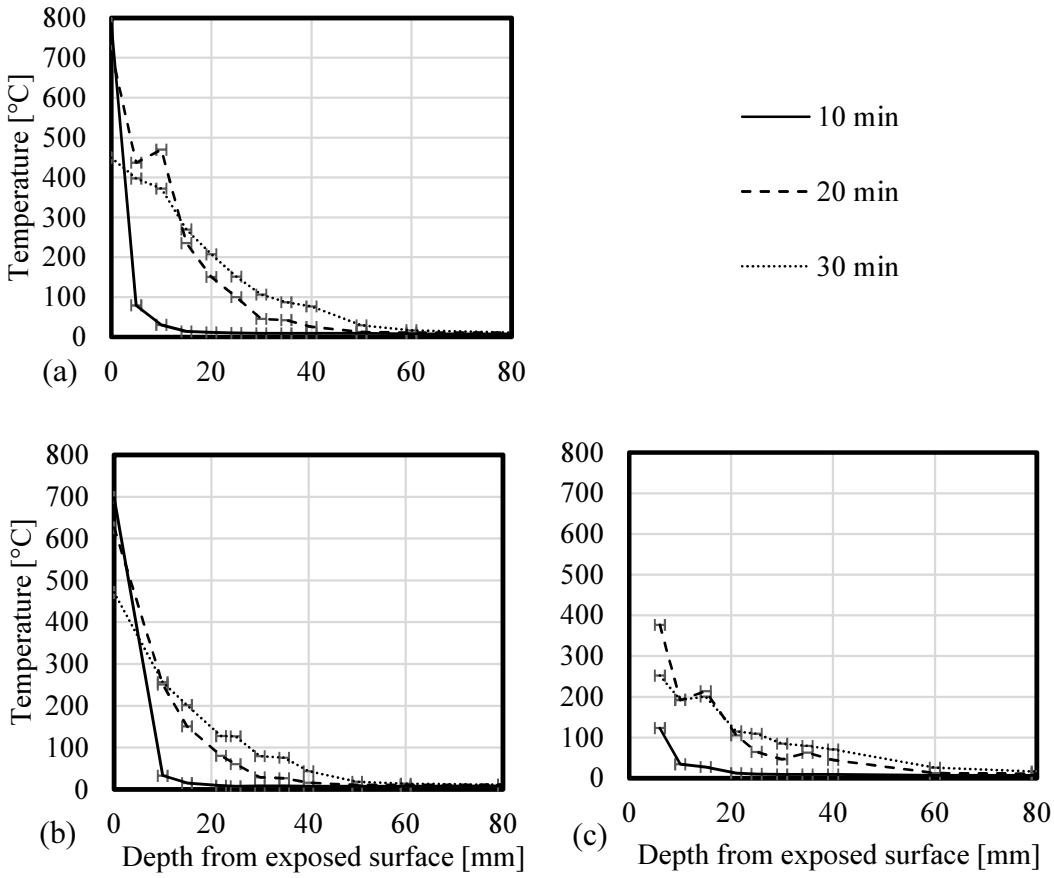

Figure 5.1: In-depth temperature profiles at positions (a) B21, (b) B23, and (c) B25 showing error bars in thermocouple positioning.

Even a slight error in thermocouple placement can result in significant differences in thermal gradients, as illustrated in Figure 5.2 for the centre of the wall at 20 minutes.

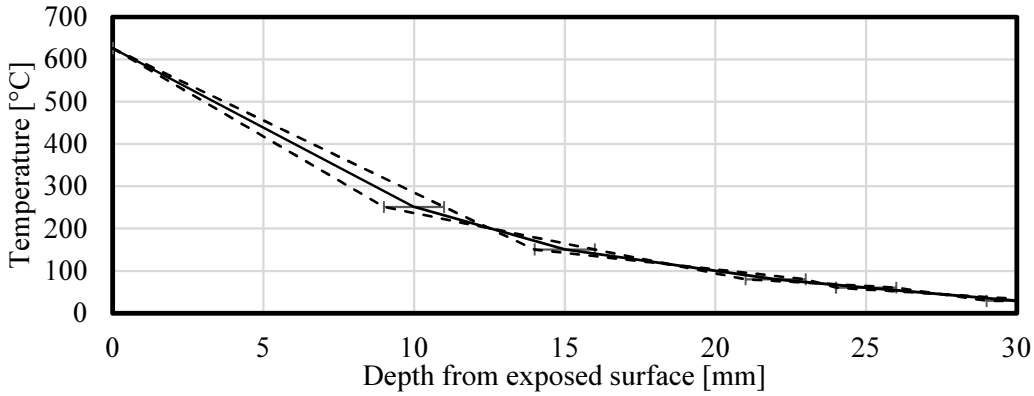

Figure 5.2: Errors associated with thermal gradients for position B3 at 20 minutes from ignition.

The resulting mass loss rates are presented in Figure 5.3 for the locations which provided meaningful results, with data for the right column of the back wall (in which only one location gave reliable results) shown in Figure 5.4. The method is very sensitive to anomalies in the data, and as such only a few locations provided meaningful results. The ceiling shows reasonable agreement across the different locations, however there is greater scatter evident in the data for the wall, with no apparent correlation due to position.

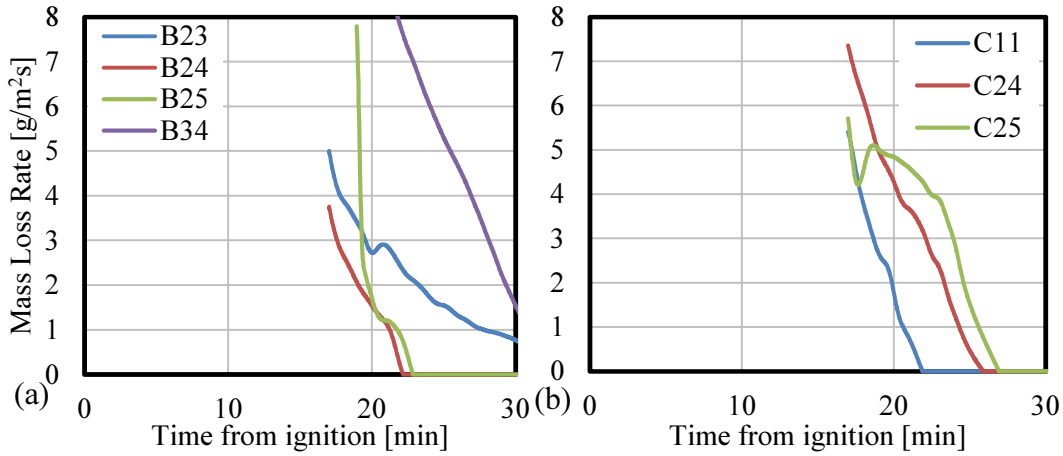

Figure 5.3: Variation in mass loss rate in experiment β-1 as calculated by firepoint theory for (a) exposed back wall, and (b) exposed ceiling.

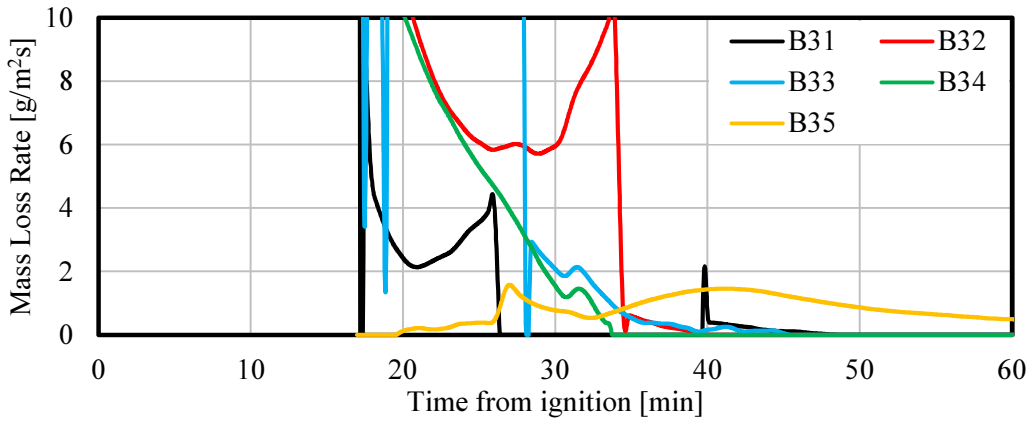

Figure 5.4: Variation in mass loss rate in experiment β-1 as calculated by firepoint theory for right column of back wall (including unreliable data).

The average mass loss rates are shown in Figure 5.5 (dashed lines) along with the critical mass loss rates determined from bench-scale experiments (Chapter 3). The values in Figure 5.5 are calculated over the locations (3 to 4 out of 13) shown in Figure 5.3, which were those with sufficient temperature resolution (i.e. a smooth temperature profile was measured) to apply Equation (5.3).

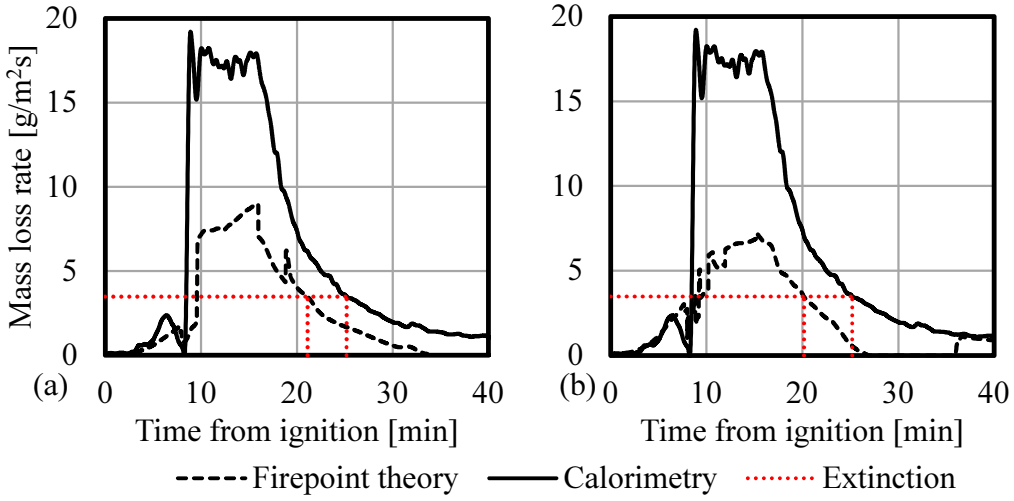

Figure 5.5: Calculated CLT mass loss rate at the (a) back wall and (b) ceiling for experiment β-1, with critical value from FPA experiments [5,6] indicated.

It can be seen from Figure 5.5 that the method is inherently robust – due to the steep gradient of the mass loss curve, small changes in the experimental values of critical mass flux will not lead to large changes in the predicted time to extinction.

To verify this method, the mass loss rate was also estimated from the calorimetry measurements. The HRR of the CLT was calculated from Equation (4.14), and the mass loss rate from Equation (5.4):

$$\dot{m}'' = \frac{\dot{Q}_{CLT}}{A\Delta H_c} \tag{5.4}$$

where the heat of combustion is assumed to be 17.5 MJ/kg [9, 11]. Estimating the burning rate from the ventilation conditions as defined by Thomas et al. [144] gives

11.2 g/m^{2}s, although this is strictly only valid for wood cribs. It is evident from Figure 5.5 that the energy balance approach and the calorimetry approach give significantly different values. As observed in Figure 5.3, significant relative errors in thermocouple placement (resulting in large relative errors in Δx in Equation (5.3)) result in large uncertainties in the firepoint theory approach. Despite these inherent uncertainties, and the resulting challenges in application, the above analysis demonstrates conceptually that the methodology is valid, and that the assumption of a critical mass loss rate of 3.48 g/m^{2}s obtained from the bench-scale experiments is valid.

Making an initial assumption of ambient oxygen concentration, this gives an extinction time of around 21 minutes for the wall, and around 20 minutes for the ceiling using firepoint theory. Using the values from calorimetry, this time is closer to 25 minutes in each case – whilst the differences in mass loss rate are significant, the differences in predicted time to extinction are smaller, and both approaches provide a reasonable estimation of extinction (± 3 minutes relative to experimentally observed extinction). Visual observations during the experiment showed that flaming on the exposed surfaces ceased at around 21 minutes, showing a very good correlation to the predictions of the energy balance approach. Extinction occurred gradually over 3-4 minutes, with external flaming reducing and the flaming area on the internal surfaces gradually decreasing. This suggests that firepoint theory can be used to predict auto-extinction in a compartment with timber surfaces, with critical mass loss rates determined from bench-scale experiments, if the inputs for Equation (3.2) are known with sufficient accuracy.

5.2.1 Effects of delamination

It should be noted that the CLT heat release rate and mass loss rate curves presented in previous sections are average values over the whole exposed surface. In reality, localised phenomena, such as delamination, could lead to higher mass loss rates locally. As discussed in Section 2.2.4, delamination is a phenomenon in which the outermost lamella, or part thereof, detaches from the lamella behind it, effectively reducing the char layer thickness at that position and thus increasing the net heat flux

(and thus mass loss rate) into the sample. After extinction was reached in experiment β-1, a small area towards the right side of the back wall delaminated at around 27 minutes into the experiment, as shown in Figure 4.11(c), leading to a locally increased mass loss rate and bringing the mass loss rate above the threshold for re-ignition. It is noteworthy that the delamination occurred locally, with only an area the width of one plank (about 200 mm wide) and approximately 500 mm tall detaching, and thus avoiding a secondary flashover, which would likely have occurred if the entire lamella had fallen off at once. This localised burning continued for approximately 25 minutes, before again reaching local extinction. During this time, a second area of similar size delaminated on the left side of the back wall, burning for approximately 20 minutes before again extinguishing. Neither of these small burning regions had significant effects on the total heat release rate, and the general downward trends in HRR, solid-phase temperature, and gas-phase temperature continued.

5.2.1.1 Relation to Firepoint Theory

Unfortunately, due to the small areas of re-ignition relative to the exposed surface area, this phenomenon was not captured at sufficient resolution by the solid phase temperature data, and thus only a qualitative analysis is possible. Current knowledge of delamination and its causes is limited, and thus it is not currently possible to accurately predict whether (or when) it will occur. Applying the firepoint equation to a delaminated area becomes more difficult due to the complex boundary conditions present; the boundary to consider is the front of the underlying lamella. A partially delaminated lamella, as observed in Figure 4.11(c), will partially shield the underlying timber from incoming radiation and also from radiation losses, whilst simultaneously re-radiating heat to the freshly exposed timber. This is a complex situation, the physics of which cannot be adequately captured by the current model. Additionally, the lack of char layer immediately after delamination will result in the same uncertainties as are present in the initial HRR peak, as discussed previously.

5.2.1.2 Delamination-Dominated Fire Dynamics

In the duplicate experiment β-2, the onset of delamination occurred before initial auto-extinction had been achieved, and the continued, localised delamination led to ignition of the second lamella, and auto-extinction was not achieved, similar to the findings of [154, 158]. The mass loss for experiment β-2, as calculated by Equation (5.4), is compared to that of experiment β-1 in Figure 5.6. Because of the delamination and the resulting, aforementioned changes in boundary conditions this caused, Equation (5.3) is inappropriate for this scenario. In Figure 5.6, times are adjusted such that t=0 is the time at which flashover occurred. It can be seen that both experiments follow similar trends for approximately the first 15 minutes, before the onset of delamination led to an increase in burning rate in experiment β-2, and before the delamination and re-flashover cycle then repeats twice. It can be seen from Figure 5.6 that the mass loss rate never drops below around 6 g/m^{2}s, and thus auto-extinction would not be expected based on the results in Chapter 3 and [98]. The same analysis for α and γ experiments is shown in Figure 5.7. Again, the mass loss rate remains significantly above the threshold for auto-extinction, and thus sustained burning is expected.

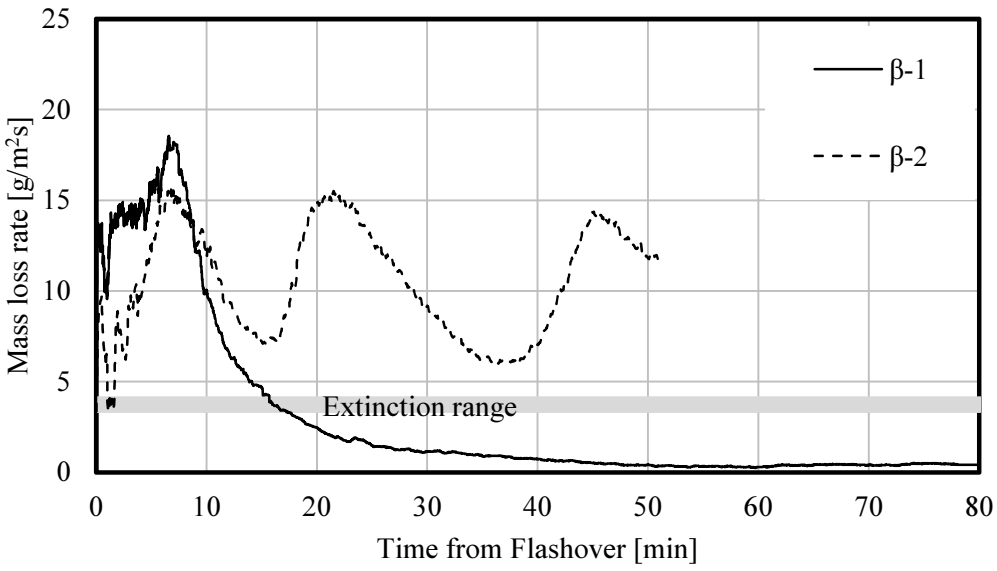

Figure 5.6: Comparison of calculated CLT mass loss rates determined from HRR data for both β-configuration experiments.

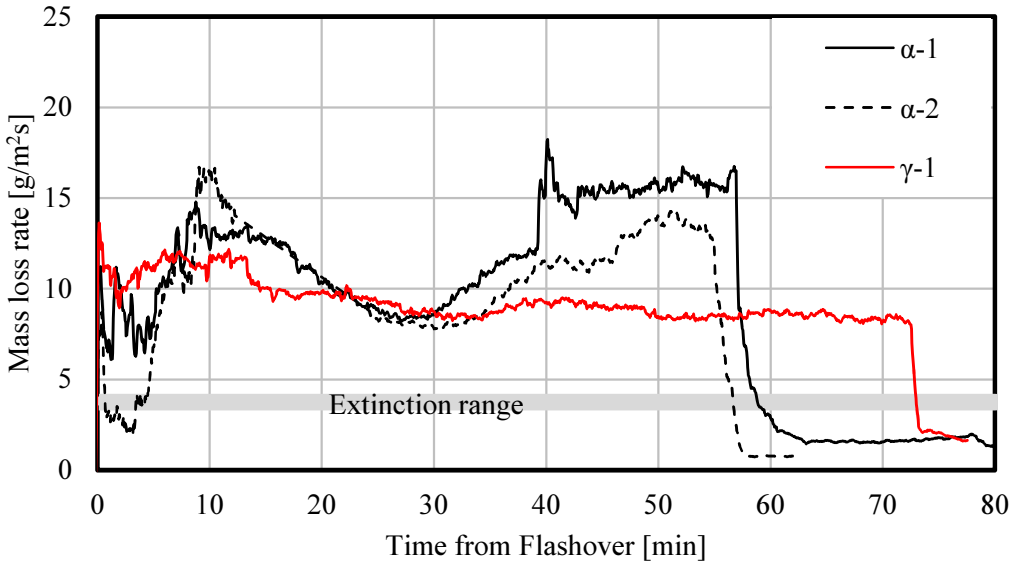

Figure 5.7: Comparison of calculated CLT mass loss rates determined from HRR data for both α-configuration experiments and experiment γ-1.

5.3 Energy balance at timber surface

Due to the shortcomings of the above model, an energy balance is explored to determine the net heat flux into the timber based on external measurements, and Equation (2.11):

$$\dot{m}''_{cr} = \frac{\dot{q}''_e + \dot{q}''_f - \dot{q}''_l}{L_v} \tag{2.11}$$

This is illustrated in Figure 5.8.

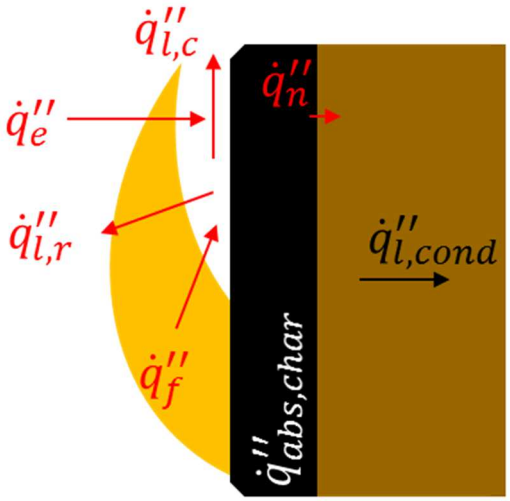

Figure 5.8: Energy balance at timber surface showing various heat transfer terms.

As the decay phase was observed to start at around 17 minutes after ignition, all subsequent analyses are shown from this point forward.

5.3.1 Incident heat flux

The first parameter in Equation (2.11) is the external heat flux, necessary to enable burning of a thermally thick wood sample [11]. This is measured in the experiment by thin skin calorimeters (TSCs) on the surface of the timber. These were calibrated as described in [169]. Surface regression due to char oxidation was not found to be significant from visual observations after the experiment, and as such, the heat flux values from the TSCs can be assumed to be valid. This gives an incident heat flux to the back wall as shown in Figure 5.9, approximately 25.3–30.5 kW/m^2 at 22 minutes, similar to the 30-31 kW/m^2 observed in the FPA. Figure 5.9 shows the average heat flux over the back wall, with maxima and minima shown. High variability is observed immediately post-flashover due to turbulence and the effects of the smoke layer. This variability then decreases, as the incident heat flux is driven by re-radiation from hot surfaces.

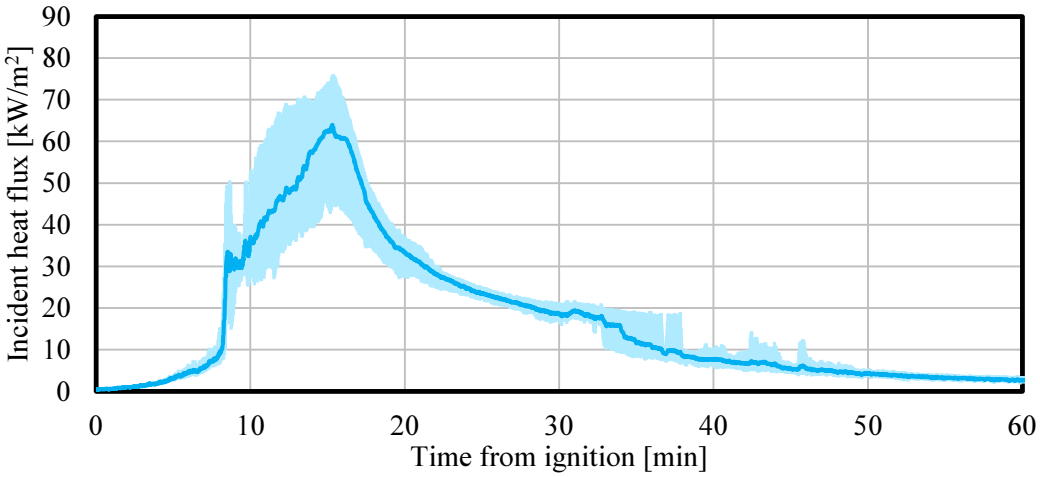

Figure 5.9: Incident heat flux averaged over back wall of experiment β-1 with maxima and minima shown.

5.3.2 Heat losses

The next parameter is the total heat losses from a burning surface. These can be broken down into: radiative losses to encapsulated surfaces, radiative losses through the opening, convective losses to the surroundings, conductive losses into the sample, and the heat absorbed by the char layer.

5.3.2.1 Radiative heat losses

The radiative losses from the timber surfaces can be calculated from Equation (5.5):

$$\dot{q}''_{l,r} = \varepsilon\sigma T_s^4 \tag{5.5}$$

where T_s is directly measured by the TSCs. This is the total heat emitted from the back wall – the heat received back from other hot surfaces is considered in the calculation of incident heat flux.

5.3.2.2 Convective losses from timber surface

Calculating the heat transfer coefficient within a compartment is extremely complex, and as such, several methods are used herein to determine the convective heat transfer

coefficient based on experimental data from experiment β-1. This is applied first to the back wall i.e. a vertical surface.

In the first instance, the convective heat transfer coefficient can be calculated by evaluating the Nusselt number over a vertical plate using Equation (5.6) [150]. This assumes free convection over a vertical surface for laminar or turbulent flow. It is not developed explicitly for application to compartment fires.

$$h_c = \frac{\left\{0.825 + \frac{0.387\left(\frac{g\beta\left(T_s - T_g\right)L^3}{\nu\alpha}\right)^{\frac{1}{6}}}{\left[1 + \left(\frac{0.492}{Pr}\right)^{\frac{9}{16}}\right]^{\frac{8}{27}}}\right\}^2 k}{L} \tag{5.6}$$

In this instance, L can be taken as the length of a piece of char, ~ 0.05 m. (This gives similar values if the height of the compartment, 2.77 m is used instead.) T_s is the surface temperature, taken from the TSCs on the back wall. T_g is the incoming gas temperature used to cool the compartment. This is assumed to be ambient air temperature, i.e. absorption of heat by the incoming air is neglected.

Secondly, Veloo and Quintiere [176] give experimental correlations for determining the convective heat transfer coefficient; given in Equation (5.7) for the decay phase. This was determined empirically for walls and ceilings of compartments with inert linings during the decay phase.

$$h_c = 9.9 \cdot 10^{-3} \frac{T_s - T_g}{T_g} \rho_g C_{p,g} \sqrt{gL} \tag{5.7}$$

Alternatively, a Reynolds number can be determined based on an assumed airflow velocity based on the inflow velocity determined by the pressure probes. Reynolds number can be calculated by Equation (5.8) [150]:

$$Re = \frac{vL}{\nu} \tag{5.8}$$

The friction coefficient and Nusselt number can then be calculated from Equations (5.9) and (5.10) [150]. This is valid for turbulent flows over an isothermal plate, where the Prandtl number is close to one.

$$C_f = 0.0592 Re^{-\frac{1}{5}} \tag{5.9}$$

$$Nu = \frac{C_f Re}{2} \tag{5.10}$$

Finally, a "direct" calculation can be made based on the energy flowing in and out of the compartment. This can be expressed through Equation (5.11):

$$\dot{q}_{l,c} = C_{p,out}\dot{m}T_{g,out} - C_{p,in}\dot{m}T_{g,in} \tag{5.11}$$

This is only applied during the decay phase, assuming change in gas temperature due to combustion is negligible. This can be expressed as a convective heat transfer coefficient by dividing by an area and the surface-gas temperature differential:

$$h_c = \frac{\left(C_{p,out}\dot{m}T_{g,out} - C_{p,in}\dot{m}T_{g,in}\right)}{A_{eff}(T_s - T_g)} \tag{5.12}$$

where A_{eff} is the effective area over which heat is lost through convection. Not all surfaces will receive equal effective cooling, and thus some approximation is necessary to provide a heat transfer coefficient. Initially it will be assumed that the air flowing in to the compartment flows across the floor, back wall, and ceiling before exiting the compartment again, and therefore the area of these three surfaces will be used for an initial estimate. The results obtained from each of these four methods are shown in Figure 5.10. It can be seen that there is significant variation between the methods, with the Reynolds number approach and vertical plate assumptions giving

very low coefficients, whereas the empirical approach from Veloo and Quintiere [176] and the gas balance approach give higher values. This is perhaps because the latter two approaches explicitly consider application to a compartment fire, whilst the first two approaches do not. As convective heat fluxes in a compartment are typically 10-40 W/m^{2}K [9], the empirical approach from Veloo and Quintiere [176] and the gas balance approach appear to be more accurate, and are thus used in the subsequent analysis.

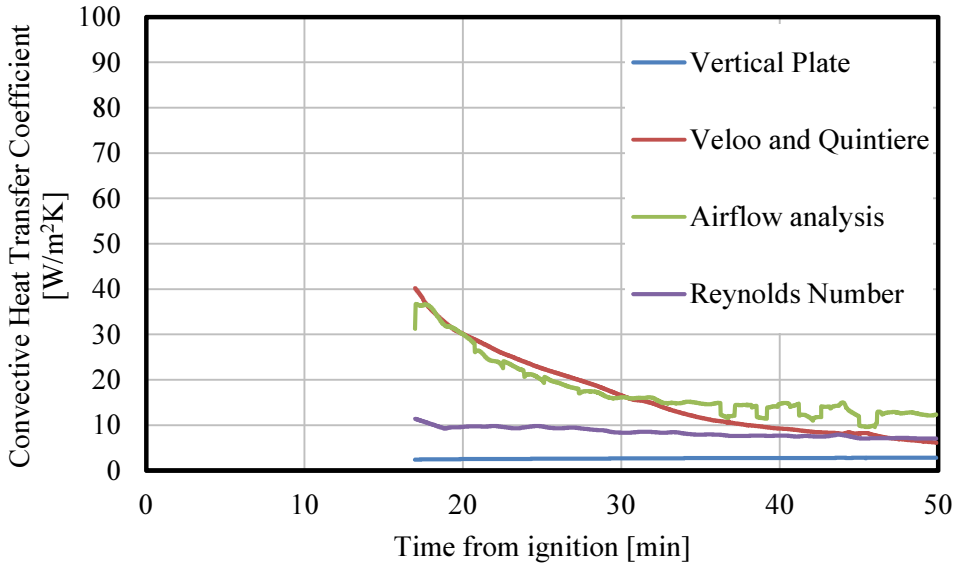

Figure 5.10: Convective heat transfer coefficient within compartment β-1 calculated by various methods

Convective heat losses can then be calculated from Equation (5.13):

$$\dot{q}''_{l,c} = h_c\left(T_s - T_g\right) \tag{5.13}$$

This is shown in Figure 5.11. It is evident that the two methods give very similar results, although there is no obvious reason for this, as Veloo and Quintiere [176] consider gas temperatures and air properties, but do not explicitly consider an energy balance of the airflow.

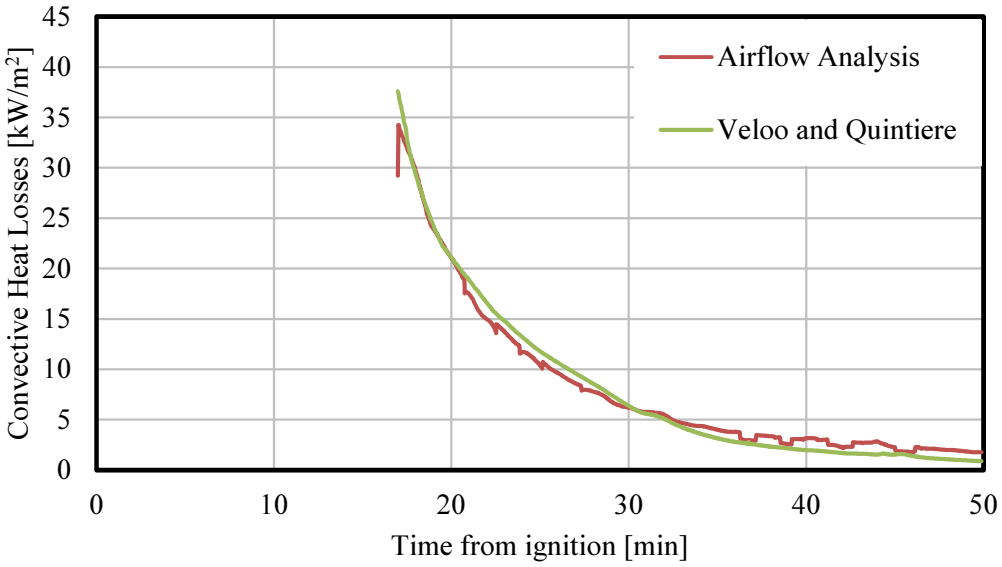

Figure 5.11: Convective heat losses within compartment β-1 calculated by various methods.

5.3.2.3 Conductive losses

Conductive heat losses can be calculated from Equation (3.15):

$$\dot{q}''_{l,cond} = -k_w \left.\frac{\partial T}{\partial x}\right|_{x=x_c} \tag{3.15}$$

where k_w is the thermal conductivity of the wood at the char line, taken as 0.18 W/mK [9]. This can be calculated as a function of time using solid phase temperature data. This is shown in Figure 5.12.

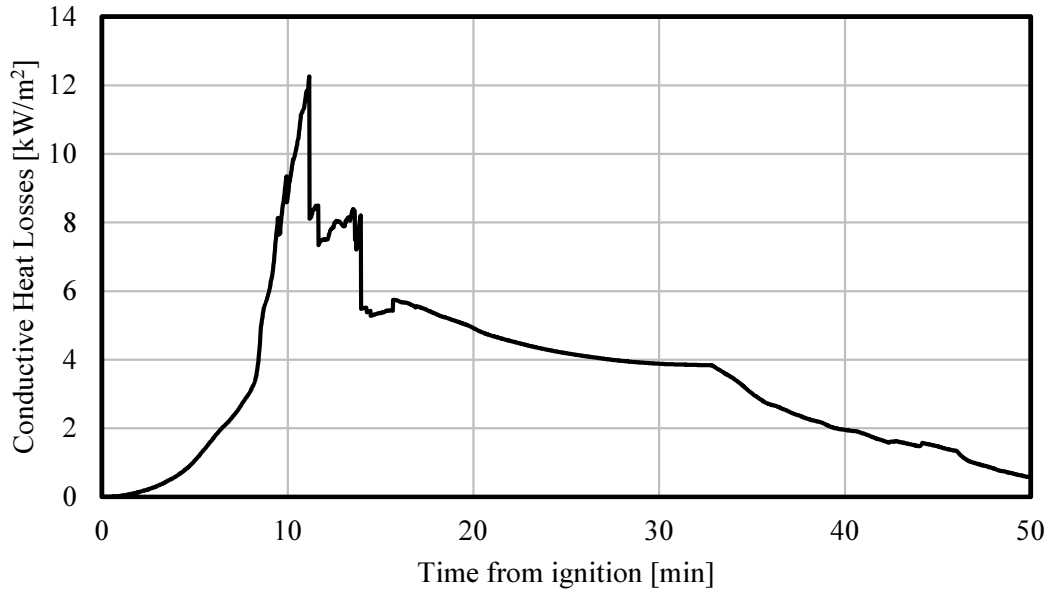

Figure 5.12: Conductive heat losses averaged over back wall as a function of time for experiment β-1.

5.3.2.4 Heat absorbed by char

Finally, the heat absorbed by the char layer can be estimated from Equation (3.17):

$$\dot{q}''_{abs,c} = \beta \int_{T_c}^{T_s} \rho(T) C_p(T) dT \tag{3.17}$$

where β is the experimentally-determined charring rate.

5.3.3 Heat flux from flames

The final parameter is the heat flux from the flames, which can be estimated using Equation (3.10) (from Rasbash et al. [88]):

$$\dot{q}''_f = \phi \Delta H_{c,n} \dot{m}'' \tag{3.10}$$

where ΔH_c can be taken as 17.5 MJ/kg ± 2.5 MJ/kg [11, 32]. is the mass loss rate of the CLT; to avoid an iterative approach, Equation (3.10) can be re-written:

$$\dot{q}_f'' = \frac{\phi \dot{Q}_{CLT}}{A_{exp}} \tag{5.14}$$

where A_{exp} is the exposed area, and ϕ is the proportion of energy from the flames transferred back to the surface and can be estimated through Equation (5.15) [88]:

$$\phi = \frac{Y_{ox}}{r\left(e^{\frac{C_{p,air}\dot{m}_{cr}''}{h_c}} - 1\right)} \tag{5.15}$$

where $C_{p,air}$ is the specific heat capacity of air, taken as 1.01 kJ/kgK [150], Y_{ox} is the mass concentration of oxygen in air (0.23 at ambient oxygen concentration), r is the stoichiometric ratio of oxygen to fuel (taken as 3.43 [88]) and h_c is the convective heat transfer coefficient.

The heat flux from the flames can now be calculated from Equation (5.14). This gives the heat fluxes as shown in Figure 5.13. It should be noted that the correlation in Equation (5.14) is only valid when flames are approaching extinction (i.e. the period of interest).

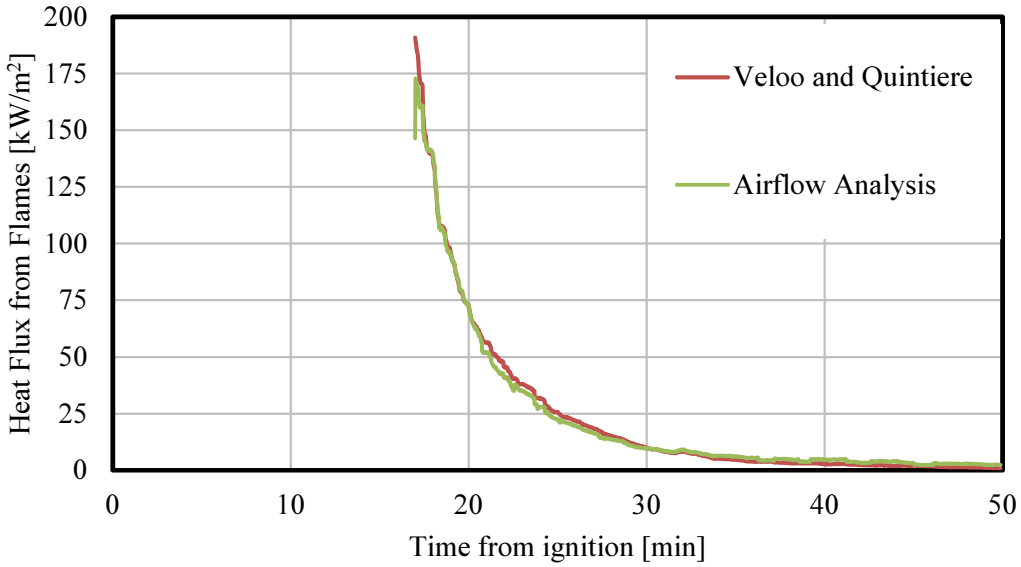

Figure 5.13: Heat flux from flames within compartment β-1 calculated by various methods.

5.3.4 Application of energy balance

These factors can now be combined to give the net heat flux, which can be compared to the critical net heat flux for extinction, equal to $L_v \dot{m}''_{cr}$. Using values from Chapter 3, this gives the values shown in Figure 5.14. This is plotted using the values from the airflow analysis; due to the aforementioned similarities, using the values calculated from Veloo and Quintiere's [176] method yield similar results. The energy balance again predicts the mass loss rate dropping below the critical value for extinction, but this time at around 45 minutes. This differs significantly from the local energy balance undertaken and from the visual results. This is likely due to the large uncertainties associated with many of the terms in the energy balance – convective heat losses and the heat flux from the flames have significant error bars – this variation can be visualised in Figure 5.10. The governing term in the calculation of the convective heat transfer coefficient is the airflow velocity into the compartment. The pressure transducers are accurate to ± 1% of the total range, which at the point of extinction, results in relative errors in velocity of up to 26%.

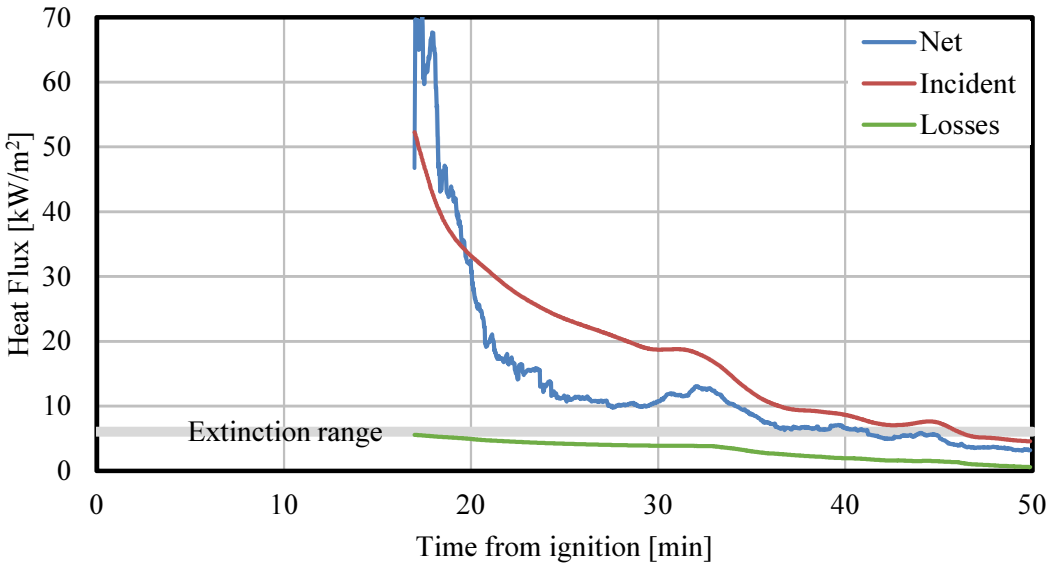

Figure 5.14: Incident heat flux, heat losses, and net heat flux at the charline averaged over the back wall for experiment β-1. Extinction range shows the critical net *heat flux for extinction.*

The resulting mass loss rate is shown in Figure 5.15.

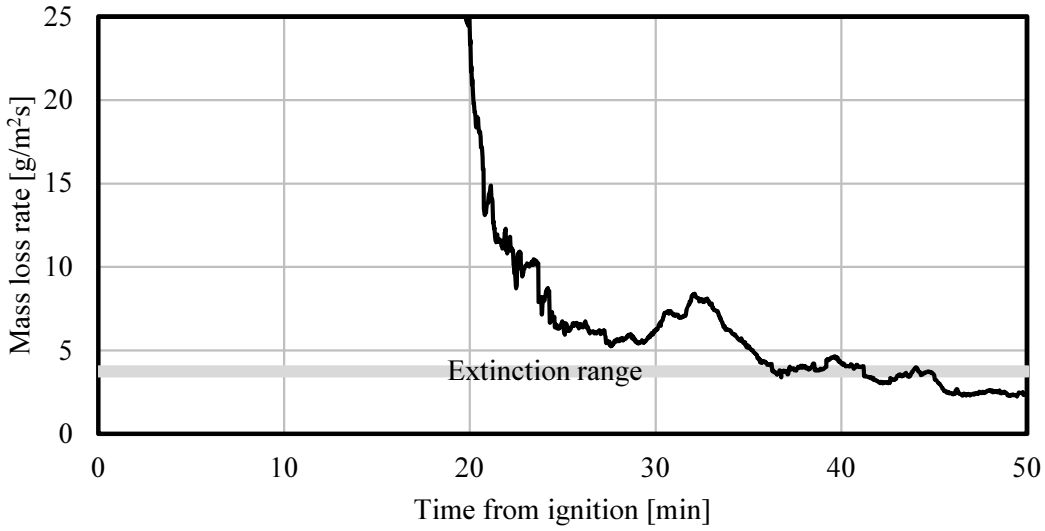

Figure 5.15: Mass loss rate for experiment β-1 as calculated by a global energy balance.

5.3.5 Experiment β-2

The same analysis can be attempted for the repeat experiment, β-2, which did not auto-extinguish. Due to data acquisition issues, the data necessary for the analysis is only valid for the first 32 minutes. The results are shown in Figure 5.16. The predicted mass loss rate does not drop below the critical value of 3.48 g/m^{2}s – however the values are much higher than those predicted by calorimetry in Figure 5.6.

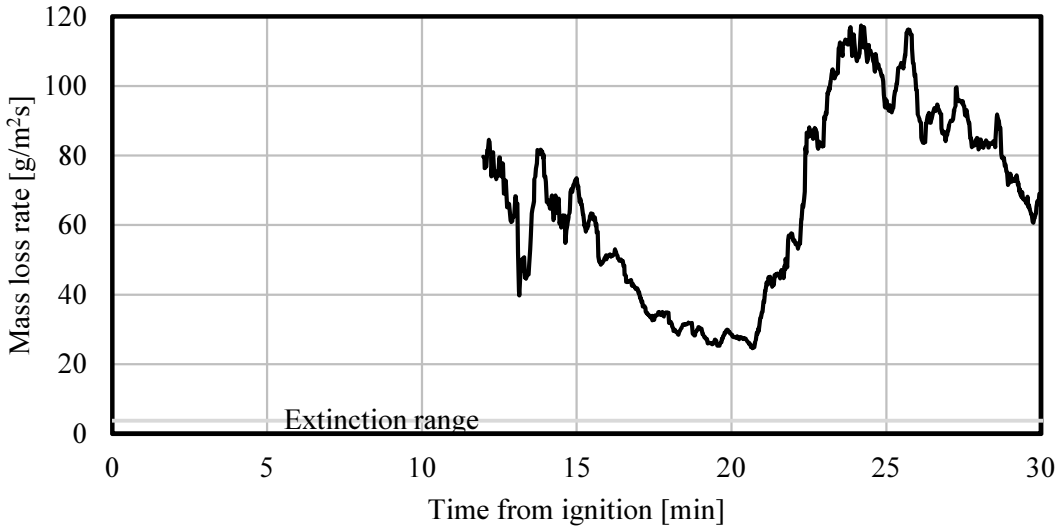

Figure 5.16: Mass loss rate for experiment β-2 as calculated by a global energy balance.

5.4 Conclusions and Further Work

It can be seen from the above experiments that auto-extinction of timber in full-scale compartments can occur if delamination does not occur and the encapsulation of unexposed surfaces remains in place. From the analyses presented above, the critical mass loss rate of 3.48 g/m^{2}s obtained from bench-scale experimentation appears to be applicable to full-scale compartment fires, as experiments which did not drop below this value underwent sustained burning, however further data are needed to verify this. This can be expressed by the logic diagram in Figure 5.17.

In all experiments, the imposed fuel load burned out in around 15 minutes, significantly before the time needed for structural collapse.

Experiment β-2 did not experience encapsulation failure, and was seen to tend towards auto-extinction, however delamination prevented this from occurring.

Due to the stochastic nature of delamination, which cannot be adequately accounted for, preventing delamination is a logical approach in order to successfully design for auto-extinction. This is explored more thoroughly in Chapter 6.

Experiment β-1 did not have encapsulation failure, and no significant delamination was observed. The mass loss rate was therefore able to drop below 3.48 g/m^{2}s, resulting in auto-extinction.

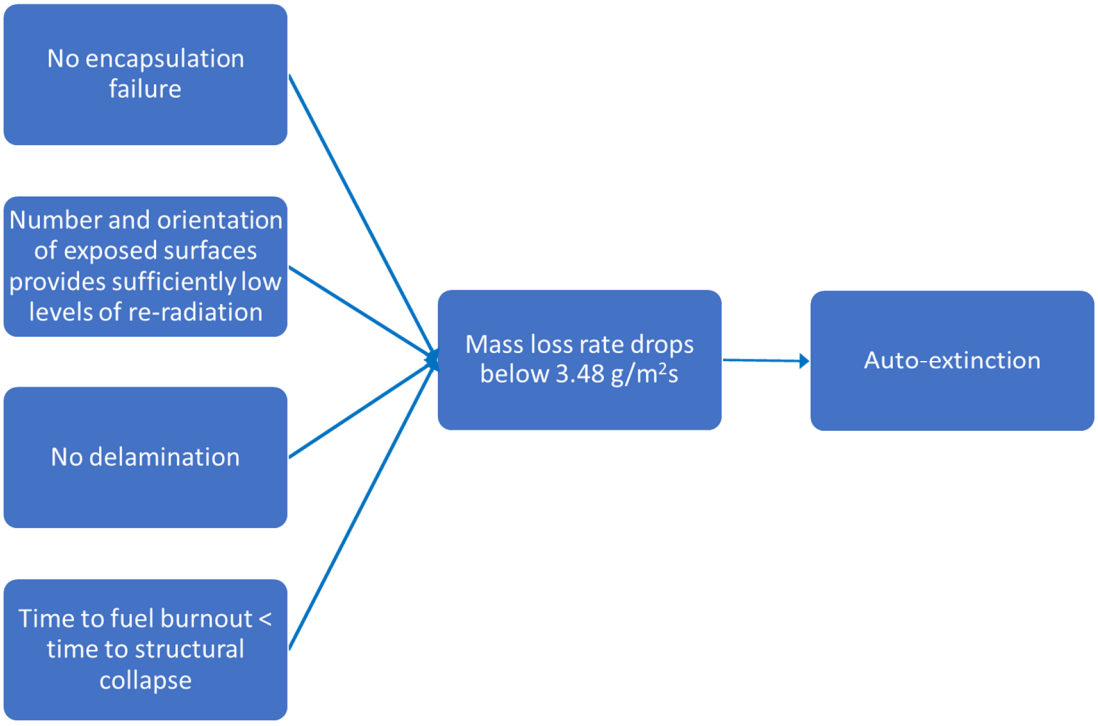

Figure 5.17: Logic diagram showing conditions necessary for auto-extinction.

Two energy balances were employed in an attempt to model the evolution of mass loss rate. The local energy balance described in Section 5.2 showed some success in predicting the mass loss rate. However due to limitations in boundary conditions, it is not appropriate for modelling fires in which delamination occurs. Furthermore, it is extremely sensitive to anomalies in the data, and is therefore unlikely to be suitable for robust analysis and prediction of auto-extinction. In particular, the errors in thermocouple placement, whilst kept relatively small at ± 1 mm, were too large for successful application of this approach. Whilst this method was shown to work conceptually, the sensitivity to thermocouple positioning creates significant challenges in its suitability for design application.

A global energy balance, theoretically less sensitive to delamination, was also unsuccessful in accurately predicting the evolution of mass loss rate. This can be mostly attributed to large uncertainties in obtaining the convective heat transfer coefficient, on which the heat flux from the flames and the convective heat losses are dependent. Due to a lack of data generally in convective heat transfer within

compartments [176], and particularly with exposed combustible surfaces, the error bars associated with the convective heat transfer coefficient, and thus the next heat flux and mass loss rate are deemed too large for this method to be useful at the present time.

Whilst both methods work conceptually, due to inherent uncertainties, a detailed firepoint theory analysis cannot currently be used for predicting auto-extinction in the context of a compartment fire. It is evident that delamination is key in preventing or enabling auto-extinction, and as such will be the focus of the next chapter. In order to verify the applicability of fundamental extinction criteria, direct measurements of mass loss rate will also be made.

Chapter 6 Intermediate-Scale Compartment Fire Experiments with Exposed Timber Surfaces

6.1 Introduction and Background

It has been demonstrated in the preceding chapters that auto-extinction can be achieved in full-scale compartment fires, and a methodology has been developed to allow calculation using firepoint theory if the uncertainties can be reduced sufficiently. These uncertainties include the influence of fuel load, the causes of delamination, the effects of configuration, and the influence of the opening factor. It was demonstrated in Chapters 4 and 5 that in order for auto-extinction to be achieved: the encapsulation must remain in place, delamination must be prevented and, the radiative feedback from one exposed surface to another must be limited. It can be hypothesised that delamination can be prevented if the outer lamella is sufficiently thick – i.e. the imposed fuel load can burn out before the thermal penetration is sufficient to induce failure at the glue line. To test this hypothesis, a series of reduced-scale experiments was undertaken, to explore the relationship between fuel load and outer lamella thickness.

It was seen from the full-scale experiments that configurations with an exposed wall and ceiling extinguished or tended towards extinction whereas configurations with two exposed walls did not. Both these configurations were explored further at intermediate-scale to attempt to quantify the differences between the configurations, and to see if auto-extinction is possible with two exposed walls as a function of the fuel load.

6.2 Scaling Approach

In order to scale the full-scale compartment to a reasonably sized laboratory-scale compartment, it was desired to keep the following two components constant: 1) aspect ratio – the interior was kept approximately cubic to keep the same configuration factors from one surface to another; 2) opening factor – this was kept the same to allow the same regime of burning [144].

6.3 Experimental Programme

A total of seven experiments were carried out with three different configurations of exposed timber – configurations α and β as described in Chapter 4, and a fully encapsulated compartment, to obtain a "baseline" case. 78 mm thick CLT panels with layup 19 mm, 40 mm, 19 mm were used for all surfaces, with the exception of experiment β-6, in which a 140 mm thick panel with layup 34 mm, 19 mm, 34 mm, 19 mm, 34 mm was used for the back wall and a 182 mm thick panel with layup 34 mm, 40 mm, 34 mm, 40 mm, 34 mm was used for the ceiling. Wall panels were of dimensions 800 mm x 700 mm, and ceiling panels 900 mm x 900 mm. An opening 300 mm wide and 400 mm high was cut in the panels to be used for the front of the compartments. Due to a manufacturer error in the positioning of the door, the same overlap configuration as used for the full-scale experiments was not possible. Instead, the layout as shown in Figure 6.1 was used. The same encapsulation system was used as detailed in Section 4.2.

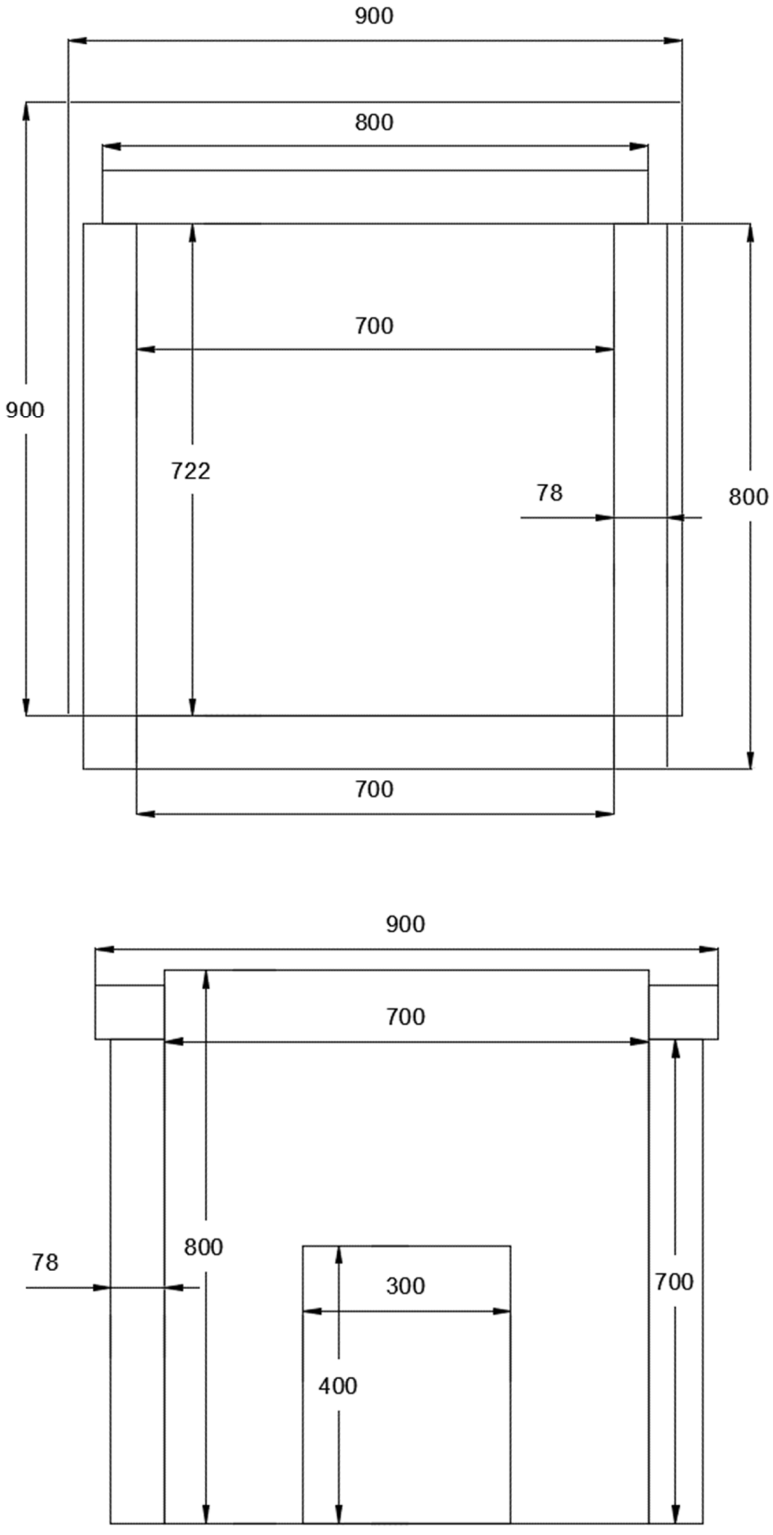

Figure 6.1: Section view (top) and elevation (bottom) of compartment. All dimensions in mm.

One completely encapsulated experiment was carried out, as well as two experiments in configuration α, three in configuration β, and one in configuration β with thick panels. The full dimensions for each different configuration are given in Table 6.1. Opening dimensions in each case were 300 mm x 425 mm, thus having an area of 0.1275 m^2.

Table 6.1: Internal and opening dimensions of compartments.

Configuration	Encapsulated	α	β
Width [mm]	575	637.5	575
Depth [mm]	597	659.5	659.5
Height [mm]	637.5	637.5	700
Opening factor [$m^{-1/2}$]	20.6	23.4	23.8

The opening factors as defined by Thomas and Heselden [144] for the medium-scale compartments are thus very similar (within 20%) to those in the full-scale compartments, however the variation between configurations is larger due to the increased thickness of the encapsulation build up as a proportion of the compartment area.

6.3.1 Fuel Load

Wood cribs were used as the fuel load, with the fuel load per unit area the same as that used for the full-scale experiments. As it has been hypothesised that auto-extinction will occur only if the thermal penetration is sufficiently low, three different fuel loads were used – a "low" fuel load of ~ 119 MJ/m^2 (approximately equal to that used in the full-scale experiments), a "medium" fuel load of ~235 MJ/m^2, and a "high" fuel load of ~656 MJ/m^2 – to explore the effects of different thermal penetrations on auto-extinction. As the opening factor for all experiments is the same, the burning duration will be controlled by the fuel load; increasing the fuel load will increase the burning duration, and thus the thermal penetration depth. The fuel load used in each experiment is shown in Table 6.2. The cribs used thinner sticks than those in the full-scale experiments – sticks of thickness 15 mm and length 500 mm were used, with 11 sticks per layer. This may result in a higher burning rate than the cribs used in the full-scale compartments [11]. As before, the decay phase is the period of interest, so differences

in growth rate are not of primary importance. Cribs were ignited by three heptane-soaked cardboard strips of dimensions 10 mm x 550 mm.

Table 6.2: Fuel load used in each intermediate-scale compartment fire experiment.

Experiment	Fuel load per unit floor area
Fully encapsulated	Low – 115.2 MJ/m^2
α-3	Medium – 221.9 MJ/m^2
α-4	Low – 112.4 MJ/m^2
β-3	Low – 130.1 MJ/m^2
β-4	Medium – 248.0 MJ/m^2
β-5	High – 652.4 MJ/m^2
β-6	High – 659.6 MJ/m^2

It is hypothesised that auto-extinction *can* occur if the compartment fuel load burns out before the first lamella delaminates – as such, it is expected that lower fuel loads are more likely to result in auto-extinction, and thicker lamellae are also more likely to result in auto-extinction.

6.3.2 Instrumentation

The instrumentation used for these experiments is very similar to that described in Section 4.2.2; the deviations from the full-scale experiments will be described here.

6.3.2.1 Gas phase temperature measurements

Five thermocouple trees with six thermocouples apiece were used in each compartment. These were placed at 20 mm, 30 mm, 35 mm, 40 mm, 50 mm, and 60 mm from the floor. One tree was placed in the centre of the compartment, and the other four were arranged at the corners of a 287.5 mm square around it.

6.3.2.2 Solid-phase temperature measurements

Five thermocouple bundles were placed in each exposed surface, arranged with one in the centre, and one at each corner. This grid was centred on the internal exposed area of the wall. Each bundle comprised nine thermocouples which were inserted at depths of 5 mm, 10 mm, 15 mm, 20 mm, 25 mm, 30 mm, 40 mm, 50 mm, and 60 mm. The thermocouple positions are shown in, with detailing shown in Figure 6.2 and Figure

6.3. Two additional thermocouples were inserted at each position at depths of 80 mm and 100 mm for experiment β-6 because of the increased thickness of the panels.

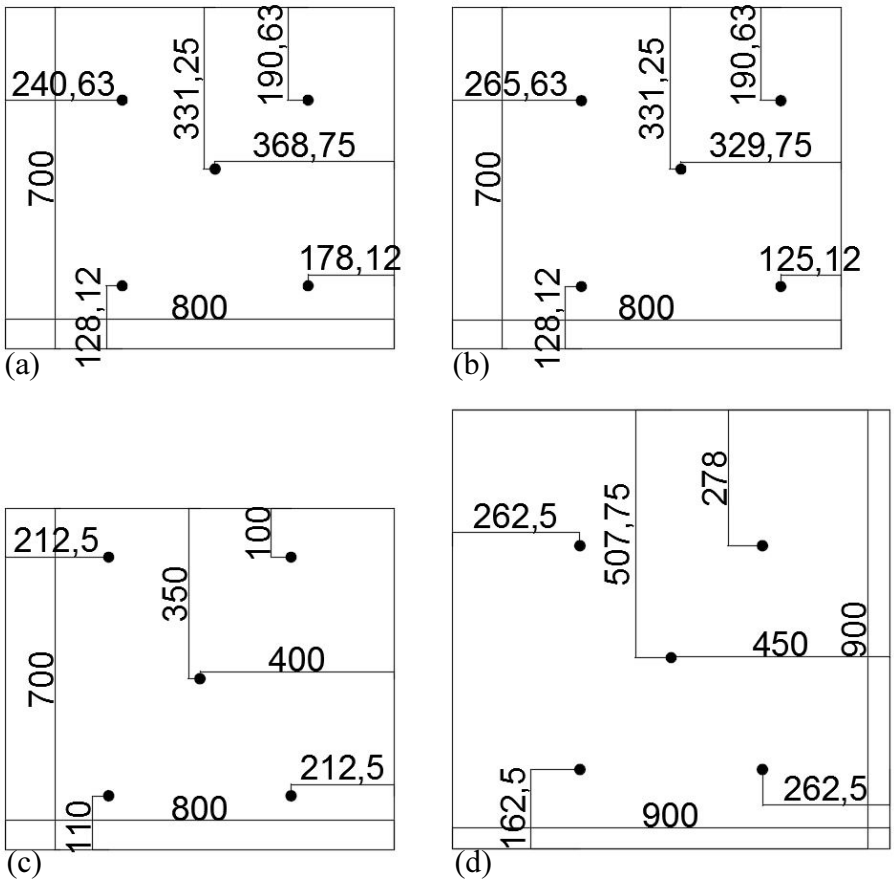

Figure 6.2: In-depth thermocouple layouts for (a) exposed back wall for configuration α; (b) exposed side wall for configuration α; (c) exposed back wall for configuration β; (d) exposed ceiling for configuration β. All dimensions in mm from timber-timber interfaces (encapsulation not considered).

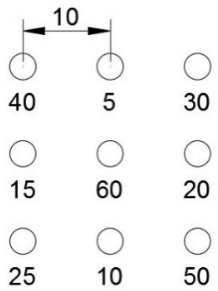

Figure 6.3: Detailed thermocouple positioning. All dimensions in mm Numbers adjacent to thermocouples indicate distance from exposed surface.

In-depth thermocouples were inserted in encapsulated surfaces at 5 mm, 10 mm, and 20 mm from the timber-plasterboard interface at locations detailed in Figure 6.4.

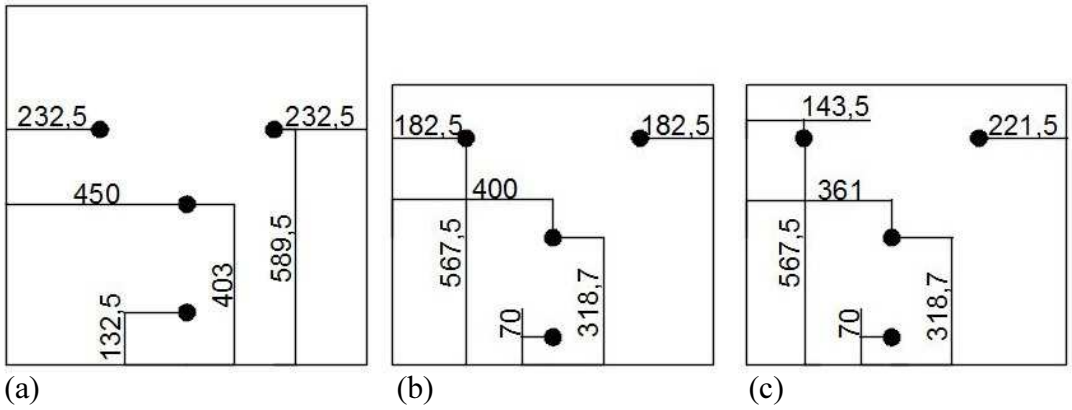

Figure 6.4: In-depth thermocouple layouts for (a) encapsulated ceilings, (b) encapsulated back wall, (c) encapsulated side walls. All dimensions in mm from timber-timber interfaces (encapsulation not considered).

6.3.2.3 Gas flow measurements

Pressure probes were not used in these experiments, as theoretical methods predicting the mass flow in/out of the compartment from gas temperature and burning rate from the full-scale experiments defined in Section 4.2.2.4 were found to be sufficiently accurate. Thermocouples were placed in the doorway at heights of 20 mm, 30 mm, and 35 mm from the floor.

6.3.2.4 Compartment mass measurements

The compartment was placed on a load cell to measure the mass loss rate. In the latter stages of the fire, this corresponds directly to the mass loss rate of the CLT. The same load cells as described in Section 4.2.2.5 were used for the majority of the experiments, with a Mettler Toledo IND429 (accuracy of ±1 g) used for the fully encapsulated experiment. A layer of vermiculite board and 2-3 layers of mineral wool were placed between the scale and the compartment to protect the load cell.

6.3.2.5 Combustion gas composition

The entire compartment was built underneath a furniture calorimeter. Oxygen, carbon dioxide, and carbon monoxide concentrations were measured as previously to determine the heat release rate.

6.3.2.6 Infrared imaging

No infrared imagery was recorded for these experiments.

6.3.2.7 Visual data

The three video cameras were positioned as described in Section 4.2.2.8. In experiment α-4, a DSLR camera with a timer was positioned low down in front of the opening focused on the back and ceiling to observe any local differences in flaming. In experiments β-4 and β-5, this was replaced with a fourth HD video camera.

6.4 Experimental Narrative

A description of each experiment is given below, as in Section 4.3. Key events are summarised in Table 6.3. Heat release rate and mass loss data are discussed for each experiment. The impact of this on the thermal penetration is discussed in Section 6.6. In each experiment where auto-extinction was not achieved, the fire was manually supressed when burn-through of the CLT panels was evident.

Table 6.3: Summary of reduced-scale compartment fire experiments

	Approximate time after ignition [min]						
Event	Encapsulated	α-3	α-4	β-3	β-4	β-5	β-6
Flashover	2.2	2.5	4.8	5.8	7	5.4	5.2
Time to peak HRR	8.5	14.8	11.9	13.4	17.6	44.3	48.4
Reduction in burning rate	10.6	20	14, 53	16	19	62	56
Increase in burning rate	n/a	81	32-43	n/a	n/a	n/a	n/a
Auto-extinction	(17.6)	n/a	28-30	21-22	38-39	n/a	n/a
Manual suppression	n/a	107	102	n/a	n/a	113	220

6.4.1 Fully Encapsulated Experiment

The heat release rate of the fully encapsulated experiment is shown in Figure 6.5. Total heat release rate was calculated using Equation (6.1), as measurements of carbon monoxide and carbon dioxide were not available for some of the experiments.

$$\dot{Q} = E\frac{\phi}{1+\phi(\alpha-1)}\dot{m}_e\frac{M_{O_2}}{M_{air}}\left(1-X_{H_2O,air}-X_{CO_2,air}\right)X_{ox,air} \tag{6.1}$$

where ϕ is calculated from Equation (6.2):

$$\phi = \frac{X_{ox,air}-X_{ox,et}}{(1-X_{ox,et})X_{ox,air}} \tag{6.2}$$

No failure of plasterboard was observed, and after the experiment, no thermal damage to the timber was evident. It can be seen from Figure 6.5 that the fully encapsulated experiment has a much lower HRR (~50%) peak, which can be attributed to the lower amount of available fuel.

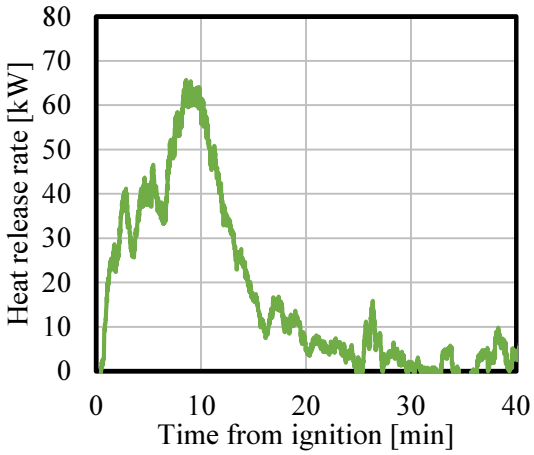

Figure 6.5: Heat release rate of fully encapsulated experiment.

6.4.2 Experiment α-3

The heat release rates and mass loss rates of experiments α-3 and α-4 are shown in Figure 6.6, along with the extinction range from Chapter 3 and [98]. Mass loss rate was calculated using the data from the load cell. 300-point LOESS smoothing was then applied to reduce the noise in the data. This was selected in order to adequately capture the maxima and fluctuations but minimising noise. This value was then divided by the exposed area to determine the mass loss rate per unit area of CLT. This calculation method is only valid after the wood cribs have burned out, as the exposed crib area is not considered. As the decay phase is the period of interest, this is not an issue for auto-extinction analyses.

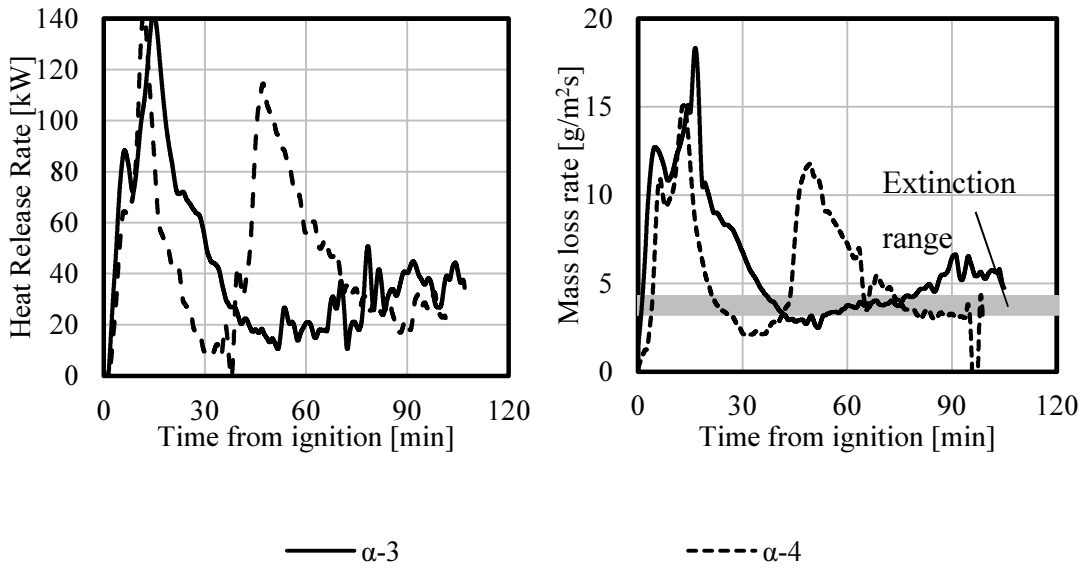

Figure 6.6: Total heat release rate and mass loss rate for each intermediate-scale compartment fire experiment undertaken in configuration α.

Key events are shown in Figure 6.7. After cessation of external flaming, localised flaming continued on the exposed timber surfaces, as shown in Figure 6.7(c), before, a secondary flashover lead towards a restart of external flaming. External flaming was less severe (flames extending ~20-40 cm rather than ~60-80 cm above the opening) than in the first post-flashover period, shown in Figure 6.7(d).

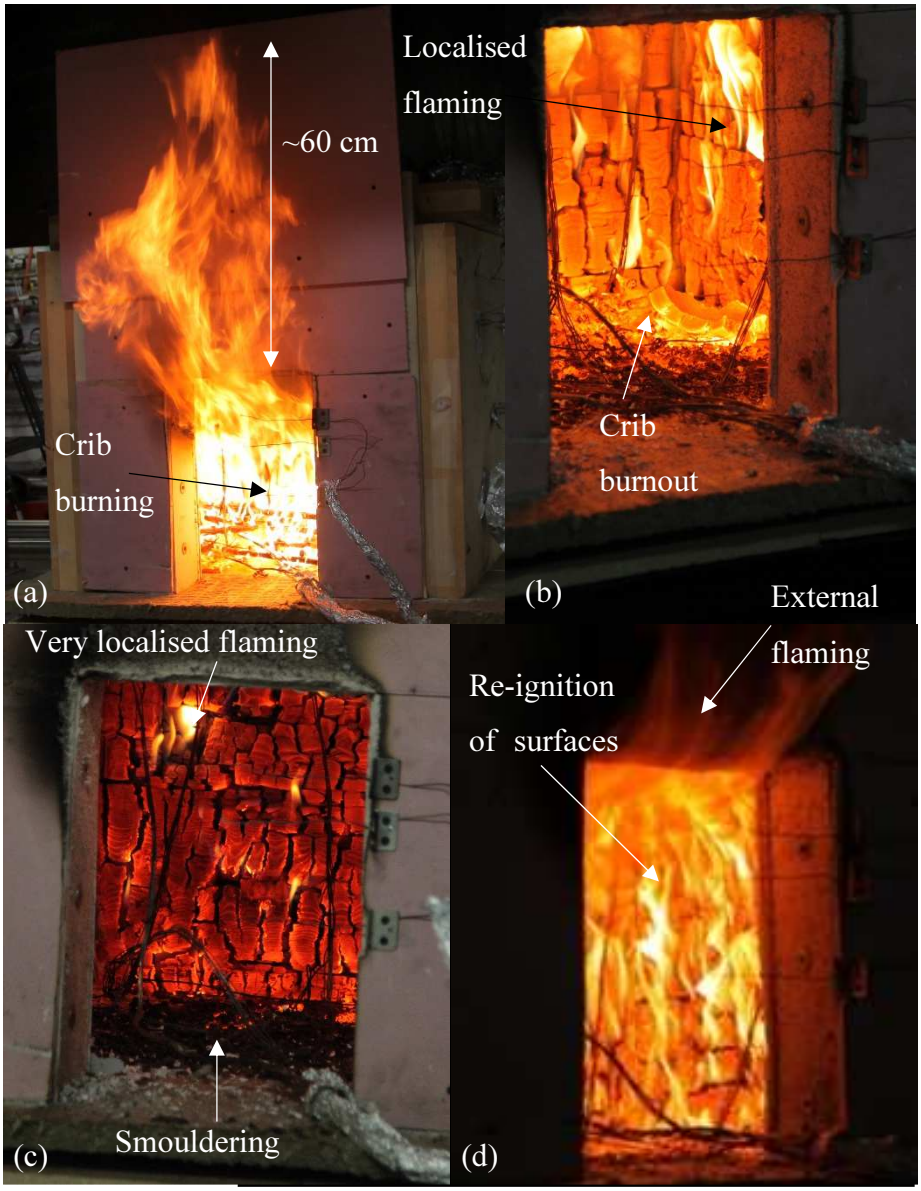

Figure 6.7: Experiment α-3 (a) 6 minutes after ignition, showing peak external flaming, (b) 35 minutes after ignition showing cessation of external flaming, (c) 49 minutes after ignition showing localised flaming on exposed timber surfaces, (d) 91 minutes after ignition showing second post-flashover period.

6.4.3 Experiment α-4

Experiment α-4 used a lower fuel load than experiment α-3. Key events are shown in Figure 6.8. As previously, after cessation of external flaming, the flaming over the exposed surfaces reduced gradually until auto-extinction was achieved after around 28-30 minutes, as shown in Figure 6.8(c). The mass loss rate as shown in Figure 6.6

passed through the extinction range from 22-24 minutes – a few minutes before this observed extinction time. Continued smouldering for a period of 3 minutes then resulted in local delamination on the back wall after around 32 minutes, resulting in local re-ignition. This then led to further delamination, resulting in flame spread over the exposed surfaces. Eventually, a secondary flashover occurred after 43 minutes, with peak external flaming reached after a further minute, shown in Figure 6.8(d), and evident from the HRR data shown in Figure 6.6. Unlike the previous experiment, external flaming was much more severe (flames extending ~60-80 cm rather than ~20-40 cm above the opening) than in the first flashover period.

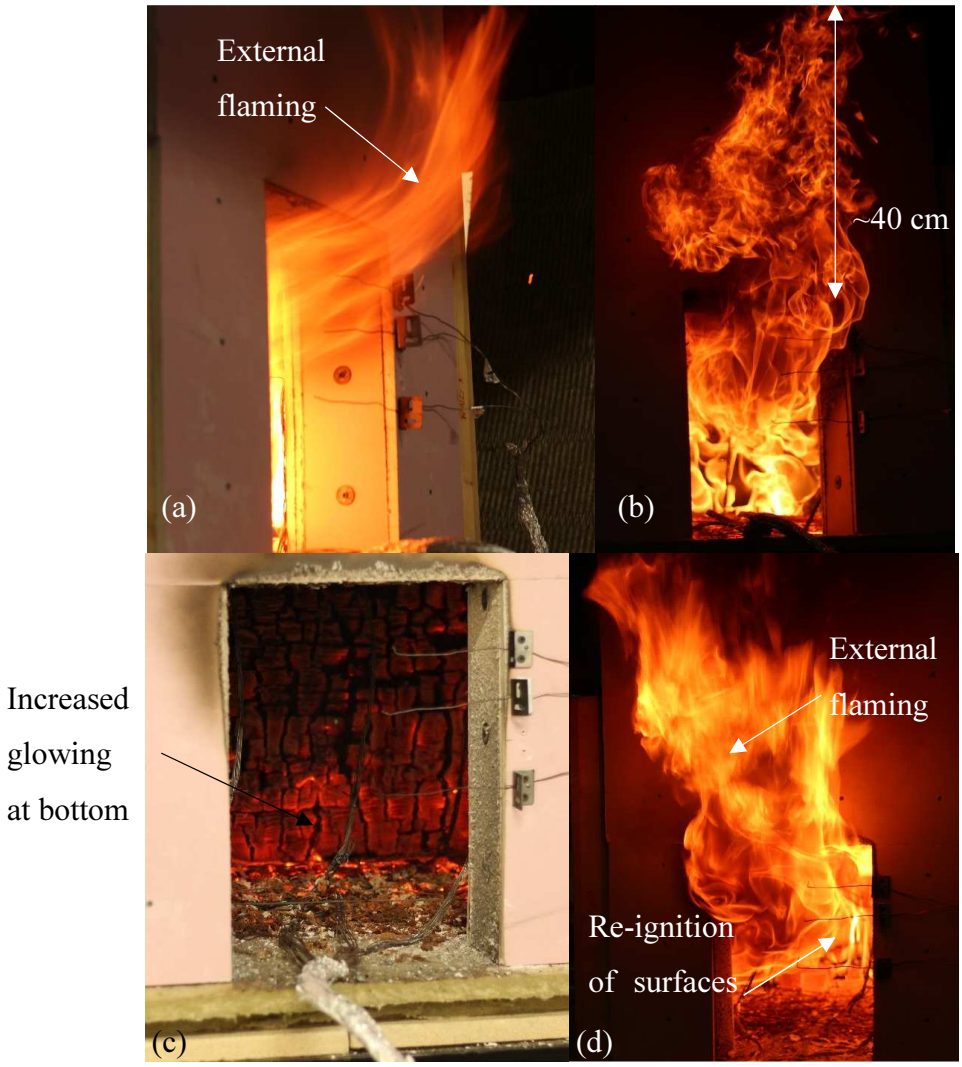

Figure 6.8: Experiment α-4 (a) 7 minutes after ignition, showing initial external flaming, (b) 10 minutes after ignition showing peak external flaming, (c) 30 minutes after ignition showing auto-extinction, (d) 45 minutes after ignition showing second post-flashover period.

6.4.4 Experiment β-3

Heat release rates and mass loss rates for each intermediate-scale experiment undertaken in configuration β are shown in Figure 6.9.

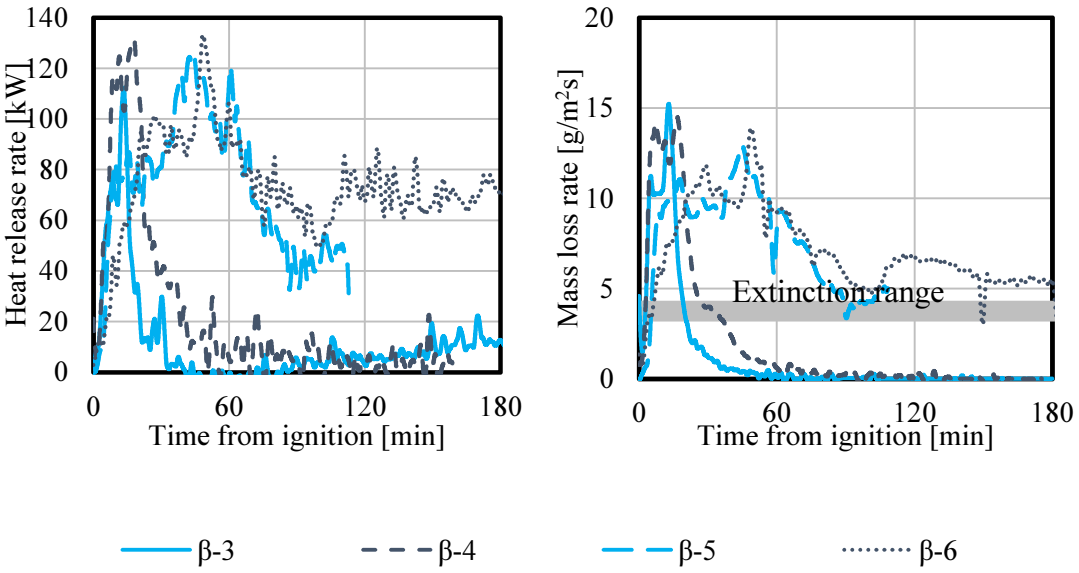

Figure 6.9: Total heat release rate and mass loss rate for each intermediate-scale compartment fire experiment undertaken in configuration β.

Flaming on the exposed surfaces gradually reduced until auto-extinction was achieved after 21-22 minutes. Again, the mass loss rate as shown in Figure 6.9 passed through the extinction range from 19-20 minutes – just before this observed extinction time. No localised re-ignition due to delamination was observed. The remains of the wood cribs continued to smoulder until around 40 minutes. It can be seen from Figure 6.9 that this follows a very similar HRR decay to the fully encapsulated experiment.

6.4.5 Experiment β-4

Experiment β-4 used a higher fuel load than experiment β-3, and thus a greater thermal penetration depth. Upon ignition, the left side of the crib ignited much more readily the right side, resulting in external flaming from around 4.3 minutes, before the right side of the crib had properly ignited. Full flashover did not occur until around 7 minutes, at which point significant external flaming was evident. Auto-extinction

was achieved at around 38-39 minutes, again slightly after the 28-35 minutes when mass loss rate passed through the critical extinction range. Localised re-ignition occurred over a small area of the back wall at around 45 minutes, spreading slightly to an adjacent panel, before re-extinguishing after 58 minutes. No further re-ignition was observed, and no secondary flashover occurred. Figure 6.9 shows that this experiment follows a slightly shallower decay curve than experiment β-3.

6.4.6 Experiment β-5

Experiment β-5 used a still higher fuel load, and thus the thermal penetration was further increased. After flashover, external flaming continued at a quasi-constant rate until manual termination. Key events are shown in Figure 6.10.

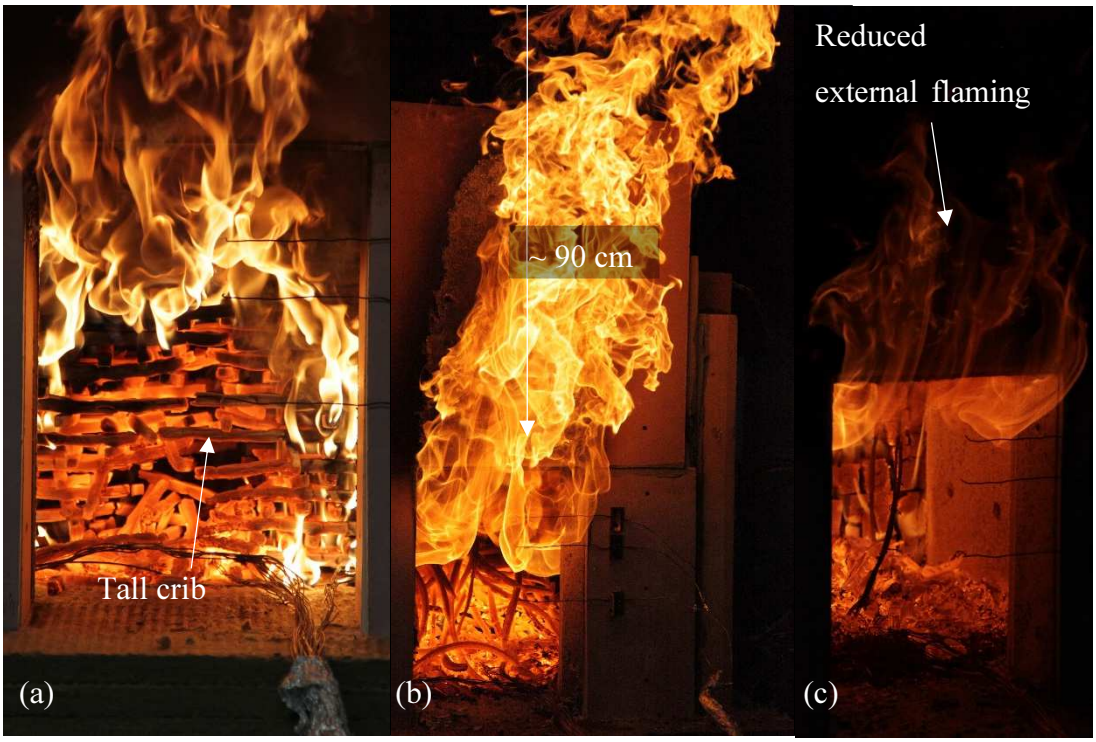

Figure 6.10: Experiment β-5 (a) 9 minutes after ignition showing peak external flaming, (b) 37minutes after ignition showing continued external flaming, (c) 70 minutes after ignition showing reduction in external flaming.

6.4.7 Experiment β-6

Having observed auto-extinction in experiment β-5, a repeat was carried out with the same fuel load (and thus the same thermal penetration depth), but using panels with thicker outer lamellae, to determine if auto-extinction would occur with the same thermal penetration depth if delamination could be delayed or prevented. As in experiment β-5, external flaming continued for the duration of the fire, gradually reducing until burn-through of the panels. As seen in Figure 6.9, the HRR is very similar to that of experiment β-5, with no effect of the thicker lamellae evident (other than the increased time to burn-through and delay in the second heat release peak).

6.4.8 Comparison

From the heat release rate data presented, it can be seen that the initial post-flashover peak heat release rates are similar for all experiments. Experiment β-3, which extinguished, is shown to follow a very similar decay curve to the fully encapsulated experiment, and β-4, which also extinguished albeit with a higher fuel load, follows a slightly shallower decay curve. Experiments β-5 and β-6 follow very similar curves, with no effect of the thicker lamellae evident (other than the increased time to burn-through and delay in the second heat release peak).

Apart from the consistent under-prediction of time to extinction, other inconsistencies with the hypothesis are evident: the mass loss rate in experiments α-3 and α-4 drop below 3.48 g/m^{2}s for about 10 minutes at 40 minutes and 80 minutes respectively, but no auto-extinction was observed; the mass loss rate of experiment β-5 drops into the extinction range briefly around 90 minutes, but auto-extinction was not observed. The uncertainty in the critical mass loss rate was found to be 0.31 g/m^{2}s in Section 3.3.4, and may partially account for this. Another likely reason is that the load cell is measuring the *average* mass loss rate over the entire exposed surfaces. As such, if enough of the surface has extinguished, an average mass loss rate of less than 3.48 g/m^{2}s may be achieved whilst areas are still burning (with local mass loss rates greater than 3.48 g/m^{2}s). This is observed in Section 4.3.4, where delamination resulted in localised re-ignition, but the mass loss rate remained below 3.48 g/m^{2}s. The

same phenomenon occurring in intermediate-scale experiments results in a much larger proportion of the exposed surfaces burning.

6.4.9 Summary

Similarly to the full-scale experiments, three distinct outcomes can be observed.

6.4.9.1 Outcome 1a: Auto-extinction

Experiments β-3 and β-4 resulted in sustained auto-extinction soon after the fuel load burned out. These experiments had the same proportion and configuration of exposed timber as experiment β-1 which extinguished. This can again be attributed to delamination not occurring.

6.4.9.2 Outcome 1b: Temporary auto-extinction

Experiment α-4 also achieved auto-extinction soon after the fuel load had burned out. In this case however, the continued smouldering was sufficient to result in delamination leading to a secondary flashover.

6.4.9.3 Outcome 2a: Decay leading to secondary flashover

Experiment α-3 behaved similarly to experiment α-4, however in this case auto-extinction did not occur, just a sharp reduction in flaming severity. This then led to a secondary flashover, as observed in experiment β-2.

6.4.9.4 Outcome 3b: Slow decay

Experiments β-5 and β-6 did not achieve auto-extinction or a cessation of external flaming. Due to the high fuel load, the duration of the peak burning period was much longer, and the decay from this much slower than observed in any other experiments. Unlike experiments α-1 and γ-1 (Outcome 3) however, the external flaming did decrease rather than remaining at the peak value until termination.

6.5 Comparison to Full-Scale Experiments

6.5.1.1 Time to flashover

The times to flashover for all experiments, full- and intermediate-scale, taken from visual observations, are shown in Figure 6.11. Full-scale experiments displayed a clear, quick flashover (growth from crib burning to peak HRR in ~20-30 s) and are represented by a single point. Intermediate-scale experiments showed a more gradual flashover, and are represented by a range showing the onset of flashover to establishment of peak heat release rate. It is clear that with three notable exceptions (experiments β-1, and α-3, and the fully encapsulated experiment), flashover always starts between 4-6 minutes after ignition, consistently across both scales. No clear dependency on fuel load is evident in times to flashover. It is interesting to note that the experiment without exposed timber reached flashover sooner than those with exposed timber, contradicting common assumptions that exposed timber surfaces will accelerate flashover. However, since only one datum is available for encapsulated timber, no meaningful conclusions from this may be drawn.

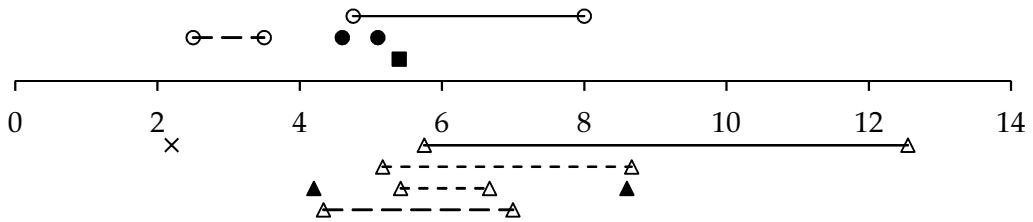

Figure 6.11: Times to flashover in minutes for all intermediate- and full-scale compartment fire experiments. ● configuration α; ▲configuration β; ■ configuration γ; × configuration 0. Filled shapes represent full-scale, hollow shapes intermediate-scale. Solid line represents low fuel load; long dashes represent medium fuel load; short dashes represent high fuel load.

As with the full-scale experiments, this can be compared with the time taken for the uppermost layer of gas-phase thermocouples to reach 600°C to allow a more robust comparison. This is shown in Figure 6.12, alongside the data from the full-scale experiments. It is clear that there is very poor agreement (average ± 319%) between the two methods for the reduced-scale experiments, whereas the full-scale experiments show very good agreement between the two methods. Unlike for the full-scale

experiments, the "600°C criterion" does not provide a good estimate for time to flashover (comparing the times for the upper layer to reach 600°C with the visual data discussed in Section 6.4 does not give feasible flashover times), and thus the less robust visual comparisons will be used.

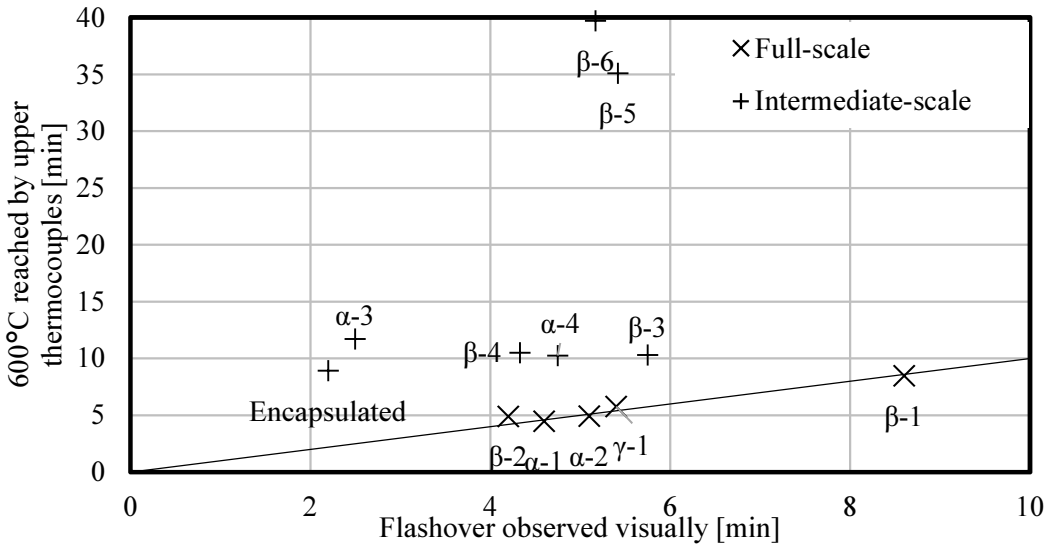

Figure 6.12: Time to flashover for each full- and intermediate-scale compartment fire experiment calculated from visual observations and the "600°C criterion".

6.5.1.2 Fuel Load

Two further issues were observed from scaling the compartments down from full-scale. The first was that of the fuel load, in particular when testing with the high fuel load. To achieve a fuel load of ~656 MJ/m^2, a wood crib with 20 layers of 11 sticks was required. This had a height of 300 mm. Whilst this is not a significant height for the full-scale compartments, it (and the difference between this and the 120 mm of the low fuel load) is significant for the intermediate-scale compartments, blocking heat from reaching the walls, and potentially increasing the time required for fuel burnout. This in turn could increase the thermal penetration into the exposed timber surfaces, promoting delamination.

6.5.1.3 Delamination

Similarly, it was observed that delaminated pieces were of similar sizes in each set of experiments. Whilst one delaminated piece is negligible in the full-scale experiments (~0.0006% compartment volume), it is much more significant in the intermediate-scale experiments (~0.04% compartment volume). This will influence the re-radiation from the delaminated char to the exposed surface. For example, a 5 cm x 5 cm x 5 cm piece landing in the centre of the compartment will have a view factor to the ceiling of 0.0012 in the intermediate-scale, compared to 0.000079 in the full-scale, an order of magnitude greater. Assuming a temperature of 600°C, this corresponds to heat fluxes of 40 W/m^2 and 2.5 W/m^2 respectively. When considering a piece landing 10 cm in front of the centre of the exposed wall, this corresponds to heat fluxes of 100 W/m^2 and 7 W/m^2 respectively. Whilst not significant heat fluxes compared to other components, the cumulative effect of multiple delaminated pieces should be borne in mind.

6.5.1.4 Effects of configuration

In the full-scale compartment fire experiments, a significant difference between configurations α and β was evident – configuration β tended toward extinction, whereas configuration α only showed a slight decay before continuing flaming with a similar severity to that post-flashover. In the intermediate-scale experiments however, the decay in configuration α was much more similar to that in β, with experiment α-4 even achieving auto-extinction (albeit unsustained). The behaviour of experiments β-3 and β-4 was very similar to that observed in experiment β-1 at full-scale.

6.6 Dependency on Fuel Load

It is clear from the above results that the imposed fuel load has a significant effect on the potential for auto-extinction and the time required to reach it. This is most evident in the experiments in configuration β – the experiments with the “low” and “medium” fuel loads achieved auto-extinction after 21-22 and 38-39 minutes respectively, whereas the experiments with the “high” fuel load did not achieve auto-extinction.

From the results of the full-scale experiments, it was observed that delamination was a key factor in preventing auto-extinction, and it was thus hypothesised that if delamination occurs before burnout of the imposed fuel load, then auto-extinction will not occur. As the entire compartment – crib and CLT – was placed on the load cell, determination of fuel burnout time from mass loss data was not possible. Approximations of time to fuel burnout can be made from the visual data, however these are subjective and susceptible to large uncertainties. Burnout of the fuel load was assumed to be when visible flaming of the wood cribs had stopped. These are given in Table 6.4 – data for experiment β-6 are not available due to an issue with the front camera in this experiment. Average burning rates are calculated over the period from flashover to flaming or smouldering extinction of the crib.

Table 6.4: Times to flashover and crib burnout for intermediate-scale compartment fire experiments. All times from ignition.

Experiment	Time to flashover [min]	Time to crib extinction [min] (flaming)	Average burning rate [g/s] (flaming)	Time to crib extinction [min] (smouldering)	Average burning rate [g/s] (total)
α-3	2.50	19.8±2.3	5.15±0.77	43±1	2.09
α-4	4.75	13.0±2.0	5.45±1.75	23±1	1.94
β-3	5.75	16.0±1.0	4.59±0.50	25±1	1.86
β-4	4.33	19.0±2.0	6.11±0.96	42±1	2.15
β-5	5.42	47.5±5.5	5.32±0.80	87±1	2.59

Whilst there is no clear trend in the average burning rate over the flaming period, there is a noticeable correlation over the total average burning rate – this increases from 1.90 ± 0.04 g/s for the "low" fuel load to 2.12 ± 0.03 g/s for the "medium" fuel load to 2.59 g/s for the high fuel load. This gives a linear correlation with a coefficient of determination of 0.97.

The temperature profiles at the centre of the back wall are shown for experiments β-3, β-4, and β-5 in Figure 6.13, with the temperature profiles at extinction shown for experiments β-3 and β-4, at 21-22 minutes and 38-39 minutes respectively. Experiments β-3 and β-4 show comparable behaviour, with shallow thermal gradients observed behind the glue line in both of these cases, suggesting no significant thermal

penetration beyond this point. In each of these cases, increases in the in-depth temperatures continue after extinction due to propagation of the thermal wave, peaking at around 100°C. Greater in-depth heating is observed in experiment β-4 than in experiment β-3 due to the higher fuel load and thus burning duration. Experiment β-5 shows continually increasing in-depth temperatures, with significantly heated timber behind the glue line.

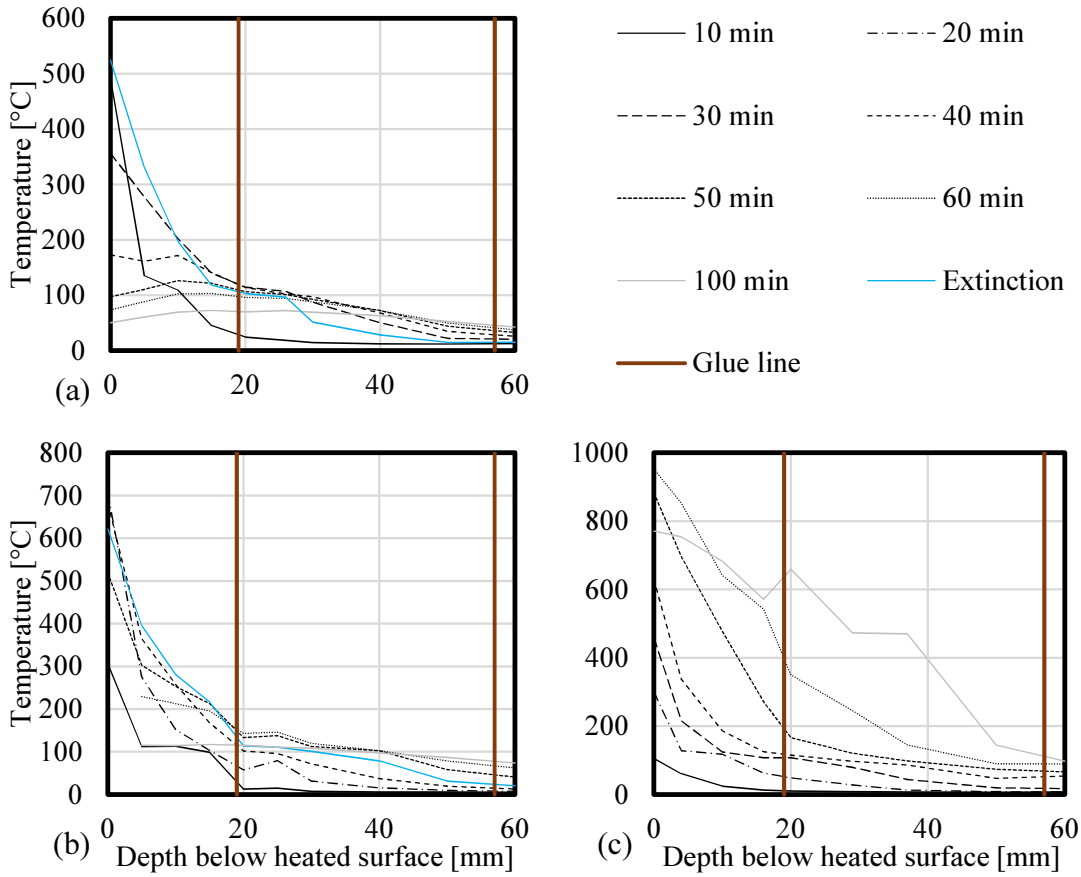

Figure 6.13: Temperature profiles at centre of back walls in experiment (a) β-3, (b) β-4, and (c) β-5.

This can then be compared to average temperatures at the glue-lines at the time to crib extinction. No direct estimation of thermal penetration depth can be made from the fuel load due to the effects of the large crib discussed in Section 6.5.1.2. For experiments β-3 and β-4, the temperature at the glue-line at the back wall was 77-91°C and 66-96°C respectively averaged over all positions (the range of temperatures represents the time uncertainty in the crib extinction time). Experiment β-5 however had glue-line temperatures of 106-235°C – significantly higher. The increase in

temperature over the crib extinction range and 5 minutes either side is shown in Figure 6.14.

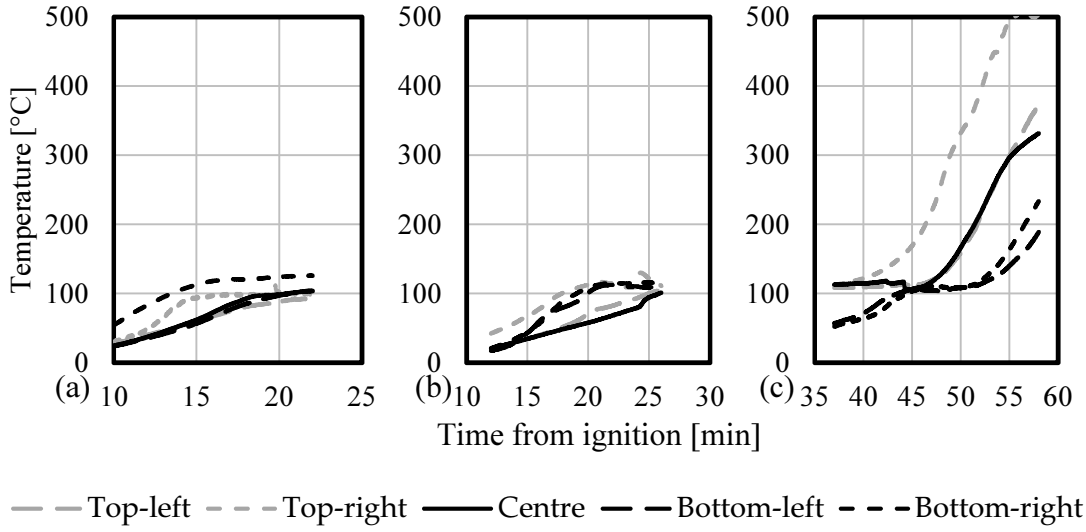

Figure 6.14:Temperature near glue-line (±2 mm) around time of crib burnout for (a) experiment β-3, (b) experiment β-4, (c) experiment β-5.

Experiments β-3 and β-4 both show gradual increases in temperature over the time of crib extinction, with temperatures not rising significantly above 100°C. This gradual increase suggests significant delamination has not occurred at this point, as the temperatures indicate that the char layer is still in place. Experiment β-5 however, shows much sharper rises in temperature. Whilst temperatures initially are little higher than those in experiments β-3 and β-4, during or shortly after crib burnout temperatures are rising sharply to over 300°C in most places (the slower temperature rise at the bottom is likely due to the larger wood crib "shielding" the bottom of the back wall from radiation), exceeding 500°C at the top-right corner. This sharp rise suggests that delamination has occurred, resulting in the additional exposed timber preventing auto-extinction as seen.

This was compared to visual observations over the crib extinction period – some minor delamination was observed in experiments β-3 and β-4 (a few pieces ~30 mm side length), however more significant delamination was observed in experiment β-5, with several pieces around 100 mm in side length observed. Due to the external plume,

there may have been more delamination in each case than could be observed visually, and the visual observations made allow only a crude comparison. This comparison does, however, support the hypothesis from the temperature data that no significant delamination occurred in the crib extinction period in experiments β-3 and β-4, but did in experiment β-5.

Post-experiment, photos were taken to allow visual calculations of the delaminated areas. Areas where delamination had occurred were identified manually, and then calculated using MATLAB. The delaminated area was identified manually by visual analysis, converted into a monochrome image by MATLAB, and then the delaminated area calculated as a percentage of the total surface area. This is shown for experiment β-3 in Figure 6.15.

Figure 6.15: Back wall of experiment β-3 after deconstruction, showing manually identified delaminated areas (left) and MATLAB-produced monochrome image (right).

Experiment β-3 was found to have around 8% of the back wall and 6% of the ceiling delaminated – confirming the assumption of minimal delamination. Delamination was slightly more extensive over the back wall of experiment β-4, approximately 26%, but only around 1.3% of the ceiling was seen to delaminate. As discussed in Section 6.4.5,

some delamination was observed to occur locally after extinction, which will account for some of the 26% measured. Experiment β-5 had burned right through and thus the entire first lamella was missing, and so it was not possible to estimate the extent of delamination at any given time.

6.7 Conclusions

A series of seven intermediate-scale experiments have been undertaken, confirming the results of the full-scale experiments that auto-extinction is possible within a compartment with exposed timber when the mass loss rate drops below a critical value. Through testing with different fuel loads, the following conclusions can be drawn:

- If significant delamination occurs before the imposed fuel load has burned out, auto-extinction will not occur;
- Local variations in mass loss rate can be significant, (more so in the intermediate-scale experiments) resulting in an average mass loss rate below the critical value when flaming is sustained;
- Auto-extinction typically occurs a few minutes *after* the mass loss rate drops below the critical rate of 3.48 g/m^{2}s obtained from bench-scale experimentation – which has been shown to be valid for full-scale compartment fire experiments – this is likely due to the aforementioned local variations being proportionally more significant at a reduced scale;
- If the temperature at the glue line is less than a critical value when the crib burns out, delamination will be prevented and auto-extinction can occur. For the PU-adhesive used herein, this temperature appears to be in the range 100-200°C;
- Performing intermediate-scale compartment fire experiments can capture the behaviour observed in full-scale experiments, but care must be taken around the physical size of the fuel load and the greater relative effects of delaminated pieces.

Thus the logic diagram in Figure 5.17 can be expanded into that in Figure 6.16. In the majority of cases, the “time to fuel burnout < time to structural collapse” requirement will be redundant, however is kept in for completeness.

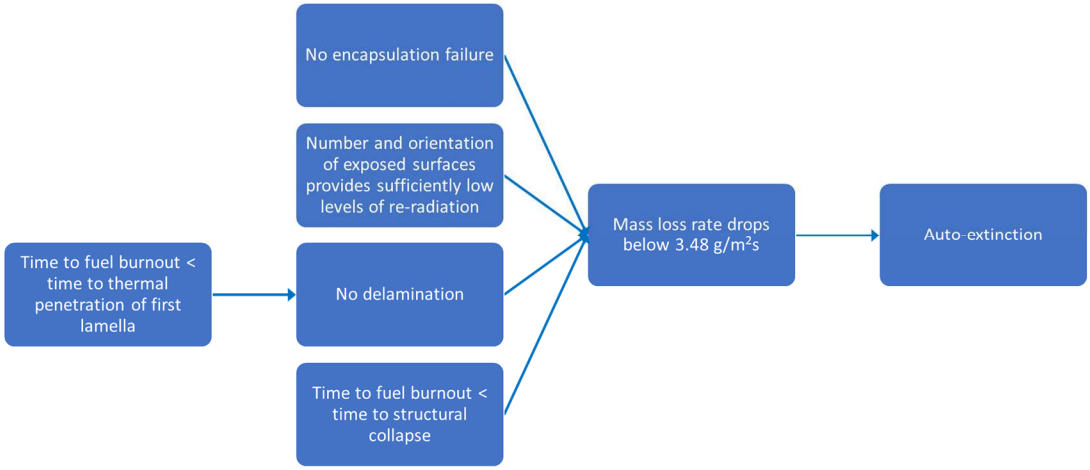

Figure 6.16: Logic diagram showing conditions necessary for auto-extinction.

Chapter 7 Conclusions and Further Work

The phenomena surrounding auto-extinction of timber have been explored, the necessary conditions to achieve it identified, and its application in full-scale compartment fires with exposed timber examined.

7.1 Key Findings

Bench-scale experimentation found a critical mass loss rate for extinction of 3.48 ± 0.31 g/m^{2}s at ambient oxygen concentration, increasing to 4.05 ± 0.51 g/m^{2}s as oxygen concentration was reduced to 17.2%. This was equivalent to an incident heat flux of ~30 kW/m^2 in the FPA. Further full-scale experimentation showed that this critical mass loss rate was valid when applied to realistic scales, and that auto-extinction could be achieved in compartments with exposed timber surfaces. However, additional requirements were identified as shown in Figure 6.16, as various experiments showed that auto-extinction would not be achieved if the encapsulation of protected surfaces did not stay in place (experiment α-1), too much timber was exposed (experiment γ-1), or delamination occurred (experiment β-2).

Further experiments at a reduced scale showed that delamination would occur if the temperature at the glue-line exceeded ~200°C. The effects of scale prevented a direct comparison between fuel load, time to burnout, and thermal penetration depth.

Two energy balances were proposed to determine the critical mass loss rate – both were demonstrated to work conceptually, however both methods are very sensitive to uncertainties in the data required – either collection of thermocouple data, or evaluation of the convective heat transfer.

7.2 Further Work

Based on the findings shown in Figure 6.16, the following areas are recommended for further research.

7.2.1 Understanding Encapsulation Failure

Based on the results of experiment α-1, it was shown that encapsulation of protected timber surfaces must be maintained in order to prevent involvement of exposed timber surfaces in the fire. It was demonstrated that, in the setup investigated, two layers of fire-rated gypsum plasterboard was insufficient to achieve this, but an additional layer, alongside a layer of mineral wool, provided the necessary protection. Further work should be undertaken to understand the characteristic failure modes of different encapsulation systems.

7.2.2 Prevention of Delamination

Experiment β-2 demonstrated the importance of preventing delamination. Experiments β-3 and β-4 demonstrated that controlling the thermal penetration depth (e.g. by managing the fuel load) can prevent delamination.

From experiment β-5, the glue-line temperature at which delamination was observed appears to be in the range 100-200°C, however detailed fundamental research into the failure mode of commonly used adhesives is required to provide a more robust critical temperature and therefore allow an prediction of if and when delamination may occur.

7.2.3 Number and Orientation of Exposed Surfaces

Critical to achieving auto-extinction is the number and orientation of the exposed timber surfaces. At the full-scale, the importance of the relative position of the exposed timber surfaces was identified; it was demonstrated that experiments with an exposed back wall and ceiling extinguished or tended towards extinction, whereas experiments with two exposed walls did not.

Further experiments should be undertaken to explore in particular the effects of different aspect ratios and opening factors – the work herein has focused solely on (approximately) cubic compartments with a fixed opening factor.

7.2.4 Heat Transfer

A key barrier to successful implementation of the energy balance is the uncertainty associated with the convective heat transfer – this is a key cooling mechanism within the decay phase of a compartment fire. In future experiments, it is recommended that velocity measurements are made in front of exposed and encapsulated timber surfaces, to allow better estimations of the convective conditions.

The energy balance presented in Chapter 5 was implemented using heat flux data from thin skin calorimeters. Future work should explore the re-radiation between exposed and encapsulated surfaces, as well as any effect of the smoke layer, to quantify the radiation exchange for a given configuration.

7.2.5 Summary

A model was developed to predict the auto-extinction behaviour of exposed timber surfaces in a compartment fire, however the further work recommended above will reduce the uncertainties. This will enable a greater understanding of the phenomena present in compartment fires with exposed timber surfaces, in particular enabling the heat transfer within the compartment to be better understood. More precise quantification of the abovementioned areas will enable more robust energy balance calculations to be performed.

References

[1] William the Conqueror (1086) *Domesday Book,* England.

[2] Trueman, C. (2014) *Stone Keep Castles*, Available: http://www.historylearningsite.co.uk/stone_keep_castles.htm [Accessed 2 April 2015].

[3] Guan, Z. and Rodd, P. (2001) Hollow steel dowels—a new application in semi-rigid timber connections. *Engineering Structures, 23*(1), pp. 110-119.

[4] CEN (2004) Eurocode 5. Design of timber structures. . in *Part 2: Bridges*,Brussels: European Committee for Standardisation.

[5] Östman, B., Brandon, D. and Frantzich, H. (2017) Fire safety engineering in timber buildings. *Fire Safety Journal*.

[6] CEN (2004) Eurocode 5. Design of timber structures. . in *Part 1-2: General. Structural fire design*,Brussels: European Committee for Standardisation.

[7] ISO (1999) ISO 834-1: Fire resistance tests. Elements of building construction. in *Part 1: General Requirements.*,Geneva, Switzerland: Internatinal Organisation for Standardization.

[8] Law, A. and Hadden, R. (2017) Burnout Means Burnout. *SFPE Europe*.

[9] Inghelbrecht, A. (2014) *Evaluation of the burning behaviour of wood products in the context of structural fire design*. Unpublished International Master of Science in Fire Safety Engineering MSc, The University of Queensland, Ghent University, .

[10] Lautenberger, C., Sexton, S., & Rich, D. (2014) Understanding Long Term Low Temperature Ignition of Wood. In Paper Presented to the International Symposium on Fire Investigation Science and Technology, College Park, MD.

[11] Drysdale, D. (2011) *An introduction to fire dynamics,* John Wiley & Sons.

[12] Ragauskas, A. *Chemical Overview of Wood*. Georgia Tech: College of Sciences.

[13] Guo, X., Wang, S., Zhou, Y. and Luo, Z. (2011) Catalytic pyrolysis of xylan-based hemicellulose over zeolites.

[14] Moore, J. (2011) *Wood properties and uses of Sitka spruce in Britain,* Forestry Commission.

[15] Hirschler, M. M. and Morgan, A. B. (2008) Thermal decomposition of polymers. *SFPE handbook of fire protection engineering, 3*, pp. 1-112-1-143.

[16] Murty Kanury, A. and Blackshear Jr, P. L. (1970) Some considerations pertaining to the problem of wood-burning. *Combustion Science and Technology, 1*(5), pp. 339-356.

[17] Reszka, P. and Torero, J. (2008) In-depth temperature measurements in wood exposed to intense radiant energy. *Experimental Thermal and Fluid Science, 32*(7), pp. 1405-1411.

[18] Friquin, K. L. (2011) Material properties and external factors influencing the charring rate of solid wood and glue-laminated timber. *Fire and Materials, 35*(5), pp. 303-327.

[19] Yang, L., Chen, X., Zhou, X. and Fan, W. (2003) The pyrolysis and ignition of charring materials under an external heat flux. *Combustion and Flame, 133*(4), pp. 407-413.

[20] Matson, A., DuFour, R. and Breen, J. (1959) Survey of Available Information on Ignition of Wood Exposed to Moderately Elevated Temperatures. *Part II of Bulletin of Research,* (51).
[21] Di Blasi, C. (1993) Modeling and simulation of combustion processes of charring and non-charring solid fuels. *Progress in Energy and Combustion Science, 19*(1), pp. 71-104.
[22] Browne, F. L. (1958) Theories of the combustion of wood and its control.
[23] Association, T. D. (1953) *Timber and Fire Protection,* London, UK: The Timber Development Associaion Ltd.
[24] Bamford, C. (n.d.) *The combustion of wood.*
[25] Mikkola, E. (1991) Charring of wood based materials. in *Fire Safety Science–Proceedings of the Third International Symposium. London: Elsevier Applied Science*. pp. 547-556.
[26] Buchanan, A. H. (2001) *Structural design for fire safety,* Wiley New York.
[27] Grønli, M. G. and Melaaen, M. C. (2000) Mathematical model for wood pyrolysis comparison of experimental measurements with model predictions. *Energy & Fuels, 14*(4), pp. 791-800.
[28] Schmid, J., Just, A., Klippel, M. and Fragiacomo, M. (2014) The Reduced Cross-Section Method for Evaluation of the Fire Resistance of Timber Members: Discussion and Determination of the Zero-Strength Layer. *Fire Technology*, pp. 1-25.
[29] Gerhards, C. C. (1982) Effect of moisture content and temperature on the mechanical properties of wood: an analysis of immediate effects. *Wood and Fiber Science, 14*(1), pp. 4-36.
[30] Schaffer, E. (1973) Effect of pyrolytic temperatures on longitudinal strength of dry Douglas-fir. *Journal of Testing and Evaluation, 1*(4), pp. 319-329.
[31] Di Blasi, C., Hernandez, E. G. and Santoro, A. (2000) Radiative pyrolysis of single moist wood particles. *Industrial & engineering chemistry research, 39*(4), pp. 873-882.
[32] White, R. H. and Dietenberger, M. (2001) Wood products: thermal degradation and fire.
[33] Shen, D., Fang, M., Luo, Z. and Cen, K. (2007) Modeling pyrolysis of wet wood under external heat flux. *Fire Safety Journal, 42*(3), pp. 210-217.
[34] Li, W., Sun, N., Stoner, B., Jiang, X., Lu, X. and Rogers, R. D. (2011) Rapid dissolution of lignocellulosic biomass in ionic liquids using temperatures above the glass transition of lignin. *Green Chemistry, 13*(8), pp. 2038-2047.
[35] Sakata, I. and Senju, R. (1975) Thermoplastic behavior of lignin with various synthetic plasticizers. *Journal of Applied Polymer Science, 19*(10), pp. 2799-2810.
[36] Salmén, L. (1984) Viscoelastic properties ofin situ lignin under water-saturated conditions. *Journal of Materials Science, 19*(9), pp. 3090-3096.
[37] Moraes, P., Rogaume, Y., Bocquet, J. and Triboulot, P. (2005) Influence of temperature on the embedding strength. *Holz als Roh-und Werkstoff, 63*(4), pp. 297-302.
[38] Wichman, I. S. and Atreya, A. (1987) A simplified model for the pyrolysis of charring materials. *Combustion and Flame, 68*(3), pp. 231-247.

[39] Hugi, E., Wuersch, M., Risi, W. and Wakili, K. G. (2007) Correlation between charring rate and oxygen permeability for 12 different wood species. *Journal of wood science, 53*(1), pp. 71-75.
[40] Schaffer, E. L., Marx, C. M., Bender, D. A. and Woeste, F. E. (1986) Strength validation and fire endurance of glued-laminated timber beams.
[41] Ohlemiller, T., Kashiwagi, T. and Werner, K. (1987) Wood gasification at fire level heat fluxes. *Combustion and Flame, 69*(2), pp. 155-170.
[42] Roberts, A. (1971) Problems associated with the theoretical analysis of the burning of wood. in *Symposium (International) on Combustion*: Elsevier. pp. 893-903.
[43] Yang, H., Yan, R., Chen, H., Lee, D. H. and Zheng, C. (2007) Characteristics of hemicellulose, cellulose and lignin pyrolysis. *Fuel, 86*(12), pp. 1781-1788.
[44] Várhegyi, G., Grønli, M. G. and Di Blasi, C. (2004) Effects of sample origin, extraction, and hot-water washing on the devolatilization kinetics of chestnut wood. *Industrial & engineering chemistry research, 43*(10), pp. 2356-2367.
[45] Milosavljevic, I., Oja, V. and Suuberg, E. M. (1996) Thermal effects in cellulose pyrolysis: relationship to char formation processes. *Industrial & Engineering Chemistry Research, 35*(3), pp. 653-662.
[46] Shen, D. and Gu, S. (2009) The mechanism for thermal decomposition of cellulose and its main products. *Bioresource Technology, 100*(24), pp. 6496-6504.
[47] Kashiwagi, T., Ohlemiller, T. and Werner, K. (1987) Effects of external radiant flux and ambient oxygen concentration on nonflaming gasification rates and evolved products of white pine. *Combustion and Flame, 69*(3), pp. 331-345.
[48] Kawamoto, H., Morisaki, H. and Saka, S. (2009) Secondary decomposition of levoglucosan in pyrolytic production from cellulosic biomass. *Journal of Analytical and Applied Pyrolysis, 85*(1), pp. 247-251.
[49] Drysdale, D. (1995) Thermochemistry. *SFPE Handbook of Fire Protection Engineering*, pp. 1-146.
[50] Quintiere, J. G. (2006) *Fundamentals of fire phenomena,* John Wiley England.
[51] Torero, J. L. (2008) Flaming ignition of solid fuels. *SFPE Handbook of Fire Protection Engineering*, pp. 2-260-2-277.
[52] Babrauskas, V. (2005) Charring rate of wood as a tool for fire investigations. *Fire Safety Journal, 40*(6), pp. 528-554.
[53] Hosoya, T., Kawamoto, H. and Saka, S. (2007) Pyrolysis behaviors of wood and its constituent polymers at gasification temperature. *Journal of Analytical and Applied Pyrolysis, 78*(2), pp. 328-336.
[54] Hottel, H. C. (1942) *Report on "wood flammability under various conditions of irradiation"*: National Defense Research Committee of the Office of Scientific Research and Development.
[55] Simms, D. (1963) On the pilot ignition of wood by radiation. *Combustion and Flame, 7*, pp. 253-261.
[56] Simms, D. and Law, M. (1967) The ignition of wet and dry wood by radiation. *Combustion and Flame, 11*(5), pp. 377-388.
[57] Ashton, L. A. (1965) Behaviour in fire of wood-based panel products. *Plywood and other Wood-based panels, IV*.

[58] Moghtaderi, B., Novozhilov, V., Fletcher, D. and Kent, J. (1997) A new correlation for bench-scale piloted ignition data of wood. *Fire Safety Journal, 29*(1), pp. 41-59.
[59] Shields, T., Silcock, G. and Murray, J. (1993) The effects of geometry and ignition mode on ignition times obtained using a cone calorimeter and ISO ignitability apparatus. *Fire and materials, 17*(1), pp. 25-32.
[60] McAllister, S., Finney, M. and Cohen, J. (2011) Critical mass flux for flaming ignition of wood as a function of external radiant heat flux and moisture content. in *7th US national technical meeting of the Combustion Institute, Georgia Institue of Technology, Atlanta, GA*. pp. 20-23.
[61] McAllister, S. (2013) Critical mass flux for flaming ignition of wet wood. *Fire Safety Journal, 61*(0), pp. 200-206.
[62] Janssens, M. (1991) Piloted ignition of wood: a review. *Fire and Materials, 15*(4), pp. 151-167.
[63] Angell, H., Gottschalk, F. and McFarland, W. (1949) Ignition Temperature of Fireproofed Wood, Untreated Sound Wood and Untreated Decayed Wood. *British Columbia Lumberman, 33*(57-58), pp. 70-72.
[64] Markwardt, L. J., Bruce, H. D. and Freas, A. D. (1954) Brief Descriptions of Some Fire-test Methods Used for Wood and Wood-Base Materials. In Paper Presented to the Third Conference on Wood Technology, Paris, France.
[65] Ashton, L. A. (1970) *Fire and timber in modern building design*.
[66] Crielaard, R. (2015) *Self-extinguishment of Cross-Laminated Timber*. Unpublished Master of Science in Civil Engineering MSc, Delft University of Technology.
[67] Ohlemiller, T. (2002) Smoldering combustion. in DiNenno, P. J., Drysdale, D., Beyler, C. L., Walton, W. D., Custer, R. L. P., Hall, J. R. and Watts, J. M., (eds.) *SFPE Handbook of Fire Protection Engineering*,Quincy, MA: National Fire Protection Association. pp. 2-200-2-210.
[68] Atreya, A. and Wichman, I. (1989) Heat and mass transfer during piloted ignition of cellulosic solids. *Journal of Heat Transfer, 111*(3), pp. 719-725.
[69] Atreya, A., Carpentier, C. and Harkleroad, M. (1986) Effect of sample orientation on piloted ignition and flame spread. *Fire Safety Science, 1*, pp. 97-109.
[70] Bixel, E. C. and Moore, H. J. (1910) Are Fires Caused by Steam Pipes. *Case School of Applied Science. Pittsburgh*.
[71] Brown, C. R. (1935) The Determination of the Ignition Temperatures of Solid Materials. *Fuel, 14*(2), pp. 14-18, 56-59, 80-85, 112-116, 144-152, 173-179.
[72] Brown, C. R. (1934) The Ignition Temperatures of Solid Materials. *Quarterly of the National Fire Protection Association, 28*(2), pp. 135-145.
[73] Fangrat, J., Hasemi, Y., Yoshida, M. and Hirata, T. (1996) Surface temperature at ignition of wooden based slabs. *Fire Safety Journal, 27*(3), pp. 249-259.
[74] Fons, W. L. (1950) Heating and ignition of small wood cylinders. *Industrial & Engineering Chemistry, 42*(10), pp. 2130-2133.
[75] Graf, S. (1949) Ignition Temperatures of Various Papers. *Woods, and Fabrics (Oregon State College Bull. 26), Oregon State College, Corvallis (March 1949)*.

[76] Hill, H. B. and Comey, A. M. (1886) On the Behavior of Sound and Decayed Wood at High Temperatures. in *Proceedings of the American Academy of Arts and Sciences*: JSTOR. pp. 482-487.
[77] Lawson, D. I. and Simms, D. L. (1952) The ignition of wood by radiation. *British Journal of Applied Physics, 3*(9), pp. 288.
[78] Simms, D. (1960) Ignition of cellulosic materials by radiation. *Combustion and Flame, 4*, pp. 293-300.
[79] Simms, D. and Hird, D. (1958) On the pilot ignition of materials by radiation. *Department of Scientific and Industrial Research and Fire Offices' Committee, Joint Fire Research Organization FR Note,* (365).
[80] Smith, W. and King, J. B. (1970) Surface temperature of materials during radiant heating to ignition. *Journal of Fire and Flammability, 1*(4), pp. 272-288.
[81] Spearpoint, M. and Quintiere, J. (2000) Predicting the burning of wood using an integral model. *Combustion and Flame, 123*(3), pp. 308-325.
[82] Tran, H. C. and White, R. H. (1992) Burning rate of solid wood measured in a heat release rate calorimeter. *Fire and materials, 16*(4), pp. 197-206.
[83] Mikkola, E. (1992) Ignitability of solid materials. *Heat Release in Fires*, pp. 225-232.
[84] Dai, J., Delichatsios, M. A., Yang, L. and Zhang, J. (2013) Piloted ignition and extinction for solid fuels. *Proceedings of the Combustion Institute, 34*(2), pp. 2487-2495.
[85] Koohyar, A. N., Welker, J. R. and Sliepcevich, C. M. (1968) Ignition of wood by flame radiation. in *Spring Meeting of the Western States Section of the Combustion Institute*,University of Southern California, Los Angeles, California.
[86] Koohyar, A. N., Welker, J. R. and Sliepcevich, C. M. (1968) The irradiation and ignition of wood by flame. *Fire Technology, 4*(4), pp. 284-291.
[87] Lau, P. W., White, R. and Van Zeeland, I. (1999) Modelling the charring behaviour of structural lumber. *Fire and materials, 23*(5), pp. 209-216.
[88] Rasbash, D., Drysdale, D. and Deepak, D. (1986) Critical heat and mass transfer at pilot ignition and extinction of a material. *Fire Safety Journal, 10*(1), pp. 1-10.
[89] White, R. H. and Nordheim, E. V. (1992) Charring rate of wood for ASTM E 119 exposure. *Fire Technology, 28*(1), pp. 5-30.
[90] Ritchie, S. J., Steckler, K. D., Hamins, A., Cleary, T. G., Yang, J. C. and Kashiwagi, T. (1997) The effect of sample size on the heat release rate of charring materials. in *Fire Safety Science: Proceedings of the Fifth International Symposium*. pp. 177-188.
[91] Butler, C. (1971) *Notes on charring rates in wood,* Department of the Environment and Fire Offices' Committee, Joint Fire Research Organization.
[92] Delichatsios, M. A. (2005) Piloted ignition times, critical heat fluxes and mass loss rates at reduced oxygen atmospheres. *Fire Safety Journal, 40*(3), pp. 197-212.
[93] Quintiere, J. G. and Rangwala, A. S. (2004) A theory for flame extinction based on flame temperature. *Fire and Materials, 28*(5), pp. 387-402.
[94] Tewarson, A. and Pion, R. F. (1976) Flammability of plastics—I. Burning intensity. *Combustion and Flame, 26*, pp. 85-103.

[95] Bamford, C., Crank, J. and Malan, D. (1946) The combustion of wood. Part I. in *Mathematical Proceedings of the Cambridge Philosophical Society*: Cambridge Univ Press. pp. 166-182.
[96] Hottel, H. C. (1931) Radiant heat transmission between surfaces separated by non-absorbing media. *Journal of Heat Transfer, 53*, pp. 265-273.
[97] Hamilton, D. C. and Morgan, W. R. (1952) *Radiant-interchange configuration factors*. Washington: NASA.
[98] Emberley, R., Inghelbrecht, A., Yu, Z. and Torero, J. L. (2017) Self-extinction of timber. *Proceedings of the Combustion Institute, 36*(2), pp. 3055-3062.
[99] Rangwala, A. S. (2006) Flame spread analysis using a variable B-number.
[100] König, J. (2006) Effective thermal actions and thermal properties of timber members in natural fires. *Fire and materials, 30*(1), pp. 51-63.
[101] Cachim, P. B. and Franssen, J.-M. (2010) Assessment of Eurocode 5 charring rate calculation methods. *Fire Technology, 46*(1), pp. 169-181.
[102] Hall, G. S. (1970) *The charring rate of certain hardwoods*.
[103] White, R. H. and Tran, H. C. (1996) Charring rate of wood exposed to a constant heat flux.
[104] Schaffer, E. L. (1967) *Charring Rate of Selected Woods - Transverse to Grain*: DTIC Document.
[105] White, R. H. (2000) Charring rate of composite timber products. in *Wood and Fire Safety*,Technical Universty of Zvolen.
[106] Collier, P. C. R. (1992) *Charring rates of timber,* Building Research Association of New Zealand.
[107] Lizhong, Y., Yupeng, Z., Yafei, W. and Zaifu, G. (2008) Predicting charring rate of woods exposed to time-increasing and constant heat fluxes. *Journal of Analytical and Applied Pyrolysis, 81*(1), pp. 1-6.
[108] White, R. H. (2002) Analytical methods for determining fire resistance of timber members. *The SFPE handbook of fire protection engineering. 3rd ed. Quincy, MA: National Fire Protection Association*.
[109] Yang, T.-H., Wang, S.-Y., Tsai, M.-J. and Lin, C.-Y. (2009) Temperature distribution within glued laminated timber during a standard fire exposure test. *Materials & Design, 30*(3), pp. 518-525.
[110] Yang, T.-H., Wang, S.-Y., Tsai, M.-J. and Lin, C.-Y. (2009) The charring depth and charring rate of glued laminated timber after a standard fire exposure test. *Building and Environment, 44*(2), pp. 231-236.
[111] Njankouo, J. M., Dotreppe, J. C. and Franssen, J. M. (2004) Experimental study of the charring rate of tropical hardwoods. *Fire and materials, 28*(1), pp. 15-24.
[112] Cachim, P. B. and Franssen, J. M. (2009) Comparison between the charring rate model and the conductive model of Eurocode 5. *Fire and Materials, 33*(3), pp. 129-143.
[113] Lie, T. (1994) Structural fire protection, manuals and reports on engineering practice, No. 78. *ASCE, New York, NY*.
[114] Cedering, M. (2006) Effect on the charring rate of wood in fire due to oxygen content, moisture content and wood density. in *Proceedings of the Fourth International Conference Structures in Fire (SiF'06)*.

[115] Simpson, W. T. (1998) *Equilibrium moisture content of wood in outdoor locations in the United States and worldwide,* US Dept. of Agriculture, Forest Service, Forest Products Laboratory.
[116] Di Blasi, C., Branca, C., Santoro, A. and Gonzalez Hernandez, E. (2001) Pyrolytic behavior and products of some wood varieties. *Combustion and Flame, 124*(1), pp. 165-177.
[117] Frangi, A. and Fontana, M. (2003) Charring rates and temperature profiles of wood sections. *Fire and Materials, 27*(2), pp. 91-102.
[118] Hadden, R., Alkatib, A., Rein, G. and Torero, J. (2014) Radiant Ignition of Polyurethane Foam: The Effect of Sample Size. *Fire Technology, 50*(3), pp. 673-691.
[119] Schmid, J., König, J. and Köhler, J. (2010) Design model for fire exposed cross-laminated timber. in *Proc of the sixth International conference Structures in Fire, Lancaster, US*.
[120] Frangi, A., Fontana, M., Hugi, E. and Jöbstl, R. (2009) Experimental analysis of cross-laminated timber panels in fire. *Fire Safety Journal, 44*(8), pp. 1078-1087.
[121] Frangi, A., Fontana, M., Knobloch, M. and Bochicchio, G. (2008) Fire behaviour of cross-laminated solid timber panels. *Fire Safety Science*, pp. 1279-1290.
[122] Schmid, J., König, J. and Köhler, J. (2010) Fire-exposed cross-laminated timber-modelling and tests. in *World Conference on Timber Engineering*.
[123] Fragiacomo, M., Menis, A., Clemente, I., Bochicchio, G. and Ceccotti, A. (2012) Fire Resistance of Cross-Laminated Timber Panels Loaded Out of Plane. *Journal of Structural Engineering, 139*(12).
[124] Schmid, J., Klippel, M., Just, A. and Frangi, A. (2014) Review and analysis of fire resistance tests of timber members in bending, tension and compression with respect to the reduced cross-section method. *Fire Safety Journal, 68*, pp. 81-99.
[125] Friquin, K. L., Grimsbu, M. and Hovde, P. J. (2010) Charring rates for cross-laminated timber panels exposed to standard and parametric fires. in *World Conference on Timber Engineering*. pp. 20-24.
[126] Wakefield, T., He, Y. and Dowling, V. (2009) An experimental study of solid timber external wall performance under simulated bushfire attack. *Building and Environment, 44*(10), pp. 2150-2157.
[127] Schaffer, E. L. (1964) *An approach to the mathematical prediction of temperature rise within a semi-infinite wood slab subjected to high-temperature conditions,* Forest Products Laboratory.
[128] Hakkarainen, T. (2002) Post-flashover fires in light and heavy timber construction compartments. *Journal of Fire Sciences, 20*(2), pp. 133-175.
[129] Silcock, G. and Shields, T. (2001) Relating char depth to fire severity conditions. *Fire and materials, 25*(1), pp. 9-11.
[130] Reszka, P. (2006) *In-depth temperature measurements of timber in fires*. Unpublished.
[131] Lizhong, Y., Zaifu, G., Yupeng, Z. and Weicheng, F. (2007) The influence of different external heating ways on pyrolysis and spontaneous ignition of some woods. *Journal of Analytical and Applied Pyrolysis, 78*(1), pp. 40-45.

[132] Jowsey, A. (2006) *Fire imposed heat fluxes for structural analysis*. Unpublished PhD Thesis, The University of Edinburgh.
[133] Heselden, A. J. M., Smith, P. G. and Theobald, C. R. (1966) *Fires in a Large Compartment Containing Structural Steelwork. Detailed Measurements of Fire Behaviour.* Fire Research Note.
[134] Lie, T. (1974) Characteristic temperature curves for various fire severities. *Fire Technology, 10*(4), pp. 315-326.
[135] ASTM (2014) ASTM E 119 Standard Test Methods for Fire Tests of Building Construction and Materials. in,West Conshohocken, PA: ASTM International.
[136] Lie, T. (1988) *Fire Temperature-time relations*.
[137] Torero, J. L., Majdalani, A. H., Abecassis-Empis, C. and Cowlard, A. (2014) Revisiting the Compartment Fire. *Fire Safety Science, 11*, pp. 322-322.
[138] Waterman, T. E. (1968) Room flashover—Criteria and synthesis. *Fire Technology, 4*(1), pp. 25-31.
[139] Hägglund, B., Jansson, R. and Onnermark, B. (1974) *Fire development in residential rooms after ignition from nuclear explosions*: Foersvarets Forskningsanstalt, Stockholm (Sweden).
[140] Babrauskas, V. (1980) Estimating room flashover potential. *Fire Technology, 16*(2), pp. 94-103.
[141] Thomas, P. H. (1981) Testing products and materials for their contribution to flashover in rooms. *Fire and Materials, 5*(3), pp. 103-111.
[142] McCaffrey, B., Quintiere, J. and Harkleroad, M. (1981) Estimating room temperatures and the likelihood of flashover using fire test data correlations. *Fire Technology, 17*(2), pp. 98-119.
[143] Thomas, P. H., Heselden, A. and Law, M. (1967) *Fully-developed Compartment Fires: Two Kinds of Behaviour,* HM Stationery Office.
[144] Thomas, P. H. and Heselden, A. (1972) *Fully-developed fires in single compartments*. Fire Research Note.
[145] Tewarson, A. (2002) Generation of heat and chemical compounds in fires. *SFPE handbook of fire protection engineering, 3*, pp. 83-161.
[146] Hagglund, B. and Persson, L. (1974) An experimental study of the radiation from wood flames. *Försvarets Forskningsanstalt Huvudenhet, FoU-brand, Stockholm*.
[147] ASTM (2013) ASTM E 2058 Standard Test Methods for Measurement of Material Flammability Using a Fire Propagation Apparatus (FPA). in,West Conshohocken, PA: ASTM International.
[148] Comeford, J. (1972) The spectral distribution of radiant energy of a gas-fired radiant panel and some diffusion flames. *Combustion and Flame, 18*(1), pp. 125-132.
[149] Grosshandler, W. and Monteiro, S. (1982) Attenuation of thermal radiation by pulverized coal and char. *Journal of Heat Transfer, 104*(4), pp. 587-593.
[150] Incropera, F. and DeWitt, D. (2002) *Fundamentals of Heat and Mass Transfer,* 5th ed., New York: John Wiley and Sons.
[151] CEN (2002) Eurocode 1. Actions on structures. in *Part 1-2: General actions – Actions on structures exposed to fire*,Brussels: European Committee for Standardisation.

[152] Frangi, A. and Fontana, M. (2005) Fire performance of timber structures under natural fire conditions. in *Fire Safety Science Symposium*.
[153] Frangi, A., Bochicchio, G., Ceccotti, A. and Lauriola, M. P. (2008) Natural full-scale fire test on a 3 storey XLam timber building. in *Proceedings of 10th world conference on Timber Engineering (WCTE), Miyazaki, Japan*.
[154] Li, X., McGregor, C., Medina, A., Sun, X., Barber, D. and Hadjisophocleous, G. (2016) Real-scale fire tests on timber constructions. In Paper Presented to the World Conference on Timber Engineering, Vienna, Austria.
[155] McGregor, C., Hadjisophocleous, G. and Craft, S. (2013) Contribution of Cross Laminated Timber Panels to Room Fires. In Paper Presented to the Interflam, University of London.
[156] Li, X., Zhang, X., Hadjisophocleous, G. and McGregor, C. (2014) Experimental Study of Combustible and Non-combustible Construction in a Natural Fire. *Fire Technology*, pp. 1-28.
[157] Hox, K. and Baker, G. (2016) Full-scale fire test of CLT structure used for student housing. In Paper Presented to the 14th International Conference and Exhibition on Fire Science and Engineering, Interflam, Nr Windsor, UK.
[158] Crielaard, R., van de Kuilen, J.-W., Karel, T., Ravenshorst, G., Steenbakkers, P. and Breunese, A. (2016) Self-extinguishment of cross-laminated timber. In Paper Presented to the World Conference on Timber Engineering, Vienna, Austria.
[159] Torero, J. (2016) Flaming ignition of solid fuels. in *SFPE Handbook of Fire Protection Engineering*: Springer. pp. 633-661.
[160] Bartlett, A., Hadden, R., Bisby, L. and Law, A. (2015) Analysis of cross-laminated timber charring rates upon exposure to non-standard heating conditions. In Paper Presented to the Fire and Materials, San Francisco, CA.
[161] Boulet, P., Parent, G., Collin, A., Acem, Z., Porterie, B., Clerc, J. P., Consalvi, J. L. and Kaiss, A. (2009) Spectral emission of flames from laboratory-scale vegetation fires. *International Journal of Wildland Fire, 18*(7), pp. 875-884.
[162] ASTM (2003) ASTM D 4442-92 Standard Test Methods for Direct Moisture Content Measurement of Wood and Wood-Base Materials. in,West Conshohocken, PA: ASTM International.
[163] Mowrer, F. W. (2005) An analysis of effective thermal properties of thermally thick materials. *Fire Safety Journal, 40*(5), pp. 395-410.
[164] Gross, U., Spindler, K. and Hahne, E. (1981) Shapefactor-equations for radiation heat transfer between plane rectangular surfaces of arbitrary position and size with parallel boundaries. *Letters in heat and mass transfer, 8*(3), pp. 219-227.
[165] Emberley, R., Do, T., Yim, J. and Torero, J. L. (2017) Critical heat flux and mass loss rate for extinction of flaming combustion of timber. *Fire Safety Journal, 91*, pp. 252-258.
[166] Maluk, C., Linnan, B., Wong, A., Hidalgo, J. P., Torero, J. L., Abecassis-Empis, C. and Cowlard, A. (2017) Energy distribution analysis in full-scale open floor plan enclosure fires. *Fire Safety Journal, 91*, pp. 422-431.
[167] Smith, P. and Thomas, P. (1968) *The Rate of Burning of Cribs of Wood*. Fire Research Note. Borehamwood.

[168] Hu, L., Li, Y., Wang, H. and Huo, R. (2006) An empirical equation to predict the growth coefficient of burning rate of wood cribs in a linear growth model. *Journal of Fire Sciences, 24*(2), pp. 153-170.
[169] Hidalgo, J. P., Maluk, C., Cowlard, A., Abecassis-Empis, C., Krajcovic, M. and Torero, J. L. (2017) A Thin Skin Calorimeter (TSC) for quantifying irradiation during large-scale fire testing. *International Journal of Thermal Sciences, 112*, pp. 383-394.
[170] Laschutza, T. (2017) *Numerical and experimental investigation of a Thin Skin Calorimeter (TSC)*. Unpublished MSc, University of Edinburgh, Edinburgh, UK.
[171] Maluk, C., Bisby, L., Krajcovic, M. and Torero, J. L. (2016) A Heat-Transfer Rate Inducing System (H-TRIS) Test Method. *Fire Safety Journal*.
[172] OIML (2000) OIML R 60 - Metrological Regulation for Load Cells in,Paris: International Organization of Legal Metrology.
[173] Janssens, M. (2002) Calorimetry. *SFPE Handbook of Fire Protection Engineering, 3*, pp. 3-38.
[174] Emmons, H. W. (1995) Vent flows. *SFPE Handbook of fire protection engineering, 29*, pp. 4.20-4.
[175] Karlsson, B. and Quintiere, J. (1999) *Enclosure fire dynamics,* CRC press.
[176] Veloo, P. S. and Quintiere, J. G. (2013) Convective heat transfer coefficient in compartment fires. *Journal of Fire Sciences, 31*(5), pp. 410-423.